

FIRST 5 TOWER WIMP-SEARCH RESULTS FROM THE CRYOGENIC
DARK MATTER SEARCH WITH IMPROVED UNDERSTANDING OF
NEUTRON BACKGROUNDS AND BENCHMARKING

by

RAUL HENNINGS-YEOMANS

A dissertation submitted in
partial fulfillment of
the requirements for the degree of
Doctor of Philosophy
in the subject of

Physics

CASE WESTERN RESERVE UNIVERSITY

Cleveland, Ohio

January 2009

**CASE WESTERN RESERVE UNIVERSITY
SCHOOL OF GRADUATE STUDIES**

We approve the thesis/dissertation of the Ph. D. candidate:

Raul Hennings-Yeomans

Daniel S. Akerib, Committee Chair
Department of Physics, Chair

Thomas Shutt
Department of Physics

Corbin E. Covault
Department of Physics

Christopher Mihos
Department of Astronomy

(Date) July, 2008

Copyright © 2008 by Raul Hennings-Yeomans
All rights reserved

Contents

1	The Dark Matter problem	19
1.1	Introduction	19
1.2	Evidence at Scales of Galaxies	20
1.2.1	Spiral Galaxies	20
1.2.2	Elliptical Galaxies	23
1.3	Clusters of Galaxies	24
1.4	Gravitational Lensing	25
1.5	Studies of the Early Universe	29
1.5.1	Big Bang Nucleosynthesis	30
1.5.2	The Cosmic Microwave Background Radiation	33
1.6	Observations of Type Ia Supernovae	37
1.7	Large-scale Structure Formation	38
1.8	Dark Matter particle candidates	42
1.8.1	WIMP Candidates From Particle Physics: SUSY	44
1.8.2	Expected WIMP relic density	46
1.8.3	Axions	49
2	WIMP Detection	53
2.1	Direct detection experiments	54
2.1.1	Cryogenic Particle Detectors	63
2.1.2	Noble liquid detectors	65
2.1.3	Directional Detectors and Other Technologies	67
2.1.4	The DAMA annual modulation	68
2.2	Indirect detection experiments	72
2.2.1	Gamma ray searches	72
2.2.2	Neutrino detectors	73
2.2.3	Cosmic antimatter detectors	75
2.3	New Particles at the High-Energy Colliders	78
3	The Cryogenic Dark Matter Search	82
3.1	Cryogenics	84
3.2	Measurement of the Ionization Energy	86
3.3	Measurement of the Phonon Energy	90

3.4	Background Rejection	94
3.5	Gamma and Neutron Calibrations	97
3.6	Passive and Active Shielding	101
4	CDMS backgrounds	105
4.1	Electromagnetic Backgrounds	106
4.1.1	Ambient photons	106
4.1.2	Surface backgrounds	108
4.2	Neutron Backgrounds	109
4.2.1	Neutrons from Radioactivity	110
4.2.2	Modeling the Cosmogenic Backgrounds	113
4.2.3	Cosmic Rays Underground: the muon generator	117
4.2.4	A 5 Tower and 7 Supertower FLUKA-MCNPX cosmogenic neutron simulation	120
4.2.5	First muon-induced nuclear recoils at Soudan	128
4.2.6	Systematic Uncertainty and Benchmarking	132
5	First 5 Tower Data at Soudan	135
5.1	Event Reconstruction	137
5.2	Charge position correction	138
5.3	Phonon position correction	140
5.4	Analysis pipeline	143
5.4.1	Blinding Cut	144
5.4.2	Quality Cuts	146
5.4.3	Fiducial Volume Cut	149
5.4.4	Thresholds	150
5.4.5	Singles Cut	151
5.4.6	Yield Bands	154
5.4.7	Veto Cut	156
5.4.8	Timing Cut	159
5.5	WIMP search results	161
6	An Underground Cosmogenic Neutron Detector	165
6.1	Introduction	165
6.2	Underground Neutron Data	166
6.3	Principle of the Instrument	169
6.4	Instrument Design Studies	171
6.5	Statistical Predictors of the Neutron Leakage	184
6.6	A new background predictor for CDMS at Soudan	187
6.7	Gd-loaded water as detector medium	189
6.8	Prospects for the Cosmogenic Neutron Detector Benchmarks	194
7	Conclusions and Prospects for CDMS at Soudan	197

List of Tables

1.1	The spectrum of particles predicted by the minimal supersymmetric standard model [43]. The neutralino is most probably the lightest supersymmetric particle in the MSSM (Minimal Supersymmetric Standard Model) and a good WIMP candidate [50].	45
2.1	Lifetimes of the singlet and triplet excimer states for neon, argon and xenon [87, 88].	66
4.1	The U/Th contamination levels in parts per billion (ppb g/g) of the main cold hardware components, icebox, inner polyethylene and gamma-ray shield (Pb) of the CDMS-II experiment.	111
4.2	Neutron flux and multiplicity counted at the outside of the simulated CDMS-II veto system from the FLUKA simulation equivalent to 14 years of underground muons in a model of the Soudan cavern.	125
4.3	Results from the FLUKA-MCNPX simulation equivalent to 14 years of underground muons in a model of the Soudan cavern with the 5 Tower CDMS-II (4.74 kg of Ge, 1.1 kg of Si) and a 7 Supertower (26.67 kg of Ge) target mass. All errors in the table are statistical.	127
4.4	Runs 123 and 124 veto-coincident nuclear recoil events [181]	131
4.5	Comparison between veto-coincident data from runs 123 and 124 and the FLUKA-MCNPX cosmogenic neutron simulation.	132
5.1	Analysis thresholds in keV for the ZIP detectors used in Run 123 [195]. The rows correspond to each ZIP detector and the columns to each tower. Ge detectors are in bold and the rest are Si detectors.	152
5.2	Analysis thresholds in keV for the ZIP detectors used in Run 124 [195]. The rows correspond to each ZIP detector and the columns to each tower. Ge detectors are in bold and the rest are Si detectors.	152

List of Figures

1.1	Two-component fits to the universal rotation curve of galaxies. The dotted line corresponds to the galaxy disk, the dashed line to the halo and the solid to the universal rotation curve. Figure from [3].	22
1.2	Snapshots of two equal mass spiral galaxies merging into a single elliptical galaxy. Figure from [10].	23
1.3	Line-of-sight velocity dispersion profiles. The lower and upper thin (green) curves represent the predictions of Romanowsky et al. [9], respectively without and with dark matter. Figure from [10].	24
1.4	Galaxy Cluster Abell 2218 with Giant Luminous Arcs and many arclets, imaged with the Hubble Space Telescope.	26
1.5	The spectroscopically measured velocity dispersion σ_P vs. the dark matter velocity dispersion σ_{DM} . The error bars shown are at 1σ . The dotted line indicates a slope of one. Figure from [46].	27
1.6	Mass to light ratio as a function of scale. The horizontal dashed lines correspond to different matter densities. The mass-to-light ratios stay constant at approximately $\Omega_m = 0.3$ after $R \sim 1$ Mpc. The plotted points for rich clusters, Morgan groups, Hickson groups, CfA groups, spirals and ellipticals are median values of these samples. The plotted circles are values for the clusters studied by [45]. Figure from [46, 47, 48].	28
1.7	Hubble diagram of distance vs. velocity by the Hubble Space Telescope Key Project. A slope of $H_0=72$ is shown, flanked by $\pm 10\%$ lines. The bottom box shows the Hubble constant vs distance and the horizontal line is the best fit to data. Figure from [18].	30
1.8	Predictions and measurements of the baryon density from big bang nucleosynthesis for deuterium, ^3He and lithium. The solid vertical band is constrained by the primordial measurements of deuterium. Note that even relatively large errors in deuterium measurements give small errors on the baryon density. Figure from [17].	31
1.9	The spectrum of the Cosmic Microwave Background as measured by the FIRAS instrument on board of the COBE satellite. The measured temperature by the COBE team was 2.728 ± 0.004 K. Error bars on the measurement are smaller than the thickness of the line. Figure from [20].	34

1.10	North (left) and South (right) sky maps of the temperature of the Cosmic Microwave Background as measured by WMAP. Figure from [21].	35
1.11	WMAP power spectrum in black compared with other measurements of the CMB power spectrum such as Boomerang [22], Acbar [23], CBI [24] and VSA [25]. Figure from [21] and references therein.	36
1.12	The normalized matter (Ω_m) versus the energy density (Ω_Λ) for three independent sets of observations: high-redshift supernovae, galaxy cluster surveys, and the cosmic microwave background. These three independent observations converge near $\Omega_m = 0.3$ and $\Omega_\Lambda = 0.7$. The black diagonal with a negative slope indicates the expectation from a flat cosmos ($\Omega_m + \Omega_\Lambda = 1$ or Λ CDM model). The small yellow contour in this region indicates how SNAP, a satellite experiment, is expected to deliver on the sensitivity to this parameters. Figure from [30].	39
1.13	The 2dF Galaxy Redshift Survey (2dFGRS) projected distribution of galaxies (about 250000) as a function of redshift. The 2dFGRS has provided the first clear detection the redshift-space clustering anisotropy on large scales. Figure from [31].	40
1.14	The mass power spectrum predicted with a range of parameters consistent with the WMAP-only parameters (shown as the band with a width determined by the 68% confidence interval) compared with the mass power spectrum as measured by the SDSS galaxy survey [32]. The figure shows that the Λ CDM model, when normalized to observations at $z \sim 1100$, accurately predicts the large-scale properties of the matter distribution in the nearby Universe. Figure from [29].	41
1.15	The bullet cluster (right) passing through the cluster on the left. The hot gas that is stripped off the colliding clusters is colored in red-yellow. The green and white curves denote the levels surfaces of gravitational lensing convergence; the two peaks of this do not coincide with those of the gas which is mostly all the mass, but are skewed in the direction of the galaxy concentrations. The white bar corresponds to 200 kpc. Figure from [39].	43
1.16	Comoving number density of WIMPs in the early Universe. Dashed lines correspond to the forming relic abundance of WIMPs, and the solid curve corresponds to the equilibrium abundance. Shortly after T drops below m_χ , the number density of WIMPs drops exponentially, and the rate for annihilation of χ 's ($\Gamma = \langle \sigma_{A\nu} \rangle n_\chi$) drops below the expansion rate, $\Gamma \lesssim H$. At this moment, WIMPs no longer annihilate and fall out of equilibrium, forming a relic cosmological abundance that remains at present times. Figure from [59].	47
1.17	The 90% confidence upper limit on axion-to-photon conversion power and coupling $g_{a\gamma\gamma}$, assuming an axion halo density of 0.45 GeV/cm^3 . Figure from [65].	51
2.1	The Helm form factors for Ge, Si and Xe as a function of recoil energy [142].	58

2.2	Integrated interaction rates for Ge (dashed line), Si (solid line) and Xe (dash dotted line). In order to take advantage of the cross section enhancement for spin-independent interactions, which goes as A^2 , a low threshold is necessary together with a heavy target nuclei [143].	59
2.3	The triangle depicts the energy after a nuclear recoil interaction from a WIMP, each corner represents a channel where the energy from the interaction appears. Each detection technique exploits one or more of these channels. Most of the energy goes into phonons and ionization, the two channels used by CDMS and EDELWEISS. Figure from[76].	62
2.4	Ionization energy as a function of recoil energy. The upper band (blue) are events from a ^{133}Ba source, and the lower band (green) contains events from a ^{252}Cf source[142]. Note that there are some green events in the upper blue band. This is because the ^{252}Cf neutron source emits a significant amount of gamma-rays in addition to the low-energy neutrons.	64
2.5	The residual single-hit events in the 2–4, 2–5 and 2–6 keV energy intervals for the DAMA/NaI and DAMA/LIBRA experiments with an exposure of 0.53 and 0.29 ton-year, respectively. The zero of the time scale is January 1st. The solid lines correspond to the superimposed cosinusoidal functions $A\cos[\omega(t-t_0)]$ with a period of one year, a phase $t_0 = 152.5$ days (June 2nd) and with an amplitude A (0.0215 ± 0.0026) cpd/kg/keV, (0.0176 ± 0.0020) cpd/kg/keV and (0.0129 ± 0.0016) cpd/kg/keV for the (2–4) keV, for the (2–5) keV and for the (2–6) keV energy intervals, respectively[102].	70
2.6	The event rate produced by neutrinos from WIMP annihilations in the Sun in a kilometer-scale detector such as IceCube as a function of the effective WIMP elastic scattering cross section for several annihilation modes. The dashed, solid and dotted lines correspond to a WIMP mass of 100, 300 and 1000 GeV respectively [51].	75
2.7	The fraction of the positron flux relative to the sum of positrons and electrons flux together with what is expected from dark matter annihilations compared to the measurement of the HEAT experiment [120]. The WIMP masses considered are for 100, 300 and 600 GeV. In the left plot, the WIMPs originate from $b\bar{b}$ annihilations. On the right plot, WIMPs are originated from a mixture of ZZ and W^+W^- . In order to make the HEAT data comparable to the expected WIMP annihilations, a cross section of $\sigma v = 3 \times 10^{-26}$ cm ³ /sec and a local density of 0.3 GeV/cm ³ is assumed together with a factor of 50 or more “boost factor”. The solid line corresponds to a Galactic cosmic ray model [123].	77
2.8	The interstellar flux of secondary antideuterons (solid curve starting at $T_{\bar{D}}$ of ~ 0.3 GeV/n) decreases at lower energy (the background) and the energy spectrum of the antideuterons from WIMP annihilations (curves a to d) remain approximately constant at low energy [124]. Figure from [125]. . .	78

2.9	The possible reach of the next generation of direct and indirect neutralino dark matter searches. (a) <i>Top left</i> : Direct Searches, (b) <i>Top right</i> : Indirect Searches via high-energy neutrinos from the Sun, (c) <i>Bottom Left</i> : Indirect Searches via a gamma-ray line from the Galactic halo, (d) <i>Bottom Right</i> : Indirect Searches looking for antideuteron component in cosmic rays. The y-axis, the neutralino component, is expressed by the ratio of the gaugino and higgsino fractions $Z_g/(1 - Z_g) = Z_g/Z_h$. The green full dots are values that can be reached in the respective search, the blue triangles are values that some but not all can be reached and red open circles correspond to values that none of the searches can reach [129, 130].	79
2.10	The range of mass of the heavy CP-odd Higgs for the benchmark model LCC1 is shown in the case of constraints from collider data only (left) and also the effect of combining the collider data together with direct detection data from the Supercdms 25 kg experiment [132]. The mass of the distribution for the CP-odd Higgs, when combined with the proposed CDMS 25 kg experiment, improves dramatically for LHC and also there is even mild improvement with measurements of the LHC+ILC.	81
3.1	A ZIP detector such as those used in the Cryogenic Dark Matter Search at the Soudan Underground Laboratory. The detector, inside its hexagonal copper housing has nearly cylindrical shape with 1 cm thickness, 3 inch diameter, and masses of 250 g in the case of Ge and 100 g for Si.	83
3.2	Drawing of the laboratory space assigned to CDMS-II at the Soudan Underground Laboratory, in Soudan, Minnesota.	85
3.3	The innermost copper can with a “tower” consisting of a stack of six detectors. Note that there is no material in between the top and bottom faces of the detectors. The tower has four nominal temperature stages: 4 K, 600 mK, 50 mK and base. The FET cards are the cold electronics for the ionization channels, the SQUIDS are the readout for the phonon channels and are mounted on the 600 K stage.	87
3.4	The charge energy measurement of the ZIP detector for the ^{133}Ba gamma calibration source used in CDMS-II. The mean of each gamma-line is shown and additionally the standard deviation of a gaussian fit for the 356 keV line.	88
3.5	A neutron activation-induced gamma line observed in the Ge detectors after neutron calibrations. A resolution of $\sim 5\%$ is observed in Ge detectors at the low energy scale using the ^{71}Ga line at 10.36 keV from neutron activation of ^{70}Ge with a halflife of 11.4 days. The mean and standard deviation of a gaussian fit are shown in green [140].	89
3.6	(a) Charge side of a CDMS ZIP detector. The inner and outer electrodes are shown. (b) Phonon side of the detector showing the four quadrants A, B, C and D. In each quadrant there are 37 dies and each of these dies contains 28 QETs. (c) shows a die and (d) shows a QET which consists of 1 μm wide tungsten strip connected to 8 aluminum fins.	91

3.7	Drawing of the cross section of the ZIP detector showing the Ge/Si substrate, the aluminum fin and the tungsten. Quasiparticle diffusion occurs when ballistic phonons with a frequency higher than 82 GHz break the Cooper pairs in the Al and cause quasiparticle production for which a smaller energy gap in the tungsten region allows diffusion to the tungsten TES. The TES is operated at its transition temperature and tends to increase in resistance when energy is deposited and cooper pairs broken. Electrothermal feedback reduces the Joule heating that maintains the TES in its transition. This feedback forms the pulse that is produced by a particle interaction in the Ge/Si substrate.	92
3.8	The phonon energy as measured by a CDMS ZIP detector when it was exposed to a ^{133}Ba gamma-ray source. The resolution for the 356 keV line is about 3 times worse than the ionization measurement resolution.	93
3.9	Ionization yield for a gamma calibration source ^{133}Ba . Most of the gammas are centered around a yield value of 1, while the green dots, which correspond to surface events, leak into the 2σ nuclear recoil band (dotted purple line) around a yield value of 0.3.	95
3.10	The CDMS ZIP detector pulses are shown for an event. The four phonon pulses (one for each quadrant) are shown, together with the two ionization pulses (the inner and outer electrodes). The biggest phonon pulse corresponds to the quadrant in which the event occurred. Also it is shown graphically how the primary delay and primary risetime are defined. Figure courtesy of J. Filippini.	97
3.11	In this plot it is shown how the timing parameter can help discriminate between electron recoils (red dots from a ^{133}Ba calibration) from the neutron events (blue circles from a ^{252}Cf calibration). The black crosses are surface events. The black box contains only neutron events and indicates the acceptance window for WIMPs. The ionization yield and the timing parameter that utilizes the phonon rise time is what gives the ZIP detector the sensitivity for WIMP nuclear recoils.	98
3.12	Gamma calibration data using a ^{133}Ba gamma-ray source (black) compared to a GEANT4 Monte Carlo simulation (red) for a Ge detector. There is good agreement between data and simulation [147].	99
3.13	Comparison between neutron calibration data (^{252}Cf neutron source) and GEANT3 Monte Carlo simulations. The events correspond to single scatters in Ge detectors [149].	100
3.14	Comparison between neutron calibration data (^{252}Cf neutron source) and GEANT3 Monte Carlo simulations. The events correspond to single scatters in Si detectors [149].	100
3.15	Thickness vs Incident Neutron Energy. The thickness is referred to a hydrogenated material such as water or polyethylene with a density of 1 g/cm^3 . The curves correspond to the final neutron energy achieved after traveling a certain thickness (y-axis) and beginning with an incident energy (x-axis).	102

3.16	The CDMS shield top and side views. The blue in the figure corresponds to the polyethylene shield, the gray and dark gray to the Pb layer and the green to the plastic scintillator panels. The outer polyethylene has a thickness of 40 cm, the Pb layer is 27 cm thick with the inner 4.5 cm being ancient Pb with reduced activity from ^{210}Pb ($T_{1/2} = 22$ years). The inner polyethylene layer has a thickness of 10 cm.	104
4.1	Comparison of the Q-inner energy spectra between Monte Carlo simulations of the main radionuclide contaminants in CDMS (^{238}U , ^{232}Th , ^{60}Co and ^{40}K) with data from Tower 3 Ge detectors [151].	108
4.2	Energy spectra summed over the Ge ZIP detectors for events before the neutron calibration (black histogram) and after the two days following the neutron calibration was taken (red histogram). The 511 keV line shows evidence of neutron activation of ^{64}Cu [154].	109
4.3	Energy spectrum of the neutron flux produced by (α , n) reactions in the Copper (cold hardware and icebox cans) of the CDMS-II experiment [158].	112
4.4	Energy spectrum of the neutron flux produced by (α , n) reactions in the inner polyethylene layer of the CDMS-II shield [158].	112
4.5	Vertical muon intensity as a function of underground depth in units of meters of water equivalent (mwe) [162].	115
4.6	Neutron yield as a function of muon energy. Data at different sites is shown in black circles. The fit obtained with FLUKA in this work is the solid (red) line, and the fit obtained with FLUKA by Wang and coworkers [216] is the dashed line (blue). For the references on the data, see Wang et al. [216]. .	117
4.7	Vertical muon intensity as a function of depth. The data corresponds to Crouch (open diamonds) [170], Baksan (open squares) [171], LVD (open circles) [169] and Frejus (filled circles) [167]. Figure from [163]. The shaded region corresponds to muons produced by neutrinos (upper line) and by vertically upward muons (lower line). Figure from [172].	118
4.8	Angular (left) and energy (right) distributions of the muons as they crossed the rock-cavern boundary. The muon generator by Yellin [175] was used as input to model the cosmic rays and their secondaries at the Soudan Underground Laboratory.	120
4.9	Angular distribution produced by the muon generator by Yellin (dotted) [175] compared to that of the muon generator based on measurements of the slant depth distribution by Kasahara [179] and MUSIC [180].	121
4.10	Energy spectrum produced by the muon generator by Yellin (dotted) [175] compared to that of the muon generator based on measurements of the slant depth distribution by Kasahara [179] and MUSIC [180].	121
4.11	A side and top view of the FLUKA and MCNPX geometries. The rock shell has dimensions of $28 \times 24 \times 24 \text{ m}^3$ with the cavern inside being $8 \times 4 \times 4 \text{ m}^3$	124

4.12	<i>Left:</i> Neutron flux above 1 MeV (black solid), above 10 MeV (dashed red) and above 100 MeV (dashed green) at the rock-cavern boundary as a function of energy. <i>Right:</i> Angular distribution of the neutron flux above 1 MeV (black solid), above 10 MeV (dashed red) and above 100 MeV (dashed green) at the rock-cavern boundary	125
4.13	Yield as a function of recoil for the Run 123 veto-coincident neutron data. Gamma-like hits (green crosses) lie mostly around yield of 1. Single betas are represented by red dots and neutron hits by blue dots.	130
4.14	Yield as a function of recoil for the Run 124 veto-coincident neutron data. Gamma-like hits (green crosses) lie mostly around yield of 1. Single betas are represented by red dots and neutron hits by blue dots.	130
4.15	Comparison of the measured neutron spectra by the Karmen (<i>Top</i>) and LVD (<i>Bottom</i>) experiments with the FLUKA simulation by Wang and coworkers [216].	134
5.1	Top view looking into the inside of the icebox (innermost copper can). The five towers are shown with a drawing superimposed on the picture, describing the tower number configuration (T1 for tower one and so forth). The white ring surrounding the innermost copper can corresponds to the inner polyethylene shield (10 cm thick).	136
5.2	The configuration of the five stacks of detectors for each tower. Germanium detectors are colored green and the silicon detectors, orange.	137
5.3	Pulse traces from the phonon and ionization channels for all detectors in one tower (tower 1). The red traces correspond to the sum of the four phonon channels and the blue to the inner electrode channel. The pulses are made from 2048 data points and are digitized at a rate of 1.25 MHz. Figure from [187]	139
5.4	Delay plot of a Ge detector (right) of the corresponding source configuration (left). The calibration sources used were ^{241}Am , which was located between channels A and B. A beta source, ^{109}Cd (small dots), was used as well to mimic electron background surface events. On the figure in the right, the non-circular shape of the source “blobs” is an indication of the loss of position resolution along the radial coordinate. Figure from [188].	140
5.5	Charge collection as a function of y -delay for detector T5Z5 (tower 5, ZIP 5) before (a) and after (b) the position correction. Figure from [189].	141
5.6	Phonon and charge noise spectra for a Ge ZIP detector located in tower 5. The most basic data quality check that is performed just after the data was recorded is to examine the noise level for 500 traces, and the average noise spectra for special features below 2 kHz for the phonon side and below 10 kHz for the charge noise spectra.	147

5.7	A snap shot of “Pipedisplay”, an event display that allows us to evaluate a given event on a run by looking at the traces for all 30 detectors including the veto panel traces on the right. It also includes the fridge base temperature and live time accumulated since the beginning of the run.	148
5.8	Events from a neutron calibration in the inner vs outer electrode space. The Q-inner cut is defined to maximize the inner electrode event population and excluding outer electrode events. The Q-inner cut is made calculating the mean (purple dots) of the Q-outer events as a function of Q-inner energy bins. The cut selects events in the $\pm 2\sigma$ band [193].	150
5.9	Q-inner events as a function of the total phonon energy (pt) for a Ge detector in Tower 1. The events were taken within the first 500 random triggers of the run, and therefore all were consistent with noise. The charge threshold cut is set at $\mu + 4\sigma$ where μ is the mean of the gaussian fit to the Q-inner events, and σ is the standard deviation [194].	151
5.10	Time variation of the mean total phonon noise from the Tower 1 ZIP detectors [196]. The Run 123 and 124 Singles Cut takes into account the variation in the noise by doing a run-by-run estimation of fit parameters used to calculate the low (for tagging multiples) and high phonon thresholds.	153
5.11	Yield as a function of recoil energy in detector T1Z5 (Ge) for events in a gamma calibration data set. The electron recoil band (or gamma band) is centered around ~ 1 (solid red) and the nuclear recoil band is shown as solid blue (see Figure 5.12) [198].	155
5.12	Yield as a function of recoil energy in detector T1Z5 (Ge). The nuclear recoil band is populated with nuclear recoils caused by neutrons from a ^{252}Cf source. There are also events in the electron recoil band that are caused by gammas emitted by the neutron source [198].	156
5.13	Schematic drawing of the CDMS-II veto system that consists of 40 plastic scintillator panels covering the passive shielding, icebox and towers holding the ZIP detectors. The cylindrical structure outside the veto system is the dilution refrigerator.	157
5.14	The charge deposited (black histogram) by cosmic rays and ambient photons in one of the scintillator panels that are part of the veto system. The events that peak at ~ 100 pC correspond mostly to muons passing through the 5 cm thick plastic scintillator. The vertical dashed line is where the veto cut was set for this panel [200].	159
5.15	Delay vs. risetime parameter for a sample of neutron (green dots) and beta (red dots) events. The circled red dots are betas that pass the timing cut (dashed blue). Neutrons and WIMPs are selected by the blue dashed and the two perpendicular black dashed curves [201].	161
5.16	Efficiency (or acceptance) of several cuts as a function of recoil energy. Note that the main steps that reduce the efficiency (about $\sim 40\%$) are the fiducial volume cut and the phonon timing cut.	162

5.17	The ionization yield as a function of recoil energy or all the events in all detectors passing all cuts before (top) and after (bottom) applying the phonon timing cut. The four events that are shown on the bottom plot are able to pass the timing cut but lie outside the 2σ nuclear recoil band where neutrons and WIMPs are expected.	162
5.18	Spin-independent WIMP-nucleon cross-section upper limits at 90% C.L. as a function of WIMP mass. The blue dash-dot upper curve corresponds to the result of a re-analysis [142, 206] of our previously published data. The upper red solid line is the limit from the Run 123 and 124 data analysis. The combined CDMS limit (lower solid black line) has the same minimum cross-section as XENON10 [207] (orange dash) reports, but has more parameter space at higher masses. WIMP masses and cross section ranges expected from supersymmetric models described in [208] (grey) and [209] are shown (95% and 68% confidence levels in green and blue, respectively). Figure courtesy of [210].	164
6.1	Conceptual drawing of the Neutron Multiplicity Meter for Deep Underground Muon-Induced High Energy Neutron Measurements.	171
6.2	Polar angular distribution of the neutrons with energy greater than 60 MeV incident on the CDMSII shield. Neutrons tend to have downward direction at an angle of about 0.88π radians with respect to the normal vector from the floor. Therefore the area of the target is proportional to the rate of incident high energy neutrons.	172
6.3	Neutron fluence plot of a FLUKA simulation that propagates a beam of 100 MeV neutrons on a 60-cm-thick Pb target. The upper and lower rectangles are reference surfaces delimiting the counting boundary for the upper and lower neutrons, respectively. The central rectangle from $z=0$ to 60 is the Pb target. The plot shows more evaporated neutrons going upwards than downwards (the forward direction relative to the beam) due to backscattering. This effect also causes very few neutrons to go forward as the thickness increases above about 20 cm.	173
6.4	Simulation with FLUKA to explore optimal target thickness and position of the Gd-loaded scintillator tank with respect to the Pb target. The parameter P is defined as the fraction of events (relative to the number of 100-MeV incident neutrons) that has 3 or more neutrons of 10 MeV or less going towards the top or the bottom of the Pb target. (See text for details.) Since a given event may have 3 or more neutrons going to the top and 3 or more going to the bottom, it is possible to have $P_{\text{TOP}} + P_{\text{BOTTOM}} > 1$, for example as observed for 40-, 60- and 80-cm thickness.	174

6.5	A FLUKA simulation was done with a fixed target thickness of 100-cm and varying the incident neutron beam energy in order to explore the correlations between the energy of the incident high-energy neutron on the target and the detectable multiplicity. If I reference the beam direction a “downward,” the detectable multiplicity is determined by counting the neutrons that reach a surface just above the Pb target.	176
6.6	The detectable multiplicity from a Pb slab of 200 cm by 200 cm area and 60 cm thickness for the events estimated to be anticoincident with an energy deposition of 2 MeV or more from charged particles, including muons and hadrons. The detectable multiplicity was counted only by looking at neutrons with energy less than 10 MeV going towards a surface on top of the Pb target.	177
6.7	The total number of events as a function of minimum multiplicity. The total number of events changes only by about 10% between a minimum multiplicity of 3 and 10.	178
6.8	Energy spectrum of secondary neutrons produced by high-energy neutrons (flux shown in Fig. 6.2) incident on the Pb target. Neutrons mostly have energy below 5 MeV energy, and indicates that the thickness of the scintillator is not driven by the moderation requirements. Rather, I found that the thickness is driven by the need to efficiently contain the gammas emitted by the Gd.	180
6.9	Simulation with MCNP-PoliMi [183] of the Pb target with Gd-loaded scintillator contained in tanks placed on top of the target. A beam of neutrons with energy 0.5 MeV was propagated from the Pb to the scintillator tank. The thickness of the scintillator tank was varied. Efficiency corresponds to the fraction of incident neutrons for which the energy deposited in the Gd-loaded scintillator by gamma rays is above 3 MeV.	181
6.10	Ambient gammas can mimic a high energy neutron event due to accidental coincidences. The rate of gamma-induced background events is plotted as a function of the multiplicity of the events for a time window of 40 microseconds and three different gamma rates [229].	182
6.11	The CDMS gamma-ray shield, inner polyethylene and a copper cylinder inside of it with a thickness similar to that of the fridge copper cans. In red, a high-energy neutron with an energy of 100 MeV is depicted. The green dotted lines depict low energy neutrons (<10 MeV). The <i>Cap</i> corresponds to a cylindrical surface on top of the Pb shield with a radius equal to that of the outer polyethylene layer (~ 1 m) and a height of 40 cm.	188
6.12	Neutron detector prototype build by the UCSB group. The detector medium is GdCl_3 and there is a 2 in and a 5 in photomultiplier tubes on each end of the cylinder. The cylinder has dimensions of 22 cm in diameter and 61 cm in height [234].	191
6.13	The ^{252}Cf multiplicity probability distribution.	192

6.14 Multiplicity distribution measured from a ^{252}Cf with GdCl_3 doped water. The blue data points correspond to the gamma background induced multiplicity distribution while the red data points correspond to the ^{252}Cf neutron source induced multiplicity distribution [234]. 193

ACKNOWLEDGEMENTS

The completion of this thesis and the work that is described in it, would not have been possible without the teachings, encouragement, support and patience of Dan Akerib. Since the beginning of my work as a graduate research assistant in the summer of 2003, Dan fostered good communication and discussions within the group that favored a smooth and gradual learning curve. The same weekly group meetings “show and tell” discussions on the white board (in the launch room) or the black board (in the Miller room) that allowed us to learn the physics of the CDMS experiment, from practical cryogenics to Supersymmetry, became the floor to talk about our own work progress and propose new ideas that I was fortunate enough to see their fruit. I will certainly miss these group meetings a lot, filled with undergrads (most notably Ben Kreis and Kristin Poinar) postdocs and research associates (Mike Dragowsky and Darren Grant), Profr. Richard Schnee (always making good points) and my fellow graduate student, Cathy Bailey. To all of you, thanks and I will always remember sharing those meetings with you. Special thanks also to Richard Schnee and Steve Yellin who always kept track of most of my work and helped me to be a better physicists too.

To my fellow Soudan teammates, Jeff Filippini, Long Duong, Jonghee Yoo, Jeter Hall, Mike Dragowsky and many more, thanks for your hard work and for making the Soudan trips an enjoyable experience. Special thanks to Jim Beaty, for keeping CDMS running and its crew safe. Also for making the trips such an enjoyable experience (ping-pong, wing nights, weekend barbecues, pool and pizza at your place, etc).

Thanks to Dan Bauer, Bernard Saduolet and Blas Cabrera for your leadership making CDMS a successful experiment over so many drawbacks, particularly over the last 3 years. Thanks to Profr. Harry N. Nelson for your interest in my work, especially on the cosmogenic neutron detector, I have always benefited from our discussions, your experience and your good humor.

Special thanks to Solomon Duki for his friendship and help during the course of the PhD experience, especially during the last year. I enjoyed our physics discussions as well as our multicultural exchanges with respect to Ethiopia (where coffee was invented) and Mexico (where tequila was invented :-)

On a more personal side, the PhD degree at Case Western would not have been possible without the continuous support from Marcela, who was with me “al pie del cañon” even before the qualifying exams. Thanks to my parents, and to Pablo and Dieter, my two brothers, who have always helped me. I enjoyed going to Pittsburgh and Rochester to visit, as well as those times when I was in Cleveland and you guys were around. Also, thanks to “mi nana Licha” (my grandmother) and to Chacha, Manuel, Natalia and Daniel (“la familia Rosales”) for your support, especially during my undergraduate studies. Thanks to my aunt Laura and uncle Acuña both theoretical physicists who have always given me their most generous support and have certainly shaped me as a scientist since my days as an undergraduate in the Department of Physics at University of Sonora in Hermosillo, México. Also to my cousins “China y Calcaneo” for their encouragement in my undergrad years too. To all the Yeomans family, especially to my mother’s sisters, who have always helped me as I grew up in Hermosillo and with my homework during my high-school studies. Special thanks to “Tío Héctor” for your support to Marcela, my brothers and me which has made possible to continue with our academic goals and hence, with our professional careers.

Finally a special thanks to my teachers in University of Sonora, Angelina, Jau-regui, and many others, for your support and encouragement (which was crucial) during my undergrad years. Also, to the mexican particle physicists whose summer internship programs allowed me to be a summer intern at Fermilab in 2002. The internship program, led by Roger Dixon and Erick Ramberg, opened the door of experimental particle physics as a field of study that I decided to follow.

First 5 Tower WIMP-search Results from the Cryogenic Dark Matter Search
with Improved Understanding of Neutron Backgrounds and Benchmarking

Abstract

by

RAUL HENNINGS-YEOMANS

Non-baryonic dark matter makes one quarter of the energy density of the Universe and is concentrated in the halos of galaxies, including the Milky Way. The Weakly Interacting Massive Particle (WIMP) is a dark matter candidate with a scattering cross section with an atomic nucleus of the order of the weak interaction and a mass comparable to that of an atomic nucleus. The Cryogenic Dark Matter Search (CDMS-II) experiment, using Ge and Si cryogenic particle detectors at the Soudan Underground Laboratory, aims to directly detect nuclear recoils from WIMP interactions.

This thesis presents the first 5 tower WIMP-search results from CDMS-II, an estimate of the cosmogenic neutron backgrounds expected at the Soudan Underground Laboratory, and a proposal for a new measurement of high-energy neutrons underground to benchmark the Monte Carlo simulations.

Based on the non-observation of WIMPs and using standard assumptions about the galactic halo [68], the 90% C.L. upper limit of the spin-independent WIMP-nucleon cross section for the first 5 tower run is $6.6 \times 10^{-44} \text{cm}^2$ for a $60 \text{ GeV}/c^2$ WIMP mass.

A combined limit using all the data taken at Soudan results in an upper limit of $4.6 \times 10^{-44} \text{cm}^2$ at 90% C.L. for a $60 \text{ GeV}/c^2$ WIMP mass. This new limit corresponds to a factor of ~ 3 improvement over any previous CDMS-II limit and a factor of ~ 2 above $60 \text{ GeV}/c^2$ better than any other WIMP search to date.

This thesis presents an estimation, based on Monte Carlo simulations, of the nuclear recoils produced by cosmic-ray muons and their secondaries (at the Soudan

site) for a 5 tower Ge and Si configuration as well as for a 7 supertower array. The results of the Monte Carlo are that CDMS-II should expect $0.06 \pm 0.02_{-0.02}^{+0.18}$ /kg-year unvetoes single nuclear recoils in Ge for the 5 tower configuration, and $0.05 \pm 0.01_{-0.02}^{+0.15}$ /kg-year for the 7 supertower configuration. The systematic error is based on the available underground neutron data (that we are aware of) relevant to the unvetoes neutron population. Therefore, for the first 5 tower run, a prediction of < 0.2 events from cosmogenic neutrons was obtained.

Furthermore, this thesis describes a proposal for a new measurement of the absolute flux of high-energy neutrons (>60 MeV) deep underground. The cosmogenic neutron detector could measure, at a depth of 2000 meters of water equivalent, a rate of 70 ± 8 (stat) events/year. Based on these studies, the benefits of using a neutron multiplicity meter as a component of active shielding in experiments with similar background concerns are described.

Chapter 1

The Dark Matter problem

1.1 Introduction

Throughout the history of life on this planet, humans have asked themselves what the world is made of? What is the Universe made of? How did the Universe evolve? Today, inspired by these same questions, we look up at the sky with our most potent telescopes looking at the electromagnetic spectrum to try to understand the cosmos and down into matter with our most potent microscopes –particle accelerators– to understand matter, how it formed and what is made of.

Scientists use particle accelerators to recreate a mini big-bang in the laboratory, searching for new phenomena that will improve our understanding of particle physics that will yield a better understanding of what we see in the cosmos. The Dark Matter problem is a good example of the interplay between particle physics and cosmology into what has become today Astroparticle physics.

In the 1930's Fritz Zwicky [1] made the observation that the galaxies of the Coma cluster move faster than expected if the mass of the cluster was deduced from its luminosity. During the last 70 years this observation has only undergone a small correction and still holds today. Vast observations from scales of galaxies (a few Mpc)

to clusters of galaxies (hundreds of Mpc) have the same problem: the mass that shines falls short in accounting for the gravitational effect. As a solution, Zwicky proposed that there should be a non-luminous matter component that was later referred to as “Dark Matter”. In this chapter a review of the main evidence for Dark Matter is presented including evidence at scales of galaxies, galaxy clusters and evidence in large-scale structure formation. Also it is discussed how studies of the early Universe point towards the conclusion that Dark Matter is not made of any known particle to date. The last section presents the best candidates for dark matter from particle physics beyond the Standard Model.

1.2 Evidence at Scales of Galaxies

In this section the evidence from galaxy dynamics is presented both for spiral and elliptical galaxies. Evidence of Dark Matter halos from galaxies was first presented about 30 years ago when Vera Rubin and W.K. Ford [2] measured the rotation curves of the outermost stars of the Andromeda galaxy.

1.2.1 Spiral Galaxies

Spiral galaxies have of the order of billions of stars, they have a central disc of young stars as well as extended spiral arms in which active star formation is still taking place. They correspond to about 80% of light galaxies in areas of low density, while in core areas of galaxy clusters they are very rare (about 10%). Assuming that the stars in the spiral galaxy have a circular orbit around the center of the galaxy, we can calculate the rotation velocity by equating the gravitational and centrifugal forces using Newtonian dynamics as

$$F = \frac{GmM}{r_s^2} = \frac{mv^2}{r_s} \tag{1.1}$$

where M is the mass contained by the orbit of radius r_s . Therefore, the velocity of the star would be

$$v(r_s) = \sqrt{\frac{GM}{r_s}} \quad (1.2)$$

where the mass of the bulge can be written as $M = \rho V \sim \rho r_s^3$. Therefore, the velocity of a star as a function of the distance from the center of the galaxy can be written as $v(r) \sim r$ for $r < r_s$ and $v(r) \sim r^{1/2}$ for $r > r_s$. Nevertheless, the observations of spiral galaxy rotation curves, for example those shown in Figure 1.1, show that $v(r) = \text{constant}$ after about 5 kpc, which means that $M \sim r$, or in other words, indicates the existence of a large amount of mass extending around the center of the galaxy and extending far beyond the visible region but this mass by itself is optically invisible.

The rotation curves of spiral galaxies can be fitted to a Universal Rotation Curve (URC) that is determined solely by the luminosity as a function of radius [3]. These rotation curves constitute some of the most robust evidence for dark matter halos in galaxies and although some of the “invisible matter” is certainly baryonic –composed of neutrons and protons– for example, faint stars and black holes, there is strong evidence from studies of the early Universe (to be discussed in Section 1.5) that the bulk of Dark Matter is not composed of baryons.

Navarro, Frenk and White [4] (hereafter NFW) have done N-body simulations to predict the structure of dark matter halos on kpc and sub-kpc scales, where it can be compared to observations of galactic dynamics. They have found a “universal” structure between the density profiles of dark matter halos of galaxies independent of mass and of the value of cosmological parameters. The universal density profile proposed by NFW can be written as

$$\frac{\rho(r)}{\rho_{crit}} = \frac{\delta_c}{(r/r_s)(1+r/r_s)^2} \quad (1.3)$$

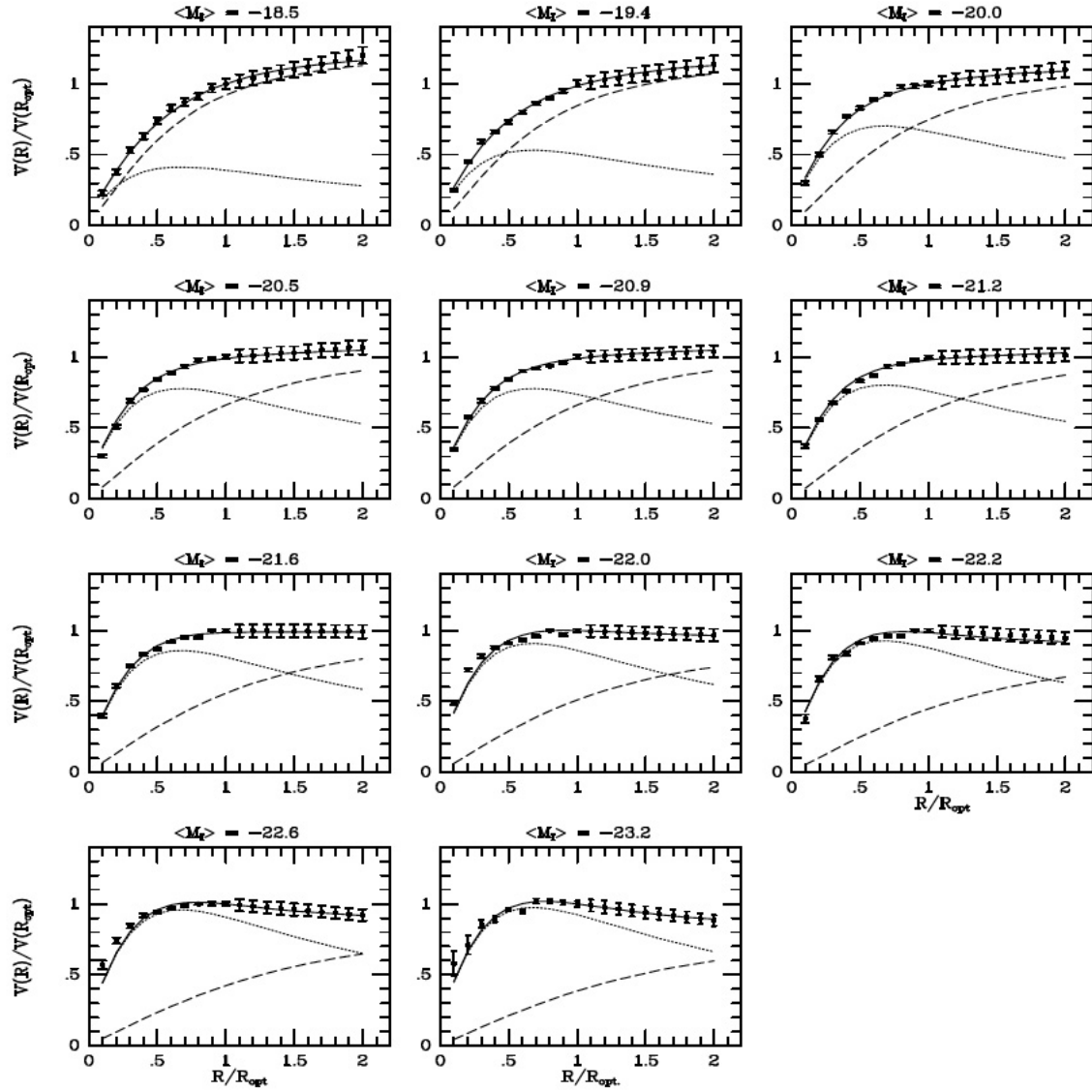


Figure 1.1: Two-component fits to the universal rotation curve of galaxies. The dotted line corresponds to the galaxy disk, the dashed line to the halo and the solid to the universal rotation curve. Figure from [3].

and describes the density profile of *any* halo with only two parameters, a characteristic density contrast δ_c , and a scale radius r_s .

1.2.2 Elliptical Galaxies

It is believed that elliptical galaxies originate from major mergers of spiral galaxies and therefore, they should also contain dark matter halos [5, 6, 7, 8]. The merger of two spiral galaxies in which the initial galaxies had a spherical bulge and a thin exponential disk, as well as a thin gaseous disk and a spherical NFW dark matter halo. The galaxies are made incident at each other (see Figure 1.2) and followed 2-3 Gyr after the final merger. The similarity between the observed and simulated velocity dispersion profiles is shown in Figure 1.3, hence demonstrating that the simulations, including normal amounts of dark matter, reproduce the observed velocity dispersion profiles.

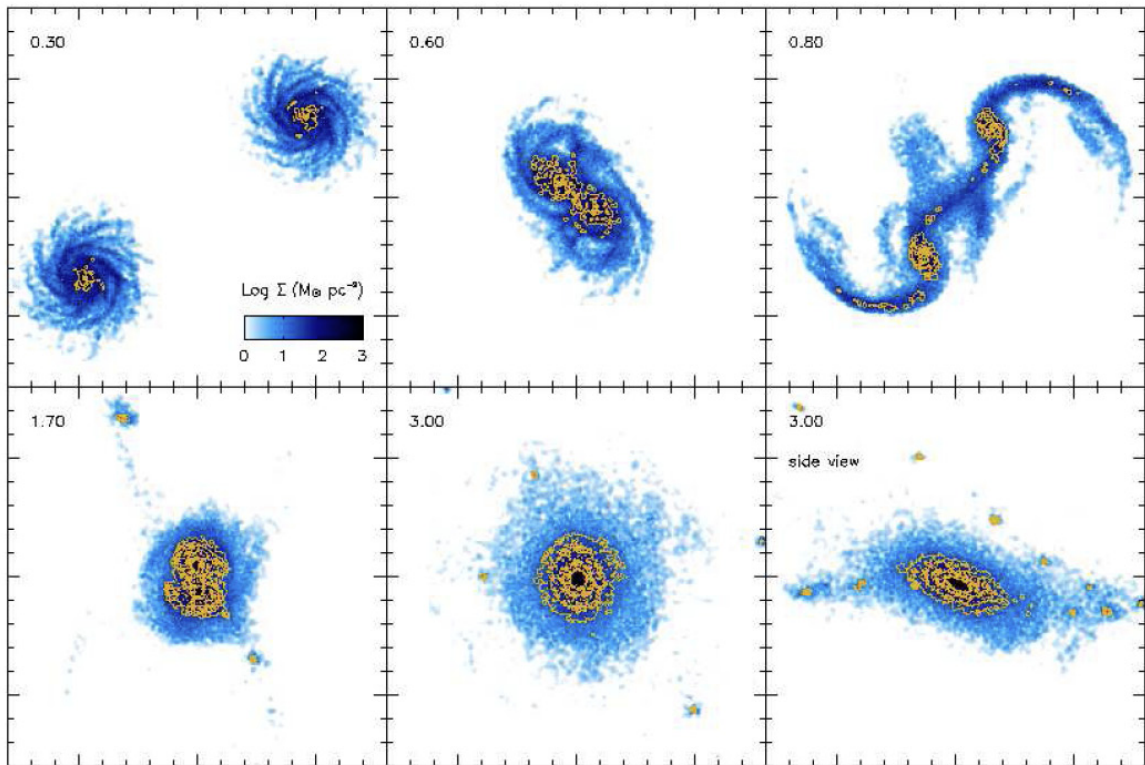


Figure 1.2: Snapshots of two equal mass spiral galaxies merging into a single elliptical galaxy. Figure from [10].

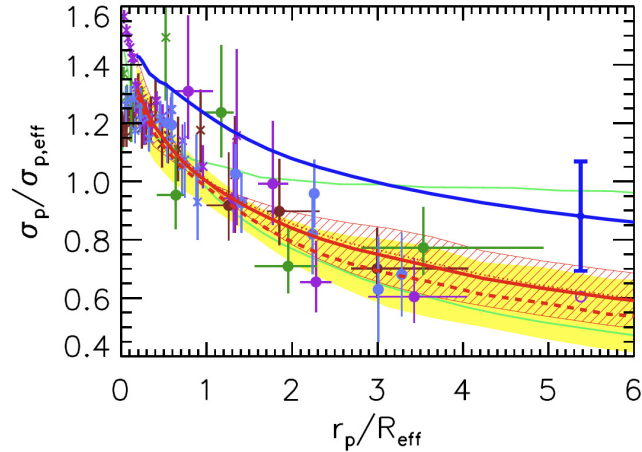


Figure 1.3: Line-of-sight velocity dispersion profiles. The lower and upper thin (green) curves represent the predictions of Romanowsky et al. [9], respectively without and with dark matter. Figure from [10].

1.3 Clusters of Galaxies

Clusters of galaxies are the largest well defined building blocks of the Universe. They are formed by gravitational pull of cosmic matter over a region of several megaparsecs. They contain hundreds to thousands of galaxies to form a total mass up to 10^{15} solar masses. One of the first confrontations between luminous and gravitational matter came from the analysis of the the Coma cluster by Zwicky in 1937 [11]. It was found by Zwicky that the measurement of the velocities and distance of the galaxies yield an estimate on the gravitational mass of the cluster. Other proposed solutions invoke alterations to the gravitational force law [12, 13, 14]. The virial theorem for a central force states

$$2\langle E_{kin} \rangle + \langle E_{pot} \rangle = 0, \quad (1.4)$$

however, the use of the virial theorem implies that the system is closed and in mechanical equilibrium. If we write the kinetic energy of N galaxies in a cluster by

$\langle E_{kin} \rangle = \frac{1}{2}N\langle mv^2 \rangle$, then the potential energy of the cluster would be

$$\langle E_{pot} \rangle = -\frac{1}{2}GN(N-1)\frac{\langle m^2 \rangle}{\langle r \rangle} \quad (1.5)$$

hence the dynamic mass is given by

$$M \simeq \frac{2\langle r \rangle \langle v^2 \rangle}{G}, \quad (1.6)$$

where for large number of galaxies $(N-1) \simeq N$, and $N\langle m \rangle = M$. Hence, by measuring r and v an estimate on the mass of the cluster M can be done. Another method to estimate the mass of the cluster is analyze the X-ray-emitting gas in the intra-cluster medium. Assuming hydrostatic equilibrium, the temperature of the X-ray-emitting gas can be related to the energy in the system which in turn depends on the mass of the cluster. Other methods include the use of gravitational lensing and the Sunyaev-Zeldovich effect to be discussed in section 1.4 and 1.5.2 respectively. All of these methods yield a gravitational mass that is significantly higher than the luminous mass.

1.4 Gravitational Lensing

Einstein deduced with his theory of General Relativity that the deflection angle α of a light ray passing at a distance r from a body of mass M is

$$\alpha = \frac{4GM}{c^2} \frac{1}{r}, \quad (1.7)$$

where G is the gravitational constant and c is the velocity of light. Putting in the values for our Sun, Einstein obtained

$$\alpha_{\odot} = \frac{4GM_{\odot}}{c^2} \frac{1}{R_{\odot}} = 1.74 \text{ arcsec}. \quad (1.8)$$

During a solar eclipse in 1919 Arthur Eddington measured a value within 20% of the prediction, becoming one of the first experimental confirmations of General Relativity [15]. More advanced observations have measured and confirmed the predicted value to better than 0.02% [16]. Today, gravitational lensing -the deflection of light by matter- is a widely used astrophysical tool that is used, for example, to estimate the amount of dark matter in clusters.

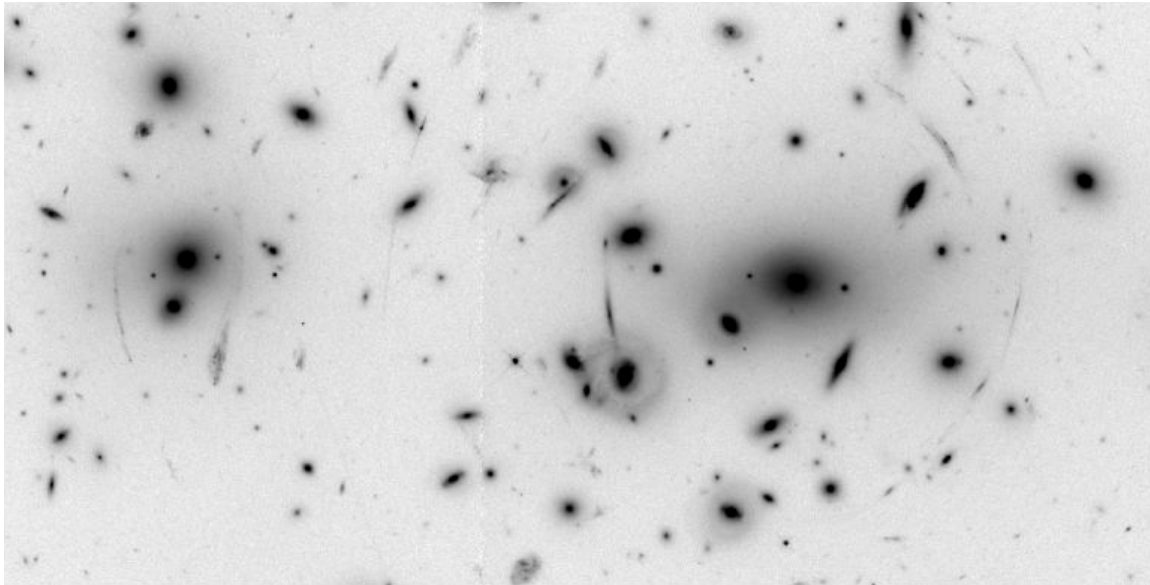


Figure 1.4: Galaxy Cluster Abell 2218 with Giant Luminous Arcs and many arclets, imaged with the Hubble Space Telescope.

Weak gravitational lensing is a method that can be used to measure the mass of a body by knowing that the path of a light bundle passing a gravitational potential will be bent according to the strength of the potential. For example, the images of background galaxies that are near a cluster of galaxies are deflected away from the cluster, becoming enlarged while preserving the surface brightness and distorted tangentially to the center of the potential (also known as gravitational shear). Figure 1.4 shows the galaxy cluster Abell 2218 with luminous arcs of the background galaxy. The gravitational shear effects are used to measure the mass of the structure(s) caus-

ing the lensing. This technique does not assume anything about the dynamical state of the mass and therefore it is particularly robust when applied to a system with an unknown dynamical perturbation. Dahle et al. [45] found, for a sample of 40 clusters, a mass-to-light ratio derived using gravitational lensing of $M/L = 377 \pm 17$.

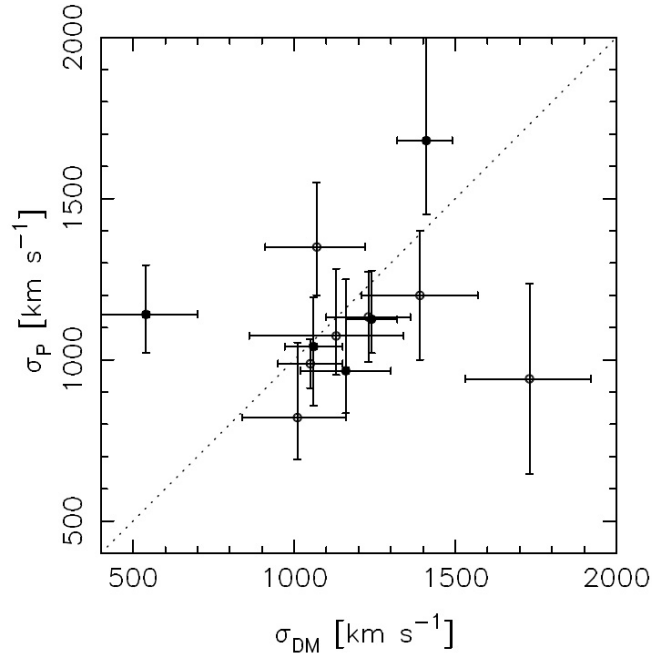


Figure 1.5: The spectroscopically measured velocity dispersion σ_P vs. the dark matter velocity dispersion σ_{DM} . The error bars shown are at 1σ . The dotted line indicates a slope of one. Figure from [46].

Since many of the clusters in the sample studied by Dahle et al. have also been studied using X-ray temperature measurements or galaxy velocity dispersion measurements, it is possible to compare the weak lensing measurements to the velocity dispersion measurements by fitting an isothermal sphere model to the measured shear profiles around the clusters. Figure 1.5 shows the comparison between the dispersion velocities of the galaxies as obtained by X-ray measurements or velocity distribution measurements against the dispersion velocities obtained from weak lensing. The spectroscopically measured velocity dispersion tends to be somewhat larger than the dark

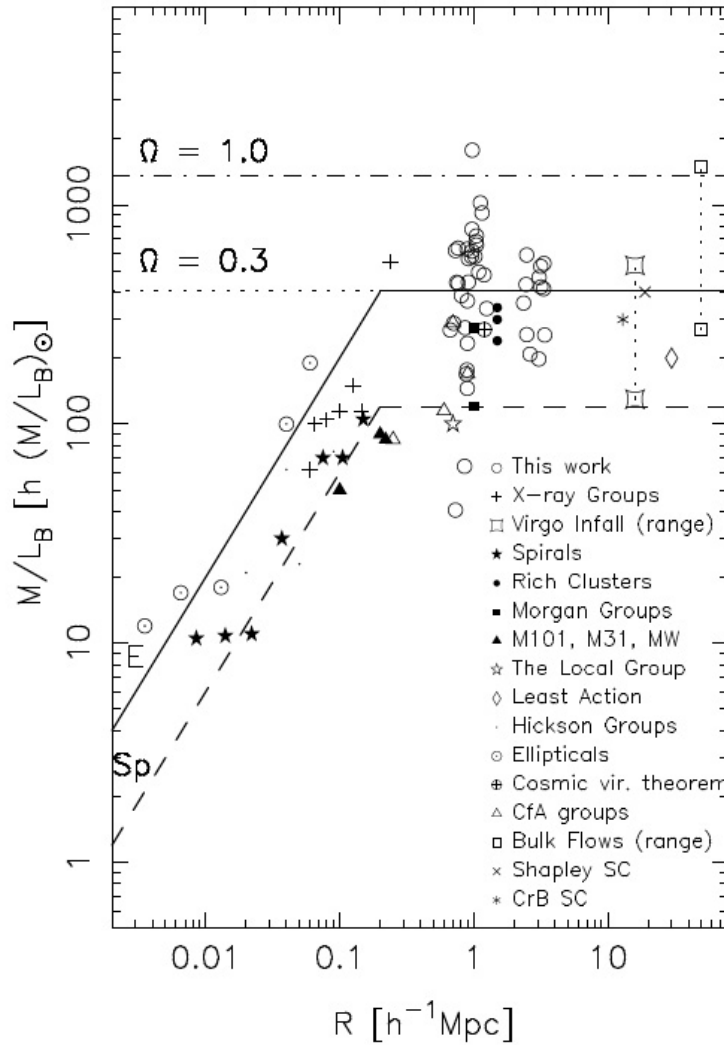


Figure 1.6: Mass to light ratio as a function of scale. The horizontal dashed lines correspond to different matter densities. The mass-to-light ratios stay constant at approximately $\Omega_m = 0.3$ after $R \sim 1$ Mpc. The plotted points for rich clusters, Morgan groups, Hickson groups, CfA groups, spirals and ellipticals are median values of these samples. The plotted circles are values for the clusters studied by [45]. Figure from [46, 47, 48].

matter dispersion (derived from the weak lensing measurements) for about half of the cluster sample, but there is a good agreement between these two methods that further supports the dark matter hypothesis of Zwicky. Figure 1.6 shows the inferred mass-to-light ratio of many systems that have scales ranging from galaxies (10^{-2} Mpc) to superclusters (10 Mpc). Bahcall et al. [48] have found that mass-to-light ratio remains

flat at $\Omega_m = 0.3$ after $R \simeq 1$ Mpc.

1.5 Studies of the Early Universe

In the previous sections we have described astrophysical evidence for Dark Matter from scales of stars within galaxies to galaxies within clusters. In the following sections, I will describe the less intuitive studies of the early universe, starting with big-bang nucleosynthesis, which sheds light on the nature of dark matter, and following with measurements of the cosmic microwave background radiation, which opened the field of precision observational cosmology and has become one of the best tools to study the composition of the universe.

The understanding of the early Universe begins with the observation that almost all galaxy spectra (except those nearby galaxies) are red shifted. The light that we see today was emitted when the Universe was a few billion years old. The luminosity distance d_L and the redshift of a galaxy z can be written in a power series

$$H_0 d_L = z + \frac{1}{2} (1 - q_0) z^2 + \dots \quad (1.9)$$

where $d_L \equiv (L/4\pi F)^2$ and L being the luminosity of the object and F the measured flux. Therefore we can write

$$z = H_0 d_L + \frac{1}{2} (q_0 - 1) (H_0 d_L)^2 + \dots \quad (1.10)$$

where the Hubble constant, $H_0 \equiv (dR/dt) / R(t_0)$ is the expansion rate of the Universe at present time, and $q_0 \equiv -(d^2 R/dt^2) / R H_0^2$ measures the rate at which the Universe is slowing down. The Hubble constant has a value of [18]

$$H_0 = 72h \text{ km sec}^{-1} \text{ Mpc}^{-1} \quad (1.11)$$

$$0.9 \lesssim h \lesssim 1.1. \quad (1.12)$$

The Hubble diagram, shown in Figure 1.7, is the most direct evidence of the expansion of the Universe. The age of the Universe can be measured in a variety of different ways [59], among them by using the expansion rate and computing the time back to the big bang, by dating the oldest stars in globular clusters and by dating the radioactive elements such as ^{238}Th (mean lifetime $\tau = 20.27$ Gyr). All techniques yield results consistently within the range of 10 to 20 Gyr. The current best estimate is 12.6 Gyr, with a 95% confidence level lower limit of 10.4 Gyr [19].

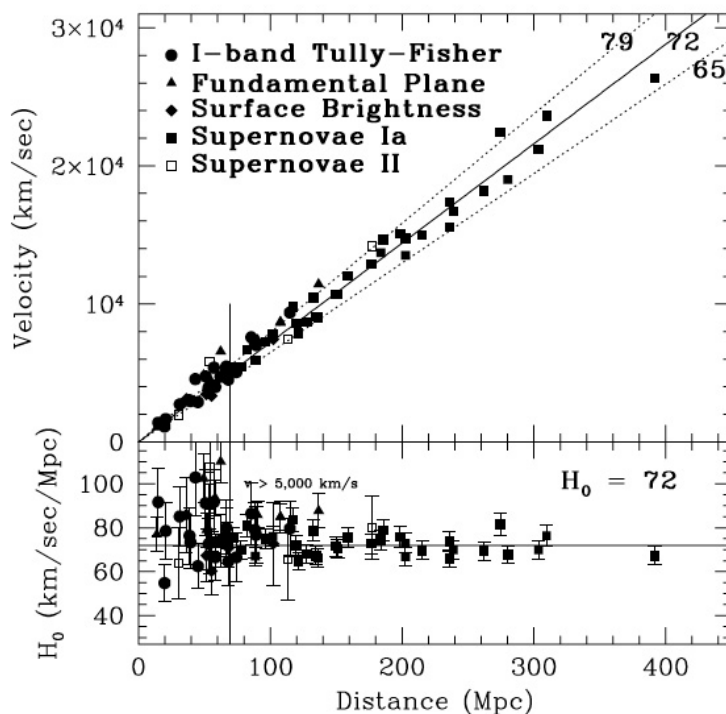


Figure 1.7: Hubble diagram of distance vs. velocity by the Hubble Space Telescope Key Project. A slope of $H_0=72$ is shown, flanked by $\pm 10\%$ lines. The bottom box shows the Hubble constant vs distance and the horizontal line is the best fit to data. Figure from [18].

1.5.1 Big Bang Nucleosynthesis

Studies of big bang nucleosynthesis lead to robust and independent measurement of the baryon density of the Universe, and therefore it is the cornerstone for the existence

of nonbaryonic dark matter. Big bang nucleosynthesis is a nonequilibrium process that took place over the course of a few minutes in an expanding, radiation-dominated plasma with high entropy and many free neutrons [17]. Due to its relevance to the prediction of dark matter, I will describe in the following paragraph, a brief history of the formation of the lightest elements, following the guidelines of S. Burles et al. [17].

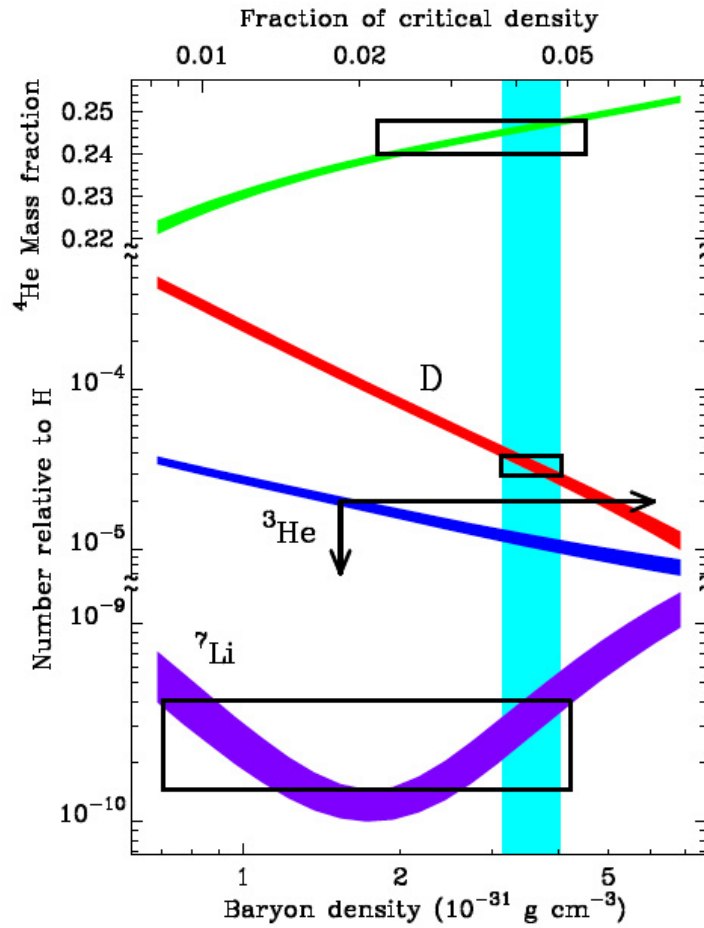


Figure 1.8: Predictions and measurements of the baryon density from big bang nucleosynthesis for deuterium, ${}^3\text{He}$ and lithium. The solid vertical band is constrained by the primordial measurements of deuterium. Note that even relatively large errors in deuterium measurements give small errors on the baryon density. Figure from [17].

At times much less than a second after the big bang, there were roughly equal numbers of electrons, positrons, neutrinos and antineutrinos and photons. The ratio of nucleons to photons was more than a billion to one. The nuclei had not been formed and the ratio of neutrons and protons was unity due to the weak processes that interconvert them and due to the small mass difference of the proton and neutron, for example through reactions like $\nu + n \leftrightarrow p + e^-$. At about one second, when the Universe had cooled to around 10^{10} K, the weak processes were not able to keep the same number of neutrons and protons and the first formations of D, ^3He , ^3H and ^4He took place. As the Universe continued to expand and cool, the processes maintaining equilibrium slowed relative to the temperature evolution and, after five minutes, most neutrons were in ^4He nuclei, and most protons remained free. There was also formation, although in much smaller amounts, of D, ^3He , ^7Li but the low density and temperature caused the elemental composition of the Universe to remain unchanged until the formation of the first stars several billion years later.

The predictions of big bang nucleosynthesis for the light element abundances are shown in Figure 1.8 in which the boxes and arrows show the current estimates for the light element abundances and they are consistent with the corresponding predictions. This result not only provides another confirmation of the big bang, but the theoretical predictions of the light element abundances depend on the density of protons and neutrons (baryon density) at the time of nucleosynthesis. Deuterium is the most robust predictor of the baryon density, resulting in $\Omega_b = 0.05 \pm 0.005$. This means that all that we see directly through the electromagnetic spectrum in the sky, and all the baryonic matter that we are made of and that we study at particle accelerators, constitutes only 5% of the energy density of the universe.

1.5.2 The Cosmic Microwave Background Radiation

The expansion of the Universe implies that at earlier times, the Universe was hotter and denser. As a result, the interactions among particles when the Universe was at its early stage occurred more frequently than they do today with only a small probability of being scattered by gas or dust. At present, a photon is likely to travel several Hubble distances (3700-4700 Mpc) before being scattered or absorbed. As we “rewind” the Universe in time, the energy density and therefore the temperature become higher and at the gas will be made hotter by the radiation. When the temperature reaches about 3000 K, then the hydrogen starts to become ionized and the high scattering rate of free electrons puts an end to the transparency of radiation. This is called the epoch of *decoupling* of matter and radiation. Before this moment, matter and radiation were in thermal equilibrium. Therefore the radiation should have the Planck blackbody spectrum

$$\int_0^\infty \frac{\nu^3 d\nu}{\exp(h\nu/kT_r) - 1} \propto T_r^4, \quad (1.13)$$

where T_r is the radiation temperature. In 1963, Arno Penzias and Robert Wilson, using a horn-reflector radio antenna sensitive to wavelengths ~ 7 cm, measured an excess noise when they turned the antenna towards the sky that was isotropic and constant with time. Dicke and collaborators had deduced that the Universe should be filled with a microwave radiation (hereafter Cosmic Microwave Background or CMB) if it began in a hot and dense state as we have described at the beginning of this section.

The FIRAS instrument inside the COBE satellite (COsmic Background Explorer) measured, at any angular position on the sky, the spectrum of the CMB to be that of an ideal blackbody up to 1 part in 10^4 . Figure 1.9 shows spectrum measured by the FIRAS instrument [20]. The COBE satellite also found that the CMB has a dipole anisotropy, which means that even though each point in the sky has a blackbody spectrum, in approximately one half of the sky the spectrum is redshifted, and in the

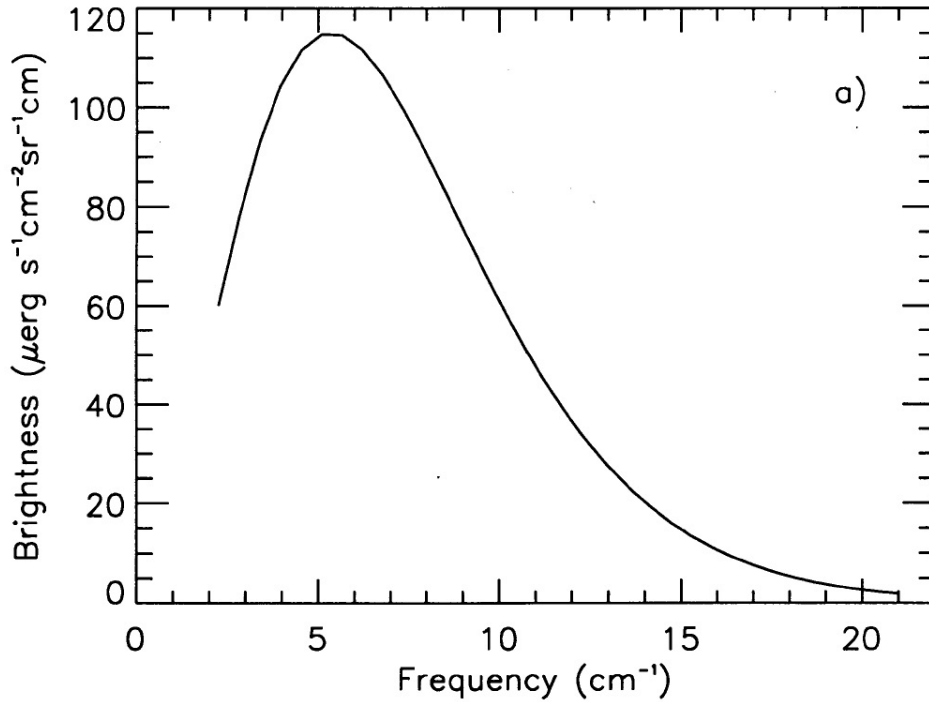


Figure 1.9: The spectrum of the Cosmic Microwave Background as measured by the FIRAS instrument on board of the COBE satellite. The measured temperature by the COBE team was 2.728 ± 0.004 K. Error bars on the measurement are smaller than the thickness of the line. Figure from [20].

other is blueshifted. This is caused by the doppler shift that occurs due to the motion of the COBE satellite with respect to a reference frame in which the CMB is isotropic. When this dipole distortion is subtracted, the root mean square of the temperature fluctuation measured was

$$\left\langle \left(\frac{\delta T}{T} \right)^2 \right\rangle^{1/2} = 1.1 \times 10^{-5} \quad (1.14)$$

where we have defined

$$\frac{\delta T}{T}(\theta, \phi) \equiv \frac{T(\theta, \phi) - \langle T \rangle}{\langle T \rangle}. \quad (1.15)$$

More recent experiments have measured the CMB with a better angular resolution, for example the MAXIMA experiment (balloon-borne), the DASI experiment (located at the South Pole), and the BOOMERANG experiment (a balloon-borne experiment

launched from Antarctica) have provided measurements of $\delta T/T$ at scales of order $\delta\theta \sim 10$ arcminutes. The Wilkinson Microwave Anisotropy Probe (WMAP) was a

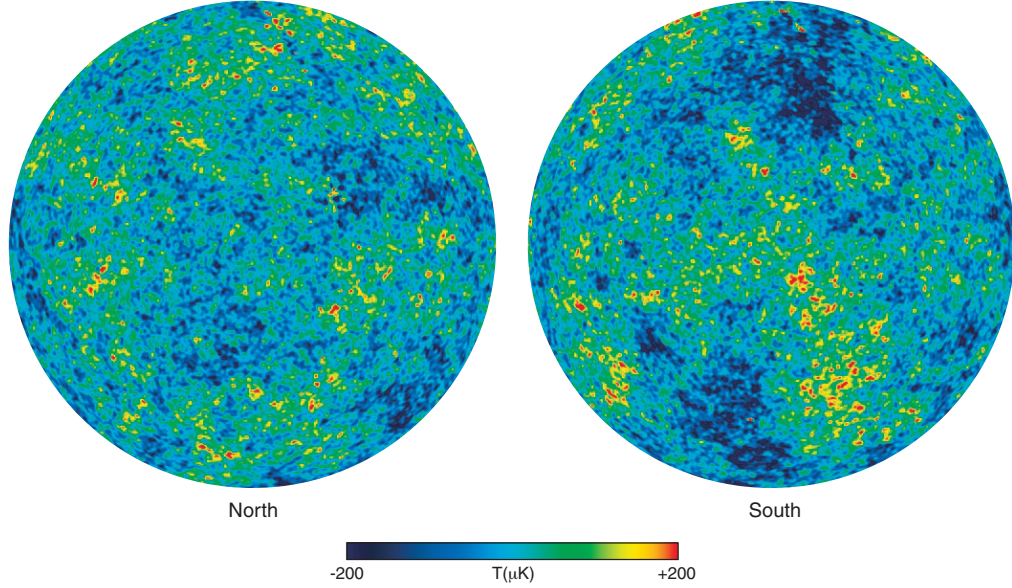


Figure 1.10: North (left) and South (right) sky maps of the temperature of the Cosmic Microwave Background as measured by WMAP. Figure from [21].

mission designed to measure the CMB anisotropy in the full sky. Figure 1.10 shows the temperature fluctuations of the CMB as measured by WMAP.

In order to analyze the temperature fluctuations we can represent a sky map $T(\mathbf{n})$ in spherical harmonics as

$$T(\mathbf{n}) = \sum_{l=0}^{\infty} \sum_{m=-l}^l a_{lm} Y_{lm}(\mathbf{n}) \quad (1.16)$$

where

$$a_{lm} = \int d\mathbf{n} T(\mathbf{n}) Y_{lm}^*(\mathbf{n}), \quad (1.17)$$

and \mathbf{n} is a unit direction vector. For a gaussian CMB, we would have that

$$\langle a_{lm} a_{l'm'}^* \rangle = \delta_{ll'} \delta_{mm'} C_l, \quad (1.18)$$

where C_l is the angular power spectrum and δ is the Kronecker symbol. The C_l can be interpreted as the mean variance per l that would be observed by a hypothetical ensemble of observers distributed through-out the Universe, but the real power spectrum that is observed in the sky is [21]

$$C_l^{sky} = \frac{1}{2l+1} \sigma_{m=-l}^l |a_{lm}|^2. \quad (1.19)$$

In other words, a term C_l is a measure of the temperature fluctuations at an angular scale $\theta \sim 180^\circ/l$. The moments with $l \geq 2$ tell us about the fluctuations present at the time of last scattering. Figure 1.11 shows the CMB power spectrum as a function of multipole l from various experiments.

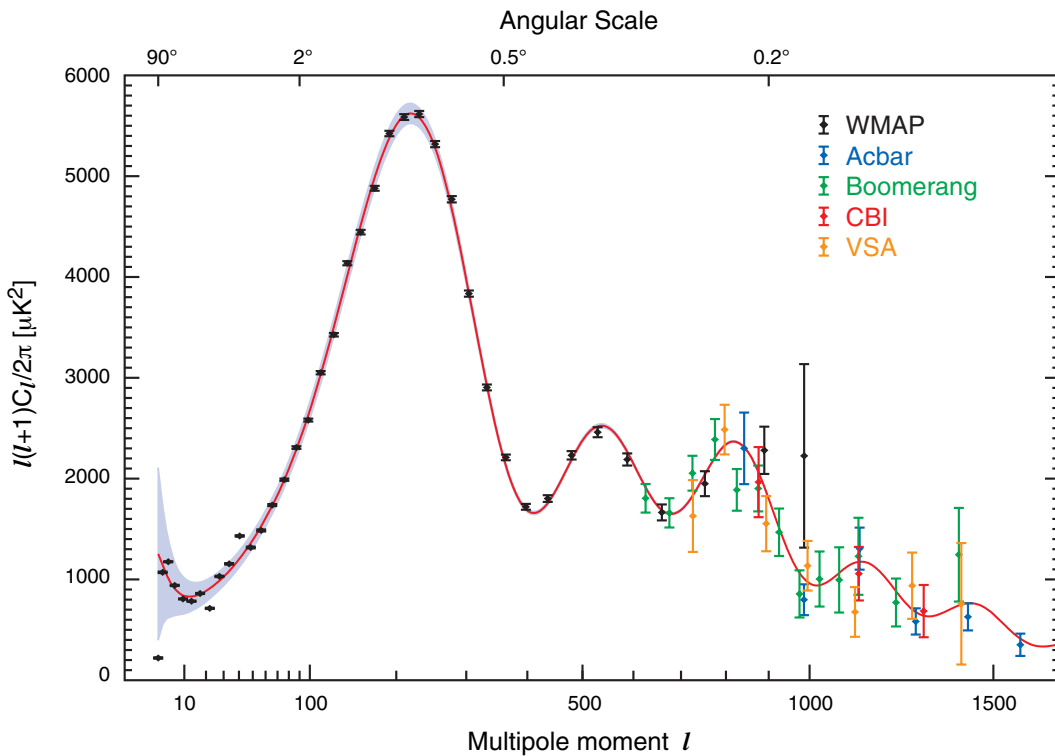


Figure 1.11: WMAP power spectrum in black compared with other measurements of the CMB power spectrum such as Boomerang [22], Acbar [23], CBI [24] and VSA [25]. Figure from [21] and references therein.

Using WMAP data only, the best fit values for cosmological parameters for the

power-law flat Λ cold dark matter (Λ CDM) model [29] are

$$\Omega_m h^2 = 0.1277^{+0.0080}_{-0.0079} \quad (1.20)$$

$$\Omega_b h^2 = 0.02229 \pm 0.00073. \quad (1.21)$$

The result of Ω_b is in agreement with estimations using arguments from big bang nucleosynthesis that we have described in Section 1.5.1. Furthermore, when the knowledge of the baryon density is combined with that of the total matter density, we are able to conclude that approximately 25% of the matter density of the universe is not baryonic and therefore a natural solution is to search for undiscovered particles.

1.6 Observations of Type Ia Supernovae

In the late 1930's, Walter Baade, working closely with Fritz Zwicky, pointed out that supernovae were extremely promising candidates for measuring the cosmic expansion. Their peak brightness seemed to be very uniform, and they were bright enough to be seen at extremely large distances [26]. In the early 1980's supernovae with no hydrogen features in their spectra had been classified as type I. Later on this class was subdivided into types Ia and Ib, depending on the presence or absence of a silicon absorption feature at 6150 Å in the spectrum of the supernovae. A remarkable consistency between the type Ia supernovae was found, and this was further confirmed and improved when their spectra were studied in detail as they brightened and then faded. The detailed uniformity of the type Ia supernovae implies that they must have some common triggering mechanism. This uniformity provides standard spectral and light-curve templates to measure the expansion rate of the cosmos, or the Hubble constant H_0 [27, 28].

The best fit to measurements of supernovae Ia imply that, at the present epoch, the vacuum energy density ρ_Λ is larger than the energy density associated with mass

$\rho_m c^2$, and this means that the expansion of the Universe is accelerating. If the Universe has no large-scale curvature, as indicated by the WMAP data [29], we can conclude that about 70% of the total energy density is vacuum energy and 30% is mass [27, 28]. Specifically the matter density has been measured to be

$$\Omega_m = 0.3 \pm 0.04 \tag{1.22}$$

and from big-bang nucleosynthesis it has been inferred that there are too few baryons to account for this:

$$\Omega_b = 0.05 \pm 0.005. \tag{1.23}$$

Figure 1.12 shows the normalized matter as a function of energy density as obtained using high-redshift supernovae, galaxy clusters, and the cosmic microwave background. The Figure shows how all the three type of observations converge in a model where $\Omega_\Lambda + \Omega_m = 1$ (called the Λ CDM model).

In the following section we will describe why this unseen matter, dark matter, is regarded to be *cold* or in other words traveling at speeds much slower than the speed of light. Further, I will review the most well motivated particle candidates, from particle physics, to make up the dark matter.

1.7 Large-scale Structure Formation

The large-scale structure of the Universe is sensitive to the energy and matter it contains. A model that can predict measurements of the large-scale structure of the nearby Universe needs the energy and matter content of the Universe as input parameters. In this Section, I describe how the Λ CDM model ($\Omega_m + \Omega_\Lambda = 1$) is in agreement with measurements of galaxy redshifts and therefore it provides yet another astrophysical piece of evidence for the dark matter content of the Universe.

The 2dF Galaxy Redshift Survey (2dFGRS team) measured the redshifts of about

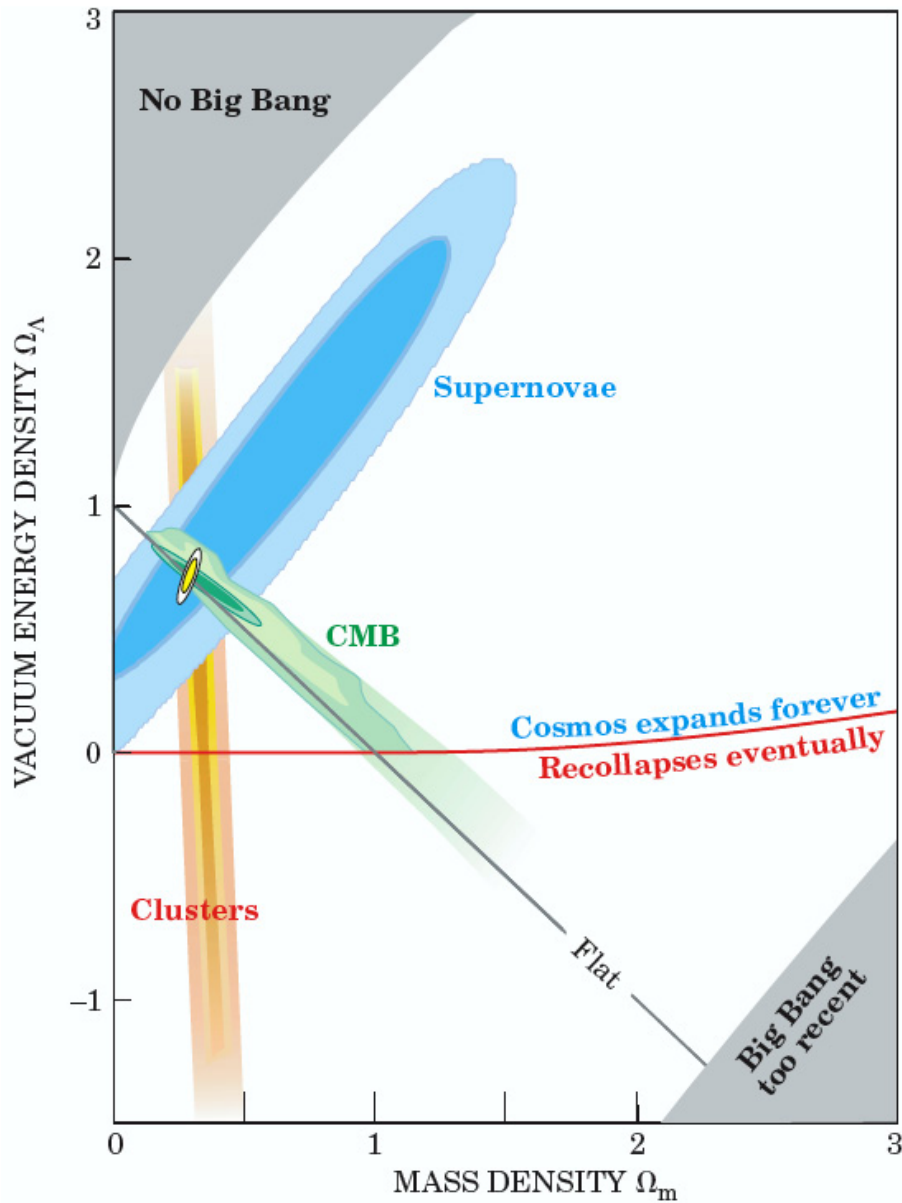


Figure 1.12: The normalized matter (Ω_m) versus the energy density (Ω_Λ) for three independent sets of observations: high-redshift supernovae, galaxy cluster surveys, and the cosmic microwave background. These three independent observations converge near $\Omega_m = 0.3$ and $\Omega_\Lambda = 0.7$. The black diagonal with a negative slope indicates the expectation from a flat cosmos ($\Omega_m + \Omega_\Lambda = 1$ or Λ CDM model). The small yellow contour in this region indicates how SNAP, a satellite experiment, is expected to deliver on the sensitivity to this parameters. Figure from [30].

a quarter million galaxies in order to have a detailed picture of the galaxy population and its large-scale structure in the nearby Universe. The 2dFGRS team has measured the galaxy power spectrum $P(k)$ on scales up to a few hundred Mpc, filling the gap between the small scales where $P(k)$ is known from previous galaxy redshift surveys and the largest scales where $P(k)$ is well-determined by observations of the cosmic microwave background anisotropies [31]. Figure 1.13 shows the projected distribution

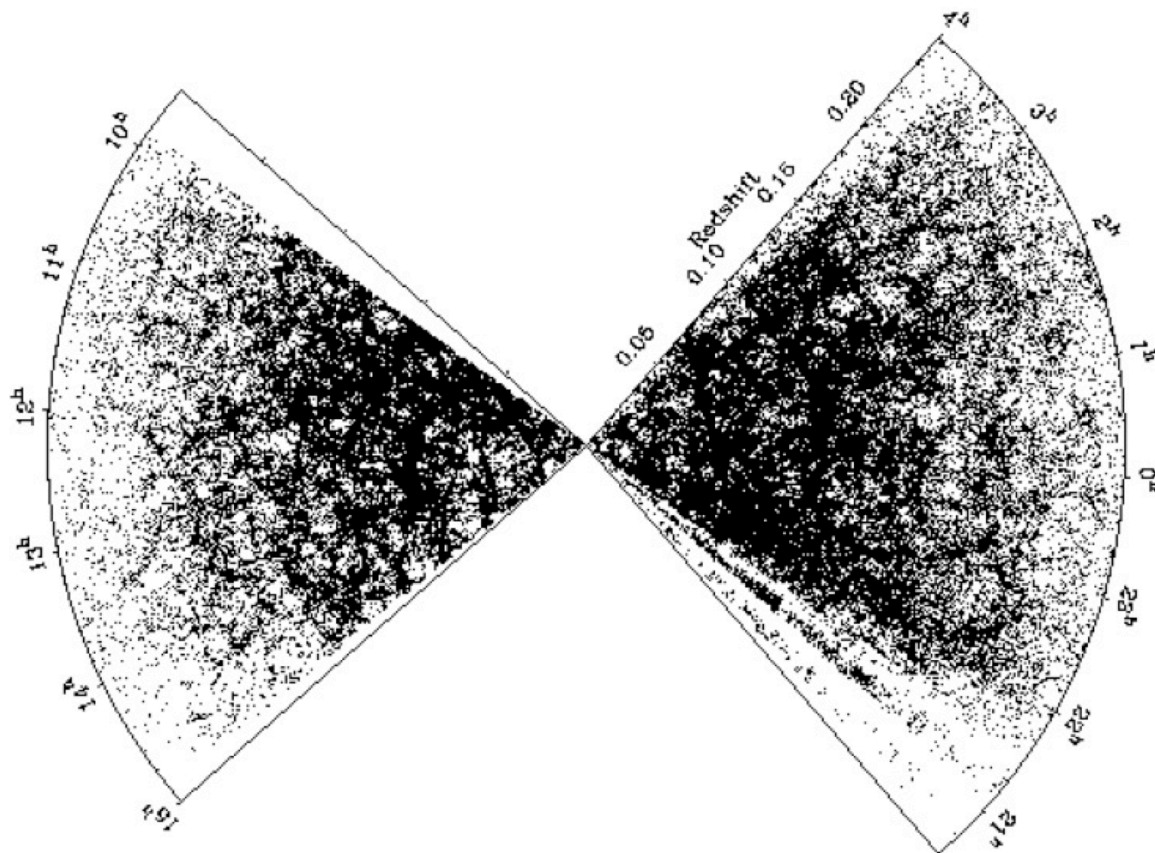


Figure 1.13: The 2dF Galaxy Redshift Survey (2dFGRS) projected distribution of galaxies (about 250000) as a function of redshift. The 2dFGRS has provided the first clear detection of the redshift-space clustering anisotropy on large scales. Figure from [31].

of the galaxies measured by the 2dFGRS team and provides the first detection of the redshift-space clustering anisotropy on large scales. Using only the WMAP data, a

prediction can be made of the amplitude and shape of the matter power spectrum. The band in Figure 1.14 shows the 68% confidence interval for the matter power spectrum.

The points in the Figure show the Sloan Digital Sky Survey (SDSS) galaxy power spectrum [32] with the amplitude of the fluctuations normalized by the galaxy lensing measurements of the 2dFGRS data [33]. This Figure shows that the Λ CDM model accurately predicts the large-scale properties of the matter distribution in the nearby Universe when normalized to observations at $z \sim 1100$, the scale at which the CMB was formed.

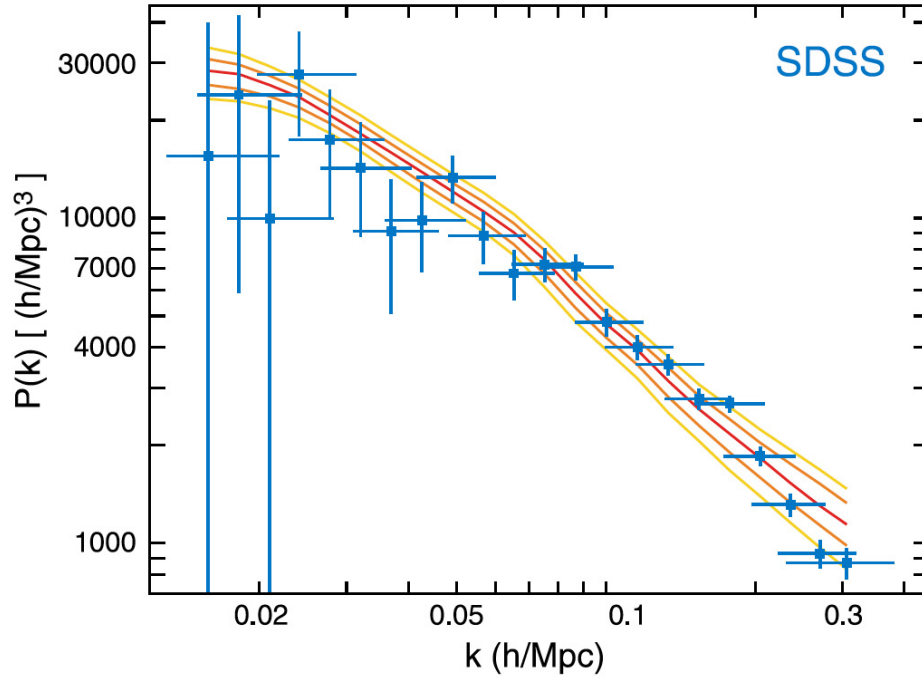


Figure 1.14: The mass power spectrum predicted with a range of parameters consistent with the WMAP-only parameters (shown as the band with a width determined by the 68% confidence interval) compared with the mass power spectrum as measured by the SDSS galaxy survey [32]. The figure shows that the Λ CDM model, when normalized to observations at $z \sim 1100$, accurately predicts the large-scale properties of the matter distribution in the nearby Universe. Figure from [29].

1.8 Dark Matter particle candidates

There is a wide range of possible dark-matter candidates. Their mass could be as small as that of axions with $m = 10^{-5} \text{ eV} = 9 \times 10^{-72} M_{\odot}$ to black holes of mass $m = 10^4 M_{\odot}$. There can be baryonic and non-baryonic dark matter. The main baryonic candidates are massive compact halo objects (MACHOs) [34, 35, 36] such as brown dwarfs (balls of H and He with masses below $0.08 M_{\odot}$), jupiters (masses near $0.001 M_{\odot}$), stellar black-hole remnants (masses near $100 M_{\odot}$) and neutron stars. Astronomical surveys for MACHOs indicate that these objects cannot make up all the amount of dark matter that is needed in our galactic halo. The rest of the dark-matter candidates are nonbaryonic, and this can be divided between *hot* and *cold*. A dark-matter candidate is called hot if it was moving at relativistic speeds at the time galaxies form (when the horizon first contained about $10^{12} M_{\odot}$). If it was moving at nonrelativistic speeds at that time, then its called *cold* dark-matter.

Studies with N -body simulations of structure formation in a Universe dominated by hot dark-matter cannot reproduce the observed structure [37]. The hypothetical nonbaryonic cold-dark-matter candidates are particles that have not yet been discovered. The leading nonbaryonic cold-dark-matter candidates are axions and weakly interacting massive particles (WIMPs). In the following sections I will describe these two main particle candidates for cold dark matter.

There is also the possibility that the dark matter problem could be explained by non-Newtonian gravity models, in which the strength of the gravitational force decreases less rapidly than r^{-2} at large distance. Gravitational lensing by the colliding galaxy clusters 1E0657-56 has been claimed to give theory independent proof of dark matter dominance at large scales [38]. In this dynamical system, shown in Figure 1.15, a smaller cluster (called bullet cluster) has crashed through a larger one and the intracluster gas of both clusters has been stripped by the collision, and is interpreted

as the bullet's gas trailing behind its galaxy component. When this system is studied and mapped with weak lensing, it shows that the lensing mass is concentrated in the two regions containing the galaxies, rather than in the two clouds of stripped gas which contain most of the baryonic mass [38, 39]. Weakly interacting dark matter would move together with the galaxies, and therefore explains the observed system. Hence the inference that much dark matter continues to accompany the bullet. These observations present a difficulty for alternative gravity theories.

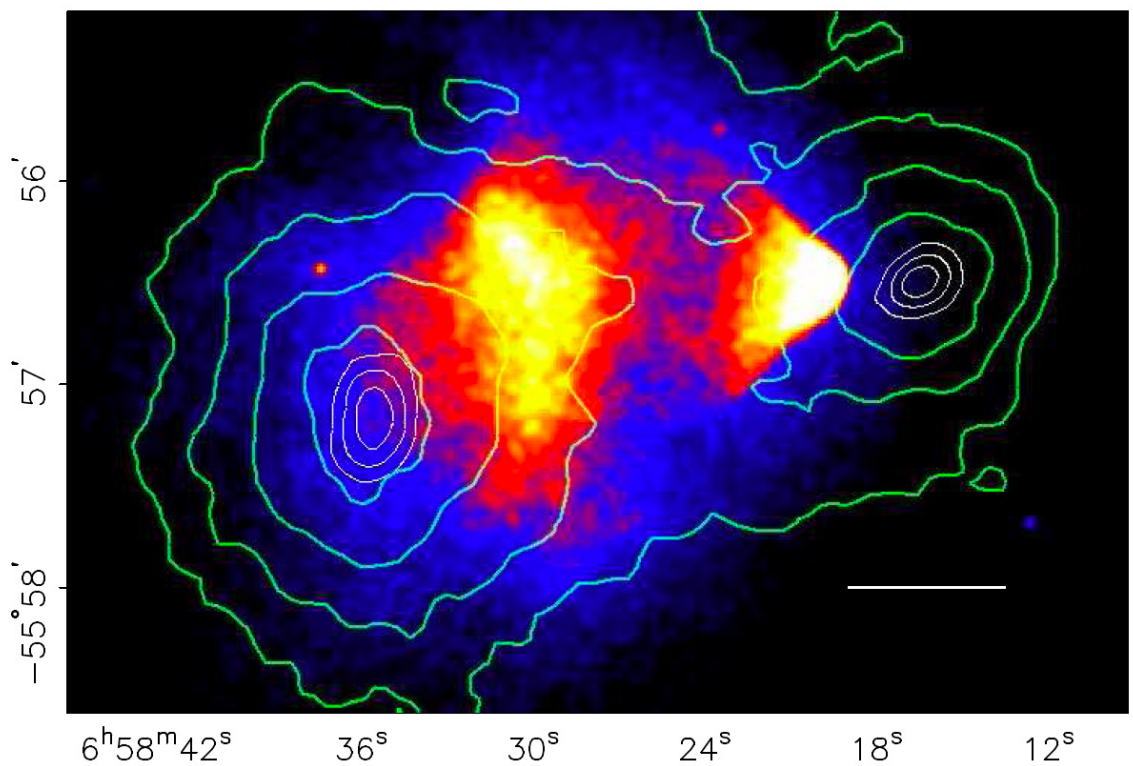


Figure 1.15: The bullet cluster (right) passing through the cluster on the left. The hot gas that is stripped off the colliding clusters is colored in red-yellow. The green and white curves denote the levels surfaces of gravitational lensing convergence; the two peaks of this do not coincide with those of the gas which is mostly all the mass, but are skewed in the direction of the galaxy concentrations. The white bar corresponds to 200 kpc. Figure from [39].

1.8.1 WIMP Candidates From Particle Physics: SUSY

The Standard Model of particle physics has been tested since the 1970's over a wide range of experiments and energies that have supported its validity. Nevertheless, it remains to find the Higgs boson, a missing ingredient of the Standard Model. Furthermore, the Standard Model cannot explain the so-called hierarchy problem, where as Supersymmetry introduces a solution, among other benefits, to some of the unnaturalness of the standard model. Solving the hierarchy problem means that Supersymmetry explains how the weak and gravitational scales are determined. Supersymmetry was not conceived or crafted to solve the hierarchy problem in particular, but it did. Furthermore, Supersymmetry can explain one of the central problems of the standard model of how electroweak symmetry is broken. If supersymmetry is relevant to electroweak-symmetry breaking, it should manifest in physics near the electroweak scale, $E \lesssim O(TeV)$.

Among the many theoretical motivations for low energy supersymmetry, a particularly interesting feature is that supersymmetry transformations yield a spacetime transformation, and hence theories of local supersymmetry contain local spacetime transformations, and therefore they contain gravity.

Well motivated cold dark matter particle candidates in models that contain supersymmetry is a pleasant coincidence. The feature that gives rise to a supersymmetric cold dark matter candidate is R parity. In terms of the implications of R parity on the fields of the theory is that

$$R = (-1)^{3(B-L)+2S}, \quad (1.24)$$

where B , L and S are the baryon, lepton and spin number operators respectively. When $R = 1$ this corresponds to ordinary particles and if $R = -1$ to the corresponding superpartners. If R -parity is broken, it means that there are no selection rules to prevent the decay of the supersymmetric particles in the spectrum with masses of

Normal Particles		SUSY partners	
Symbol	Name	Symbol	Name
$q = u, c, t$	up quarks	$\tilde{q}_u^1, \dots, \tilde{q}_u^6$	up squarks
$q = d, s, b$	down quarks	$\tilde{q}_d^1, \dots, \tilde{q}_d^6$	down squarks
$l = e, \mu, \tau$	leptons	$\tilde{l}_1, \dots, \tilde{l}_6$	sleptons
ν	neutrinos	$\tilde{\nu}_1, \dots, \tilde{\nu}_3$	sneutrinos
g	gluons	\tilde{g}	gluinos
W^\pm	W boson	$\tilde{\chi}_1^\pm, \dots, \tilde{\chi}_1^\pm$	charginos
H^\pm	charged Higgs		
γ			
Z^0	Z boson		
$h^0(H_2^0)$	light scalar Higgs	$\tilde{\chi}_1^0, \dots, \tilde{\chi}_4^0$	neutralinos
$H^0(H_1^0)$	heavy scalar Higgs		
$A^0(H_3^0, P_0)$	pseudoscalar Higgs		

Table 1.1: The spectrum of particles predicted by the minimal supersymmetric standard model [43]. The neutralino is most probably the lightest supersymmetric particle in the MSSM (Minimal Supersymmetric Standard Model) and a good WIMP candidate [50].

order a few GeV or heavier. The scale of R -parity violation regulates the strength of baryon- and lepton-number violation processes, which have not been observed in nature so far and severe constraints on R -parity violation arise. For each fermionic degree of freedom there is a bosonic degree of freedom and vice versa, causing an extension of the particle spectrum (see Table 1.1). For example, quarks have spin $\frac{1}{2}$, and the supersymmetric partners would be the *squarks* and are bosons. The neutralino is most probably the lightest supersymmetric particle in the MSSM (Minimal Supersymmetric Standard Model) [50]. The neutralino would be stable and weakly interacting and therefore a good WIMP dark-matter candidate.

1.8.2 Expected WIMP relic density

If a WIMP-like stable particle (call it χ) existed in the early Universe, it could have a significant cosmological abundance today [40, 41, 42]. The particle χ would have existed in thermal equilibrium and in abundance in the early Universe, when the temperature of the expanding Universe exceeds the mass m_χ of the particle. The equilibrium abundance could be conserved by the annihilation of the particle with its antiparticle into lighter particles $\chi\bar{\chi} \rightarrow \bar{l}l$ and also through the inverse reaction $\bar{l}l \rightarrow \chi\bar{\chi}$. As the Universe expands and cools to temperature below m_χ , the equilibrium abundance drops exponentially until the rate for annihilation reaction $\chi\bar{\chi} \rightarrow \bar{l}l$ falls below the expansion rate H and at this point the interactions which maintained the thermal equilibrium *freeze out*, and a relic cosmological abundance remains [43]. The conclusion of the cosmological-abundance calculation for a thermal relic is essential to the arguments for WIMP dark matter.

In order to do a simple estimate of the cosmological abundance of WIMPs, I follow the steps outlined in the review paper by Jungman, Kamionkowski and Griest [43] and first proposed by Lee and Wienberg [44]. Suppose that in the early Universe, in addition to the known particles of the standard model, there is a new stable (or long-lived) WIMP χ . In thermal equilibrium, the number density of χ particles is

$$n_\chi^{eq} = \frac{g}{(2\pi)^3} \int f(\vec{\mathbf{p}}) d^3\vec{p}, \quad (1.25)$$

where g is the number of internal degrees of freedom of the particle and $f(\vec{p})$ is the Fermi-Dirac or Bose-Einstein distribution. At high temperatures ($T \gg m_\chi$), $n_\chi^{eq} \propto T^3$ so that the number of photons and WIMPs is roughly the same. Furthermore, WIMPs are abundant and rapidly converting to lighter particles and vice versa. At low temperatures ($T \ll m_\chi$), $n_\chi^{eq} \simeq g (m_\chi T / 2\pi)^{3/2} \exp(-m_\chi/T)$ hence, the WIMP density is Boltzmann suppressed¹. Shortly after T drops below m_χ , the number density of

¹If the species is in equilibrium, then $f(\vec{\mathbf{p}}) = 1 / (\exp[(E - \mu)] \pm 1)$, where μ is the chemical

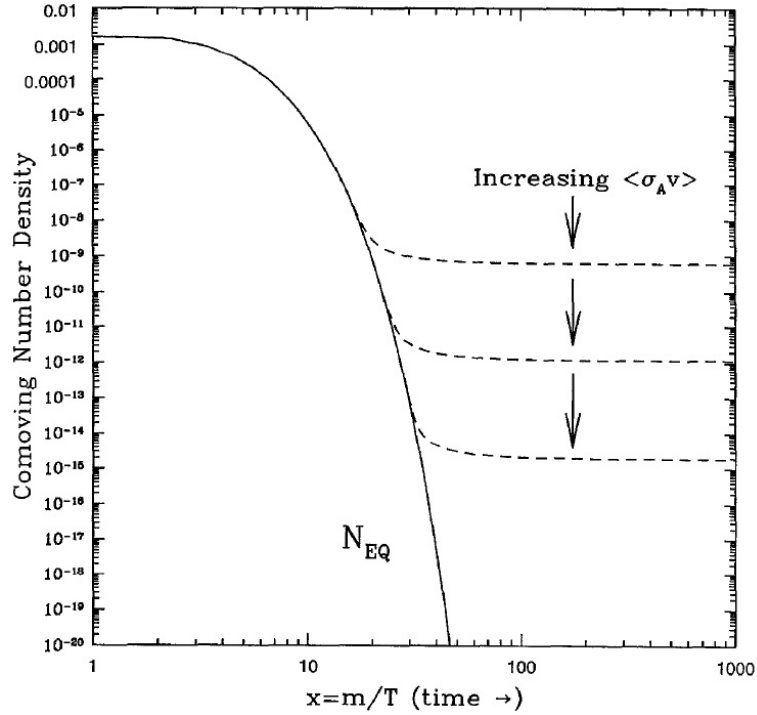


Figure 1.16: Comoving number density of WIMPs in the early Universe. Dashed lines correspond to the forming relic abundance of WIMPs, and the solid curve corresponds to the equilibrium abundance. Shortly after T drops below m_χ , the number density of WIMPs drops exponentially, and the rate for annihilation of χ 's ($\Gamma = \langle\sigma_A v\rangle n_\chi$) drops below the expansion rate, $\Gamma \lesssim H$. At this moment, WIMPs no longer annihilate and fall out of equilibrium, forming a relic cosmological abundance that remains at present times. Figure from [59].

WIMPs drops exponentially, and the rate for annihilation χ 's ($\Gamma = \langle\sigma_A v\rangle n_\chi$) drops below the expansion rate, $\Gamma \lesssim H$. At this moment, WIMPs no longer can annihilate and fall out of equilibrium, forming a relic cosmological abundance that remains at present times. The quantitative way of describing this process is done by using the Boltzmann equation, which describes the time evolution of the number density $n_\chi(t)$ potential of the species and $+(-)1$ corresponds to the Fermi-Dirack (Bose-Einstein) distributions. In the non-relativistic limit ($m \gg T$) the number density would be $n = g \left(\frac{mT}{2\pi}\right)^{3/2} \exp[-(m - \mu)/T]$, where the total energy E is replaced by the rest mass m .

of WIMPs:

$$\frac{dn_\chi}{dt} + 3Hn_\chi = -\langle\sigma_{Av}\rangle \left[(n_\chi)^2 - (n_\chi^{eq})^2 \right], \quad (1.26)$$

where $H = \dot{a}/a$ is the Hubble expansion rate, and a is the scale factor of the Universe. The second term on the left-hand side accounts for the expansion of the Universe. The first term in brackets on the right-hand side accounts for depletion of WIMPs due to annihilation, and the second term arises from creation of WIMPs from the inverse reaction. This equation can be derived by imposing that, in equilibrium, the rate for annihilation and creation of WIMPs is equal. The analytic approximation that yields a solution to about 10% to equation 1.26 is presented in Kolb and Turner [59]. Figure 1.16 shows numerical solutions to the Boltzmann equation for WIMPs. The equilibrium (solid line) and actual (dashed lines) abundances per comoving volume are plotted as a function of $x \equiv m_\chi/T$. As the annihilation cross section decreases, the WIMPs stay in equilibrium longer, and a smaller relic abundance is formed. The fact that generally, the annihilation cross section depends on the kinetic energy and mass of the WIMP produces a temperature of the freeze out to be $T_f \simeq m_\chi/20 \ll m_\chi$, hence WIMPs are moving at nonrelativistic velocities when they freeze out. The resulting density is the *relic density* of the WIMP. The ratio of the relic density to the closure density is given by [43, 59]

$$\Omega_\chi h^2 = \frac{s_0}{\rho_c/h^2} \left(\frac{45}{\pi g_*} \right)^{1/2} \frac{x_f}{m_{Pl}} \frac{1}{\langle\sigma v\rangle} \quad (1.27)$$

where s_0 is the current entropy density of the universe, ρ_c is the critical density, h is the scaled Hubble constant ($H_0 = 100h$ km/sec/Mpc), g_* is the number of relativistic degrees of freedom at the time the WIMP falls out of equilibrium, m_{Pl} is the Planck mass, $x_f \approx 25$ ² and $\langle\sigma v\rangle$ is the thermal average of the dark matter pair annihilation

² $x_f = x$ at the time of the ‘freeze out’ which is when the rate of annihilation is equal to the cosmic expansion.

cross section times the relative velocity. Using $\Omega_\chi = 0.2$, we find that

$$\langle\sigma v\rangle \sim 0.9 \text{ pb.} \tag{1.28}$$

In terms of mass, this means for example that if $\langle\sigma v\rangle = \pi\alpha^2/8m^2$ (the value obtained for a generic electroweak mass particle annihilating through the exchange of the electroweak gauge or Higgs bosons [51]), then $m \sim 100 \text{ GeV}$, giving the order of magnitude for the WIMP mass.

In the next chapter I will review the current proposed detection techniques, direct and indirect, of WIMP dark matter. First, I will review calculations for the expected WIMP rates and potential signatures for direct detection, and following that with a summary of the most promising experimental techniques.

1.8.3 Axions

The axion is a dark matter particle candidate that arises as a consequence of a theory by Peccei and Quinn [52] that proposes a dynamical mechanism to conserve strong CP symmetry. This symmetry, according to the Standard Model of particle physics, should be violated and therefore produce a neutron magnetic moment 10 orders of magnitude larger than the current experimental lower limit of $10^{-28} e\text{-cm}$ [53]. Therefore, this upper limit requires a mechanism to preserve CP symmetry.

The axion is described by the spontaneous symmetry breaking scale of the Peccei-Quinn symmetry, f_a , and its related to the mass, m_a , as

$$m_a \simeq 6\mu eV \left(\frac{10^{12} GeV}{f_a} \right) \tag{1.29}$$

and the axion-photon coupling $g_{a\gamma\gamma}$ is defined as

$$g_{a\gamma\gamma} \equiv \frac{\alpha g_\gamma}{\pi f_a} \tag{1.30}$$

where α is the fine structure constant and g_γ is a dimensionless model dependent coupling parameter. If g_γ is ~ 0.97 then these axions are denominated KSVZ (for

Kim-Shifman-Vainshtein-Zakharov) [54, 55] and if this parameter is ~ -0.36 then the axions are denoted DFSZ (for Dine-Fischler-Srednicki-Zhitnitshi) [56, 57]. This values of g_γ can constrain the axion-to-photon conversion rates an order of magnitude at any axion mass.

The axion mass has been constrained with observations of nuclear burn off times in different stellar phases [58] since axions, like neutrinos, are byproducts of stellar nuclear reactions and can carry some of its energy. Also, the axion mass can be constrained by studying the neutrino emission from the supernova SN1987a [59] for which there is experimental data from the Kamiokande and IMB experiments. The measured duration of the time period of neutrino emission can rule out axion masses between 2 eV and 10^{-3} eV [60], otherwise the length of the period would be shorter. Cosmological considerations can yield constraints on the axion mass since at the time of the big bang axions would be produced and the total contribution to the energy density from axions, for a flat Universe, puts a lower limit on the axion mass of $m_a \geq 10^{-6}$ eV. The current allowed axion mass range is from 10^{-6} eV to 10^{-3} eV, with lower masses if they are a major component of dark matter [61].

At present times, we expect axions to be gravitationally bound in our own galaxy, forming a large halo of particles moving with relative velocities of order $10^{-3}c$ [62]. For an axion to be gravitationally bound to our galaxy means they are moving slower than the escape velocity of $2 \times 10^{-3}c$. In principle, a flux of axions traversing a microwave cavity permeated by a strong magnetic field could be converted to radio frequency (RF) photons when the cavity is tuned to the resonant frequency determined by their mass. This detection principle, based on the axion-photon coupling, was first proposed by Pierre Sikivie in 1983 [63] and has marked the way to the most sensitive searches to date of the cosmological axions.

The axion to photon conversion power is proportional to B^2VQ , where B is the magnetic-field strength, V the cavity volume and Q its quality factor. The expected

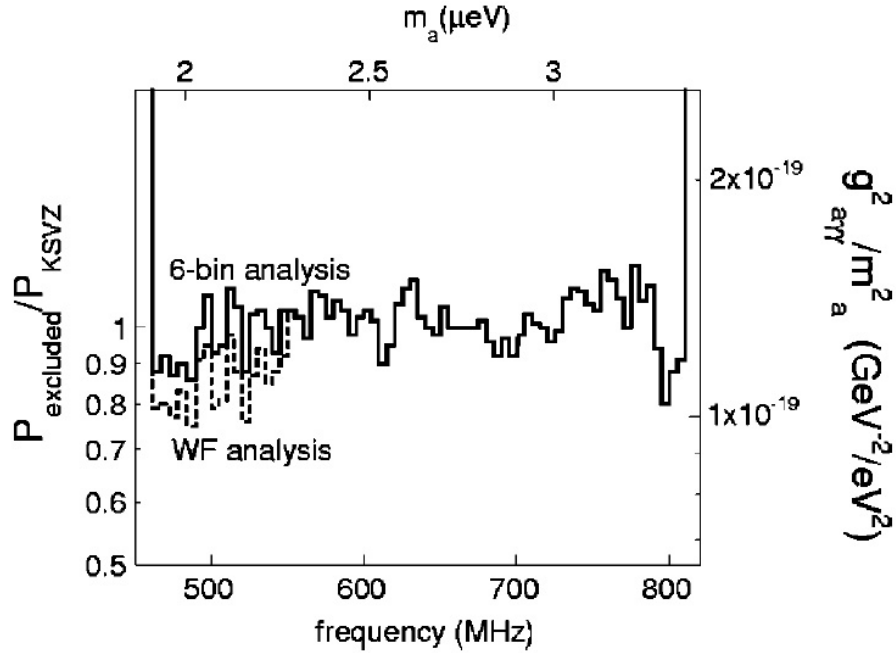


Figure 1.17: The 90% confidence upper limit on axion-to-photon conversion power and coupling $g_{a\gamma\gamma}$, assuming an axion halo density of $0.45 \text{ GeV}/\text{cm}^3$. Figure from [65]

signal is of the order of $10^{-24}W$. The signal-to-noise ratio for an actual experiment is determined by the bandwidth of the signal, the integration time, the signal and noise power and the noise temperature of the system. At Lawrence Livermore National Laboratory the Axion Dark Matter Experiment (ADMX) consists of an 8-tesla superconducting magnet, a high-Q tunable cavity and an ultrasensitive microwave amplifier used to search for an axion-to-photon signal as proposed by Sikivie [61]. The first phase of the ADMX experiment excluded KSVZ axions over an octave in mass, setting the best limits to date, as shown in Figure 1.17. The next generation of the ADMX experiment will scale up the cavity volume and will use ultra-low-noise microwave technology [64].

The sensitivity of the ADMX experiment was limited by the noise in the cryogenic HFET amplifiers and its being improved by the implementation of Superconducting Quantum Interference Devices (SQUIDS) at the cryogenic stage [66]. Future upgrades

of the ADMX experiment will use SQUID amplifiers with a dilution refrigerator to be able to operate at ~ 100 mK allowing a significant improvement in the scanning rate and ultimately reach the DFSZ axion couplings.

* * *

In the next Chapter, I will focus on WIMPs, how can we aim to detect them in experiments underground, or detect their products, in space-based experiments. Also, I will review the prospects for producing WIMPs at future high-energy colliders experiments and how all these measurements could complement each other in order to measure the properties of WIMP dark matter.

Chapter 2

WIMP Detection

In this chapter the signatures expected for direct and indirect detection for WIMPs will be described and the estimation of expected rates in a terrestrial detector target for direct detection will be derived. Furthermore, the experimental techniques of a wide variety of direct and indirect detection experiments will be described briefly, with emphasis on how all these experiments underground, in space and at accelerators can constrain the properties of dark matter.

Direct detection of dark matter encompasses all those experiments that search for a dark matter particle interacting *directly* with the detector, such as via elastic scattering with a target nuclei causing a nuclear recoil of about 15 keV. Indirect detection experiments search for a non-WIMP particle originating from WIMPs that interact with the detector (hence the term *indirect detection*). For example, WIMP annihilation could be observed through gamma ray, positron, antiproton, antideuteron, and neutrino signals. There are already claims, although controversial, of an excess of gamma rays from the galactic center providing evidence for WIMP dark matter [67].

The fact that WIMPs are expected to be a thermal relic from the Big-Bang makes direct detection experiments particularly important due to the long lifetime of the dark matter particle. In collider experiments a new particle may be detectable but it

can not be determined if it has the necessary stability to be a “freeze out” product from the Big-Bang. In addition, signatures at collider experiments will consist of “missing energy” or missing transfer momentum and therefore a measurement of the couplings is highly unlikely. Nevertheless, direct detection experiments will be able to provide information on the WIMP couplings to the Standard Model. Furthermore, comparing direct to indirect detection which relies on the observation of the annihilation products of the dark matter particles, it is expected that this measurements will have significant model dependence and therefore have higher uncertainty compared to the direct detection case. In the following sections I will describe the expected event rates for direct detection experiments, some of the main experimental approaches to direct detection as well as indirect detection techniques and also will discuss what we can learn about dark matter in collider experiments, with emphasis in the fact that not one approach or experiment alone will be able to fully determine the properties of dark matter, but only a combination of all of direct, indirect and collider experiments.

2.1 Direct detection experiments

Before going on to describe each experimental technique, it is necessary to derive the expected rates in a given terrestrial detector for nuclear recoils from WIMPs. The differential rate per unit mass of a particle with a velocity v incident on a detector is:

$$dR = \frac{N_0}{A} \sigma_0 v dn, \quad (2.1)$$

where N_0 is Avogadro’s number, A the atomic mass of the target nucleus and σ_0 is the WIMP-nucleus scattering cross section assuming zero-momentum transfer. In the case of WIMPs, dn is the differential particle density in the reference frame of a detector stationary in the galaxy:

$$dn = \frac{n_0}{k} f(\vec{v}, \vec{v}_E) d^3v, \quad (2.2)$$

where \vec{v} and \vec{v}_E are the WIMP and Earth's velocities and k is a normalization constant such that

$$\int_0^{v_{esc}} dn = n_0, \quad (2.3)$$

and n_0 is the mean WIMP density in the galaxy. Hence, equation 2.1 becomes:

$$\begin{aligned} dR &= \frac{N_0}{A} \sigma_0 v \frac{n_0}{k} f(\vec{v}, \vec{v}_E) d^3v \\ &= R_0 \frac{\sqrt{\pi} v}{2K v_0} f(\vec{v}, \vec{v}_E) d^3v \end{aligned}$$

where in the last step, I have introduced the following constants:

$$\begin{aligned} R_0 &= \frac{2N_0}{\sqrt{\pi}A} n_0 v_0 \sigma_0 \\ K &= \int_0^{2\pi} d\phi \int_{-1}^1 d(\cos\theta) \int_0^{v_{esc}} f(\vec{v}, \vec{v}_E) v^2 dv \end{aligned}$$

and v_0 is such that in the limit of $v_{esc} \rightarrow \infty$, k becomes:

$$k = k_0 = (\pi v_0^2)^{3/2}. \quad (2.4)$$

The recoil energy of a nucleus of mass M_T , for an incident WIMP particle with energy E and mass M_χ is given by:

$$E_R = \frac{1}{2} E r (1 - \cos\theta) \quad (2.5)$$

where

$$r = \frac{4M_\chi M_T}{(M_\chi + M_T)^2}. \quad (2.6)$$

The Earth speed has been measured to be

$$v_E = 232 + 15 \cos\left(2\pi \frac{t - 152.5}{365.3}\right) \text{ km/s}. \quad (2.7)$$

The velocity distribution of the WIMPs, assuming that the WIMPs do not interact with each other, is given by a Maxwellian velocity distribution:

$$f(\vec{v}, \vec{v}_E) \sim \exp\left(-\frac{(\vec{v} + \vec{v}_E)^2}{v_0^2}\right), \quad (2.8)$$

where v_0 is defined by $M_\chi v_0^2/2 \sim 230\text{km/s}$ [68]. The differential recoil energy spectrum is:

$$\frac{dR}{dE_R} = \int_{E_{min}}^{E_{max}} \frac{1}{Er} \frac{dR}{dE} dE, \quad (2.9)$$

where $E_{min} = E_R/r$ and E_{max} is the WIMP escape velocity. Also, we can write equation 2.9 in terms of velocity instead of energy:

$$\begin{aligned} \frac{dR}{dE_R} &= \int_{\sqrt{2M_\chi E_R/r}}^{v_{esc}} \frac{2}{rM_\chi v^2} \frac{dR}{dv} dv \\ &= \frac{R_0}{rE_0} \frac{2\pi^{3/2}v_0}{K} \int_{\sqrt{2M_\chi E_R/r}}^{v_{esc}} v \exp\left(\frac{-(v+v_E)^2}{v_0^2}\right) dv \end{aligned}$$

where $E_0 = M_\chi v_0^2/2$. When we take the limits $v_E \rightarrow 0$ and $v_{esc} \rightarrow \infty$, $K \rightarrow (\pi v_0^2)^{3/2}$, the differential energy rate is given by:

$$\frac{dR}{dE_R} = \frac{R_0}{rE_0} e^{-E_R/rE_0}. \quad (2.10)$$

Taking into account the velocity of our Galaxy to be of order $10^{-3}c$, then the values of M_χ in the 10-1000 GeV/c² would produce recoils up to 100 keV in energy. The majority of the direct detection experiments searching for WIMPs aim to measure the left hand side of equation 2.10 as a function of recoil energy mostly between 10 and 100 keV. These experiments are very low threshold neutron detectors searching for nuclear recoils from WIMPs and therefore they have to be performed underground to shield from cosmic rays and inside gamma-ray and neutron shielding. In the next chapters I will describe the backgrounds that these experiments need to address with emphasis on the neutron backgrounds. When an experiment has set an upper limit on the differential rate at a particular value of E_R , then the right-hand side of equation 2.10 can set a corresponding limit for the dark matter signal R_0 that can be calculated as a function of the WIMP mass.

A more realistic right-hand side of equation 2.10 will consider the kinematics of the earth (where the detector is located) with respect to the Galaxy, detector efficiency,

several target elements in the detector, instrumental resolution and threshold effects, spin-dependent versus spin-independent interactions, and form factor corrections that can suppress the differential scattering rate significantly. The recoil energy spectrum, in general, can be written as

$$\frac{dR(v_E, v_{esc})}{dE_R} = \frac{dR'(v_E, v_{esc})}{dE'_R} F^2(q) S, \quad (2.11)$$

where dR'/dE'_R is the recoil spectrum at zero momentum transfer but for a finite escape velocity v_E and for a finite threshold velocity, given by [68]:

$$\frac{dR'(v_E, v_{esc})}{dE'_R} = \frac{k_0}{k_1} \left[\frac{dR(v_E, \infty)}{dE_R} - \frac{R_0}{E_0 r} e^{v_{esc}^2/v_0^2} \right], \quad (2.12)$$

where

$$\begin{aligned} \frac{dR(v_E, \infty)}{dE_R} &= \frac{R_0}{E_0 r} \frac{\sqrt{\pi}}{4} \frac{v_0}{v_E} \left[\operatorname{erf} \left(\frac{v_{min} + v_E}{v_0} \right) - \operatorname{erf} \left(\frac{v_{min} - v_E}{v_0} \right) \right] \\ k_0 &= (\pi v_0^2)^{3/2} \\ k_1 &= k_0 \left[\operatorname{erf} \left(\frac{v_{esc}}{v_0} \right) - \frac{2}{\sqrt{\pi}} \frac{v_{esc}}{v_0} e^{-v_{esc}^2/v_0^2} \right]. \end{aligned}$$

and, for spin-independent interactions

$$\begin{aligned} S &= A^2 \mu_N^2 / \mu_p^2 \\ \mu_{N,p} &= \frac{M_N M_p}{M_N + M_p} \end{aligned}$$

where M_N and M_p is the mass of the nucleus and proton respectively.

The Helm form factor $F(q)$, for $q = \sqrt{2M_T E_R}$ is determined empirically, and there is one for each type of interaction (spin-independent or spin-dependent). For a spin

independent interaction the Helm form factor is given by [68]:

$$\begin{aligned}
 a &= 0.52 \text{ fm} \\
 s &= 0.9 \text{ fm} \\
 c &= 1.23A^{1/3} - 0.6 \text{ fm} \\
 r_n^2 &= c^2 + \frac{7}{3}\pi^2 a^2 - 5s^2 \\
 F(qr_n) &= 3 \frac{j_1(qr_n)}{qr_n} e^{-(qs)^2/2} \\
 &= 3 \frac{\sin(qr_n) - qr_n \cos(qr_n)}{(qr_n)^3 e^{(qs)^2/2}}.
 \end{aligned}$$

Figure 2.1 shows the form factor as a function of recoil energy for Ge, Si and Xe.

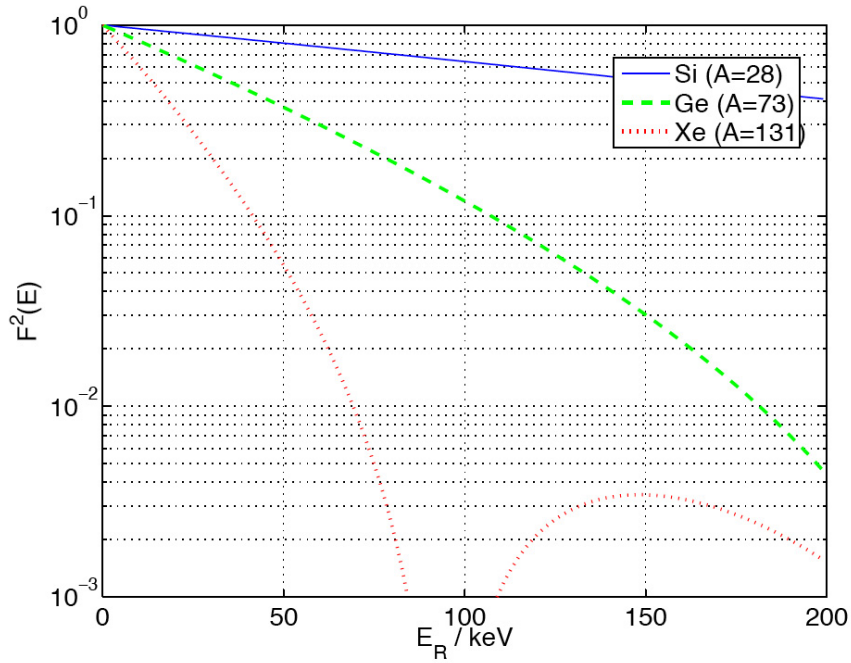


Figure 2.1: The Helm form factors for Ge, Si and Xe as a function of recoil energy [142].

Assuming the spin-independent coupling dominates, using standard halo parameters, and the formalism described here and developed by Lewin and Smith [68], the interaction rate is shown in Figure 2.2 for a WIMP mass of 100 GeV and a cross

section normalized to that of a single nucleon. Shown in figure are the expected differential and integrated WIMP event rates as a function of recoil energy for Xe, Ge and Si. We can see from the plot that higher WIMP rates favor heavier nuclei due to coherence enhancement of the rate ($\sim A^2$) and also due to a more effective transfer of the recoil energy with respect to lighter nuclei (lighter than an WIMP). Furthermore, the form factor is suppressed at high recoil energy for Xe. The parameters needed to optimize the expected rate are: target nuclei, threshold and scalability (or detector mass). The effect of threshold energy is magnified when an experiment searches for low-mass WIMPs due to the reduction of kinetic energy that can be transferred to the nucleus from the WIMP.

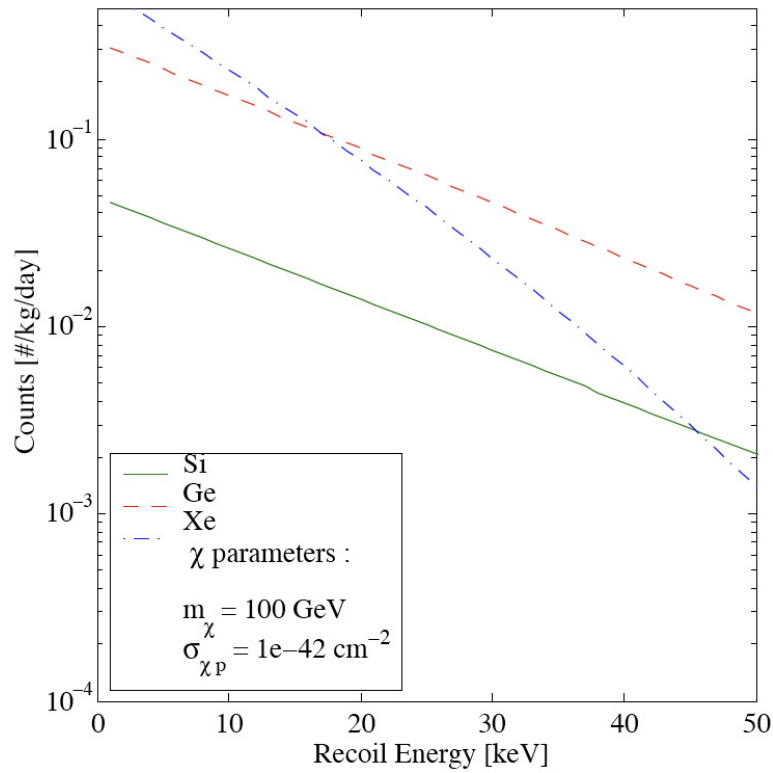


Figure 2.2: Integrated interaction rates for Ge (dashed line), Si (solid line) and Xe (dash dotted line). In order to take advantage of the cross section enhancement for spin-independent interactions, which goes as A^2 , a low threshold is necessary together with a heavy target nuclei [143].

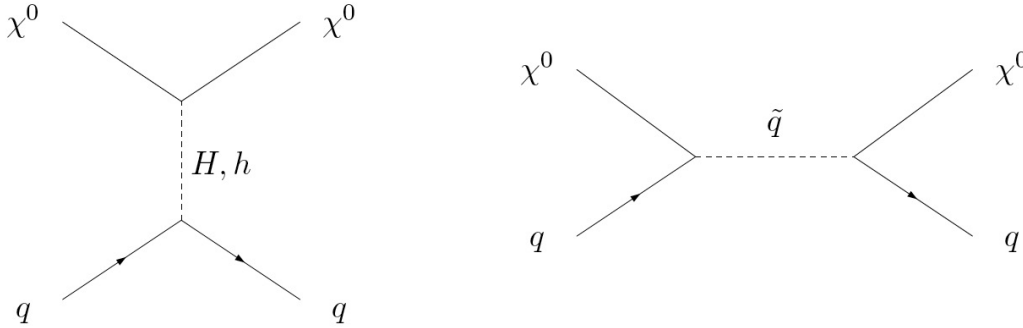
The spin independent WIMP-nucleus elastic scattering cross section can be written as:

$$\sigma \simeq \frac{4M_\chi^2 M_T^2}{\pi (M_\chi + M_T)^2} [Z f_p + (A - Z) f_n]^2, \quad (2.13)$$

where A and Z are the common notation for the atomic number and atomic mass respectively for the target nucleus. The WIMP couplings are f_p for protons and f_n for neutrons and are given by:

$$f_{p,n} = \sum_{q=u,d,s} f_{T_q}^{(p,n)} a_q \frac{m_{p,n}}{m_q} + \frac{2}{27} f_{TG}^{(p,n)} \sum_{q=c,b,t} a_q \frac{m_{p,n}}{m_q}, \quad (2.14)$$

where the WIMP mass couplings are given by a_q and the quark content of the nucleon is denoted by $f_{T_q}^{(p,n)}$. Interpreting each term in the sum of equation 2.14, the first term corresponds to the contribution from interactions with the quarks of the target nuclei which, for neutralino dark matter, can occur via t -channel CP-even Higgs exchange, or s -channel squark exchange [51]:



The interactions with the gluons of the target nuclei correspond to the second term through a loop diagram. Aside from the determination of the WIMP mass, in order to understand the nature of this particle we need to know its quark couplings a_q which, in the case of neutralino dark matter, depend on the underlying supersymmetric theory. Direct detection experiments will not be capable of revealing much about supersymmetry or the underlying physics behind the dark matter particles. Only by

using the information from colliders, together with direct and indirect detection can we hope to understand the nature of dark matter and its composition. Furthermore, it is noteworthy the pace at which direct detection experiments are gaining sensitivity with high likelihood of reaching $\sim 10^{-45}$ cm² by 2010 and therefore in a position to discover a signal in the same time scale that the Large Hadron Collider is expected to produce results on searches for new particles.

Most of the direct detection experiments, including CDMS, aim to measure the rate of WIMP induced nuclear recoils and their energy with an average of 15 keV. A few events of this kind will represent a positive signal for a zero background experiment such as CDMS. After a few events are seen and good statistical significance is obtained, an annual modulation is expected at the few percent level due to the Earth's motion around the Sun [70, 71]. Other approaches aim at detection of the direction of the nuclear recoils since we expect a directional dependence of the WIMP scattering rate with respect to the direction of solar motion. If sensitivity to the direction of the WIMP nuclear recoil is achieved, the scattering rate is expected to be significantly larger when moving in the direction of the solar motion [72]. Certainly having a directional signal improves the signal confidence level since the background events will be isotropic compared to the expected anisotropic signal. Nevertheless, sensitivity to the nuclear recoil direction usually means a low density target material and therefore very large arrays are needed since the mass of the target will be proportional to the sensitivity as well. The sensitivity of a directional detector, aside from mass, threshold and exposure, depends on whether it measures the recoil momentum in two or three dimensions and whether the sense (head/tail effect) of the recoil momentum vector can be measured [73, 74].

In the following subsections I will discuss the main detection techniques for direct detection of dark matter. These consist mainly in very low threshold (few to tens of keV) neutron detectors (via nuclear recoil) build with low radioactivity materials

and under passive shielding such as hydrogenated materials, lead and the earth's crust (underground). Muon vetoes are also used in some experiments such as CDMS in order to have an extra order of magnitude background discrimination against cosmogenic neutrons, these will be discussed in more detail in Chapter 4. In Figure 2.3 the main detection techniques are shown around a triangle that depicts the energy from the interaction of a WIMP-nuclear recoil. When the recoil occurs, the energy is partitioned in ionization, heat/phonons and scintillation. Each detection technique exploits one or more of this channels or degrees of freedom that help to make the discrimination between nuclear recoils (neutrons and WIMPs) and electron recoils (majority of backgrounds).

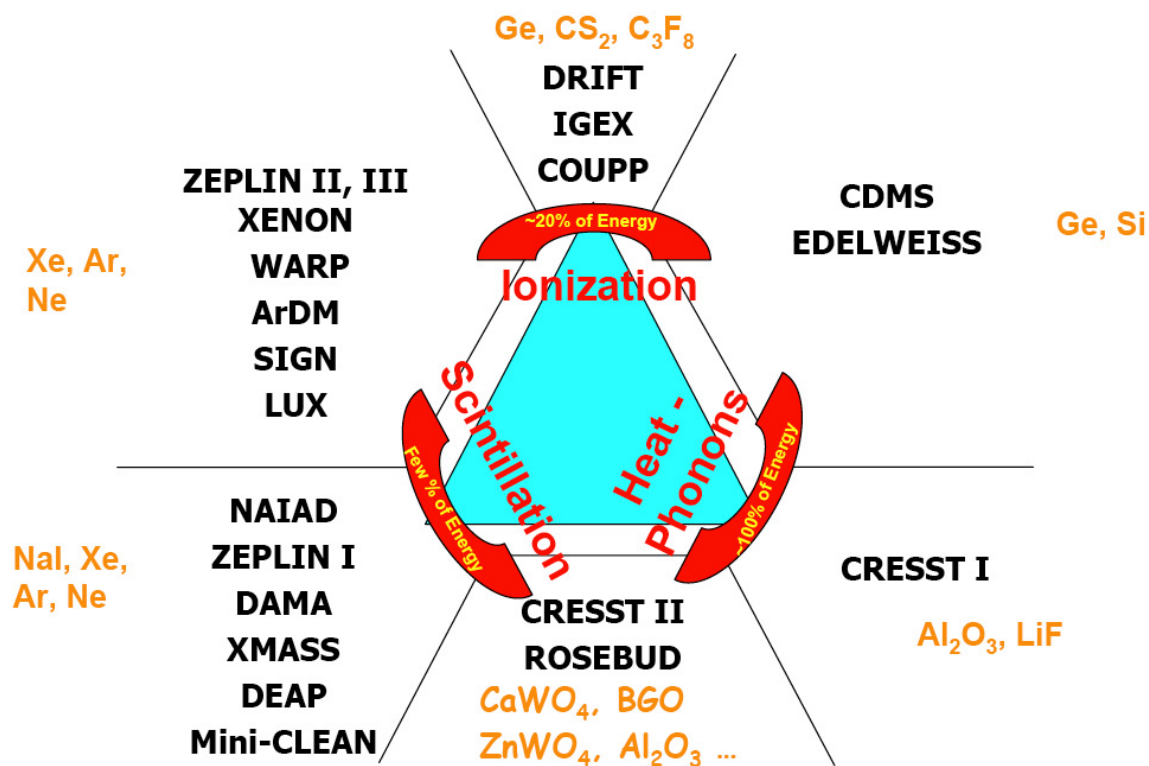


Figure 2.3: The triangle depicts the energy after a nuclear recoil interaction from a WIMP, each corner represents a channel where the energy from the interaction appears. Each detection technique exploits one or more of these channels. Most of the energy goes into phonons and ionization, the two channels used by CDMS and EDELWEISS. Figure from [76].

2.1.1 Cryogenic Particle Detectors

The detection of energetic particles through their calorimetric effects is based on the first law of thermodynamics. It is believed that as far back as 1880 Langley [77] developed a resistive bolometer to measure infrared radiation from the sun [78]. Some of the main applications of the calorimetric detection of particles includes high resolution X-ray astronomy, material analysis, neutrino physics, Lamb shift experiments, nuclear waste determination and, for the CDMS experiment, a low threshold nuclear recoil detector.

A cryogenic calorimeter consists of an absorber weakly thermally coupled to a heat bath. The temperature of the absorber is monitored by a thermometer. When a particle interacts with the calorimeter, it produces a temperature rise $\delta T = E/C_{tot}$ as a result of the energy E transferred from the particle to the calorimeter. C_{tot} is the total heat capacity of the absorber and thermometer. When the energy transferred to the detector mass is allowed to reach thermalization among all possible degrees of freedom in the absorber/thermometer, these are called equilibrium detectors. When the detector signal consists mostly of the energy channeled through certain degrees of freedom before it thermalizes or reaches equilibrium, it is called non-equilibrium detector. The CDMS detectors lie within the non-equilibrium regime.

The CDMS experiment, on which this thesis is mainly based, makes use of phonon sensors on the surface of germanium and silicon disks with 3 inch diameter and 1 cm thickness. The experiment measures the charge and phonon energy of each particle interaction occurring in the crystal. By taking advantage of the quenching of the charge signal by a factor of 2-3 for nuclear recoils relative to electron recoils, the CDMS detectors can distinguish between neutron (and WIMPs) and the rest of the particles. Figure 2.4 shows the ionization energy as a function of recoil energy for neutron events from a ^{252}Cf source and electron recoil events from a ^{133}Ba gamma-ray

source. In Chapter 3 I will describe in detail how is that CDMS-II achieves sensitivity to WIMP-nuclear recoils.

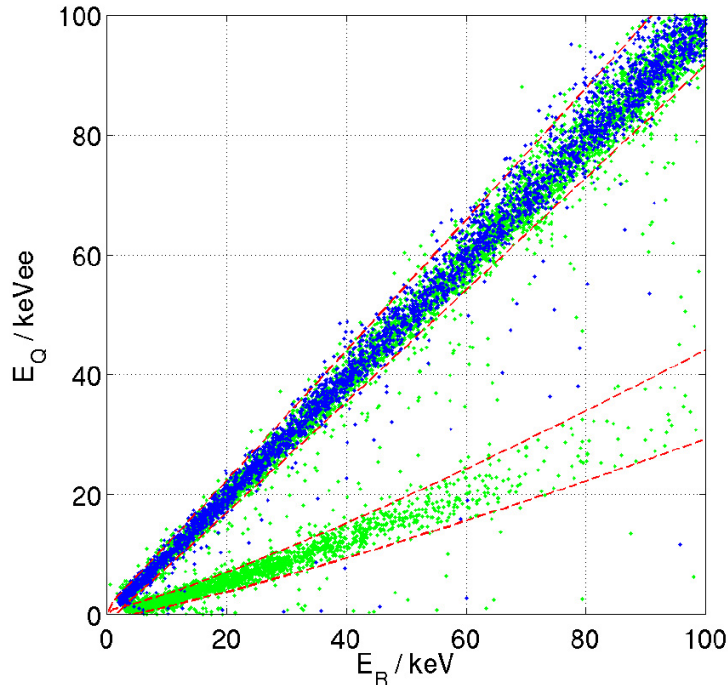


Figure 2.4: Ionization energy as a function of recoil energy. The upper band (blue) are events from a ^{133}Ba source, and the lower band (green) contains events from a ^{252}Cf source[142]. Note that there are some green events in the upper blue band. This is because the ^{252}Cf neutron source emits a significant amount of gamma-rays in addition to the low-energy neutrons.

The CRESST [79] dark matter experiment makes use of CaWO_4 crystal as the substrate, operated as a cryogenic calorimeter for the phonon channel, and also utilizes a nearby separate cryogenic detector optimized for the detection of scintillation photons, making the light channel. Since a nucleus and an electron or gamma of the same energy differ in the amount of scintillation light they produce, by measuring the phonon and light signals in an event by event way, they are able to discriminate between the electromagnetic backgrounds such as gamma-rays, electrons, positrons, alpha particles and any charged cosmic rays from neutrons or WIMPs [80]. The latest data from CRESST in 2005 consists of two 300 g detector modules, with a net

exposure of 20.5 kg-days.

Of all direct detection experiments, the one that resembles the CDMS detection technique the most is the one used by the French collaboration EDELWEISS [81]. They have used germanium detectors with a mass of 320 g each and were able to accumulate an exposure of 62 kg-days in the latest results reported for which competitive limits on the WIMP-nucleon cross section were set [82].

The operation efficiency of these cryogenic detectors is a significant part of the effort needed for the experiment to succeed given the difficulties of operating at tens of millikelvin. As I will discuss in the upcoming chapters, the CDMS experiment is at the forefront in WIMP sensitivity (for spin-independent interactions) not only with respect to the other cryogenic experiments but to all direct detection experiments so far, although noble liquid based detectors have made significant progress in the past few years and are a very promising competition to CDMS.

2.1.2 Noble liquid detectors

Noble liquid based nuclear recoil detectors for WIMP detection have put their potential on the map with the front runners using a Xe TPC (Time Projection Chamber) detector. Many noble liquids such as xenon, argon and neon have high scintillation yields, can be somewhat purified of radioactive contaminants (^{39}Ar requires isotope separation and ^{85}Kr can be removed by charcoal distillation), and are likely scalable to large masses more easily than cryogenic particle detectors. Furthermore, the fact that the scintillation light from these noble liquids does not get absorbed by the liquid itself together with their relatively high atomic weight (Xe and Ar) makes them an excellent target for WIMP detection. They also have the ability to use self shielding to set a fiducial volume cut in the central part of the target material in order to avoid external radioactive backgrounds (coming mostly from the readout system of photomultiplier tubes).

WIMP detectors based on noble liquids are based on the discrimination between nuclear recoil events that constitute the WIMP signal (and neutrons) and electron recoil events that constitute the electromagnetic backgrounds. Some experiments rely on the scintillation light as well as the ionization produced by the interaction, for example the XENON [83], ZEPLIN [84], WARP [85] and ArDM [86] experiments. These experiments are dual phase detectors, in which the liquid phase is used for the target and the gaseous phase is used to amplify the ionization signal. The ratios of light to charge signal are used as discrimination parameters to distinguish the nuclear and electron recoil event populations. Single phase detectors have been proposed as well, in which only the scintillation light using pulse shape difference is used to discriminate nuclear and electron recoils. The scintillation light in noble gases is produced by the decay of excimers that can exist in either a singlet or triplet molecular states, and are produced by particle interactions. The decay lifetimes of these singlet and triplet states for neon, argon and xenon is shown in Table 2.1. The relative amplitudes of the fast and slow emission of scintillation light according to the type of interaction can be used to discriminate between nuclear and electron recoils, although the effect is not that strong in Xe.

	Singlet Lifetime (ns)	Triplet Lifetime (ns)
Ne	$< 18.2 \pm 0.2$	14900 ± 300
Ar	7.0 ± 1.0	1600 ± 100
Xe	4.3 ± 0.6	22.0 ± 2.0

Table 2.1: Lifetimes of the singlet and triplet excimer states for neon, argon and xenon [87, 88].

The CLEAN [89] and DEAP [90] dark matter experiments are planning to use the pulse shape discrimination qualities of neon and argon, respectively. The presence of the cosmogenic ^{39}Ar in argon produces 1 Bq per kg [99], demanding a discrimination

capability for DEAP of about 10^{-8} or better [90]. Discrimination capabilities of part per billion in electron recoil contamination (the probability of incorrectly classifying an electron recoil as a nuclear recoil) have been claimed possible with these experiments. The CLEAN experiment will be sensitive to low energy neutrinos as well as for WIMPs, although the low- A of neon requires more mass compared to argon to reach the same WIMP sensitivity.

2.1.3 Directional Detectors and Other Technologies

An ongoing research and development effort is focused on directional WIMP detectors in which the ability to measure the day/night modulation of a WIMP signal would be possible by measuring the direction of the recoiling nucleus when a WIMP scatter occurs. Some detectors such as the proposed by the DRIFT [91] collaboration would be sensitive to the recoils track, other detectors such as the proposed by the DMTPC [92] collaboration aim to not only measure the recoil track but also the direction of it (the “head-tail” effect). The DRIFT detector consists of a Negative Ion Time Projection Chamber (NITPC) and operates at a pressure of $\sim 1/20$ atm and can measure recoil tracks to a few mm [93]. The DMTPC detector is being developed to have the capability of imaging the direction of the nuclear recoils by using a low pressure TPC filled with CF_4 and coupled with a CCD camera. These technologies are still under development and are not expected to have competitive WIMP sensitivity in the next several years but, if proven successful, will provide a unique measurement that could have more sensitivity to establish the galactic origin of the WIMP halo, compared to the other detectors that only measure the energy of the nuclear recoil.

Other detector technologies with radically different approaches are the superheated liquid detectors. Super heated liquid detectors, in the form of bubble chambers, were used as a particle detector in accelerator experiments [94]. The COUPP collaboration has improved the deactivation of inhomogeneous bubble nucleation centers

and has shown that it is possible to achieve a long stability in moderately superheated bubble chambers, reaching competitive sensitivity to direct detection of WIMP dark matter [95]. The thermodynamic properties of superheated liquids can be set up in a way to respond exclusively to particles that have a large stopping power and therefore muons, gamma-rays, etc. will fall below a certain bubble nucleation threshold (~ 50 keV for a WIMP search [96]). Given that a few-keV nuclear recoils will deposit much more energy than minimum ionizing particles due to the denser energy deposition, it is possible to be sensitive to WIMP nuclear recoils while insensitive to most other ionizing particles. The COUPP collaboration has recently reported on a WIMP search run with a bubble chamber containing 1.5 kg of superheated CF_3I , a target optimum for spin-dependent and independent WIMP interactions. They achieved an exposure greater than 250 kg-days, achieving improved limits on the spin-dependent WIMP-proton scattering cross section, excluding the remaining DAMA/NaI dark matter discovery claim (to be explained in section 2.1.4) under the WIMP hypothesis and standard halo.

2.1.4 The DAMA annual modulation

The Italian-Chinese collaboration, DAMA, aims at exploiting the expected annual modulation signature of dark matter caused by the Earth orbit around the Sun on the number of events induced by the dark matter particles. Therefore, this experiment expects a larger flux around June 2nd when the orbital velocity of the Earth is summed to the orbital velocity of the solar system around the Galaxy, and expect a smaller rate around December 2nd, when the orbital velocities of the Earth and of the Sun are anti-parallel [100]. The signal counting rate in the k -th energy interval as a function of time t can be written as:

$$S_k = S_{0,k} + S_{m,k} \cos [\omega (t - t_0)], \quad (2.15)$$

where $S_{0,k}$ is the constant part of the signal, $S_{m,k}$ is the modulation amplitude, ω is the frequency and t_0 the phase [100]. The DAMA detectors consist of $\simeq 100$ kg of radiopure NaI(Tl) scintillators. The latest generation of this experiment (LIBRA) has a mass of approximately 250 kg. The expected DAMA annual modulation signature from dark matter particles will have the following features [100]:

- (a) the modulation of the rate must follow a cosine function with a period of one year,
- (b) the phase of the signal modulation should be close to June 2nd and produce an effect $\simeq 7\%$ (depending on the properties of the galactic dark matter halo),
- (c) the signals producing the modulation must be low energy and be single hits.

The DAMA collaboration sees this approach as model-independent because nothing is assumed about the nature of the particle causing the energy deposition and the modulation, in contrast to all the other direct detection methods that assume that the dark matter is the Weakly Interacting Massive Particle and scatters from nuclei. The DAMA/NaI experiment [101] claims the first direct-detection model-independent evidence for the presence of dark matter particles in the Milky Way halo. In 1996, the DAMA/LIBRA experiment was proposed which consists in a 250 kg of radiopure NaI(Tl) crystals. Recently, the DAMA/LIBRA collaboration has reinforced the claim of evidence for dark matter from an observed annual modulation of the detected single rates at very low energies ($\lesssim 10$ keV).

They claim they have done a model independent analysis of the residual rates of the single-hit events in the lowest energy regions. The residual singles rates are calculated from the measured rate after some efficiency corrections and after subtracting the constant part defined by:

$$\langle r_{ijk} - flat_{jk} \rangle_{jk}, \quad (2.16)$$

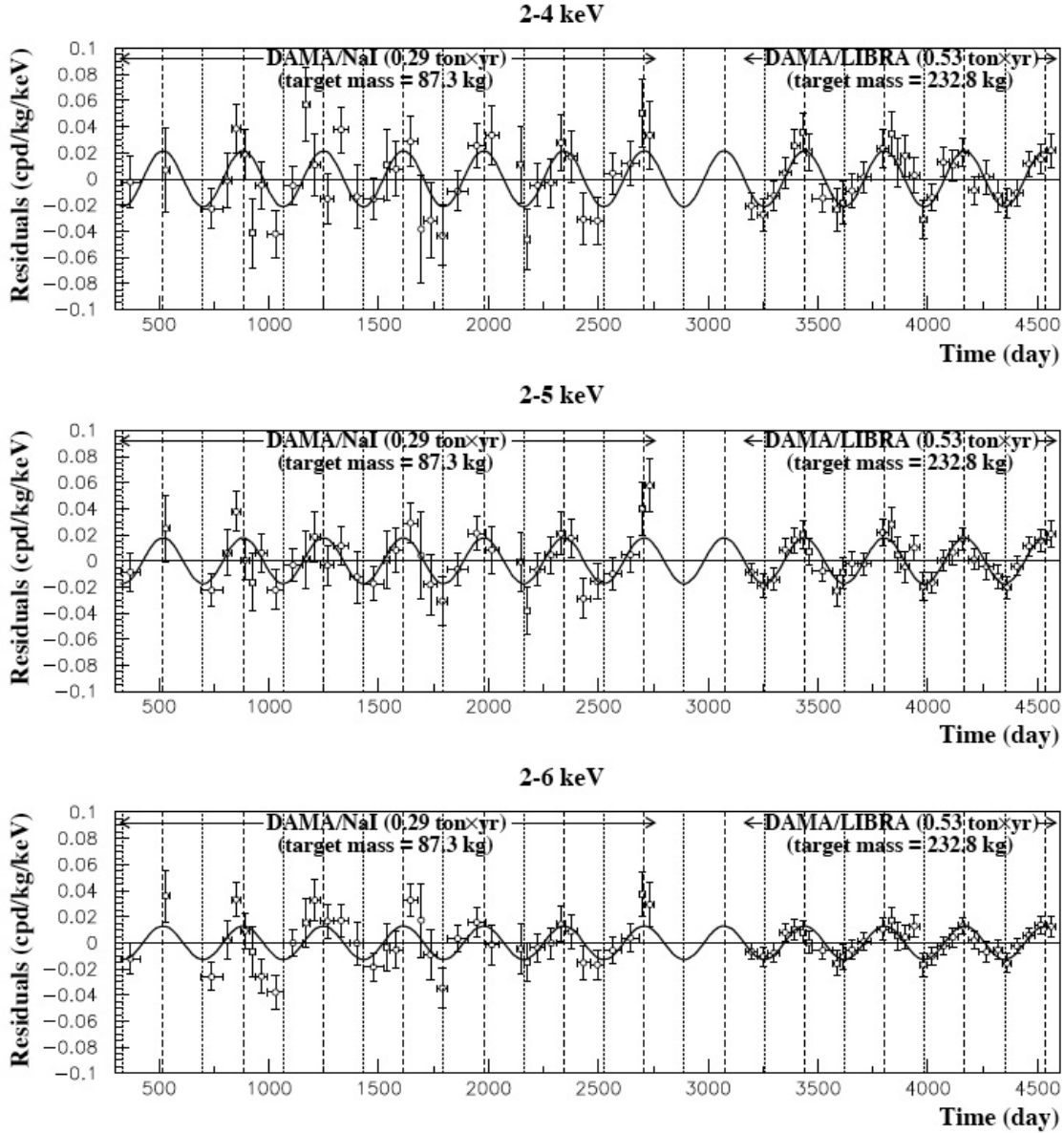


Figure 2.5: The residual single-hit events in the 2–4, 2–5 and 2–6 keV energy intervals for the DAMA/NaI and DAMA/LIBRA experiments with an exposure of 0.53 and 0.29 ton-year, respectively. The zero of the time scale is January 1st. The solid lines correspond to the superimposed cosinusoidal functions $A \cos[\omega(t - t_0)]$ with a period of one year, a phase $t_0 = 152.5$ days (June 2nd) and with an amplitude A (0.0215 ± 0.0026) cpd/kg/keV, (0.0176 ± 0.0020) cpd/kg/keV and (0.0129 ± 0.0016) cpd/kg/keV for the (2–4) keV, for the (2–5) keV and for the (2–6) keV energy intervals, respectively[102].

where r_{ijk} is the rate in the i -th time interval for the j -th detector in the k -th energy bin, and $flat_{jk}$ is the rate of the j -th detector in the k -th energy bin averaged over the cycles. The average is made on all detectors (j index) and on all the 1 keV energy bins (k index). In figure 2.5 the residual rates for single-hits in the DAMA/LIBRA experiment are shown over four annual cycles, each with 0.53 ton-year. Also the rates from the previous experiment, the DAMA/NaI which accumulated an exposure of 0.29 ton-year, are shown. The improved signal due to increased statistics is clear in this plot and the annual modulation is evident. Other possible systematic effects such as temperature effects on the noise of the photomultiplier tubes, humidity related backgrounds, radon or other systematic effects has not been conclusively established.

Assuming a spin-independent interaction and a WIMP mass of tens of GeV/c^2 or higher, the primary target would be iodine because of the low A of Na, and the WIMP-nucleus cross section extracted from the annual modulation in the DAMA/NaI experiment would correspond to $\simeq 10^{-5}$ pb. This claim has been ruled out by previous CDMS results [203, 204] and by many other experiments, including various targets and radically different techniques from that of CDMS. Nevertheless, due to the insufficiently-low energy threshold of the CDMS and majority of the other experiments, it has been proposed that light WIMPs ($\lesssim 10 \text{ GeV}/c^2$) could cause the observed modulation and still be undetected by the other experiments [103, 104]. Recently, the COUPP collaboration, using an improved bubble chamber technology, has ruled out the WIMP hypothesis for spin-dependent WIMP-nucleus interactions [96]. The remaining possibility that low-mass WIMPs undergo spin-independent interactions has been ruled out more recently by the CoGeNT collaboration [97] employing a new type of germanium radiation detector with a very low electronic noise [98].

2.2 Indirect detection experiments

In the previous section I discussed the main signatures of the dark matter particle as it interacts directly with the detector medium. In addition to direct detection signals, there are also proposed methods to detect the annihilation products of the dark matter particles. Indirect detection experiments aim to detect the annihilation products of the dark matter particles. These annihilation products could be photons, neutrinos and antimatter. In the following subsections I will discuss each of this detection channels and the main experiments that have been proposed, are operating or already have results.

2.2.1 Gamma ray searches

In considering WIMP annihilation to gamma-rays, it is important to consider the distribution of WIMPs in the Galaxy, particularly at the galactic center. One of the standard models, which is due to Navarro, Frenk and White (NFW) gives a density profile that peaks at the galactic center. This region has long been considered to be one of the most promising windows to search for gamma rays from dark matter annihilations yet the understanding of astrophysical backgrounds is essential in order to understand a potential signal. Furthermore, not only is the galactic center is expected to have enhanced probability of detection, but any high-density objects nearby such as dwarf spheroidals (see for example Evans et al. [105]) or other dark matter structures (as an example see Pieri et al. [106]) could also enhance the rate.

There are two main types of detectors that can look for WIMP-induced energetic gamma rays: space based such as the GLAST [75] and its predecessor EGRET and the Atmospheric Cerenkov Telescopes such as HESS [107], MAGIC [108], WHIPPLE [109] and CANGAROO-II [110]. The advantages of GLAST over other telescopes are the low energy threshold, allowing to probe neutralino masses greater than 10 GeV. The

background to GLAST is expected to be mainly due to the diffuse extragalactic emission and furthermore, the spatial resolution of the GLAST telescope varies with the threshold energy, allowing to probe the halo density profile [75].

According to latest reviews [51], the prospects of detecting gamma rays from dark matter annihilations in the near future lie mostly on the satellite-based experiment GLAST and several ground based Atmospheric Cherenkov Telescopes such as HESS, MAGIC and VERITAS. While GLAST will have a lower threshold (~ 300 MeV) and be more sensitive to lighter WIMPs (~ 200 MeV), it has limited effective area compared to the ground based observatories that have several orders of magnitude larger but have higher threshold (~ 100 GeV) and therefore are more sensitive to higher mass WIMPs. Furthermore, GLAST will continuously observe a large fraction of the sky in contrast to ground based telescopes that can study the emission of gamma rays from a small angular field, but with much larger exposures.

In relation to indirect detection of dark matter with photon fluxes, that studies of the WMAP data have revealed an excess of the microwave emission from the region around the center of the Milky Way (in the inner 20°). It has been suggested that this signal, known as the “WMAP Haze” [111], could be synchrotron emission from relativistic electrons and positrons generated in dark matter annihilations [112].

2.2.2 Neutrino detectors

The dark matter particles that are captured in the gravitational wells of the Sun and Earth, are expected to end their journey through the universe 13.4 billions later, through the process of annihilation, as we have mentioned in the previous section. The rate of capture in the Sun depends on whether the dark matter WIMPs are spin dependent (SD) or independent (SI) since the Sun is primarily composed of Hydrogen which has a net spin. For the case of the Earth, the contributions to the capture rate via SD interaction are negligible for heavy nuclei. Since the SD cross section is ~ 6

orders of magnitude less constrained than the SI cross section, the models that predict large SD rates are able to produce larger signals due to less constraints so far and therefore a neutrino flux from dark matter annihilations from the Sun will most likely be originated from SD WIMPs [113]. The dark matter capture rate in the Sun is given by

$$C_{\odot} = 3.4 \times 10^{20} s^{-1} \left(\frac{\rho_{local}}{0.3 \text{ GeV}/\text{cm}^3} \right) \left(\frac{270 \text{ km/s}}{v_{local}} \right)^3 \left(\frac{\sigma_{cap}}{10^{-6} \text{ pb}} \right) \left(\frac{100 \text{ GeV}}{M_{DM}} \right)^2 \quad (2.17)$$

where ρ_{local} ($\sim 0.3 \text{ GeV}/\text{cm}^3$) and v_{local} are the local density and velocity of the WIMPs. The effective capture cross section of WIMPs with solar matter, which determine how efficiently the Sun slows down and captures WIMPs is given by

$$\sigma_{cap} = \sigma_{SD}^H + \sigma_{SI}^H + 0.07\sigma_{SI}^{He} \quad (2.18)$$

where the factor 0.7 comes from the relative abundance of helium and hydrogen in the Sun [114]. The capture rate of WIMPs in the Milky Way halo by the Earth is given, approximately, by [43]

$$C_{\oplus} = 4.8 \times 10^{13} s^{-1} \left(\frac{\rho_{local}}{0.3 \text{ GeV}/\text{cm}^3} \right) f_{\oplus}(M_{\chi}) \left(\frac{\sigma_{cap}}{10^{-6} \text{ pb}} \right) \left(\frac{\mu_{p-\chi}}{1 \text{ GeV}} \right)^{-2}, \quad (2.19)$$

where $\mu_{p-\chi} = \frac{M_{\chi} m_p}{M_{\chi} + m_p}$ is the reduced mass of the WIMP-nucleon system, $\sigma_{cap} = \sigma_{SI}^H$ and the form factor $f_{\oplus}(M_{\chi})$ has been obtained in Ref. [43]. If a WIMP annihilation signal from the Earth is observed, but not from the Sun, this would strongly suggest that the WIMP particle has no significant SD couplings. In Fig. 2.6 the event rate expected in a kilometer-scale neutrino telescope with a threshold of 50 GeV is shown as a function of the WIMPs effective scattering cross section for several annihilation modes [114]. These rates are expected in experiments such as IceCube at the South Pole [115] or at the Mediterranean Sea with a similar scale [116]. The strongest limits on high-energy neutrinos from the Sun are set by the Super-Kamiokande experiment [117]. WIMPs with a largely spin-dependent scattering cross section with protons may be able to generate large event rates in high energy neutrino telescopes.

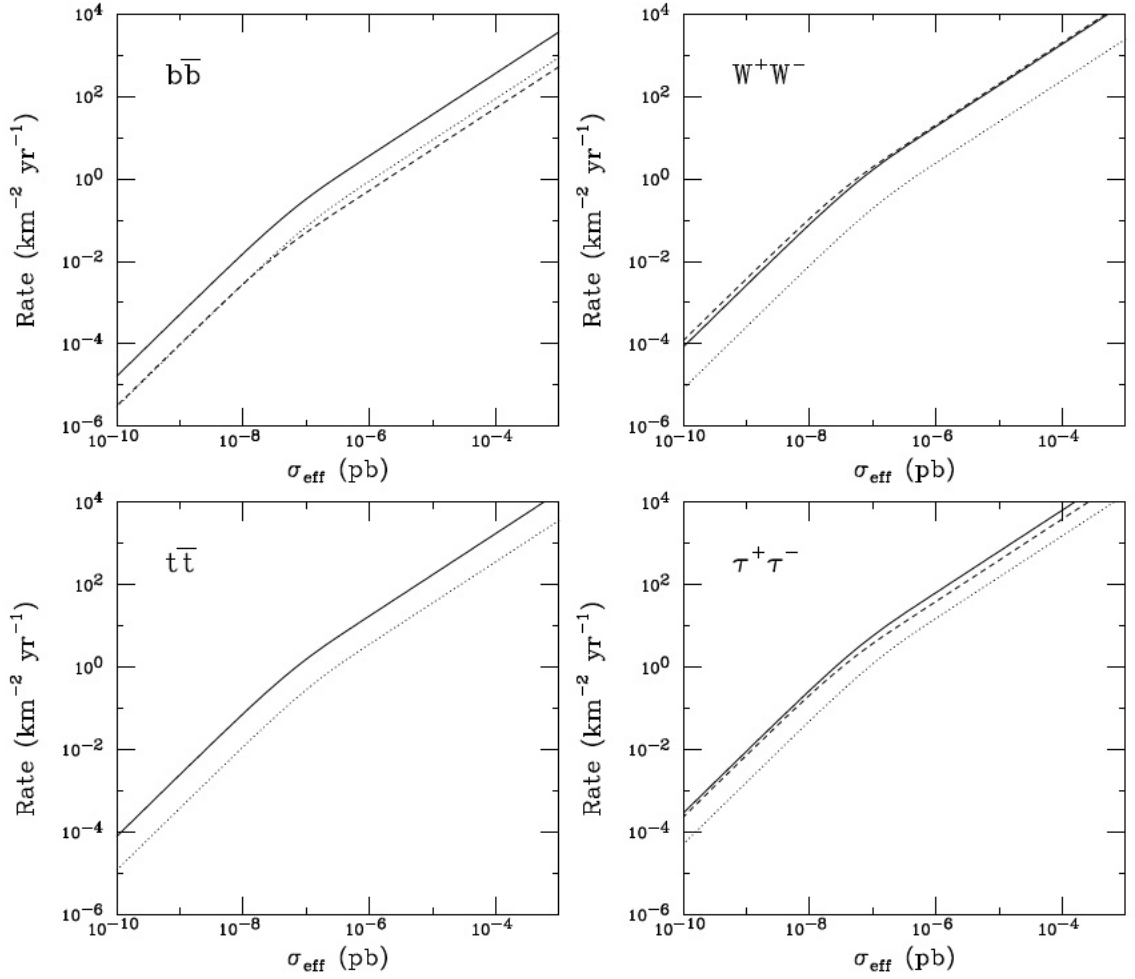


Figure 2.6: The event rate produced by neutrinos from WIMP annihilations in the Sun in a kilometer-scale detector such as IceCube as a function of the effective WIMP elastic scattering cross section for several annihilation modes. The dashed, solid and dotted lines correspond to a WIMP mass of 100, 300 and 1000 GeV respectively [51].

2.2.3 Cosmic antimatter detectors

Another product of WIMP annihilations in the galactic halo are the anti-matter charged particles: positrons, anti-protons and anti-deuterons. When WIMPs annihilate in the galactic halo, they can produce quarks, leptons, gauge bosons, Higgs bosons and gluons. The origin of positrons comes when these particles either decay and/or hadronize (produce hadron jets). Therefore, a signal is expected to be possibly made

of both monochromatic positrons (at an energy m_χ) from direct annihilation into e^+e^- and a continuum of positrons from the other annihilation channels [118]. The most recent satellite-based experiments looking for cosmic antimatter are PAMELA [119], which began a three-year satellite mission in June 2006, and AMS-02 [122] which hopes to be deployed to the International Space Station sometime soon. Collected data from the HEAT [120] and AMS-01 [121] experiments contain excess positrons that could be explained only by dark matter annihilations.

The search for cosmic positrons is motivated by the fact that positrons lose most of their energy over length scales of a few kiloparsecs and therefore can sample only the local dark matter distribution and thus are subject to less uncertainty than to an antiproton or antideuteron signal [118] owing to less well known non-local cosmic-ray backgrounds. In Fig. 2.7 the ratio of positrons to both positrons plus electrons in the cosmic ray spectrum is shown as a function of energy together with a potential contribution from dark matter annihilations and the measurements from the HEAT experiment [120] which could possibly contain an excess of positrons in comparison to the expectations at energies greater than ~ 7 GeV.

In 1999, Donato and collaborators [124] proposed to look for cosmic antideuterons (\bar{d}) as a possible indirect signature for dark matter in our galaxy. They showed that the antideuteron spectra from dark matter annihilation is expected to be much flatter than the standard astrophysical component at low kinetic energies ($T_{\bar{d}} \lesssim 2-3$ GeV/n). The production of antideuterons in our galaxy is based on the fusion process of \bar{p} and \bar{n} . Currently there are several efforts underway for space-borne experiments to measure the galactic antideuteron flux such as the GAPS experiment [125, 126, 127] although the AMS-02 experiment [128] could potentially have a window to observe antideuterons as well. The gaseous antiparticle spectrometer (GAPS) identifies antiparticles through the characteristic X-rays emitted by antimatter when it forms exotic atoms in gases. The source of background in a primary antideuteron search

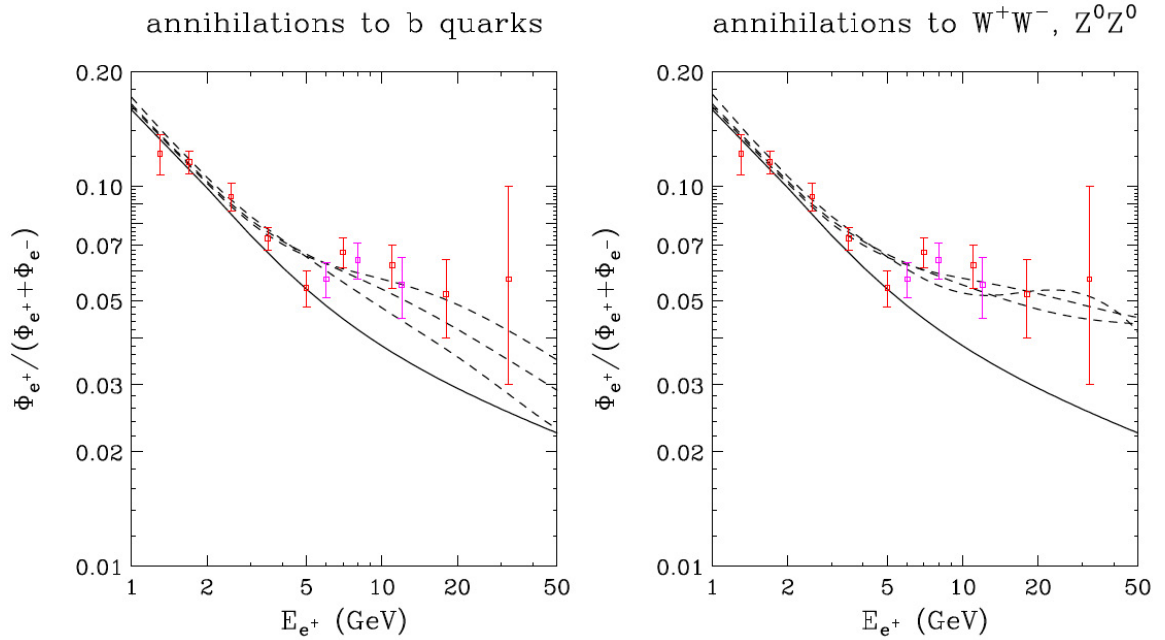


Figure 2.7: The fraction of the positron flux relative to the sum of positrons and electrons flux together with what is expected from dark matter annihilations compared to the measurement of the HEAT experiment [120]. The WIMP masses considered are for 100, 300 and 600 GeV. In the left plot, the WIMPs originate from $b\bar{b}$ annihilations. On the right plot, WIMPs are originated from a mixture of ZZ and W^+W^- . In order to make the HEAT data comparable to the expected WIMP annihilations, a cross section of $\sigma v = 3 \times 10^{-26} \text{ cm}^3/\text{sec}$ and a local density of $0.3 \text{ GeV}/\text{cm}^3$ is assumed together with a factor of 50 or more “boost factor”. The solid line corresponds to a Galactic cosmic ray model [123].

is the secondary antideuterons produced in cosmic-ray interactions, as is in the case for the antiproton induced WIMP annihilation searches. But the fact that secondary antideuterons cut off at much higher kinetic energy than in the case of secondary and tertiary antiprotons, makes the case for an antideuteron search more promising [125]. If primary antideuterons are searched for at low energy, the background contamination from secondary antideuterons would be negligible, in contrast to the antiproton background as seen in Fig. 2.8.

In summary, indirect searches could have better sensitivity than direct searches for some regions of parameter space, and play an equally significant role in others. Figure 2.9 shows the reach of the next generation searches for neutralino dark matter,

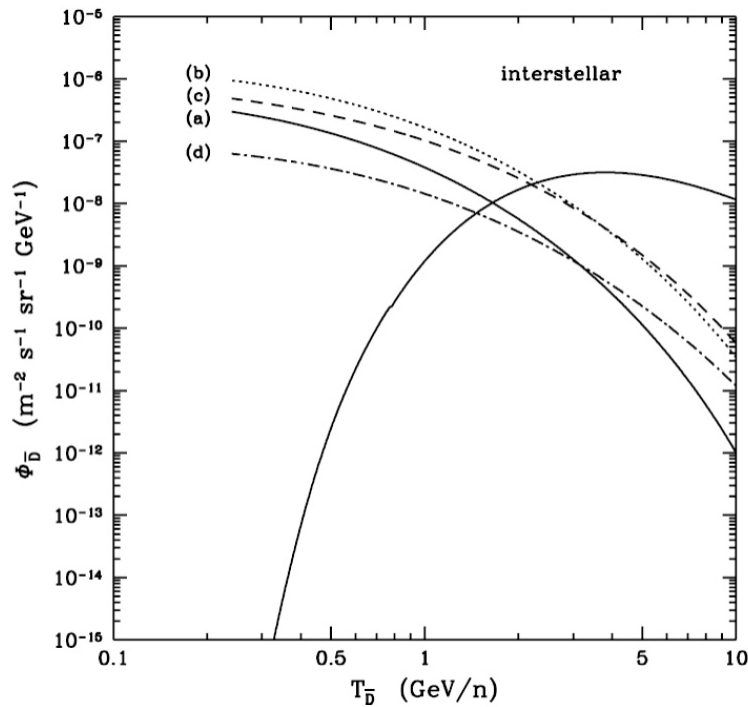


Figure 2.8: The interstellar flux of secondary antideuterons (solid curve starting at $T_{\bar{D}}$ of ~ 0.3 GeV/n) decreases at lower energy (the background) and the energy spectrum of the antideuterons from WIMP annihilations (curves *a* to *d*) remain approximately constant at low energy [124]. Figure from [125].

comparing the reach of direct and indirect searches.

2.3 New Particles at the High-Energy Colliders

If TeV-scale supersymmetry exists in nature, it will very likely be within the discovery reach of the Large Hadron Collider (LHC). Particles with TeV scale masses that originate in models of electroweak symmetry breaking also have QCD color, therefore, any particle with these properties will be pair-produced at the LHC with a cross section in the tens of picobarns [131]. The signature of these type of particles at the LHC would be events with many hadronic jets and an imbalance of measured momentum [51]. If a measurement of the supersymmetric particles is done at the LHC,

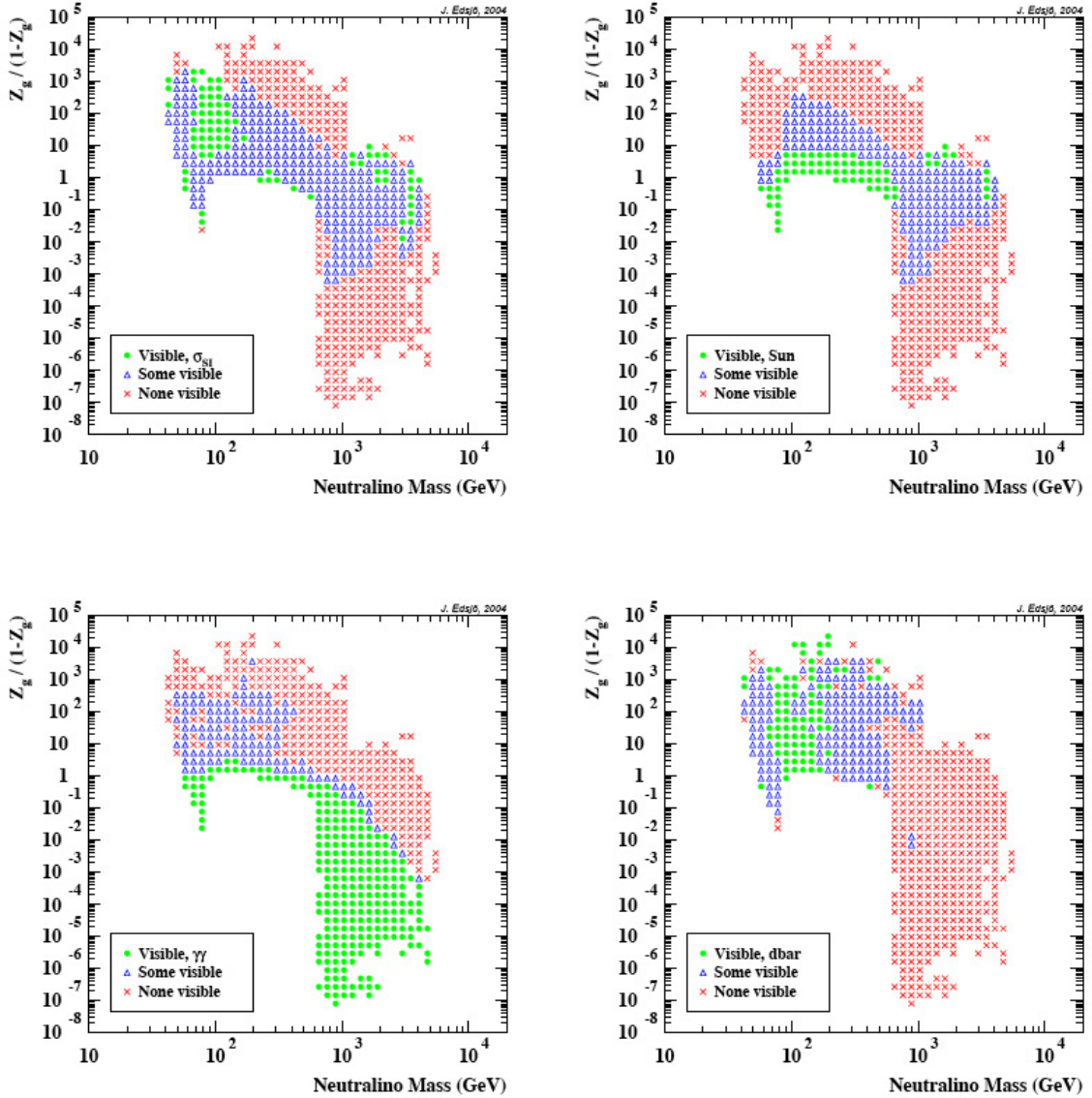


Figure 2.9: The possible reach of the next generation of direct and indirect neutralino dark matter searches. (a) *Top left*: Direct Searches, (b) *Top right*: Indirect Searches via high-energy neutrinos from the Sun, (c) *Bottom Left*: Indirect Searches via a gamma-ray line from the Galactic halo, (d) *Bottom Right*: Indirect Searches looking for antideuteron component in cosmic rays. The y-axis, the neutralino component, is expressed by the ratio of the gaugino and higgsino fractions $Z_g/(1 - Z_g) = Z_g/Z_h$. The green full dots are values that can be reached in the respective search, the blue triangles are values that some but not all can be reached and red open circles correspond to values that none of the searches can reach [129, 130].

this can provide the cross check for measurements from direct and indirect detection. Direct and indirect detection experiments provide information on the combination of density and cross section, i.e., a measured rate of nuclear recoils (or annihilation products) from a small fraction of the dark matter halo might be due to a large elastic scattering (or annihilation cross section).

Baltz and coworkers [132] have done studies of supersymmetry models with neutralino dark matter that give quantitative estimates of the expected accuracy to make predictions of the cosmic density, the annihilation cross sections, and the cross sections relevant to direct detection based on the measured microscopic properties of dark matter at accelerators such as the LHC and the ILC. Because there are many parameters of SUSY that remain unconstrained by data, Baltz and coworkers have chosen a few values in this parameter space to help define measurement scenarios for specific experimental signatures at the LHC, ILC and direct searches as well as how a set of actual measurements might constrain the SUSY parameter space. They picked certain benchmark points in the parameter space of the models and are labeled LCC1, LCC2, LCC3 and LCC4, each with a relic density of enough to explain dark matter.

The benchmark points are intentionally chosen so that the lightest particles of the supersymmetry spectrum can be observed at the ILC at its initial center of mass energy (500 GeV). Furthermore, they have chosen to analyze points in the MSSM parameter space at which simulations have been carried out to estimate the ability of colliders to measure parameters of the supersymmetry spectrum. In the LCC1 benchmark point, the LHC could measure the accessible masses of the neutralinos, sleptons (except the heavy stau), squarks (except for stops), the gluino and the light Higgs. Figure 2.10 shows how the combination of collider and direct detection data can help constrain the mass of the WIMP. Specifically, the mass of the heavy Higgs bosons is usually unconstrained until a TeV ILC measurement, unless the value of the parameter $\tan\beta$ is large.

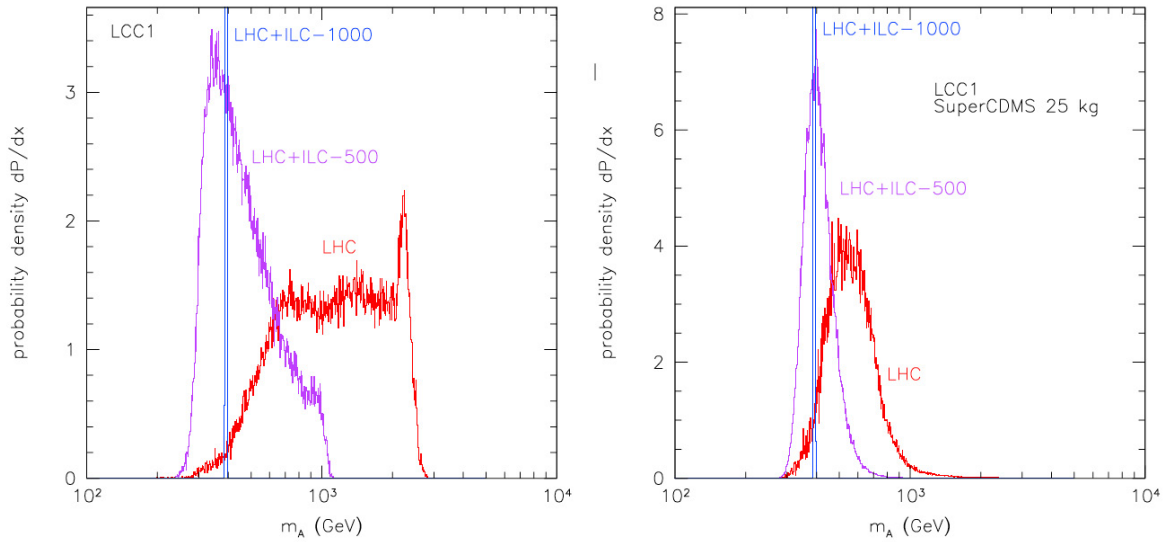


Figure 2.10: The range of mass of the heavy CP-odd Higgs for the benchmark model LCC1 is shown in the case of constraints from collider data only (left) and also the effect of combining the collider data together with direct detection data from the SuperCDMS 25 kg experiment [132]. The mass of the distribution for the CP-odd Higgs, when combined with the proposed CDMS 25 kg experiment, improves dramatically for LHC and also there is even mild improvement with measurements of the LHC+ILC.

It is clear from this chapter that not one experiment alone can determine the properties of the cosmological dark matter particle, but it will take a combination of ground, space and underground experiments. In the next chapter I will focus on the direct dark matter search experiment that this thesis is based on: the Cryogenic Dark Matter Search.

Chapter 3

The Cryogenic Dark Matter Search

In this chapter I will describe the strategy of the Cryogenic Dark Matter Search (CDMS) for nuclear recoils produced by WIMPs deep underground. To give an idea of the challenge, consider the expected event rate is < 1 event/kg/day, with an expected nuclear recoil energy of about 15 keV (as discussed in Chapter 2). The CDMS experiment can distinguish between nuclear recoils (neutron and WIMPs) and electron recoils (electromagnetic backgrounds) by simultaneously measuring the ionization and phonon energy of the particle interactions within an array of Ge and Si detectors, due to the fact that the ionization of nuclear recoils is quenched by a factor of 2-3 as compared to electron recoils. Furthermore, the pulse shape of the phonon signal provides the extra discrimination against events that could be misidentified as nuclear recoils due to an incomplete charge collection near the detector surface [133, 136] and are mainly due to low-energy electrons.

The CDMS-II experiment is located in one of the two caverns of the Soudan Underground Laboratory, close to the city of Ely, Minnesota, about an hour (by car) south of Canada. The CDMS-II infrastructure was designed and constructed jointly by Fermi National Laboratory and the University of Minnesota. The Depth of the Soudan Lab is 780 m. The rock consists of mostly Greenstone rock with a density of

2.8 g/cm³ but there is also some iron in the mine among other components (it was an iron mine).



Figure 3.1: A ZIP detector such as those used in the Cryogenic Dark Matter Search at the Soudan Underground Laboratory. The detector, inside its hexagonal copper housing has nearly cylindrical shape with 1 cm thickness, 3 inch diameter, and masses of 250 g in the case of Ge and 100 g for Si.

After the event discrimination is made using the ionization and phonon amplitudes and pulse shape of the phonon signals to reject electromagnetic backgrounds, the remaining backgrounds will be low energy (MeV) neutrons that can produce a nuclear recoil identical of that of the WIMP. CDMS can reject neutrons by using the fact that they can multiple scatter with the Ge/Si detector array while WIMPs cannot (the mean free path of an MeV neutron in Ge is a few cm). Furthermore, given that Ge and Si have similar scattering rates per nucleon for neutrons, the WIMP-nucleon cross section rate will be 5 to 7 times higher in Ge than in Si due to the difference in atomic number, while the rate of neutron events would be two times greater in a

Si than in a Ge detector. CDMS requires passive and active shielding that will be discussed in Section 3.6, to attenuate and veto neutrons from radioactivity in the rock and those that are produced by the remaining cosmic rays at the underground site (about 1 muon/minute reaches the shielding).

The detectors are almost cylindrical in shape, with a 1 cm thickness and 3 in diameter. In this chapter I will describe how they measure the ionization and phonons, the efficiency achieved for background rejection and how the passive and active shielding reduces the ambient backgrounds. Figure 3.1 shows a picture of a Ge detector in its copper housing. On top of the detector, square units can be distinguished which consist of tungsten transition edge sensors (TES) that will be described in this chapter. Each square unit has many phonon sensors totaling about 1000 per detector.

3.1 Cryogenics

The measurement of the phonon signal by the CDMS-II detectors using the TES technology require operation at tens of milikelvin in temperature. This ultracold temperature is achieved by the use of an Oxford Instruments Kelvinox 400-S dilution refrigerator. The refrigerator has an attached cold volume and many additions that allow to monitor it closely and allow remote control and good stability conditions for long term running (several months per “good” run). Surrounding the dilution refrigerator, the attached cold volume, the passive shielding and the active veto together with the outer vacuum chamber and a few electronic boxes, is the RF-shield box, known as the RF room. This RF-room is a class-10000 clean room during working hours and has achieved about class-1000 when it is being occupied. All the pumps, cryogen liquid supplies and the control systems of the dilution refrigerator unit are located outside the RF room (the “cryo pad”). The front-end electronics are in crates inside the RF-room. All the rest of the readout electronics for the detectors and veto

system are located outside the RF-room (the “electronics room”), see Figure 3.2.

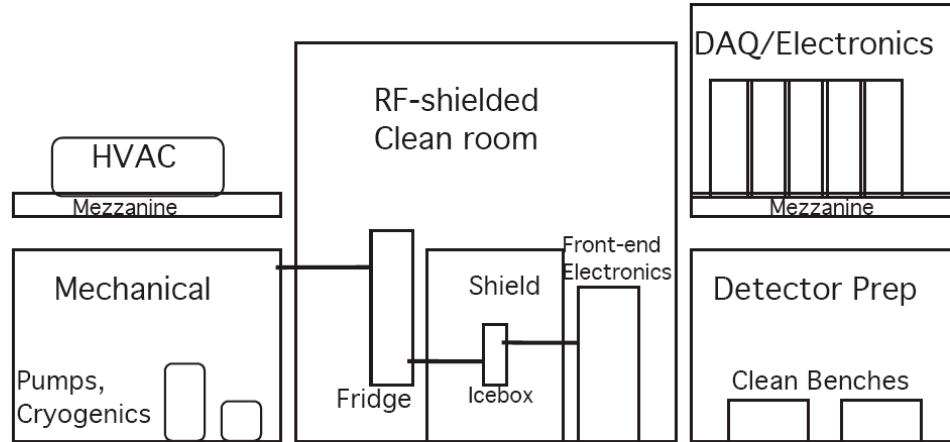


Figure 3.2: Drawing of the laboratory space assigned to CDMS-II at the Soudan Underground Laboratory, in Soudan, Minnesota.

There are six nested cylindrical cans that comprise the CDMS-II cryostat or “ice-box” [137, 138]. The copper used to make the cans is from low radioactivity copper and is thermally coupled to the temperature stages of the dilution refrigerator through a horizontal configuration of five nested copper cylinders and one cold finger, which together make the “cold stem”. The copper can housing the detectors is a cylinder with a 30 cm diameter and 30 cm height. The detectors are stacked in “towers” which consist of six detectors, one on top of the other. Each of them achieves a temperature of less than 50 mK. Figure 3.3 shows the innermost copper housing one tower. The icebox contains the cold hardware needed to mount cool and read out the detectors. Each detector tower has four temperature stages: 4 K, 600 mK, 50 mK and base. Furthermore, each detector is connected to an electronics card mounted on top of the tower. The electronics card consists of two field effect transistors (FETs) that

read out the ionization channels and are cooled to a temperature between 100-120 K to achieve optimal noise performance. At the 600 mK stage, four arrays of superconducting quantum interference devices (SQUIDs) are mounted, and they comprise the readout of each of the four phonon channels. After this stage, the signals are transported to room temperature through flexible copper-kapton striplines. All the cold hardware is made from low background materials such as copper, kapton and custom made solder [139].

3.2 Measurement of the Ionization Energy

The current design of the detectors used in CDMS-II are the ZIP (Z-dependent Ionization and Phonon mediated) detectors. The ZIP detectors consists of nearly cylindrical high-purity Ge or Si crystal that are 1 cm in thickness and 7.6 cm in diameter. Each has two concentric ionization electrodes and four independent phonon sensors (one for each quadrant) that are photolithographically patterned onto each crystal. When electromagnetic particles interact with the crystal, it will be primarily with the electrons in the crystal, for example via Compton scattering with an electron, causing an “electron recoil”, which means that the interaction deposits about 25% of its energy into the crystal through generating electron-hole pairs, and the remainder into phonons. If the interaction occurs with the nuclei, it will cause a nuclear recoil, and this will generate lattice vibrations or phonons as well as some electron-hole pairs (although only about 10% of the recoil energy). The simultaneous measurement of the ionization and phonon energy for each event allow the ZIP detectors to make an accurate measurement of the recoil energy independent of the recoil type, and more importantly, to distinguish between these electron and nuclear recoils. On average, one electron-hole pair is produced for every $\simeq 3.0$ eV of energy deposited in Ge, being $\simeq 3.6$ eV for Si. Depending on the material, energy and type of recoil, about

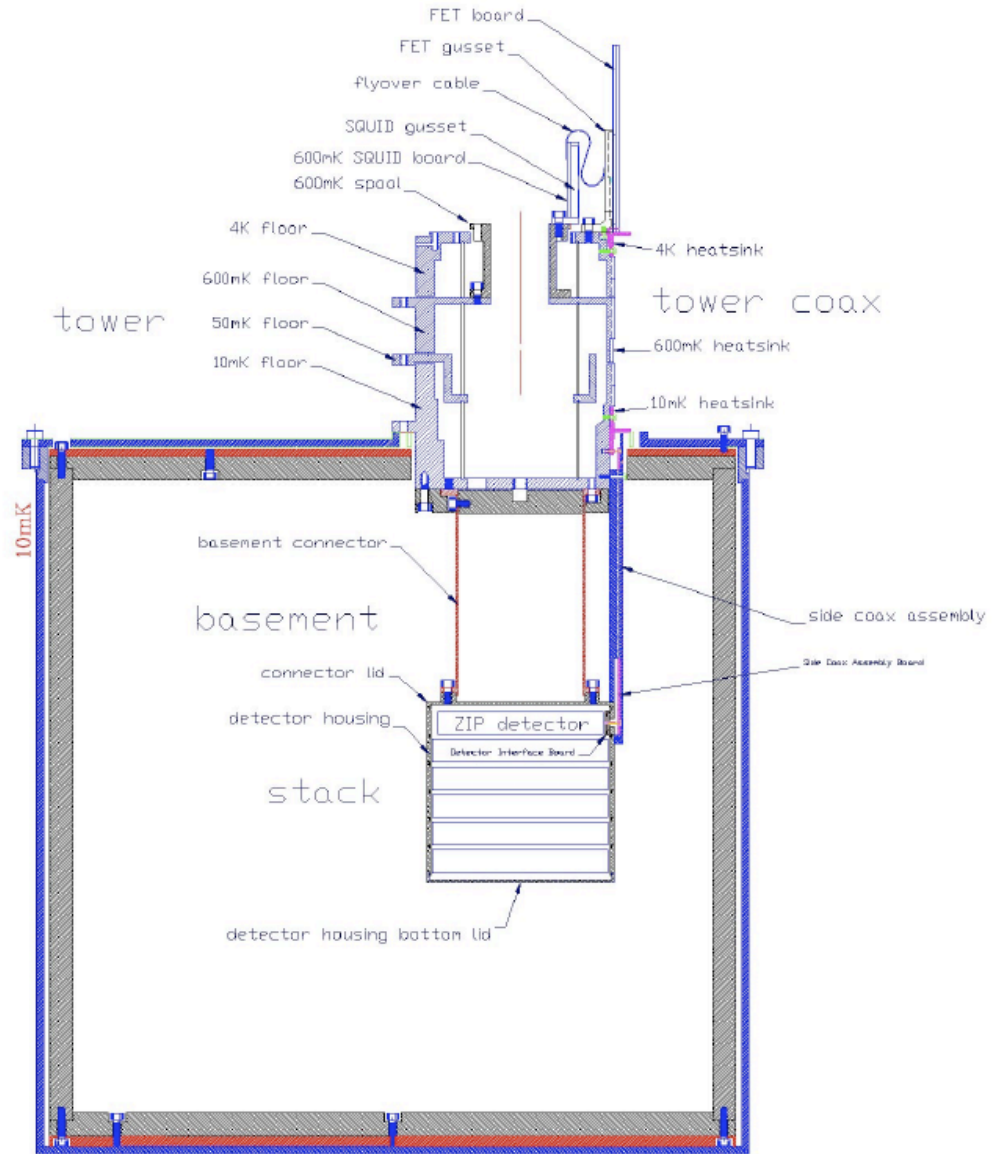


Figure 3.3: The innermost copper can with a “tower” consisting of a stack of six detectors. Note that there is no material in between the top and bottom faces of the detectors. The tower has four nominal temperature stages: 4 K, 600 mK, 50 mK and base. The FET cards are the cold electronics for the ionization channels, the SQUIDS are the readout for the phonon channels and are mounted on the 600 K stage.

6 to 33% of the recoil energy is first converted into ionization before it is converted to phonons. We define the “ionization energy” E_Q as the recoil energy as inferred

from the detected number of electron-hole pairs N_Q , by assuming that the event is an electron recoil with 100% charge collection efficiency:

$$E_Q \equiv N_Q \times \epsilon. \quad (3.1)$$

The ionization energy is conventionally reported in units of “keVee” (keV of the electron equivalent recoil determined from electron recoil calibration measurements).

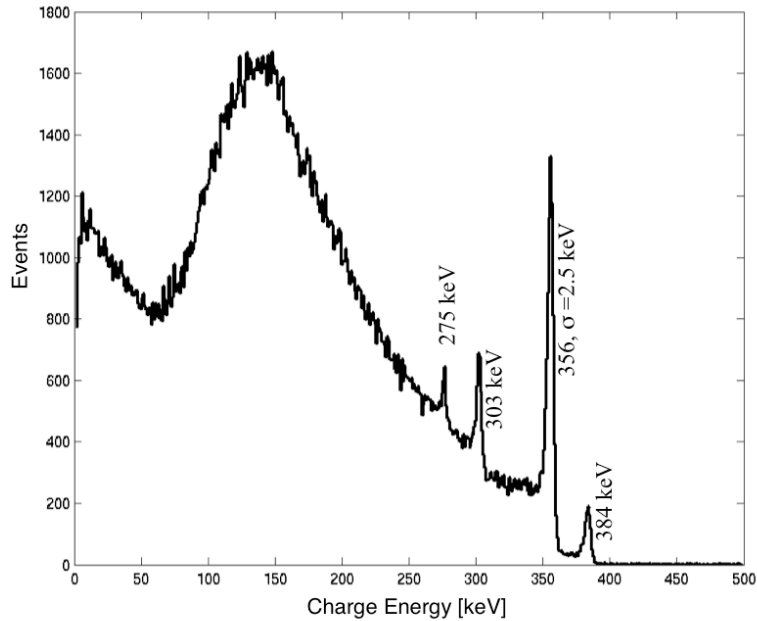
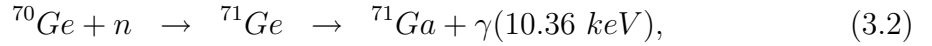


Figure 3.4: The charge energy measurement of the ZIP detector for the ^{133}Ba gamma calibration source used in CDMS-II. The mean of each gamma-line is shown and additionally the standard deviation of a gaussian fit for the 356 keV line.

Each ZIP detector has two channels from which the ionization measurement is made, the inner and the outer electrode. The outer electrode consists of a thin ring on the outside the ZIP detector, measuring about 2.0-2.7 mm in thickness, and totaling about 15-18% of the area. Figure 3.6 (a) shows the ionization side of the ZIP detector. The outer electrode (the “guard ring”) is used to reject events that occur near the bare unpolished edges of the crystal. These outer events are rejected due

to their reduced ionization signal that is degraded due to the shape of the electric field lines in this region. Also, the phonon signal is not optimum because the phonon sensors do not cover the outer edge with full efficiency (Figure 3.6 (b) shows the phonon side of the ZIP detector). Figure 3.4 shows the charge energy for the gamma calibration source ^{133}Ba . The resolution of the ionization measurement is $\sim 1\%$ for the 356 keV line. About 5% resolution is observed in Ge detectors at the low energy scale using the ^{71}Ga line at 10.36 keV from neutron activation of ^{70}Ge :



with a halflife of 11.4 days. Figure 3.5 shows the neutron activation-induced gamma line.

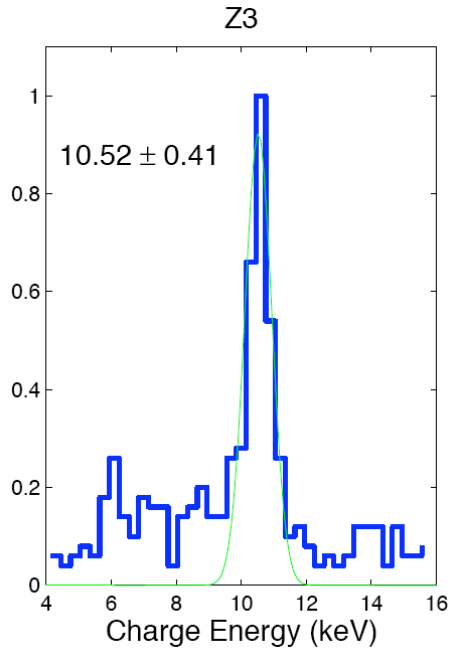


Figure 3.5: A neutron activation-induced gamma line observed in the Ge detectors after neutron calibrations. A resolution of $\sim 5\%$ is observed in Ge detectors at the low energy scale using the ^{71}Ga line at 10.36 keV from neutron activation of ^{70}Ge with a halflife of 11.4 days. The mean and standard deviation of a gaussian fit are shown in green [140].

3.3 Measurement of the Phonon Energy

The phonon measurement is made using 4 channels, each corresponding to a quadrant that has about 1000 quasiparticle-assisted electrothermal-feedback transition-edge sensors (QETs) [141], see Figure 3.6. These QETs consist of 8 aluminum thin films “fins” deposited on the Ge or Si substrate connected to tungsten (W) thin film strips. The Al fins act as quasiparticle absorbers: see Figures 3.7 and 3.6-(d). The tungsten films are operated in the superconducting transition and comprise the TESs. When a particle interaction occurs, phonons are generated (with an energy of about 10 THz for Ge and Si) and quickly decay to lower energy phonons. In a few microseconds the phonons have decayed to an energy below 1 THz, and have longer mean free paths than the dimensions of the crystals. These “ballistic” phonons travel through the crystal, hit the surface and are reflected or absorbed by the Al fins.

Following Figure 3.7, when the ballistic phonons are generated in the crystal due to an electron- or nuclear- recoil interaction, the ballistic phonons break the Cooper pairs in the Al fins and some of these Cooper pairs will eventually be absorbed by the tungsten TESs due to a difference in the energy gap. The energy needed to break a Cooper pair is about $340 \mu\text{eV}$ or a phonon frequency higher than $\sim 82 \text{ GHz}$. The ballistic phonons created by the interaction in the Ge or Si crystal have $\sim \text{THz}$ in frequency and therefore many quasiparticles are created in the Al fins and diffused to the tungsten TES, but some of the phonons created will be below the Cooper-pair break-up threshold and therefore will be lost ($\sim 50\%$ of the energy from the initial interaction will be lost in this way [143, 144]).

The phonon population that brakes the Copper pairs that in turn generate the phonon pulse in the ZIP detector contains phonons from the lattice vibrations generated by the recoil energy E_R , and also phonons generated by the energy from drifting the electrons and holes across the crystal by an applied voltage (a few volts in mag-

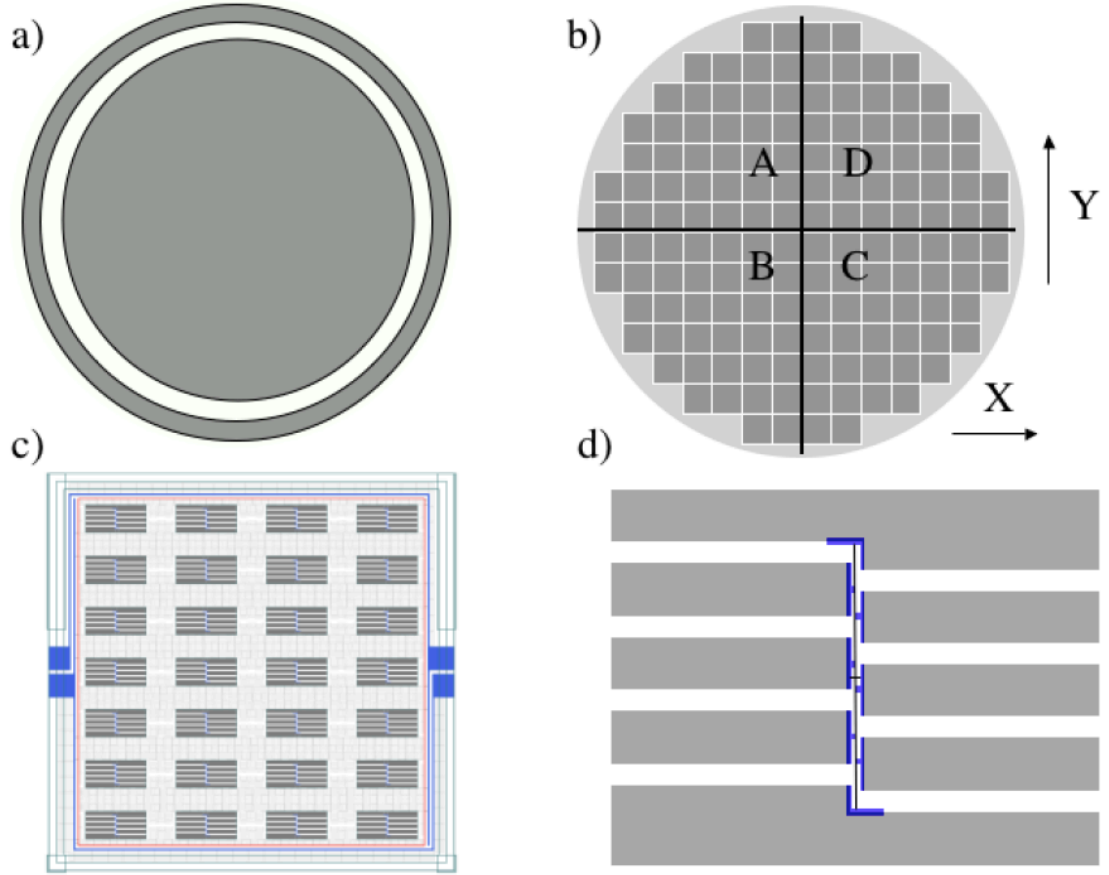


Figure 3.6: (a) Charge side of a CDMS ZIP detector. The inner and outer electrodes are shown. (b) Phonon side of the detector showing the four quadrants A, B, C and D. In each quadrant there are 37 dies and each of these dies contains 28 QETs. (c) shows a die and (d) shows a QET which consists of $1 \mu\text{m}$ wide tungsten strip connected to 8 aluminum fins.

nitude). When the electrons and holes are drifted, they generate phonons. These phonons are called Neganov-Trofimov-Luke phonons [134, 135] (Luke phonons hereafter). The energy contribution from the Luke phonons to the total phonon energy E_P is:

$$E_P = E_R + \sum_q \frac{d_q}{d_0}, \quad (3.3)$$

where d_0 corresponds to the thickness of the crystal and $V_b = Ed_0$ is the bias voltage.

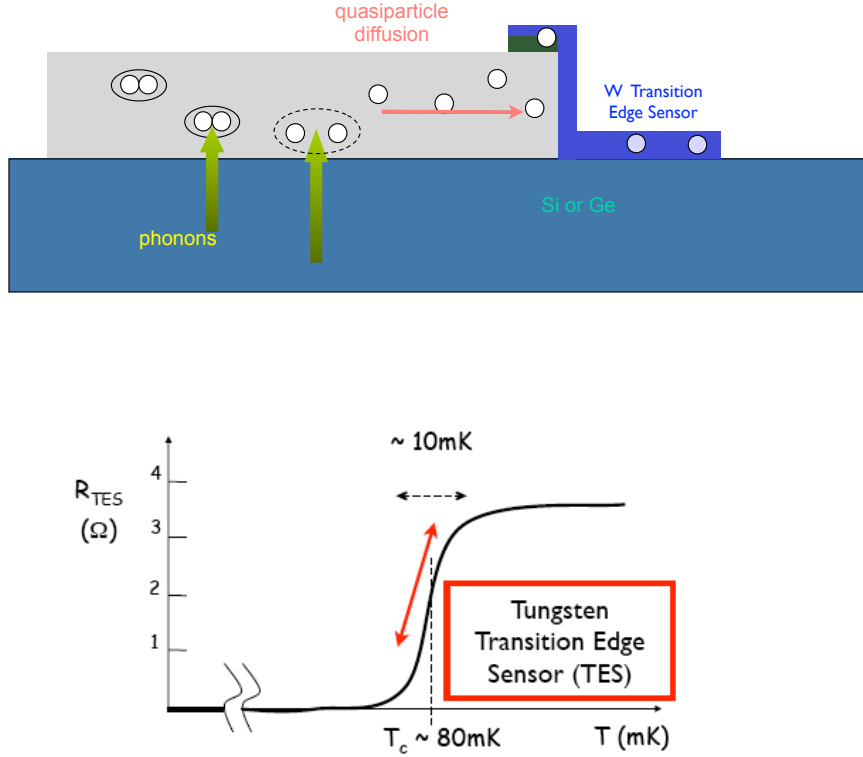


Figure 3.7: Drawing of the cross section of the ZIP detector showing the Ge/Si substrate, the aluminum fin and the tungsten. Quasiparticle diffusion occurs when ballistic phonons with a frequency higher than 82 GHz break the Cooper pairs in the Al and cause quasiparticle production for which a smaller energy gap in the tungsten region allows diffusion to the tungsten TES. The TES is operated at its transition temperature and tends to increase in resistance when energy is deposited and cooper pairs broken. Electrothermal feedback reduces the Joule heating that maintains the TES in its transition. This feedback forms the pulse that is produced by a particle interaction in the Ge/Si substrate.

Therefore, using the definition of ionization energy from equation 3.2 yields

$$E_P = E_R + eV_b N_Q = E_R + \frac{eV_b}{\epsilon} E_Q, \quad (3.4)$$

since we calibrate electron recoils with full charge collection to have $E_Q = E_R$, where ϵ has been measured to be 3 eV for Ge and 3.9 for Si by using several bias voltages and using known gamma-lines using calibrated sources. The fact that drift charges generate Luke phonons means that the recoil energy E_R of an event is inferred from

measuring both the phonon and ionization energy:

$$E_R = E_P - \frac{eV_b}{\epsilon} E_Q. \quad (3.5)$$

Figure 3.8 shows the phonon energy measured by a ZIP detector when it was exposed to a ^{133}Ba calibration source. You can see that the resolution is much worse than the ionization measurement (about a factor of 3), but as discussed in the sections that follow, what we aim in CDMS is for nuclear recoil vs electron recoil discrimination, and the phonon signal provides a powerful timing discrimination parameter.

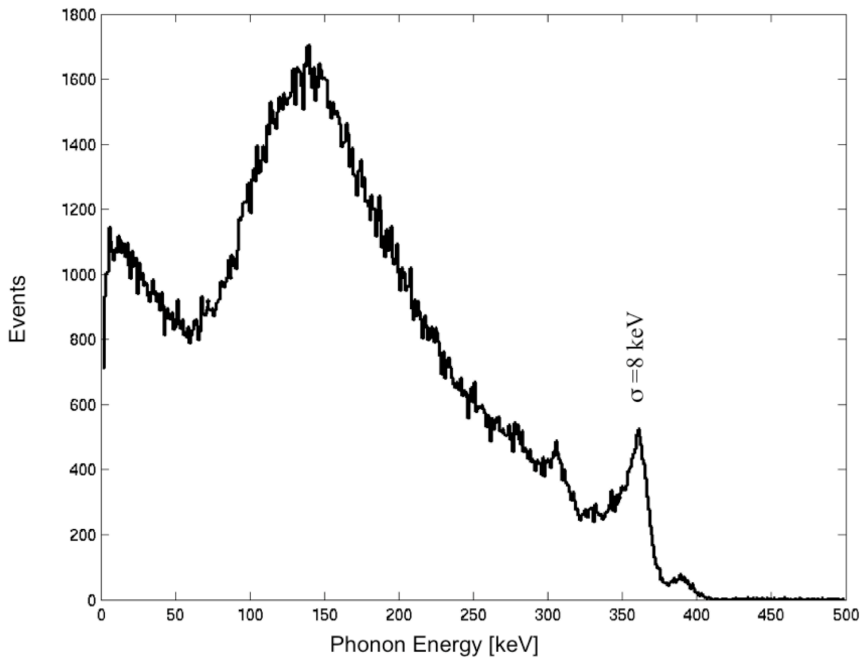


Figure 3.8: The phonon energy as measured by a CDMS ZIP detector when it was exposed to a ^{133}Ba gamma-ray source. The resolution for the 356 keV line is about 3 times worse than the ionization measurement resolution.

3.4 Background Rejection

Electron recoils that have reduced ionization can look like nuclear recoils as measured by the ZIP detector. There are two cases for which the measured charge can underestimate the total ionization [136]. In the first case, it is due to poor space-charge neutralization within the crystal. When the crystals are cooled at tens of mK, impurity sites can be left with a non-zero net charge, causing trapping sites. When the electron-holes generated after an interaction are drifted, the trapping sites will collect some of the charge and therefore cause an inefficiency in the charge collection by the inner and outer electrodes. Fortunately, by shining the crystal with an LED we can neutralize the traps with these source of photons by generating free charges. The LED energy spectrum is optimized to neutralize Ge, and therefore the Si crystals require more shining time (or “baking”).

The second case of charge loss happens when an interaction occurs close to the electrodes. The ionization charge collection is realized by drifting the electrons and holes created in the interaction to the positive and negative electrodes respectively using the external electric field. The electrons and holes can fail to reach their respective electrodes when the kinetic energy transferred to them by the incident particle produces a diffusion in the wrong direction with respect to drift direction imposed by the external electric field. This back diffusion of the charges causes some loss of the ionization charge collection. Depositing a thin film ($\sim 40 \mu\text{m}$) of amorphous silicon between each electrode and the detector surface helps to reduce number of reduced ionization events [133, 145]. Amorphous Si has a bandgap $E_g = 1.2 \text{ eV}$, significantly larger than the band gap of Ge (0.74 eV). Due to the difference in band gaps between the deposited amorphous Si layer and the bulk Ge, the amorphous Si can block the back diffusion of charges of both polarities. There would still be interactions within the $10 \mu\text{m}$ “dead layer” that have reduced ionization and are referred to as “surface

events”. In order to gain sensitivity to nuclear recoils induced by WIMPs, the ZIP detector provides timing parameters using the phonon pulse shape that allow further rejection of “dead-layer” events. Figure 3.9 shows the ionization yield for the gamma calibration source ^{133}Ba in which the green dots correspond to surface events. The surface events leak into the nuclear recoil band, around yield of ~ 0.3 and at low energy (where WIMPs are expected, too).

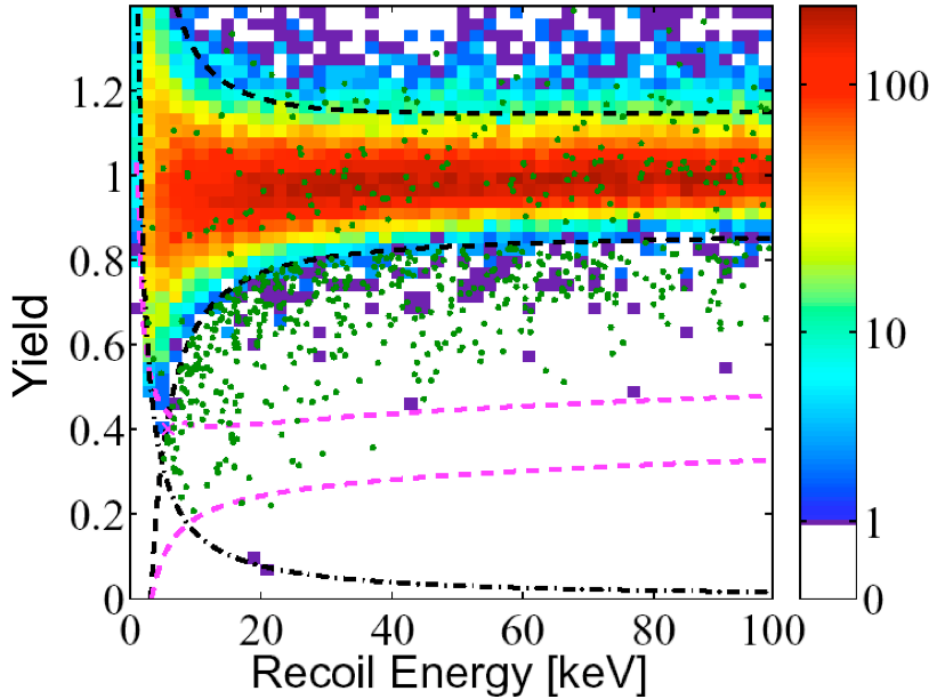


Figure 3.9: Ionization yield for a gamma calibration source ^{133}Ba . Most of the gammas are centered around a yield value of 1, while the green dots, which correspond to surface events, leak into the 2σ nuclear recoil band (dotted purple line) around a yield value of 0.3.

The physics underlying the pulse shape and timing discrimination pertains to the frequency-dependent propagation speeds of the phonons produced in an interaction and the subsequent evolution. When an interaction occurs in the crystal, it produces high-frequency phonons that propagate through the crystal. The phonon diffusion process is made by two processes: elastic scattering and anharmonic decay. Elastic scattering mixes phonon modes and anharmonic decay will increase the total number

of phonons while reducing the average phonon frequency. Eventually all initially created high-frequency phonons are converted into ballistic phonons that subsequently thermalize. After an interaction occurs in the crystal, the electron-hole pairs generated drift across the detector and yielding Luke phonons. The population of Luke phonons is higher for electron recoils than for nuclear recoils due to the difference in electron-hole production. Due to the fact that ballistic phonons move at the speed of sound, and the high-frequency phonons generated initially have a speed of approximately one third the speed of sound, there is an earlier and faster leading edge for electron recoils when compared to nuclear recoils. The two main timing parameters that are used in the analysis are: the primary rise time and the primary delay. The primary rise time is defined as the time from 10% to 40% in phonon amplitude for the largest pulse (out of the 4 phonon pulses per event). The primary delay consists in the time from 20% in charge amplitude to 20% in phonon amplitude for largest pulse. Using the yield only, CDMS achieves a rejection efficiency of $\sim 10^4$ to 1 for bulk electron recoils, and using the primary delay and risetime for surface event rejection gives us another ~ 100 to 1 allowing an overall rejection efficiency to electron recoils $> 10^6$. Figure 3.10 shows an example of the pulses in an event, and how the primary delay and risetime are defined.

Figure 3.11 shows the peak phonon delay versus ionization yield for a typical detector. The events in the plot correspond to the neutron source ^{252}Cf (blue circles) and the gamma source ^{133}Ba (red dots). The gamma events form the blob centered at a Yield value of 1 and Timing Parameter (a combination of primary delay and risetime) of $13 \mu\text{s}$. The surface events (black crosses) overlap in ionization yield with the neutron band (~ 0.2 to 0.4 in yield) but the Timing Parameter separates most of the neutron events (blue circles) from the surface events. The black box shows, in the Timing Parameter vs Yield plot, where the nuclear recoil acceptance window is defined.

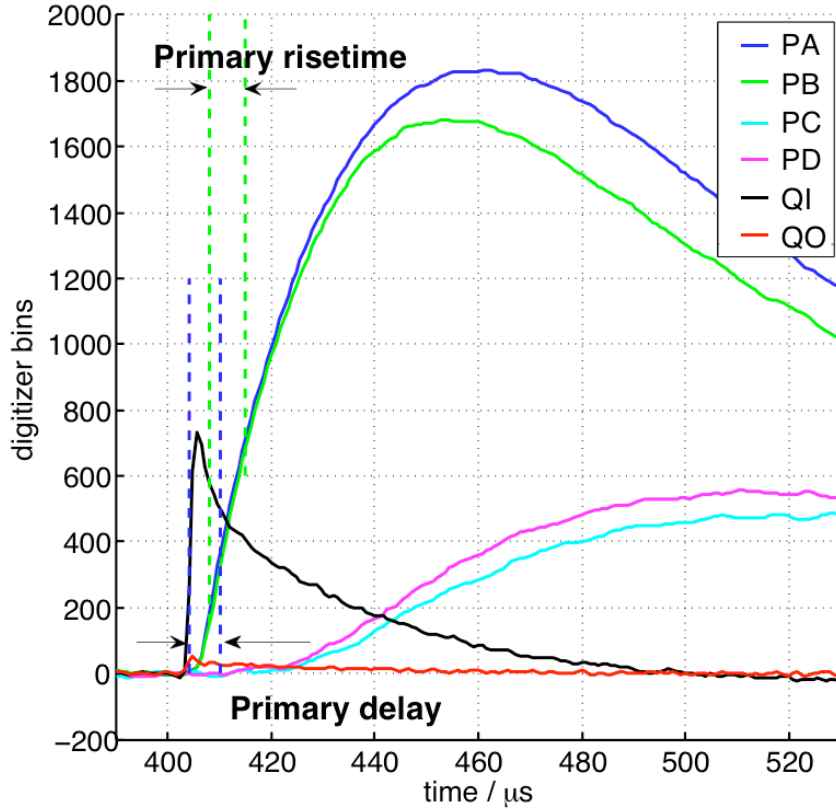


Figure 3.10: The CDMS ZIP detector pulses are shown for an event. The four phonon pulses (one for each quadrant) are shown, together with the two ionization pulses (the inner and outer electrodes). The biggest phonon pulse corresponds to the quadrant in which the event occurred. Also it is shown graphically how the primary delay and primary risetime are defined. Figure courtesy of J. Filippini.

3.5 Gamma and Neutron Calibrations

Gamma calibrations with a ^{133}Ba source are made 3 times a week spread evenly during the course of the runs and approximately once a month for neutron calibration with a ^{252}Cf source. The gamma-ray source is used to characterize the ZIP detector response to electron recoils and the neutron source to characterize the neutron recoil response such as determination of the efficiency and how the timing parameters will look for a WIMP candidate. The gamma-ray source has the following lines: 276 keV, 303 keV, 356 keV and 384 keV. Even though the source is positioned outside the copper cans

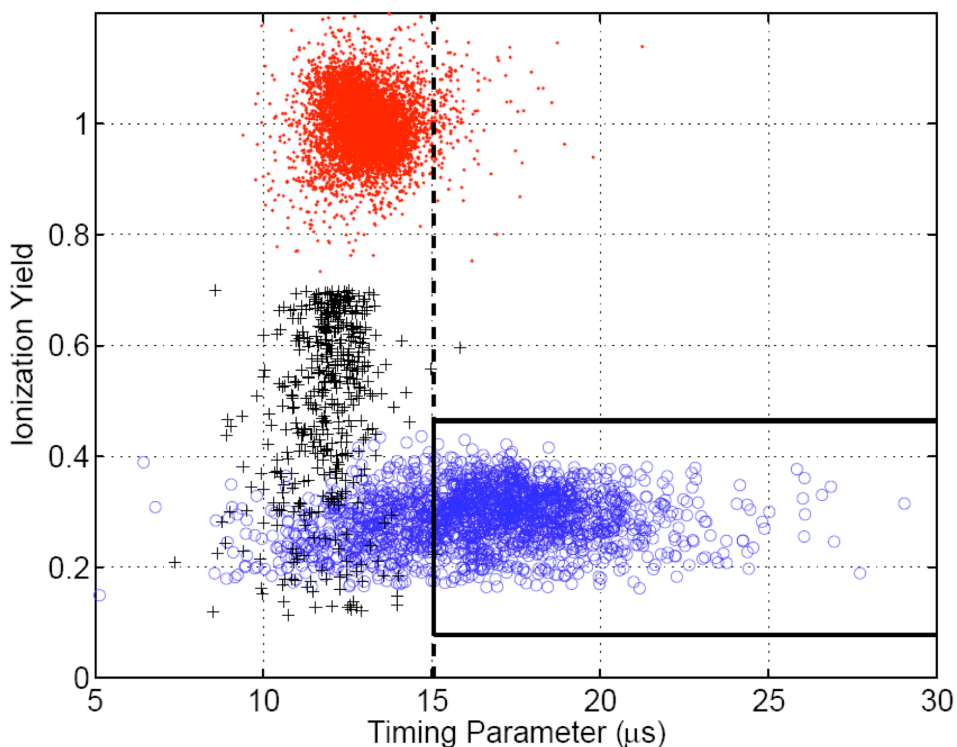


Figure 3.11: In this plot it is shown how the timing parameter can help discriminate between electron recoils (red dots from a ^{133}Ba calibration) from the neutron events (blue circles from a ^{252}Cf calibration). The black crosses are surface events. The black box contains only neutron events and indicates the acceptance window for WIMPs. The ionization yield and the timing parameter that utilizes the phonon rise time is what gives the ZIP detector the sensitivity for WIMP nuclear recoils.

that conform the different temperature stages of the refrigerator, they are energetic enough and the cans sufficiently thin (few cm in total) to be observed in the ZIP detectors. The ~ 10 keV line from Ge activation is also used as a calibration line. The ionization channels have a linear response at low and high energies. The phonon channels only have a roughly linear response up to ~ 200 keV, whereas above this energy there is significant saturation of the QETs and the ballistic phonon energy cannot be fully collected by the detector. Figure 3.12 shows good agreement between gamma calibration data from a Ge detector and Monte Carlo simulations made with GEANT4 toolkit [146].

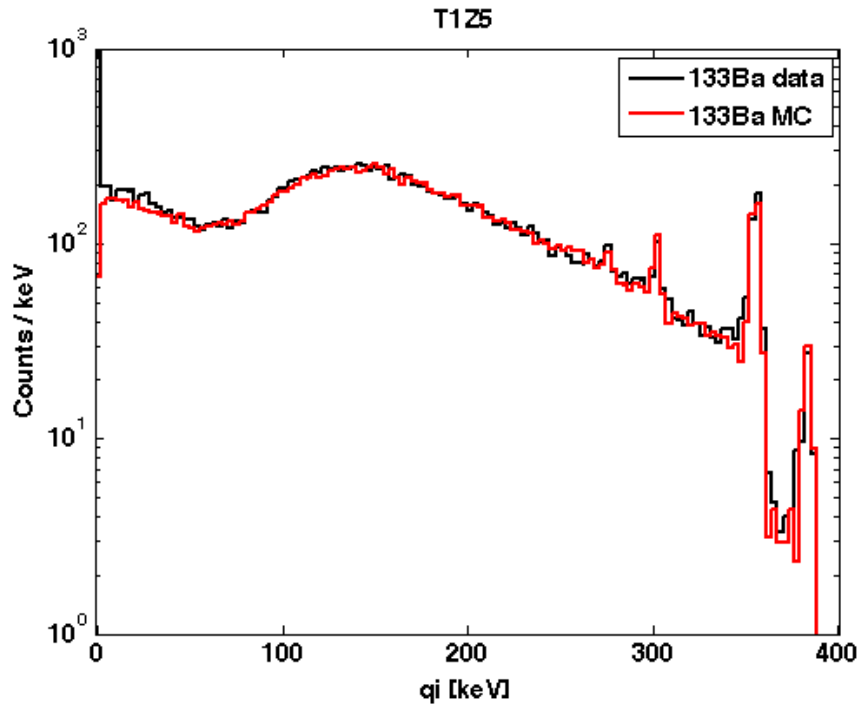


Figure 3.12: Gamma calibration data using a ^{133}Ba gamma-ray source (black) compared to a GEANT4 Monte Carlo simulation (red) for a Ge detector. There is good agreement between data and simulation [147].

For the Si detectors, the gamma lines from the ^{133}Ba source are not clearly visible since Compton scattering dominates at these energies. Therefore, the calibration for the Si detectors is made by matching the spectral shapes of the Monte Carlo simulation and the data. Furthermore, some of the Si detectors can be calibrated using the Ge detectors on top and/or bottom of them since a gamma from the source can be fully absorbed by a Ge detector after making an energy deposition on a Si detector so that, knowing the photon energy, the energy in the Si detector will be the difference between the known photon energy and the energy deposited in the adjacent Ge detector (that is already calibrated).

In order to characterize the nuclear recoil response of the detectors, we use a ^{252}Cf . The neutrons emitted from the ^{252}Cf have a peak energy of ~ 1 MeV that has the

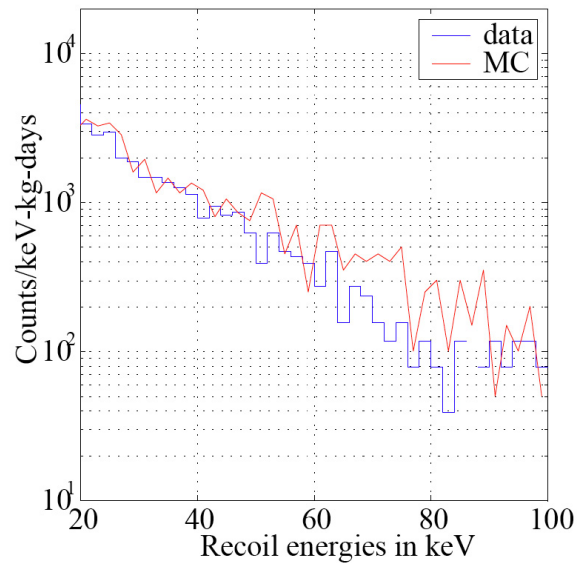


Figure 3.13: Comparison between neutron calibration data (^{252}Cf neutron source) and GEANT3 Monte Carlo simulations. The events correspond to single scatters in Ge detectors [149].

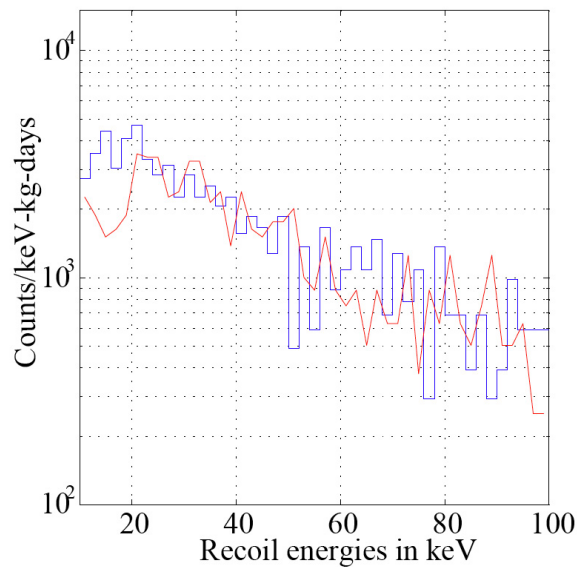


Figure 3.14: Comparison between neutron calibration data (^{252}Cf neutron source) and GEANT3 Monte Carlo simulations. The events correspond to single scatters in Si detectors [149].

following functional form, called the Watt spectrum

$$f(E) = k_1 \exp\left(-\frac{E}{a}\right) \text{Sinh}(k_2 E)^{1/2} \quad (3.6)$$

with $k_1 = 1.025$ MeV and $k_2 = 2.926$ MeV⁻¹ resulting in a distribution of Ge nuclear recoils with energies around ~ 10 keV, and therefore an excellent calibration source to define the WIMP acceptance signal region. Figures 3.13 and 3.14 show a comparison between neutron calibration data and simulations made with the GEANT3 toolkit [148], for a Ge detector. Good agreement is found between data and simulation [149], which implies that the calibration of the phonon channels using electron recoils remains valid for nuclear recoils and that the phonon measurement of the recoils and the induced Luke phonons is not recoil-type dependent.

3.6 Passive and Active Shielding

In order to achieve sensitivity to WIMP nuclear recoils, the CDMS experiment requires passive and active shielding against particles induced by radioactivity and from cosmic rays. Neutrons with an energy greater than 200 keV can generate a Ge nuclear recoil above the 10 keV energy threshold. Neutrons with an energy distribution extending to a few MeV are generated as products of the U/Th chain in the Soudan rock. Therefore CDMS utilizes passive neutron shield to attenuate the neutrons generated primarily from the radioactivity in the rock. The passive neutron shielding consists of high density hydrogenated material (polyethylene). The hydrogen in the polyethylene moderates neutrons (mainly through elastic scattering with hydrogen) with incident energies of a few MeV down to thermal energies (1/40 eV) and therefore renders them unable to produce a Ge nuclear recoil above the 10 keV threshold. If an incident neutron with an energy ϵ_i is made incident in a piece of hydrogenated material (polyethylene or water for example) the thickness (T) needed to moderate

the neutron to an energy ϵ_f is

$$T \simeq \sqrt{\frac{1}{N\sigma_i\xi} \log\left(\frac{\epsilon_i}{\epsilon_f}\right)} \quad (3.7)$$

where ξ is given by [150]

$$\xi = 1 + \frac{(A+1)^2}{2A} \log\left(\frac{A-1}{A+1}\right), \quad (3.8)$$

A is the atomic number, N is the number density of atoms, and σ_i is the n-p

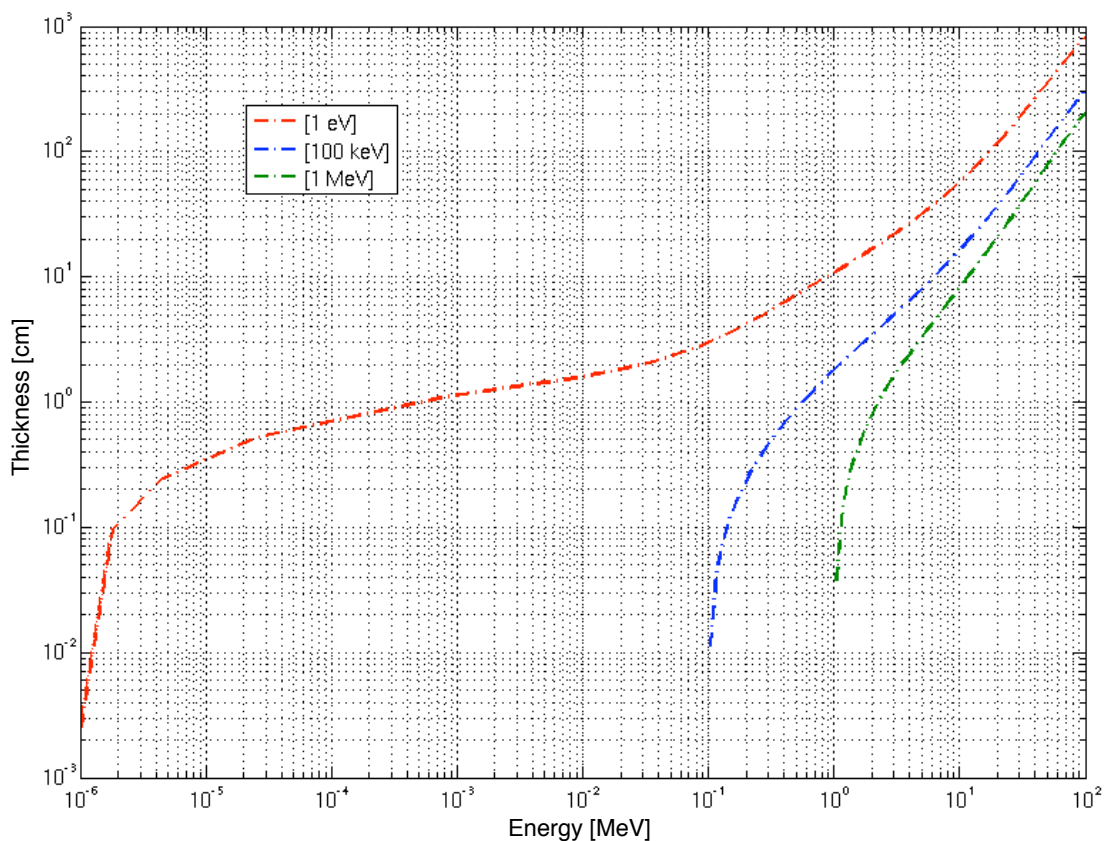


Figure 3.15: Thickness vs Incident Neutron Energy. The thickness is referred to a hydrogenated material such as water or polyethylene with a density of 1 g/cm^3 . The curves correspond to the final neutron energy achieved after traveling a certain thickness (y-axis) and beginning with an incident energy (x-axis).

elastic scattering cross section for the i -th energy bin ϵ_i . Figure 3.15 shows the thickness T of the hydrogenated material with a density of 1 g/cm^3 as a function

of incident neutron energy ϵ_i . The color curves correspond each to a final neutron energy ϵ_f after passing through a thickness T . As the incident neutron energy reaches 100 MeV, the curves slope increases such that the thickness needed to moderate a neutron with an incident energy of 100 MeV down to 100 keV is about 3 m. cosmic rays underground can produce high-energy neutrons for which the polyethylene shield cannot moderate efficiently. In Chapters 4 and 6 it will be discussed in detail the origin of these cosmogenic high-energy neutrons, their rates and how they contribute to the irreducible neutron background as well as prospects for their detection at the Soudan Underground Laboratory.

After the detectors are surrounded by the passive shielding, the shielding itself becomes a target to Cosmic rays underground. The primary component of underground cosmic rays are muons. At 2090 meters of water equivalent (m.w.e.), the rate of muons at the Soudan underground laboratory is reduced by a factor of 5×10^4 compared to the surface muon flux. The muon rate in the CDMS veto shield is about 1 muon per minute. The CDMS passive shielding is surrounded by 40 Bicron BC-406 scintillator panels (colored green in Figure 3.16) that have a thickness of 5 cm and are connected to a 2 inch Hamamatsu R329-02 photomultiplier tubes. The top panels extend well beyond the side panels (as shown in Figure 3.16) in order to avoid leaving out small gaps between the top and side panels.

The 40 scintillator panels comprise the veto system. Each panel can distinguish between muons and ambient photons since a minimum ionizing particle will deposit 2 MeV/cm and muons will travel at least 5 cm (the thickness of the plastic scintillator) most of the time, and therefore deposit 10 MeV or more. Ambient photons have a distribution that extends only to the 2.6 MeV ^{208}Th peak hence a good separation between muons and ambient gamma background is achieved.

In the following chapter I will describe the sources of the main backgrounds that CDMS faces at the Soudan site, starting from the electromagnetic backgrounds (pho-

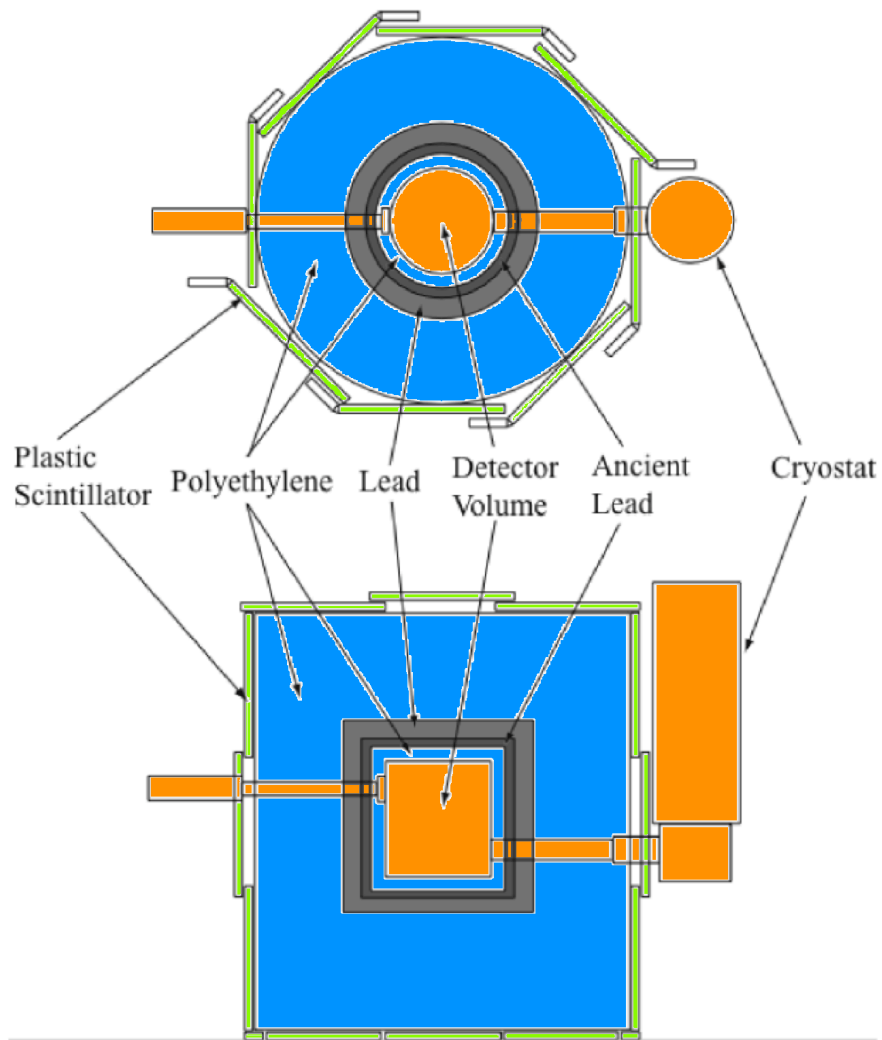


Figure 3.16: The CDMS shield top and side views. The blue in the figure corresponds to the polyethylene shield, the gray and dark gray to the Pb layer and the green to the plastic scintillator panels. The outer polyethylene has a thickness of 40 cm, the Pb layer is 27 cm thick with the inner 4.5 cm being ancient Pb with reduced activity from ^{210}Pb ($T_{1/2} = 22$ years). The inner polyethylene layer has a thickness of 10 cm.

tons and betas) and continuing with neutron backgrounds with an emphasis on those originated by cosmic rays underground.

Chapter 4

CDMS backgrounds

In the previous Chapter I described in general terms the CDMS strategy to achieve sensitivity to WIMP-nuclear recoils. The CDMS experiment is able to make a competitive WIMP-search by implementing low-threshold nuclear recoil detectors in a low background environment. A low background environment is achieved by going half-a-mile underground and utilizing passive and active shielding together with a nitrogen gas shield in order to reduce the ambient photons, ambient neutrons and neutrons induced by cosmic rays. In this Section I will describe the background levels achieved by the CDMS experiment, the methods implemented to make reliable estimations of the electromagnetic and neutron backgrounds, and the challenges that lie ahead if the experiment is to be run at the Soudan Underground Laboratory or at SNOLAB.

This chapter is divided in two main parts. In the first part I describe electromagnetic backgrounds: those interactions that occur in the detector due to a charged particle, for example a beta or alpha particle and also by ambient photons. I will describe the evidence regarding the source of the electromagnetic backgrounds, how we assess which isotopes are the source of this backgrounds, and what levels of contamination we infer from the data in order to understand future material cleanliness challenges.

The second part of the chapter consists of a description of the neutron backgrounds, what are the main sources, how can we estimate their induced nuclear recoil rate, and what are the estimates for the combined runs 123 and 124. Furthermore, I will describe the challenges on estimating nuclear recoils induced by neutrons produced by cosmic rays, in particular those cosmic rays that miss the CDMS veto system which is the main motivation for the high-energy neutron detector that I conceived together with Prof. Dan Akerib, and that is fully described on Chapter 6.

4.1 Electromagnetic Backgrounds

As mentioned above, electromagnetic backgrounds refers to those events induced by a charged particle or a photon. These events lie in the gamma band with ionization yield (discussed in Chapter 3) normalized to unity. The efficiency for rejecting electromagnetic interactions in the bulk of the ZIP detectors is above 10^4 just based on yield. Taking into account the risetime information, the rejection efficiency can reach above 10^6 . In order to maximize the sensitivity to WIMP nuclear recoils, CDMS implements a low background environment that allows the experiment to be background free. In this Section I describe the sources of the events that lie in the gamma-band, where they come from, what are the expected rates for the combined Run 123 and 124 data runs, and what are the prospects for the future with respect to this kind of background.

4.1.1 Ambient photons

Bulk electromagnetic backgrounds (those that occur deeper than about $10 \mu\text{m}$ from the detector surfaces) consist mainly of photons. We identify them as those events in the gamma-band centered at yield ~ 1 (see Figure 3.9). For the 5 tower runs 123 and 124, the rate of bulk photons in the 15(8) Ge(Si) detectors was $3.6(9.2) / \text{keV}/\text{kg}/\text{day}$

in the 10-40 keV energy range. Assuming a 75% efficiency of the Q-inner cut in the 10-40 keV energy range, the integrated bulk electron recoil event singles rate were 35 ± 11 (64 ± 26) /kg/day for Ge(Si).

By looking at the energy spectrum in the Ge detectors (which have better resolution and stopping power) we can infer the parent radionuclide by looking at the spectral lines of the nuclide in question. Primordial radionuclides are those with a long enough mean decay lifetime ($\sim 10^9$ y or more) such that, after their creation inside a star they have not decayed away and are present in the materials used in the experiment. This is not particular to CDMS, but to all low background experiments. Figure 4.1 shows the Q-inner energy spectrum for Run 123 Tower 3 (84.8 kg-d) as compared to a Geant 4 simulation of the ^{238}U and ^{232}Th in the copper cans and inner polyethylene shield, ^{40}K and ^{60}Co . The red histogram corresponds to the sum from all the simulated sources of events and the black histogram is the data. Clear agreement is observed in predicting the 2.61 MeV ^{208}Th , 1.46 MeV ^{40}K and 1.76 MeV from the $^{238}\text{U} + ^{232}\text{Th}$ induced gamma lines. Contamination in the cryostat of <0.21 ppb U and 0.42 ± 0.13 ppb Th are in agreement with the conclusions from the simulations: 0.1 ppb U and 0.5 ppb Th [151].

The contamination of the hardware materials due to primordial radionuclides and their daughters could have occurred before the raw material was extracted from the Earth, or could have been mixed with other material that is contaminated with radionuclides while the material was being manufactured.

Contamination from ambient radon, a noble gas produced in the decay chain of ^{238}U and ^{232}Th , in the volume between the cryostat and the lead gamma-ray shield is mitigated in CDMS by using a nitrogen purge. The average radon level in CDMS, inside the room where the experiment is located, is 500 Bq/m^3 . Purging the air within the cryostat with nitrogen at a rate of 8 liters/minute makes the background contribution from radon subdominant [152].

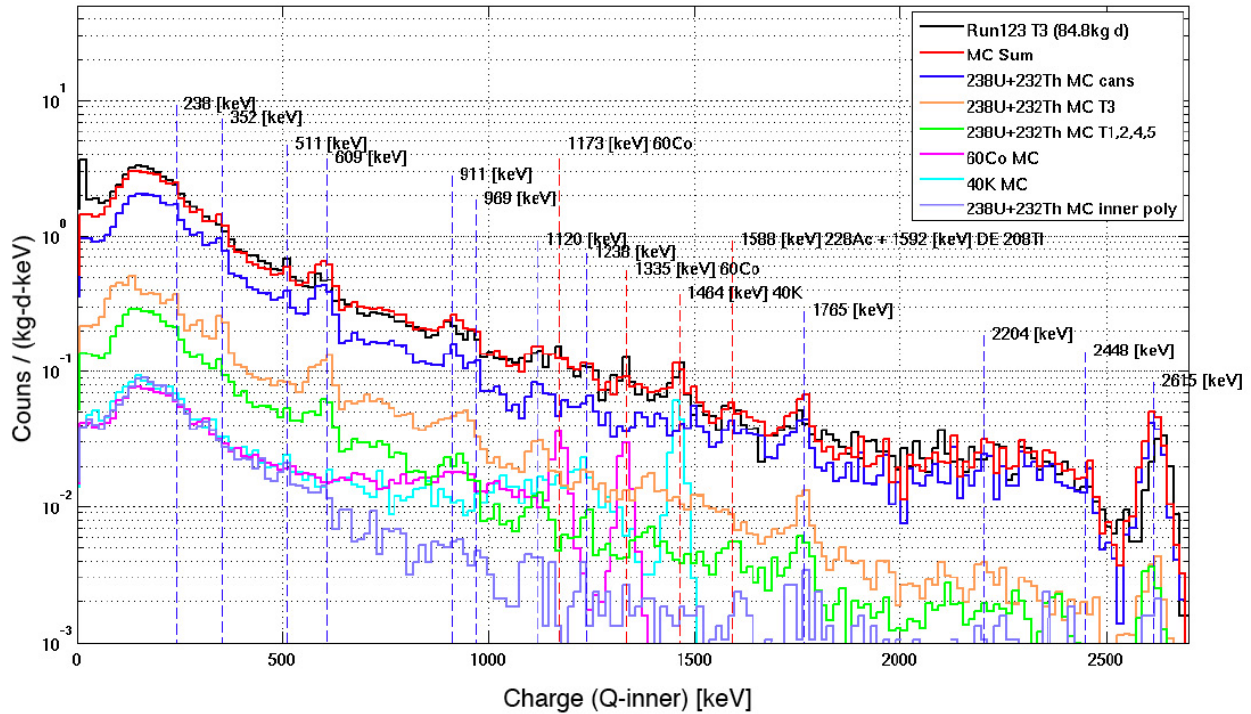


Figure 4.1: Comparison of the Q-inner energy spectra between Monte Carlo simulations of the main radionuclide contaminants in CDMS (^{238}U , ^{232}Th , ^{60}Co and ^{40}K) with data from Tower 3 Ge detectors [151].

4.1.2 Surface backgrounds

Surface backgrounds are those events such as electrons and photons that interact within the $35\ \mu\text{m}$ “dead-layer” of the ZIP detector in which charge collection is reduced relative to events in the bulk (previously discussed in Chapter 3). Low energy electrons that reach the ZIP detector will interact there and have reduced ionization signal leading to an event below the 5σ gamma band.

The main electromagnetic background observed in runs 123 and 124 consists of electrons (betas) from radioactive contamination on the detector surfaces. A correlation analysis between alpha-decay and surface event rates demonstrates that the major source of the surface events is ^{210}Pb (a daughter-product of ^{222}Rn) [202]. By using the ^{133}Ba calibration data, we estimate the leakage of surface events into the

signal region.

Surface events also come from activation of ^{64}Cu during neutron calibrations. An excess of events was noticed during runs 123 and 124 a day after the neutron calibration occurred. A close analysis of the energy spectra in the Ge ZIP detectors for those data sets just after the neutron calibration was taken shows that there is a 511 keV line that points to neutron activation of ^{64}Cu (see Figure 4.2) [154]. A cut was imposed to remove events within two days of the each neutron calibration.

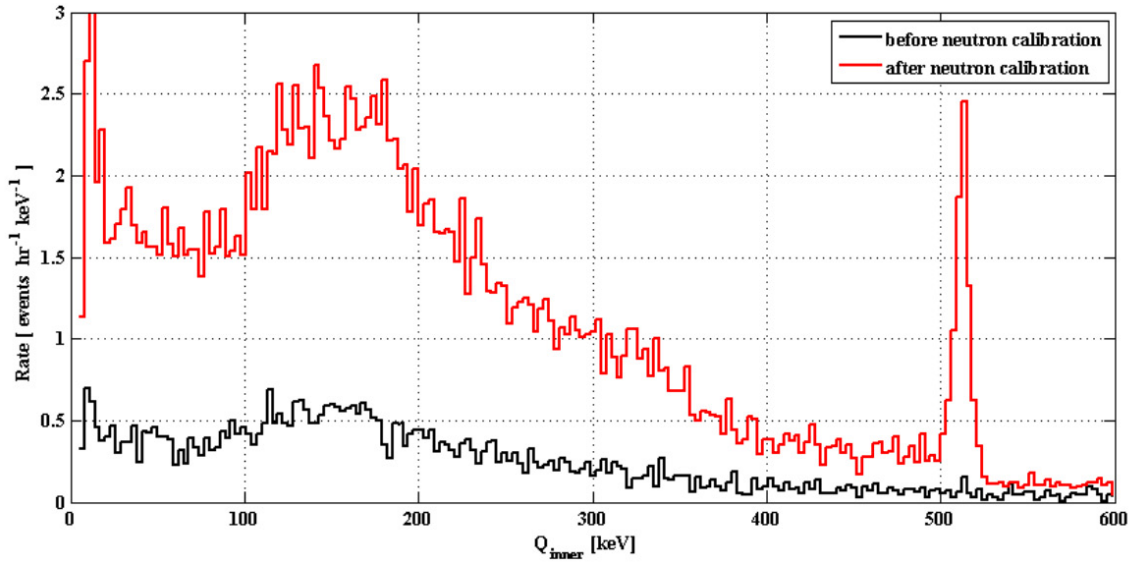


Figure 4.2: Energy spectra summed over the Ge ZIP detectors for events before the neutron calibration (black histogram) and after the two days following the neutron calibration was taken (red histogram). The 511 keV line shows evidence of neutron activation of ^{64}Cu [154].

4.2 Neutron Backgrounds

The CDMS experiment aims at detecting nuclear recoils from WIMP dark matter concentrated in the halo of the Milky Way. Furthermore, we use a radioactive neutron source ^{252}Cf to define our acceptance window. Therefore, it is clear that any neutron with enough energy to create a nuclear recoil above 10 keV can potentially mimic

the expected WIMP signal. In order to have sensitivity to WIMP-nuclear recoils, the experiment requires the earth's crust as a shield against cosmic rays, and must be performed at the Soudan Underground Laboratory. Furthermore, the experiment needs special gamma-ray and neutron shielding. In this Section I will describe the main sources of neutrons that can lead to a nuclear recoil in the ZIP detectors.

Neutrons with an energy of a few MeV can cause a nuclear recoil in the ZIP detectors above the 10 keV threshold. These low energy neutrons can be produced in nuclear reactions such as (α, n) where the α particles originate from the U/Th decay chain. Also, spontaneous fission occurring in the rock wall and in the shielding materials such as the Pb and inner polyethylene are sources of MeV neutrons. Furthermore, the remaining component of the cosmic rays, muons and their secondaries originated by interactions in the rock and in the shielding materials can generate neutrons capable of producing a nuclear recoil. In the following sections I will describe in detail how we have estimated the neutron backgrounds expected in the combined runs 123 and 124 beginning with the estimation of neutrons from radioactivity inside and outside the shield. Following that, I will present our evidence for the dominant neutron background for CDMS at the Soudan Underground Laboratory, the cosmogenic neutrons.

4.2.1 Neutrons from Radioactivity

In this section I will describe how the neutron background originated by spontaneous fission and (α, n) reactions in the shield materials has been estimated for the CDMS-II experiment.

By using SOURCES-4A [156], a program that calculates neutron production rates and spectra from (α, n) and spontaneous fission, in combination with Geant 4, we can predict the number of nuclear recoils in the 5 Tower geometry. The production of the neutron flux caused by (α, n) and spontaneous fission (knowing the U/Th

U/Th Concentration (ppb)			
Material	U	Th	U + Th
Cu Cans (Icebox)	0.08	0.3	0.38
Cu in Towers	0.2	1.0	1.2
Inner Polyethylene	0.12	0.12	0.24
Pb shield			<0.05

Table 4.1: The U/Th contamination levels in parts per billion (ppb g/g) of the main cold hardware components, icebox, inner polyethylene and gamma-ray shield (Pb) of the CDMS-II experiment.

contamination) is performed using SOURCES 4A, and this flux is then propagated using a Geant 4 simulation of the CDMS-II 5 Tower geometry. The U/Th contamination assumed for each component is shown in Table 4.2.1. The rate of neutrons emitted from 1 kg of natural uranium by spontaneous fission is estimated to be 16 neutrons/kg/s [157]. The neutrons from radioactivity originated from the Soudan greenstone rock are efficiently moderated with the 40 cm thick outer polyethylene layer (see Figure 3.16) and are not a main concern.

The spectrum of the neutrons produced by the (α, n) process using SOURCES is shown in Figures 4.3 and Figure 4.4 for the copper and inner polyethylene components respectively [158]. The differences in shapes of the spectrum shows the different cross-section thresholds that trigger the production of a neutron, which in turn depends on the Coulomb barrier of carbon and copper isotopes. The reason for the reduced spectrum for copper in Figure 4.3 compared to polyethylene in Figure 4.4 is because of the stronger Coulomb barrier for copper compared to the lower- Z of the carbon in the polyethylene. The energy of the α -particle is reduced as the Coulomb barrier is stronger.

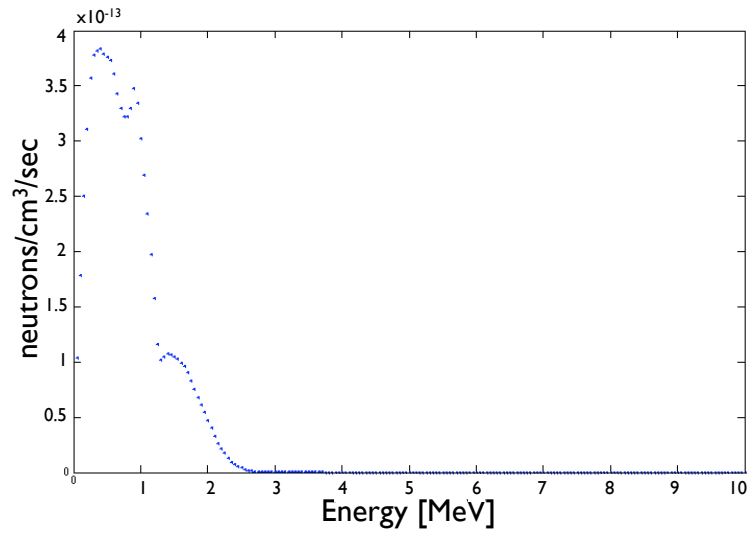


Figure 4.3: Energy spectrum of the neutron flux produced by (α, n) reactions in the Copper (cold hardware and icebox cans) of the CDMS-II experiment [158].

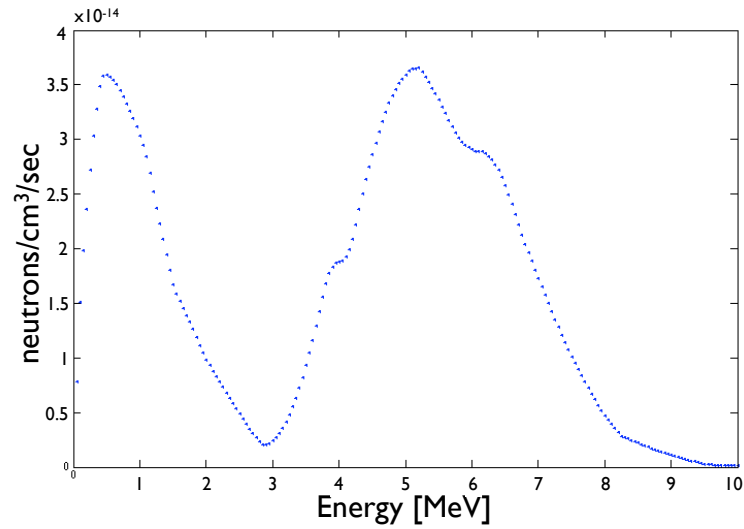


Figure 4.4: Energy spectrum of the neutron flux produced by (α, n) reactions in the inner polyethylene layer of the CDMS-II shield [158]

The number of singles from Cu in the icebox and towers and from the inner polyethylene, for the combined runs 123 and 124 estimated using the flux of neutrons produced in SOURCES and propagating it using Geant 4, results in 0.009 single scatter events. The Pb shield has been considered as a source of neutrons from radioactivity, specially from spontaneous fission processes given its high-Z, which makes the (α , n) processes subdominant. Samples of lead used in the CDMS-II shield which were counted at the Oroville facility show no uranium at the 50 ppt (g/g) level. The contamination is based on gamma-ray measurements of the daughter products of U/Th in the Pb. This limit is consistent with measurements by G. Heusser and coworkers, who have conducted measurements of uranium and thorium levels in lead, and have found an upper limit of 20 ppt [159]. Furthermore, mass spectroscopy measurements of U in Pb from the same source as the Pb used in the CDMS-II shield suggests that the 50 ppt upper limit inferred from the Orville measurement is at least an order of magnitude lower [160, 161]. The estimated background singles from the spontaneous fission processes generated by 50 ppt U/Th contamination in Pb is <0.1 for the combined runs 123 and 124 5 tower run. Therefore, the total rate of singles from radioactive contamination in the shield materials is estimated to be < 0.13 for the combined runs 123 and 124.

4.2.2 Modeling the Cosmogenic Backgrounds

As mentioned in the previous sections, any neutron with an energy greater than 200 keV inside the inner polyethylene layer of the shield could produce a signal in the ZIP detectors that would mimic the expected WIMP signal. I have discussed neutrons produced by radioactivity, which I now distinguish from neutrons produced by cosmic rays underground and their secondaries (cosmogenic backgrounds).

Cosmic rays are energetic particles dominated by ionized nuclei comprised of 90% protons, 9% alpha particles and the remainder are heavier nuclei. They have energies

comparable or greater to their masses up to $\sim 10^{20}$ eV [163]. These cosmic rays interact with the atmosphere producing hadronic showers that are well developed when they reach sea level when 75% of the particles are muons and the rest are pions, protons, neutrons, electrons and gamma-rays. As we look for cosmic rays underground, most of them are shielded by the earth overburden, and only muons survive, with their mean muon energy increasing with depth. Figure 4.5 shows the muon intensity as a function of overburden in units of water equivalent. The passive shielding that is used for radioactivity induced neutrons and the gamma-ray shield become a target for the remaining flux of muons hitting the CDMS-II shield (~ 1 muon/min) and the produced neutrons become a background to the WIMP-search experiment. Furthermore, muons interactions in the rock can produce hadronic showers that in turn produce high-energy neutrons (>60 MeV) that can produce spallation reactions leading to low energy background neutrons.

In order to estimate the rate of events expected from cosmogenic neutrons that miss the CDMS veto system, we use Monte Carlo codes such as FLUKA [164, 165], MCNPX and Geant4 [155]. I have constructed a simulation based on FLUKA and MCNPX that models the muons and their secondaries at the Soudan Underground Laboratory and propagates them with a geometry of the shielding, cryostat and ZIP detectors that will be described in the following sections.

The FLUKA code can describe hadronic and electromagnetic processes up to 20 TeV. It uses different event generators for the various aspects of the particle production depending on the energy. The high-energy hadronic processes are described using the Dual Parton Model that is followed by a pre-equilibrium-cascade model. Furthermore, it utilizes models for nuclear evaporation, break-up of excited fragments and gamma-deexcitation that treats the disintegration of excited nuclei.

Cosmogenic neutrons underground are generated due to the following processes:

- Muon spallation, which consists of a muon interacting with a nucleus via a

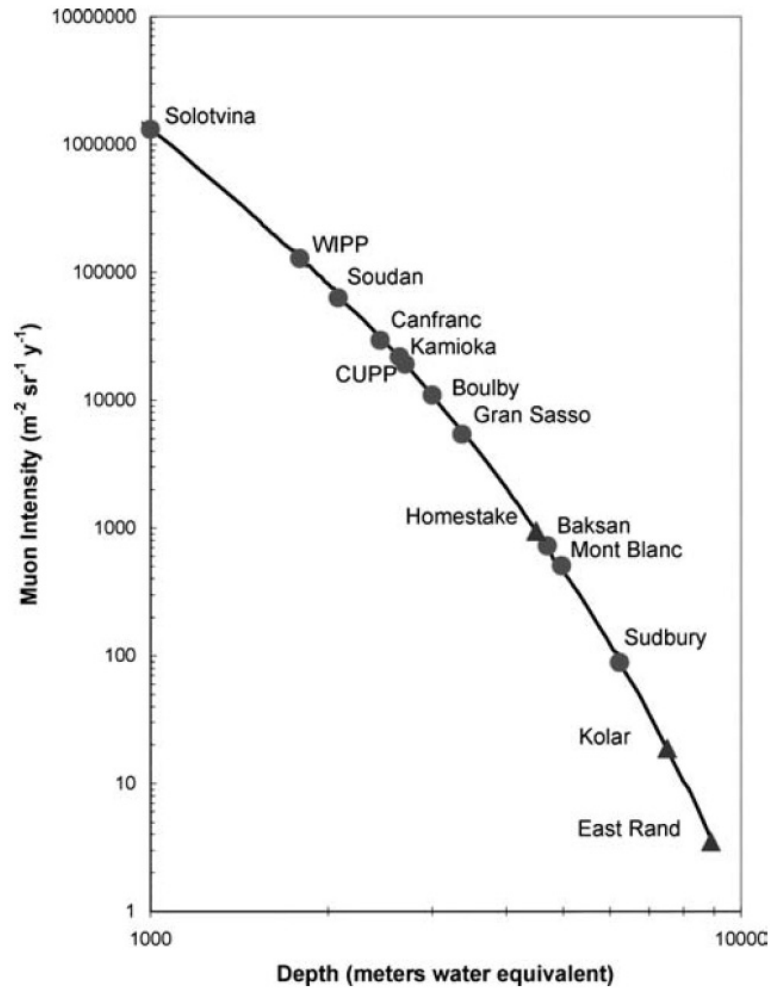


Figure 4.5: Vertical muon intensity as a function of underground depth in units of meters of water equivalent (mwe) [162].

virtual photon and causing nuclear disintegration,

- Elastic scattering of muons with neutrons bound in nuclei,
- Photo-nuclear reactions produced by electromagnetic showers, and
- Secondary neutron production following any of the processes above, such as those generated by electromagnetic and hadronic showers.

Following Wang and coworkers and in order to assess the implementation of the

code, I have used FLUKA to model the neutron production from cosmogenic muons in a cubic detector filled with liquid scintillator ($C_{10}H_{22}$). A monoenergetic beam of muons heading at the center of the scintillator is thrown, and the neutrons produced from all processes are counted. Since the number of neutrons produced is dependent on the size of the scintillator cube, the neutron production is assessed as a function of volume and from these data we can extract the neutron yield per g/cm^2 . The energies of the incident muon beams were chosen to be the mean muon energy at different depths underground, from 20 m.w.e. or mean muon energy of 13 GeV to 5 km.w.e. or muon energy of 346 GeV. The muons at the Soudan Underground Laboratory have a mean muon energy of 210 GeV. Figure 4.6 shows the neutron yield simulated with FLUKA as a function of mean muon energy (or depth). The obtained neutron yield per muon can be fit by the following function:

$$N_n = 3.43 \times \langle E_\mu \rangle^{0.79} \times 10^{-6} \text{neutron}/(\mu\text{gcm}^{-2}). \quad (4.1)$$

The total neutron yield is dominated by low energy neutrons produced in electromagnetic and hadronic interactions. Low energy neutrons are efficiently moderated by the polyethylene layers of the CDMS-II shield. The processes that give rise to these low-energy neutrons are different from those producing high-energy neutrons that lead to unvetoes nuclear recoils. As I will discuss further in Section 4.2.6 and Chapter 6 the available underground neutron data (that we are aware of) provides a systematic error of a factor of ~ 3 on an estimate of the CDMS-II unvetoes nuclear recoil rate based on FLUKA. Nevertheless, as I will describe in the remaining sections, the agreement between my FLUKA implementation and other FLUKA simulations together with comparisons to experimental data gives a sufficient level of confidence so that, for the CDMS-II combined runs 123 and 124, we expect well under one unvetoes event.

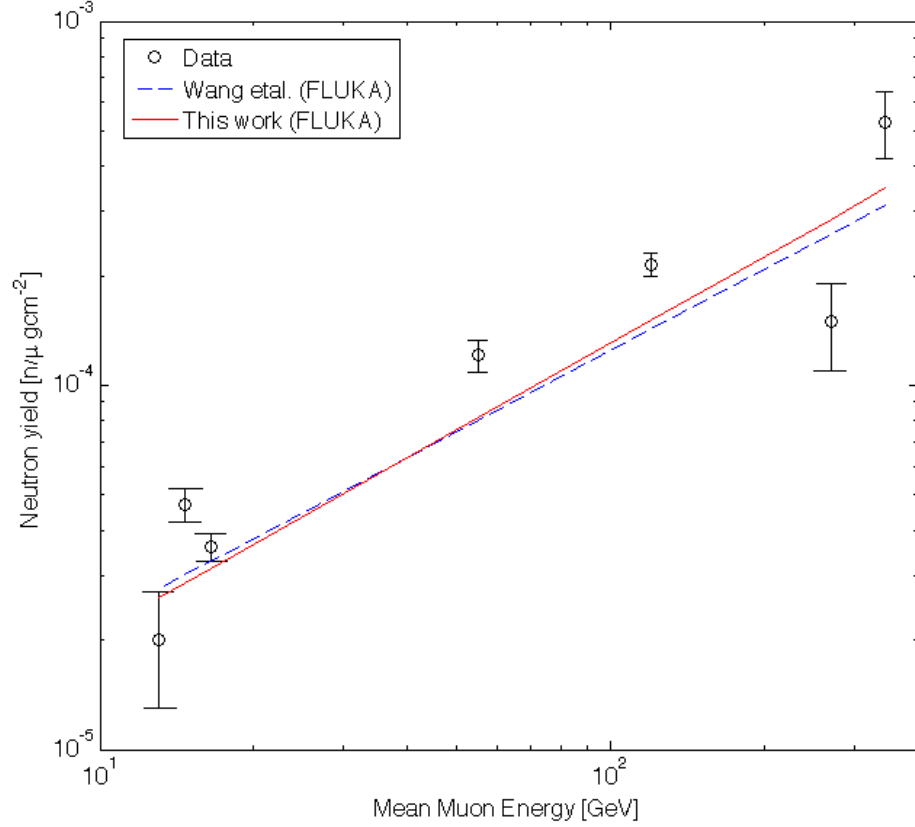


Figure 4.6: Neutron yield as a function of muon energy. Data at different sites is shown in black circles. The fit obtained with FLUKA in this work is the solid (red) line, and the fit obtained with FLUKA by Wang and coworkers [216] is the dashed line (blue). For the references on the data, see Wang et al. [216].

4.2.3 Cosmic Rays Underground: the muon generator

Muons are the only component product of the primary cosmic ray interactions in the atmosphere that survives underground beyond the ~ 10 mwe scale. The muon flux as a function of depth has been measured by Frejus [167], MACRO [168], and LVD [169] experiments as shown in Figure 4.7. The muon flux at the Soudan Underground Laboratory has been measured to be $1.86 \pm 0.05_{-0.08}^{+0.00} \times 10^{-3}/\text{m}^2/\text{s}/\text{sr}$ [174].

In order to model the underground muon flux and their particle production, a muon generator made by S. Yellin [175] was coupled into the FLUKA simulation and

used as the input muon flux that models muons at the Soudan underground site. The muon flux is made incident to a cubic rock shell with a size of $28 \times 24 \times 24 \text{ m}^3$ containing the CDMS-II active and passive shielding and Ge and Si detectors in a rectangular cavity with a size of $8 \times 4 \times 4 \text{ m}^3$.

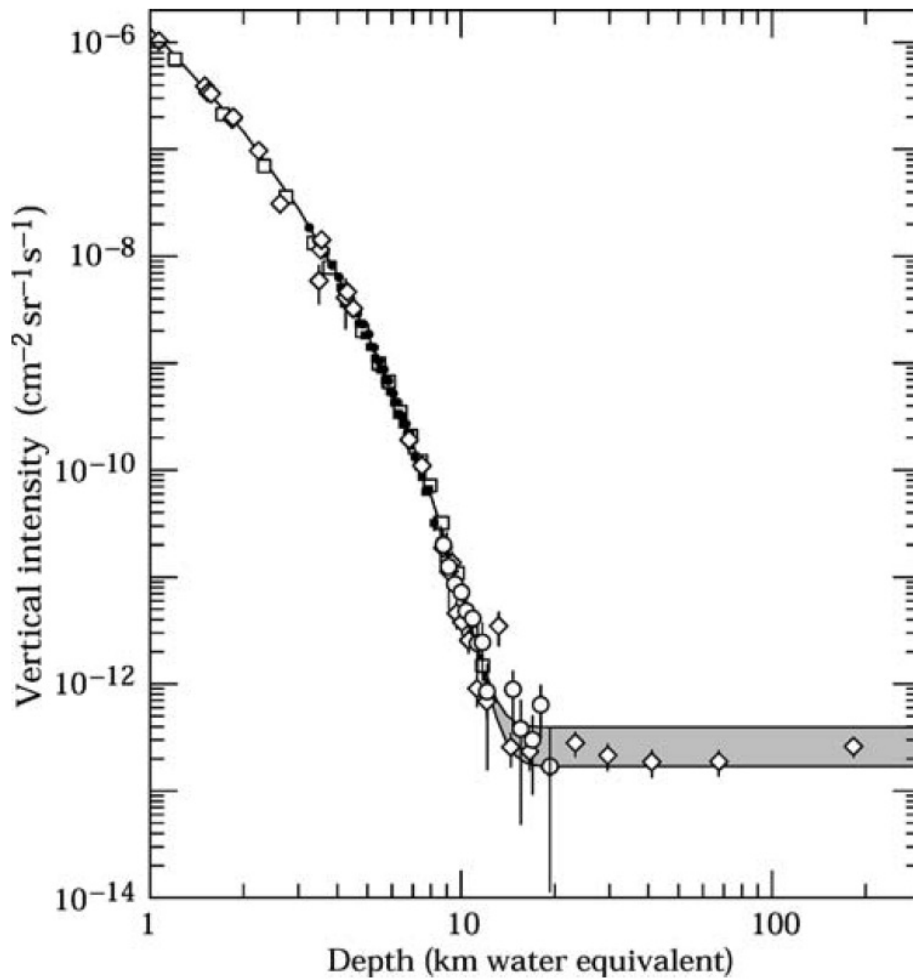


Figure 4.7: Vertical muon intensity as a function of depth. The data corresponds to Crouch (open diamonds) [170], Baksan (open squares) [171], LVD (open circles) [169] and Frejus (filled circles) [167]. Figure from [163]. The shaded region corresponds to muons produced by neutrinos (upper line) and by vertically upward muons (lower line). Figure from [172]

The muon generator takes into account the angular distribution of muons $I(\theta, \phi)$,

which can be approximated by a power law of the cosine function [176, 177] and assuming uniformity in ϕ (the azimuthal angle) it is expressed as

$$I(\theta, \phi) = I_\nu \cdot \cos^n \theta \quad (4.2)$$

where θ is the polar angle and I_ν is the vertical flux at $\cos\theta = 1$. As the depth of the mine increases, n increases too in order to generate a more vertical flux. Empirically, Miyake [177] found

$$n = 1.53 + 8.0 \cdot 10^{-4} \cdot h + \epsilon \quad (4.3)$$

where h is the depth in meters of water equivalent and ϵ is a small correction used at shallow depths due to muon decay and ionization losses that is not significant for the Soudan site. The vertical muon flux is obtained by measurements performed with scintillator panels from the CDMS-II veto system [174] and are included in the muon generator. The intensity of the muons generated approximately follows a $\cos^{3.28}\theta$ distribution. One million muons generated corresponds to about four days of CDMS-II livetime [175]. Figure 4.8 shows the polar angle and energy distribution of muons entering the cavity of the cubic rock shell. A mean muon energy of 216 GeV for vertical muons is obtained.

A muon generator that takes into account the differences between flat overburden and the actual surface shape at the Soudan site has been constructed [178] in order to improve the input muon flux for the cosmogenic neutron simulation. This muon generator is based on a slant depth distribution (distance traveled by muon from surface) at Soudan using muons measured at the Soudan2 detector [179]. Also, it utilizes MUSIC [180], a muon Monte Carlo that takes into account fluctuations in the energy loss of muons at large depths underground. Figures 4.9 and 4.10 show the comparison between the muon generator used in the FLUKA simulation, and the muon generator based on Soudan2 measurements and MUSIC. The YELLIN muon generator is more conservative in the sense that it generates harder muons and

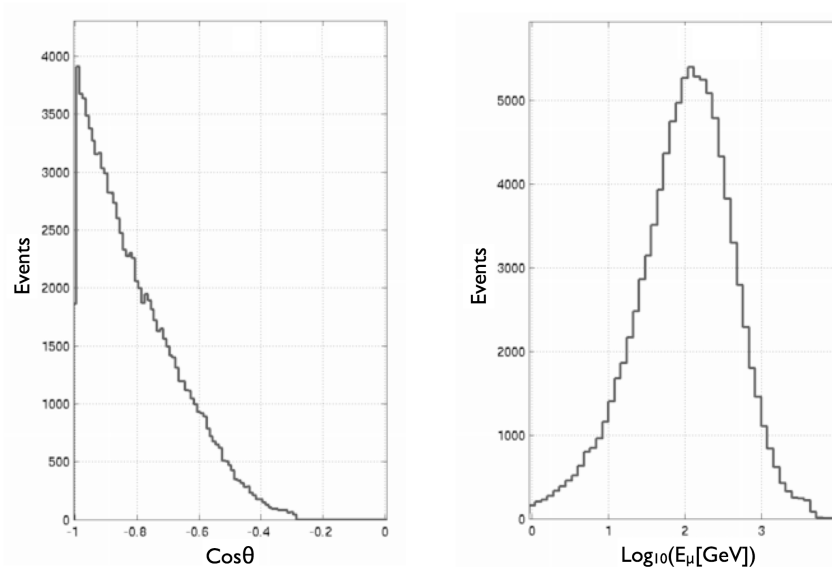


Figure 4.8: Angular (left) and energy (right) distributions of the muons as they crossed the rock-cavern boundary. The muon generator by Yellin [175] was used as input to model the cosmic rays and their secondaries at the Soudan Underground Laboratory.

at higher angles. Nevertheless, the effect of the difference between the two muon generators is much smaller than the systematic uncertainty on the processes that produce neutrons that cause background events, as I will elaborate in Chapter 6.

4.2.4 A 5 Tower and 7 Supertower FLUKA-MCNPX cosmogenic neutron simulation

In this section I describe the simulation of the muons at Soudan that, by interacting with the rock and shielding materials, can give rise to nuclear recoils such as those expected by a WIMP. A model of the cavern and the CDMS-II shielding, icebox and detectors was setup in FLUKA and MCNPX. The FLUKA Monte Carlo was used for the “high-energy” part of the simulation, starting with muons from the muon generator described in the previous section, propagating them and their secondaries

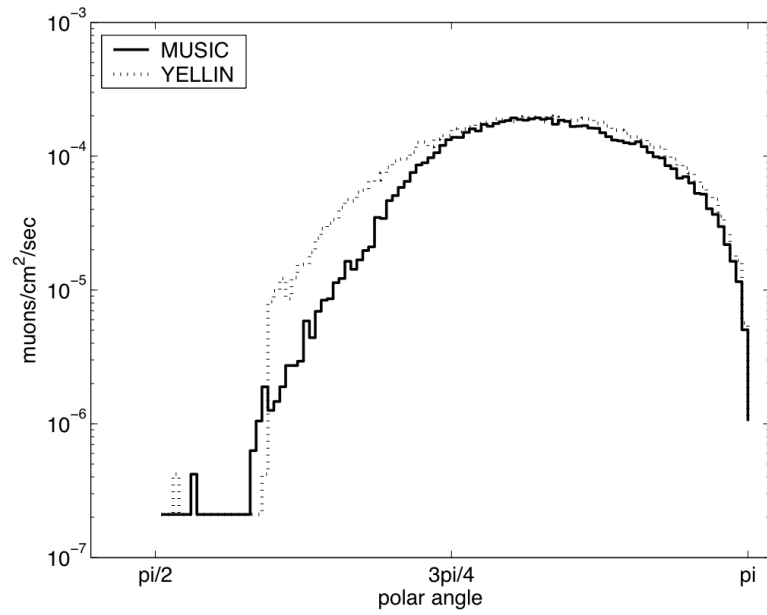


Figure 4.9: Angular distribution produced by the muon generator by Yellin (dotted) [175] compared to that of the muon generator based on measurements of the slant depth distribution by Kasahara [179] and MUSIC [180].

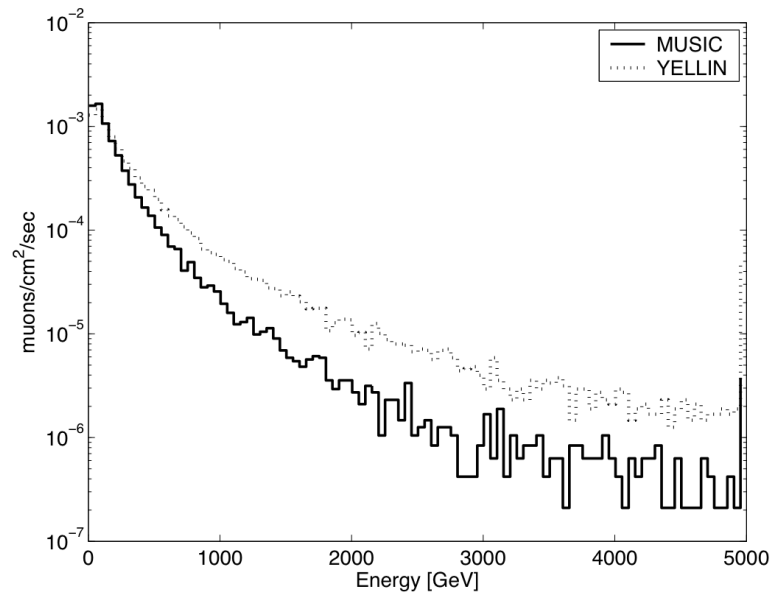


Figure 4.10: Energy spectrum produced by the muon generator by Yellin (dotted) [175] compared to that of the muon generator based on measurements of the slant depth distribution by Kasahara [179] and MUSIC [180].

through a rock shell with the CDMS-II geometry inside of it. The rock shell has a density of 2.8 g/m^3 (Greenstone rock) and dimensions of $28 \times 24 \times 24 \text{ m}^3$. Inside the rock shell there is a volume filled with air with dimensions of $8 \times 4 \times 4 \text{ m}^3$. Inside the air volume is the CDMS-II passive and active shielding, where the active shielding (the plastic scintillator panels) are modeled by a top and bottom 5 cm thick rectangular slab and with a 5 cm thick cylindrical shell surrounding the outer polyethylene layer. The FLUKA part of the simulation has the rock shell, and the CDMS-II geometry through to the innermost copper can which had vacuum in it. All particles going inside the innermost copper can were recorded in a file on an event by event basis (each particle was associated with a parent muon number). The file produced by the modified FLUKA simulation was later propagated using MCNPX in a geometry of the detectors and the copper of the cold hardware inside the innermost copper can. The nuclear recoils produced were later analyzed together with the FLUKA output from the energy deposited in the plastic scintillator, keeping track of all correlations back to each parent muon. Furthermore, the MCNPX part of the simulation (“low-energy” section) included the charge deposited in the Ge and Si detectors due to ionization from charged particles and photons in order to count how many nuclear recoils were also vetoed by the ZIP detectors.

The reason for the use of MCNPX is due to the lack of accurate simulation of the low energy neutrons recoiling with the ZIP detectors. FLUKA does not use point-wise neutron simulations (except for a few elements) that correlate the incident neutron energy with the recoil angle using angular-dependent cross section. Instead, it uses the “group method” in which the correlations are lost. I have modified MCNPX (since the source was made available) to include point-wise low-energy neutron scatters in Ge and Si using the approach implemented in MCNP-Polimi [183], which includes accurate simulation of the nuclear recoils. The MCNPX implementation was tested using a monoenergetic neutron beam with an energy of 1 MeV and compared with

the recoil energy spectrum for the same simulation in Geant 3 [184] with very good agreement at the few percent level. The Geant 3 simulation was previously well tested against ^{252}Cf calibration data [149].

In order to maximize CPU efficiency, a series of thresholds were applied at various regions of the FLUKA and MCNPX simulations. In the FLUKA simulation there is a 1 GeV threshold on photon production on the outer 9 m thick rock shell and a 1 MeV threshold for any other particle (“passive rock”), leaving the 1 m thick inner rock shell with a 1 MeV threshold on all particles (“active rock”). The simulated plastic scintillator has a 1 MeV threshold and the FLUKA table made at the innermost copper can had no threshold. The MCNPX simulation had no lower energy thresholds. Figure 4.11 shows the top and side of the geometry used in FLUKA and MCNPX. The innermost rock shell with a 1 MeV threshold is in dark grey (“active rock”), and the rest is in light grey (“passive rock”).

Table 4.2 shows the neutron flux and neutron multiplicity at the rock-cavern boundary. The neutron flux is in good agreement with that reported by Mei and Hime [222] which was obtained with a different muon generator and different cavern size. The neutron flux at the rock-cavern boundary was counted if a neutron crossed the geometrical boundary and therefore, low energy neutron scattering off the walls caused some double counting. The effect of neutron scattering off rock was established by Wulandari and coworkers, and corresponds to approximately a factor of two for neutrons with a few MeV [185].

The spectra and angular distribution of the neutrons at the rock-cavern boundary is shown in Figure 4.12. The angular distribution is shown for the neutrons above a 1, 10 and 100 MeV threshold. The energy-dependent angular distributions show that as the energy of the neutron increases, there is a preferred polar angle of the neutrons, which in turn would be related to the parent muon polar angle.

Table 4.3 shows the main results from the FLUKA-MCNPX simulation for two

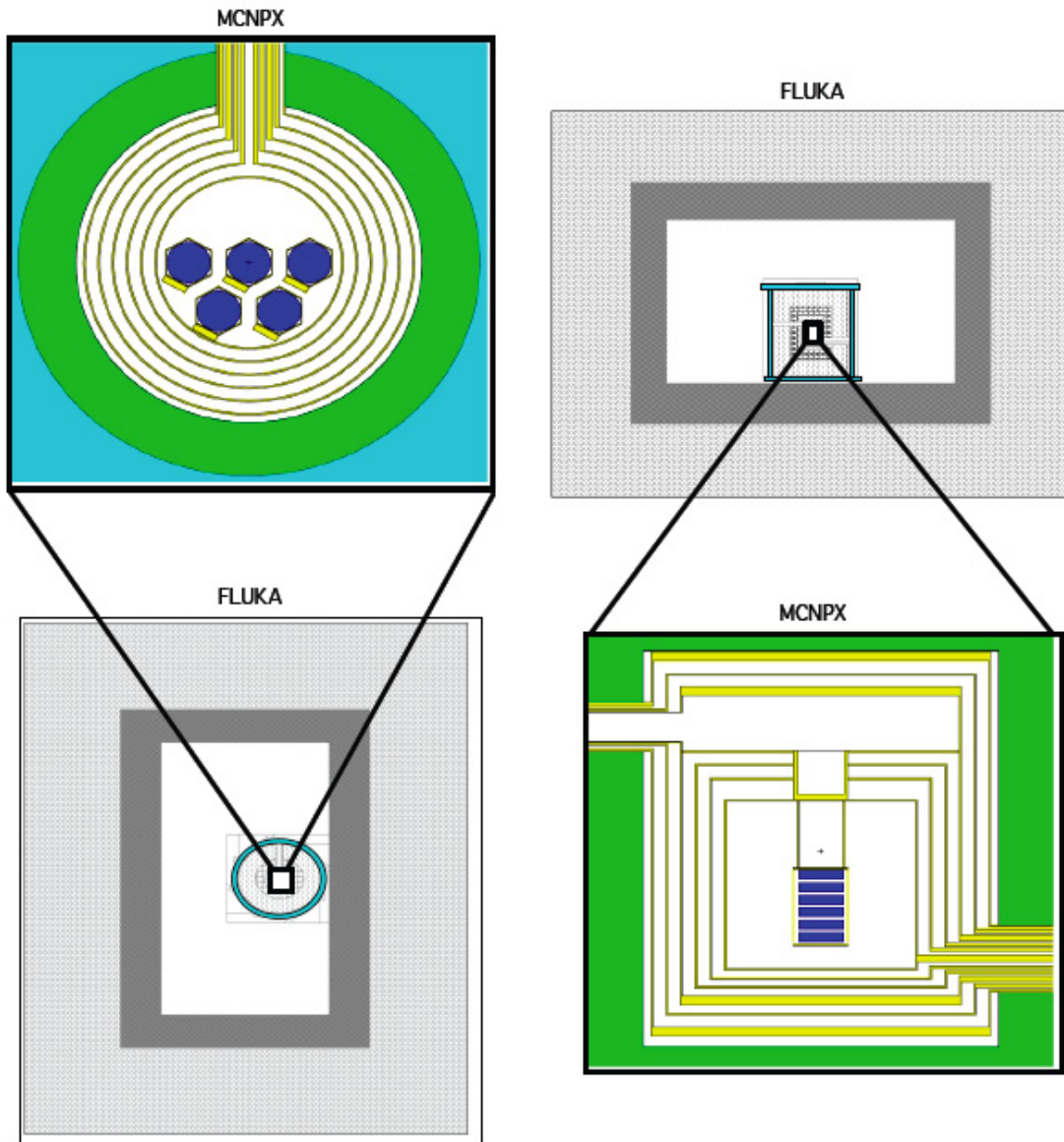


Figure 4.11: A side and top view of the FLUKA and MCNPX geometries. The rock shell has dimensions of $28 \times 24 \times 24 \text{ m}^3$ with the cavern inside being $8 \times 4 \times 4 \text{ m}^3$.

MCNPX geometries, the 5 Tower CDMS-II Ge and Si array and a 7 Supertower array proposed for a new experiment, the SuperCDMS 25 kg project. One Supertower corresponds to 6 Ge detectors except that the thickness increases from 1 cm to 2.54 cm. The cryostat at Soudan could house 7 Supertowers at the most, in terms

Quantity (FLUKA)	Energy threshold	Rate [n/cm ² /sec]
neutron flux	>1 MeV	6.11×10^{-9}
	>10 MeV	2.93×10^{-9}
	>100 MeV	1.06×10^{-9}
neutron multiplicity	>1 MeV	2.14
	>10 MeV	1.55
	>100 MeV	1.20

Table 4.2: Neutron flux and multiplicity counted at the outside of the simulated CDMS-II veto system from the FLUKA simulation equivalent to 14 years of underground muons in a model of the Soudan cavern.

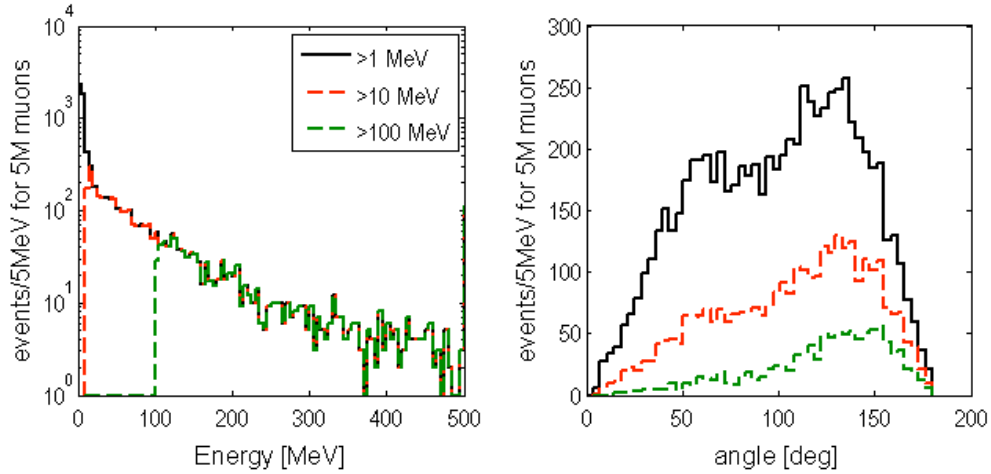


Figure 4.12: *Left*: Neutron flux above 1 MeV (black solid), above 10 MeV (dashed red) and above 100 MeV (dashed green) at the rock-cavern boundary as a function of energy. *Right*: Angular distribution of the neutron flux above 1 MeV (black solid), above 10 MeV (dashed red) and above 100 MeV (dashed green) at the rock-cavern boundary

of volume, while minimizing the modifications to the cold hardware. While the SuperCDMS project has not proposed to run a 7 Supertower array at Soudan, the 7 Supertower simulation results show the level at which such an array would be limited by irreducible cosmogenic neutron backgrounds (if no changes to the existing shield configuration were implemented). Table 4.3 provides the rates of the irreducible cosmogenic neutron background as well as rates of nuclear recoils that will occur in

coincidence with activity in the veto. Furthermore, it provides the multiples rate as well, which can be combined with the predicted singles rate and a measurement of multiples to determine if an excess of single scatter WIMP candidates are observed.

The rate of cosmic-ray induced events that will mimic the WIMP signal is $0.06 \pm 0.02/\text{kg}/\text{year}$ in Ge for the 5 Tower configuration, and $0.05 \pm 0.01/\text{kg}/\text{year}$ for the 7 Supertower configuration. All errors so far are statistical; in Section 4.2.6, I will discuss the systematic error associated with these estimates and the challenge of benchmarking the relevant neutron production processes. In order to obtain the Unvetoed Ge Singles for the 5 Tower geometry, I have used the number of Unvetoed Singles-NR and multiplied it by the fraction of Unvetoed Singles to Unvetoed Singles-NR obtained from the 7 Supertower array (row 4 divided by row 5 in the 7 Supertower column gives a factor of 2.7). The reason for this is that at the time the 5 Tower simulation results were produced, the MCNPX part of the simulation did not include energy depositions due to charged particles or photons in the ZIP detectors. Nevertheless, the 7 Supertower configuration included all processes in MCNPX and the 2.7 factor is sufficiently robust to use in the 5 Tower configuration since the systematic uncertainties in the absolute flux cancel in the ratio. Therefore, for the runs 123 and 124 we expect < 0.2 unvetoed single nuclear recoil events from cosmogenic neutrons.

The advantage of switching from FLUKA to MCNPX is that one can throw the same input file in different geometries without the need to rerun the FLUKA part of the simulation, which is CPU intensive due to the size of the rock shell and energy of the incident muons.

In the remaining Sections of the Chapter, I will describe the veto-coincident data obtained during runs 123 and 124 and how it can be compared in a sensible way to the results obtained with the FLUKA-MCNPX simulations. Furthermore, I will describe the associated systematic error with the estimation of unvetoed Singles from the FLUKA-MCNPX simulation in Section 4.2.6.

Event Type	5 Towers Ge(Si) /kg-year	7 Supertowers Ge /kg-year	Short Description
Vetoed Singles-NR	$2.9 \pm 0.2(9.8 \pm 0.8)$	2.57 ± 0.08	Singles-NR in coincidence with an energy (1 MeV threshold) in the veto system. Singles-NR are muon events with one nuclear recoil in the 10-100 keV.
Vetoed Multiples (by veto system)	$3.4 \pm 0.2(\text{Ge} + \text{Si})$	2.55 ± 0.09	Multiples in coincidence with energy in the veto system. Multiples are 2 or more nuclear recoils in the 10-100 keV with no cut in the other detectors.
Unvetoed Multiples (by veto system)	$0.25 \pm 0.05 (\text{Ge}+\text{Si})$	0.11 ± 0.02	Multiples not in coincidence with energy in the veto system.
Unvetoed Singles-NR (by veto system)	$0.17 \pm 0.05(0.85 \pm 0.22)$	0.14 ± 0.08	Singles not in coincidence with energy in the veto system.
Unvetoed Ge Singles (by veto system and ZIPs)	0.06 ± 0.02	0.05 ± 0.01	Singles are Singles-NR with the extra condition that there was no energy between 2-10 keV nor >100 keV in any other ZIP detector.
Veto fraction (by veto system)	0.93	0.95	Fraction of nuclear recoils in coincidence with energy in the veto system to those nuclear recoils in anti-coincidence with energy in the veto system.

Table 4.3: Results from the FLUKA-MCNPX simulation equivalent to 14 years of underground muons in a model of the Soudan cavern with the 5 Tower CDMS-II (4.74 kg of Ge, 1.1 kg of Si) and a 7 Supertower (26.67 kg of Ge) target mass. All errors in the table are statistical.

4.2.5 First muon-induced nuclear recoils at Soudan

In this Section, I describe the CDMS-II runs 123 and 124 veto-coincident data analysis and how it compares with the FLUKA-MCNPX simulation results presented previously. First, I describe the data cuts used to select the events, then the exposure associated with the cuts and the event topologies. I conclude with a discussion on a comparison of runs 123 and 124 combined veto-coincident nuclear recoils with the FLUKA-MCNPX simulation results discussed in the previous section.

The data selection used to search for veto-coincident events, apart from data quality cuts, contained the following cuts:

- `cQin_123`: Selects events that occurred in the inner electrode,
- `cNuMLR123`: Selects events that occurred in anti-coincidence with the GPS time-stamp of the neutrino beam coming from Fermilab towards the MINOS neutrino detector (no events were observed in coincidence for runs 123 and 124),
- `cVTStrict_123`: Selects events in coincidence with energy in the veto system above threshold,
- `cNR_123`: Selects nuclear recoils based on the energy dependent ionization yield from neutron calibration,
- `cRTChi2EDEP_123`: Rejects surface events that can occur in coincidence with activity in the veto. For example, a high-energy photon (with a few MeV) that hits a Ge detector, causes the ejection of a low energy electron that can reach the neighboring detector and gives an event with low ionization yield. Such events would be confused with nuclear recoils without the use of timing cuts.
- `nband_yic_123`: Selects events within the nuclear recoil band, and

- Singles: Selects events in the nuclear recoil band that are single hits, and for which there was no energy in any other detector between 2-10 keV and above 100 keV.

Figures 4.13 and 4.14 show the veto-coincident nuclear recoil hits. The yield bands were constructed using neutron and gamma calibrations (described in Chapter 5). The green crosses correspond to hits that occur in the inner electrode, are vetoed and have a phonon recoil energy >5 keV, that is, they are veto-coincident gammas and betas. The red dots are hits that are nuclear recoils in coincidence with energy in the veto system above threshold and also are singles that do not pass the phonon timing cut (beta rejection cut); they are due to betas. The blue dots are hits in the inner electrode, in coincidence with energy in the veto, lie inside the nuclear recoil band and pass the phonon timing cut; they are veto-coincident neutron hits. No single neutrons were observed in either runs. A total of 5 neutron-like events (8 neutron-like hits in total) occurred between runs 123 and 124, 5 in the former and 3 in the latter. The green crosses observed inside the nuclear recoil bands are multiple gamma-like hits.

Table 4.4 shows the recoil energy, detector, total energy in the veto and the number of veto-panels hit (veto multiplicity) for each of the neutron-like events in coincidence with energy above threshold in the veto system. A closer look at the event topology of these events revealed the following:

- A total of two nearest-neighbor-double neutron events occurred in Run 123, one in Tower 2 and the other in Tower 4, labeled “1” and “3” in Table 4.4,
- A non-nearest-neighbor double neutron event occurred in Run 124 in Tower 5, labeled “5”,
- A total of three neutron+gammas occurred, one in Run 123 and two in Run 124, most of them being in coincidence with several gamma events in the other detectors, labeled “2” and “4”.

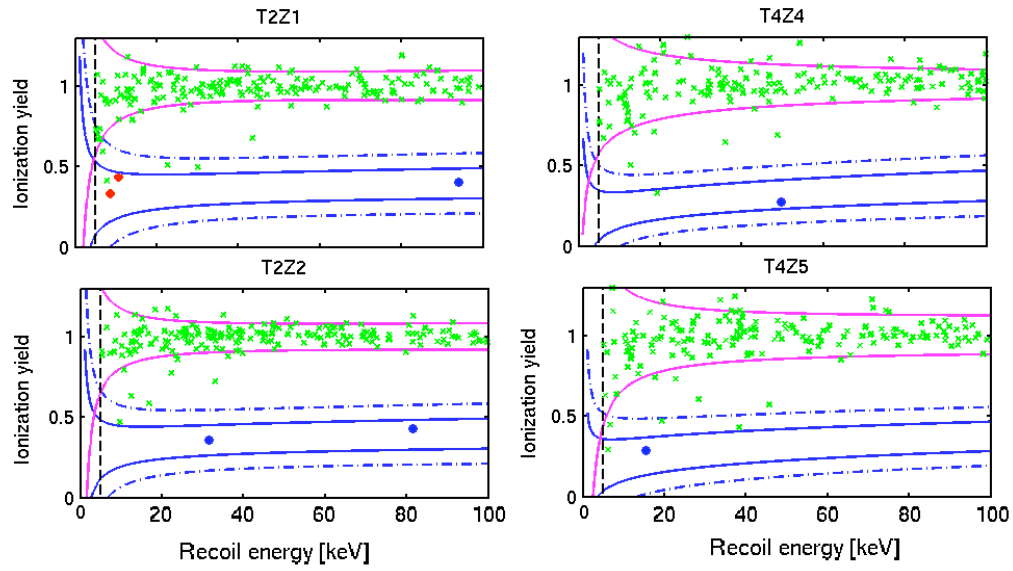


Figure 4.13: Yield as a function of recoil for the Run 123 veto-coincident neutron data. Gamma-like hits (green crosses) lie mostly around yield of 1. Single betas are represented by red dots and neutron hits by blue dots.

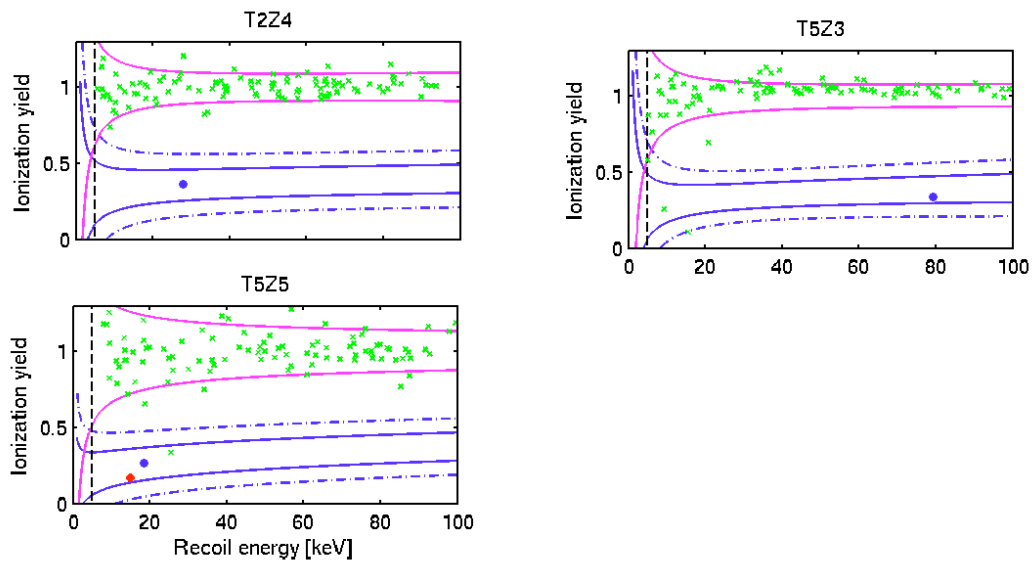


Figure 4.14: Yield as a function of recoil for the Run 124 veto-coincident neutron data. Gamma-like hits (green crosses) lie mostly around yield of 1. Single betas are represented by red dots and neutron hits by blue dots.

Label	Recoil [keV]	Yield	Detector	Veto Energy [MeV]	Veto Multiplicity
Run 123 Veto-coincident neutrons					
1a	94.1	0.40	T2Z1	100	9
1b	81.6	0.43	T2Z2	100	9
2	31.5	0.36	T2Z2	17	2
3a	49.7	0.27	T4Z4	547	26
3b	15.3	0.29	T4Z5	547	26
Run 124 Veto-coincident neutrons					
4	27.9	0.36	T2Z4	53	7
5a	79.3	0.33	T5Z3	110	6
5b	18.4	0.26	T5Z5	110	6

Table 4.4: Runs 123 and 124 veto-coincident nuclear recoil events [181]

The exposure associated with the veto-coincident neutron analysis is 1.4(0.28) kg-year of Ge(Si), which is slightly higher than the WIMP-search exposure of 1.15(0.21) kg-year of Ge(Si). In order to compare to the FLUKA-MCNPX results, the efficiency of the cuts applied to the data are taken into account by using an average efficiency of 0.4. In Table 4.5, a comparison between the runs 123 and 124 veto-coincident data and the FLUKA-MCNPX simulation equivalent to 14 years at the Soudan Underground Laboratory are presented. In order to make a sensible comparison, we have assumed that “Singles” are single nuclear recoil events in the 10-100 keV range regardless of energy deposition in another detector that is of non-nuclear-recoil type. Hence, this event class is the sum of isolated single nuclear recoils and single nuclear recoils with a gamma-like interaction in another detector. According to this comparison, there is fairly good agreement between this CDMS-II veto-coincident data and the FLUKA-MCNPX simulation described in Section 4.2.4. Nevertheless, this comparison should be taken knowing that a lack or excess of neutron events in the simulation could be due to two factors:

- (a) The neutron production processes are inaccurate in the models implemented in

the simulation.

- (b) The angular distributions of the neutrons with respect to the parent particle are inaccurate and therefore the simulation could predict an excess of nuclear recoils in coincidence with energy depositions by non-nuclear-recoil interactions in the same detector, hence producing fewer “identifiable” nuclear recoils.

Using CDMS-II data it is not possible to know which of the two factors is responsible for a discrepancy or if both factors cancel out to produce an agreement between data and simulation. Fortunately, we are mainly concerned with single nuclear-recoil events in anti-coincidence with energy in the veto system (unvetoed nuclear recoils). In order to rely on the unvetoed nuclear recoil rate produced with FLUKA-MCNPX, the processes that give rise to such event population need to be benchmarked with data. In Chapter 6, I will describe a new way to benchmark the processes involved in the production of the unvetoed population. In the next section, I will describe our best estimate of the systematic error on the unvetoed rate and why a reliable prediction of the unvetoed rate cannot be based on the measured vetoed rate.

Veto-coincident Run 123+124 vs. Simulation (FLUKA-MCNPX)		
Event Type	Data (# of events)	Simulation (# of events)
Singles (Ge)	0	1.6 ± 0.2 (stat)
Singles (Si)	2 ± 1.4	1.1 ± 0.1 (stat)
Multiples (Ge and Si)	3 ± 1.7	4.9 ± 0.2 (stat)

Table 4.5: Comparison between veto-coincident data from runs 123 and 124 and the FLUKA-MCNPX cosmogenic neutron simulation.

4.2.6 Systematic Uncertainty and Benchmarking

The origin of the systematic uncertainty in the estimate of those nuclear recoils in anti-coincidence with energy in the veto system lies in how well high-energy neutrons (> 60 MeV) that penetrate the outer polyethylene and produce low energy neutrons

in the high-Z gamma-ray shield (Pb) have been measured. As I will discuss in Chapter 6, there are no measurements to our knowledge of the muon-induced neutron flux (>100 MeV) directly or indirectly underground at any depth. The spectral shape of the neutron flux caused by muons underground from 1-400 MeV was measured by the LVD collaboration, located at Gran Sasso with a depth of 3600 mwe, and compared to FLUKA [216] (see Figure 4.15). The discrepancy between the FLUKA fit and the LVD data is approximately a factor of 3 for neutron energies of ~ 100 MeV and above. If the high-energy neutron flux is directly proportional to the production of the unvetoes population, we can assign a factor of 3 systematic uncertainty to the FLUKA-MCNPX estimate of such a population.

Since the veto-coincident neutron population is dominated by muons interacting directly with the shield, neutron production processes such as direct muon spallation and electromagnetic showers would be the dominant processes benchmarked. However, the muon-induced high-energy neutron flux, which leads to unvetoes recoils, is produced mainly by hadronic showers that develop several meters through the rock (muons interacting in the shield will produce neutrons mostly through other processes such as direct muon spallation and due to electromagnetic showers). Given the difference in neutron production processes of the neutron populations that cause the vetoed and unvetoes recoils, the vetoed neutron rate cannot be used to reliably predict the unvetoes neutron rate. A new detector (based on old technology) proposed and described in Chapter 6 could measure the high-energy neutron flux deep underground (we have chosen the Soudan depth for design studies). The proposed measurement will be able to narrow the systematic error on the unvetoes population from a factor of 3 to $\sim 12\%$ in the course of a year. Nonetheless, for the present exposure and systematic errors, we are safely in the regime of < 1 predicted background event due to cosmogenic neutrons.

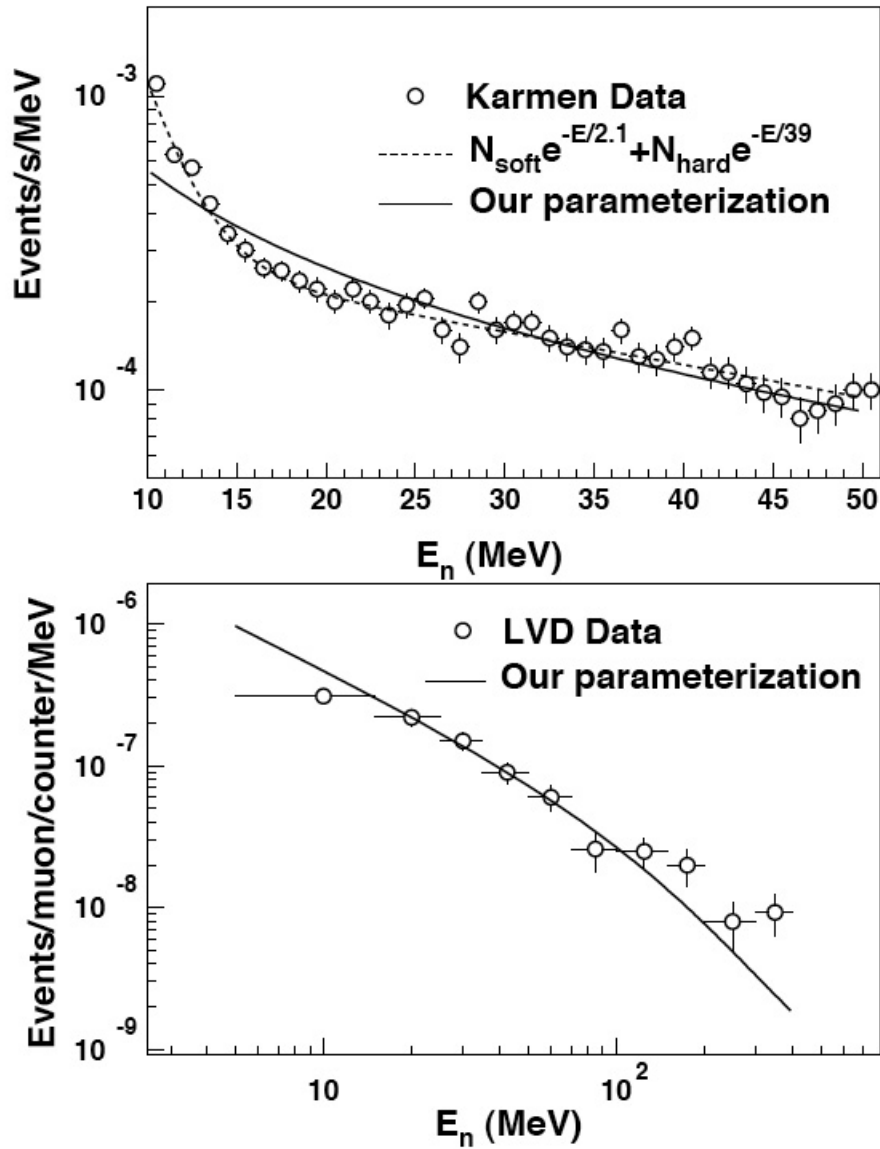


Figure 4.15: Comparison of the measured neutron spectra by the Karmen (*Top*) and LVD (*Bottom*) experiments with the FLUKA simulation by Wang and coworkers [216].

Chapter 5

First 5 Tower Data at Soudan

In this Chapter, I will describe the experimental efforts, including analysis of the data, that lead to the successful completion of the first 5 tower run, which consists of two run periods, run 123 and run 124 at the Soudan Underground Laboratory that occurred between October 2006 and July 2007. First a description of the event reconstruction, and position and energy corrections in the charge and phonon channels will be presented. Furthermore, a description of the most important data cuts will be described, including those classified as “data quality” cuts motivated by stability and quality of data, and the “physics” cuts, motivated by the search for the WIMP event topology. The latter includes a singles scatter cut, a fiducial volume cut, a yield-based nuclear recoil selection cut, and the timing cut to reject surface events with reduced ionization yield.

The five towers consist of 30 ZIP detectors, described in Chapter 3. In the analysis of runs 123 and 124, we have included 19 Ge detectors; three suffering reduced performance from readout failures and one with poor energy resolution were excluded from the analysis. Figure 5.1 and 5.2 show the top and side views of the 5 towers at the experimental site in the Soudan Lab. A total of 15 Ge detectors (3.75 kg) were used for the run 123 analysis. In run 124, a total of 7 Ge detectors (1.75 kg) were

used used due to variations in performance as compared to run 123.

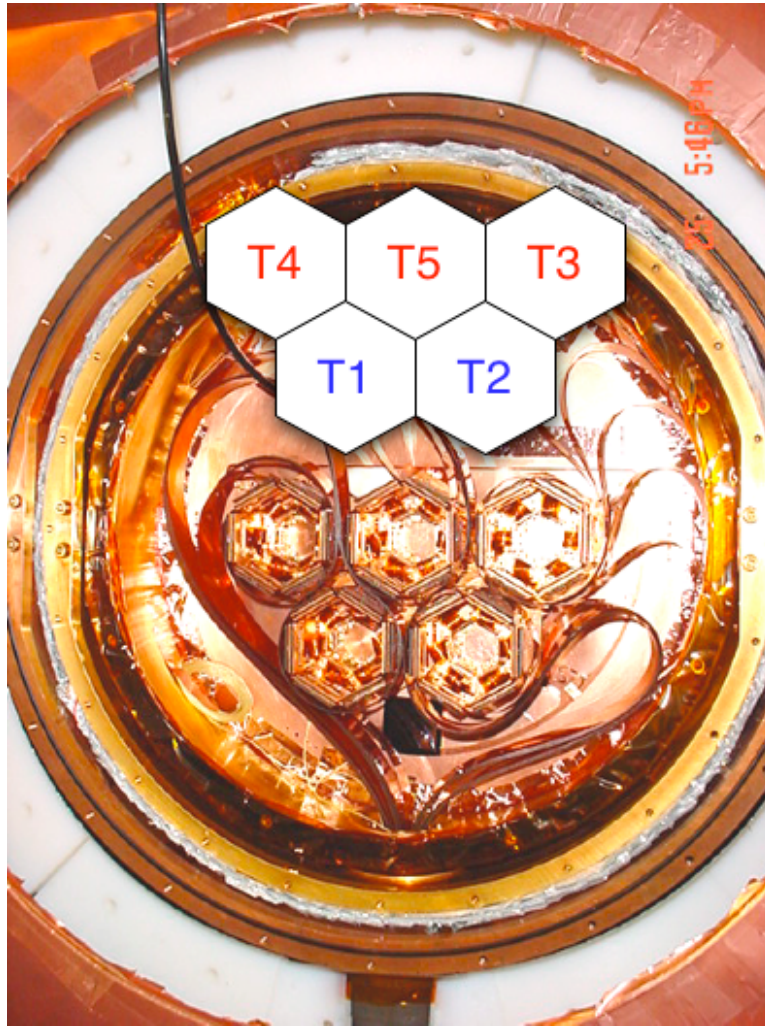


Figure 5.1: Top view looking into the inside of the icebox (innermost copper can). The five towers are shown with a drawing superimposed on the picture, describing the tower number configuration (T1 for tower one and so forth). The white ring surrounding the innermost copper can corresponds to the inner polyethylene shield (10 cm thick).

The reasons that forced the experiment to produce two different data runs instead of one “long” run are due to operational problems and detector running conditions. Run 123 began after initial commissioning period during the summer of 2006, and acquired data for more than 148 calendar days (107 live days of WIMP search running). An ice plug in the dilution refrigerator plumbing forced the experiment to warm-up

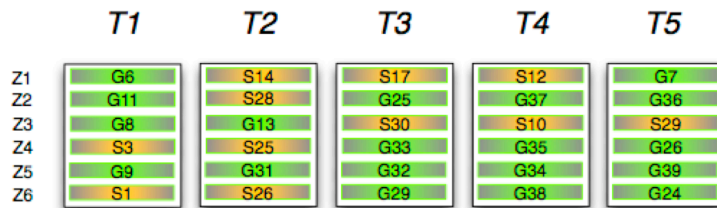


Figure 5.2: The configuration of the five stacks of detectors for each tower. Germanium detectors are colored green and the silicon detectors, orange.

in late March, and this marked the end of run 123. WIMP search running resumed in April 2007, and run 124 began data taking until mid-July 2007 for 83 calendar days or 56 live days. This run was truncated due to substantial neutralization difficulties (the accumulation of trapped charge in the bulk of the crystal) for several of otherwise “good” detectors in run 123, presumably due to a modified neutralization scheme (LED settings). Experimental work began in late June to test detector neutralization using strong radioactive sources rather than LEDs. These tests were successful and led to a substantial improvement in the neutralization of some detectors. The end of run 124 was due to problems with another blockage in the dilution refrigerator that forced a warm-up.

5.1 Event Reconstruction

The readout of the CDMS experiment includes six data channels per detector, four for phonons (one for each quadrant) and two for charge. The pulses are characterized by a 1.638 ms long trace digitized at a rate of 1.25 MHz which corresponds to 2048 bins. Besides the pulse digitation information, the biasing levels, and the veto and trigger history buffers are stored for each event. This information is further processed by Matlab based software, which takes the output from the DAQ and converts it into “Reduced Quantities” or RQs. The RQs have the information relevant for the physics

analysis.

The reconstructed traces in one tower are shown in figure 5.3. In order to make best use of the trace we use a frequency-based and noise-weighted optimal filter algorithm. This algorithm fits a template pulse to a trace, for each trace in an event. In general terms, if a real pulse has the form

$$p(t) = \mathbf{H}s(t) + n(t) \quad (5.1)$$

where $s(t)$ is the expected pulse shape (normalized to have a peak height of 1), \mathbf{H} is the amplitude (to be estimated), and $n(t)$ is a noise baseline. By minimizing (optimizing) the χ^2 of the fit of the event pulse $p(t)$ to the expected pulse shape $s(t)$ in the frequency domain, where the noise spectrum is independently measured, we can estimate \mathbf{H} . The template pulse shape in the phonon channel has the following functional form:

$$s(t) \sim -e^{(t-t_0)/\tau_{rt}} + e^{(t-t_0)/\tau_{ft}}, \quad (5.2)$$

where τ_{rt} is the risetime of the pulses, which corresponds to $\sim 30 \mu\text{s}$ for Ge and $\sim 25 \mu\text{s}$ for Si. The parameter τ_{ft} is the falltime of the pulse and is approximately $170 \mu\text{s}$ for Ge and $130 \mu\text{s}$ for Si. More details are described in reference [186].

5.2 Charge position correction

A substantial variation in the charge yield as a function of position in the ZIP detector is observed. We define the quantities x -delay and y -delay as the difference between the start times of the two neighboring phonon channels relative to the start time of the primary channel. For example, if the event occurs on quadrant A (or channel A), the x -delay is the difference in start time between channel A and channel D and y -delay would be the difference in start time between channel A and B. Figure 5.4 is a delay plot that shows the resolving power of the detector position of an event.

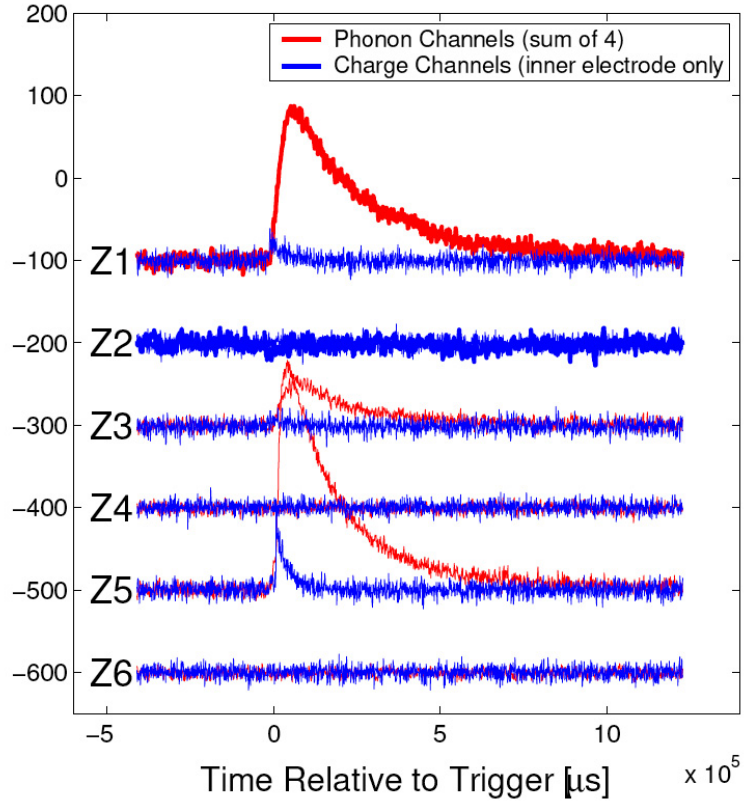


Figure 5.3: Pulse traces from the phonon and ionization channels for all detectors in one tower (tower 1). The red traces correspond to the sum of the four phonon channels and the blue to the inner electrode channel. The pulses are made from 2048 data points and are digitized at a rate of 1.25 MHz. Figure from [187]

The charge collection efficiency in the ZIP detector varies with the event position along the y-axis or along channels A and B (see figure 5.4). This variation in charge collection efficiency could be due to the variation in the amorphous silicon layer that is introduced on top of the Ge and Si substrates of the ZIP detector. The amorphous silicon layer is used to create an energy gap difference between amorphous silicon and Ge which minimizes the effect of the dead layer (previously discussed in Section 3.4) by preventing the back diffusion of electrons and holes [133, 145]. The charge collection efficiency variation with position occurs mainly on Ge detectors since the energy gap difference between Si and amorphous silicon is small.

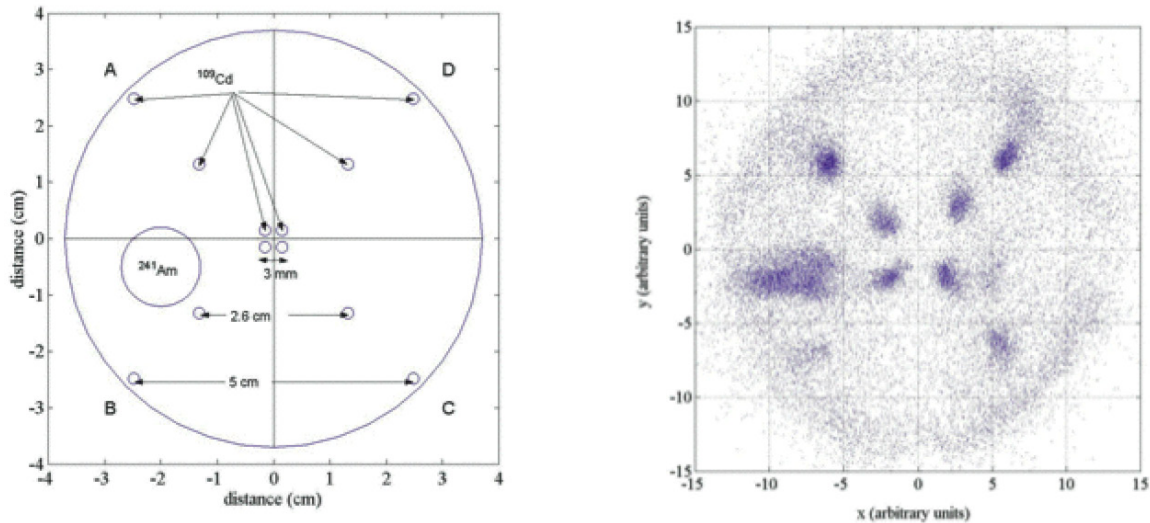
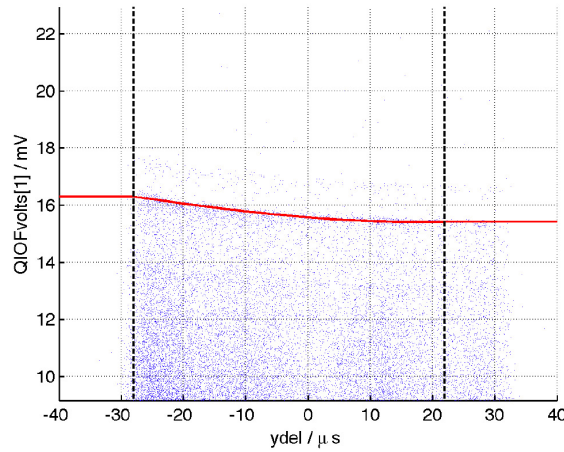


Figure 5.4: Delay plot of a Ge detector (right) of the corresponding source configuration (left). The calibration sources used were ^{241}Am , which was located between channels A and B. A beta source, ^{109}Cd (small dots), was used as well to mimic electron background surface events. On the figure in the right, the non-circular shape of the source “blobs” is an indication of the loss of position resolution along the radial coordinate. Figure from [188].

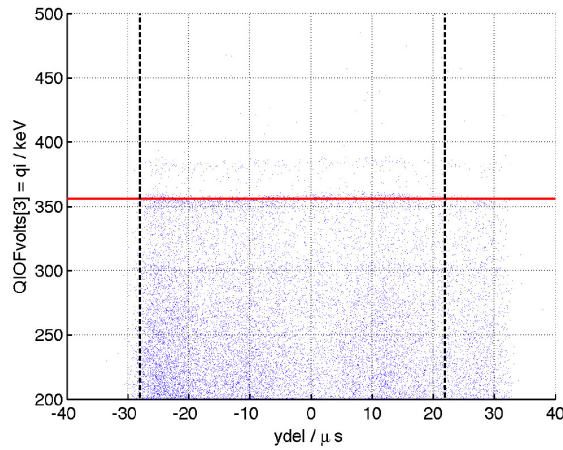
Ge detectors are position corrected in the inner electrode charge collection region (Q-inner). A 5th-order polynomial is fit to the Ba 356 keV Ba line of Q-inner events as a function of y -delay. At the extreme values of $+y$ and $-y$, a piecewise function corrects the response to become a flat line. Furthermore, Q-inner is divided by this full y -coordinate fit, calibrating it to 356 keV while making it flat in y . In Figure 5.5 the y dependence of the charge collection efficiency is shown before and after the position correction is made for T5Z5 (tower 5, ZIP detector 5), as an example.

5.3 Phonon position correction

The phonon timing parameters used for surface event discrimination and the energy of an event as determined using the phonon channels depend on the event location. The position dependence can lead to decreased surface event discrimination and worsen



(a)



(b)

Figure 5.5: Charge collection as a function of y -delay for detector T5Z5 (tower 5, ZIP 5) before (a) and after (b) the position correction. Figure from [189].

the yield estimation. In order to alleviate the decreased performance due to position dependence, a method of homogenizing the detector response across the crystal is implemented. This method, “Lookup Table Correction” consists of creating corrected quantities which compare the properties of a given event to those properties of the event nearest neighbors in a high-statistics calibration data set.

The physical reasons that cause the dependencies on event location and the phonon-based energy measurement are summarized as follows [190]:

Energy dependence

The number of saturated Transition Edge Sensors (TESs) is larger for a high energy event than for a low energy event. When a high energy event occurs the TESs that are closest to the event location have the fastest response and tend to saturate that phonon channel. Due to variations of T_c across the detector, the saturation of the TESs is position dependent as well.

x-y position dependence

Events that occur close to the center of a channel have the fastest response. As the event location moves towards the center of the detector itself or close to the outer edges, the timing parameters show a slowing down as compared to events that occur close to the phonon channels.

Z-dependence (Timing Discrimination Parameter)

If the event location is very close to a detector “wall” then the high-energy phonons are down-converted by interacting with the wall and therefore some of the phonons that otherwise contribute to making the event pulse are lost.

QETs detector coverage constraints

The shape of the QETs and the photolithographic constraints associated with detector fabrication lead to voids of detector surface in which there are no QETs such as the outer cylindrical edge. Therefore, events near the outer edge of the detector have a higher percentage of phonon loss, causing the estimation of the energy to be underestimated at large radius.

In order to make the detector phonon response more homogeneous across the detector, CDMS performs the Lookup Table Correction. In general terms, the Lookup Table Correction is made by using a sample of bulk electron recoils. For every event in the sample, a “bin” is constructed corresponding to N nearest neighbors and the

properties for each event within a bin are corrected relative to those obtained for the bin. In short, the Lookup table is like a set of position dependent calibration factors that are applied to each event depending on its initial position parameters. Once the Lookup Table has been calculated, the data are corrected by finding for each event its nearest single neighbor in the Table and using the correction factor of that nearest neighbor. For example, the corrected quantities are defined as follows:

$$pdelc = pdel \frac{\langle pdel \rangle_{all}}{\langle pdel \rangle_{NN}} \quad (5.3)$$

where $pdel$ is the time (seconds) of the event as inferred from phonon risetime and $\langle pdel \rangle_{all}$ is defined as the mean of $pdel$ for all events passing the selection cuts. This position correction is of crucial importance for the phonon timing cut to work successfully as well as to understand the detector calibration.

5.4 Analysis pipeline

In this section the analysis chain will be described, including the main physics cuts applied to the 5 tower data and a description of the WIMP-search results. First, a description of how the raw data is processed to form the further-refined “physics” quantities or RRQs (Reduced Reduced Quantities).

The CDMS-II analysis chain consists of two stages: the Data Acquisition (DAQ) system that is located underground in the mine, and the Soudan Analysis Cluster or SAC which is located at the surface, less than a mile away from the mine (the “surface building”). Raw data is written to disk in the mine by the DAQ in the form of binary files. These binary files are backed up to a tape drive and simultaneously copied to the SAC in the surface building. The event reconstruction or data reduction process occurs in the SAC cluster. The primary data reduction process in CDMS consists of two main software packages:

DarkPipe: This package performs the first reduction on the raw data, converting the digitized traces into reduced quantities (RQs). The RQs generally represent physical quantities such as energy and event timing with nominal calibrations but are not yet expressed into the most useful or physical units.

PipeCleaner: This package implements various calibrations and corrections to the RQs produced by DarkPipe, yielding RRQs. Its primary duties are energy calibration (based on externally-computed correction factors) and the position/energy correction of phonon parameters. PipeCleaner also implements the blinding cut (to be described in the following Section) on WIMP search data,

After processing by PipeCleaner is ready, the data sets produced are analyzed for WIMP-search, although some of the basic cuts use RQs produced by DarkPipe (such as the blinding cut).

5.4.1 Blinding Cut

The analysis protocol that allows us to remain unbiased when setting cuts is called “Blinding” and the cut associated with the protocol is the Blinding Cut. The Blinding protocol was determined at the beginning of the analysis and is summarized in this section.

The Blinding Cut hides from consideration until analysis cuts are determined events that have all of the following characteristics and are thus potential WIMP candidates:

1. *Veto anti-coincident cut.* Events that are not triggered by the muon veto or that occur when there was no activity in the muon veto are called veto anti-coincident, or simply “unvetoed”. A vetoed event is defined as an energy deposition above threshold in two or more scintillator panels or one that was triggered

by a ZIP detector in coincidence with an energy deposition above threshold in a single Panel in a 200 μs window. I discuss the veto cut further in Section 5.4.7 in the context of the “physics” cuts applied to Run 123 and 124.

2. *Inner electrode cut.* Events that occurred in the inner electrode or “Q-inner”. Events that occur close to the “walls” of the detector have reduced ionization and therefore could look like neutrons or WIMPs. We expect that neutrons and WIMPs will have low ionization and at the same time interact fully in the inner electrode, therefore these events are also used in the blinding cut.
3. *Energy cut.* Events that had an energy between 5 and 130 keV. Even though previous CDMS analyses have reported a threshold of 10 keV, we have blinded from 5 keV in order to explore the possibility of a WIMP-search with a lower threshold.
4. *Nuclear recoil band.* A nuclear recoil band is defined using neutron calibration data with a ^{252}Cf source. The 3σ nuclear recoil band is defined in the yield vs recoil energy plot to take into account of the energy dependence (see Figure 5.12). The upper and lower limits of the band are defined as $\mu \pm 3\sigma$ where μ is the mean per nuclear recoil energy. The definition of the yield bands (the gamma band and nuclear recoil band) will be discussed in detail in section 5.4.6.
5. *Glitch events.* Glitch events are those that have high noise or events that have trigger characteristics of electronics glitches. This events were excluded from physics analysis as well.
6. *Singles.* Since WIMPs are expected to only interact once with a ZIP detector, single event hits are hidden in order to blind the analysis from the WIMP-like events.

Blinding, or hiding, just the events that that satisfy these criteria allow us to use residual data from WIMP-search runs in conjunction with calibration data to tune the analysis without biasing the selection or exclusion of WIMP candidates

5.4.2 Quality Cuts

In order to ensure data quality, we monitor the data a few minutes after it was taken using the online analysis tools, and we also perform data quality checks using the reduced quantities that are obtained after the data has been processed by the SAC. In this section I will describe the main data quality checks that we have performed for the two data runs that comprise the first 5 tower run at the Soudan Underground Laboratory.

The most basic data quality check that is performed just after the data was recorded is to look at the noise level for a few hundred averaged pulses taken at the beginning of each data-taking period. A total of 500 of these random noise triggers are recorded and the traces are used for many data quality purposes, including noise spectra in order to check the noise level in the run.

As soon as the random triggers are completed an automatic script removes any events with pulses in order to obtain a baseline noise sample and creates a noise spectrum. After these noise spectra are completed, another script compares each detector channel spectrum to a template for that channel. If the noise level is a factor of 3 or more higher than the template, a warning is issued to the Run Control gui (a gui that displays any alarms or warnings related to the data-taking process) notifying the operator of the behavior. Figure 5.6 shows the noise spectra taken for detector T1Z2 (tower 1, second ZIP from top to bottom). All the peaks above ~ 10 kHz are filtered out by the optimal filter algorithm and have essentially no effect on the charge amplitudes. Frequencies from a few hundred Hz to a few kHz are the critical ones [191]. On the phonon side, amplitude measurements depend on noise

below ~ 2 kHz [192].

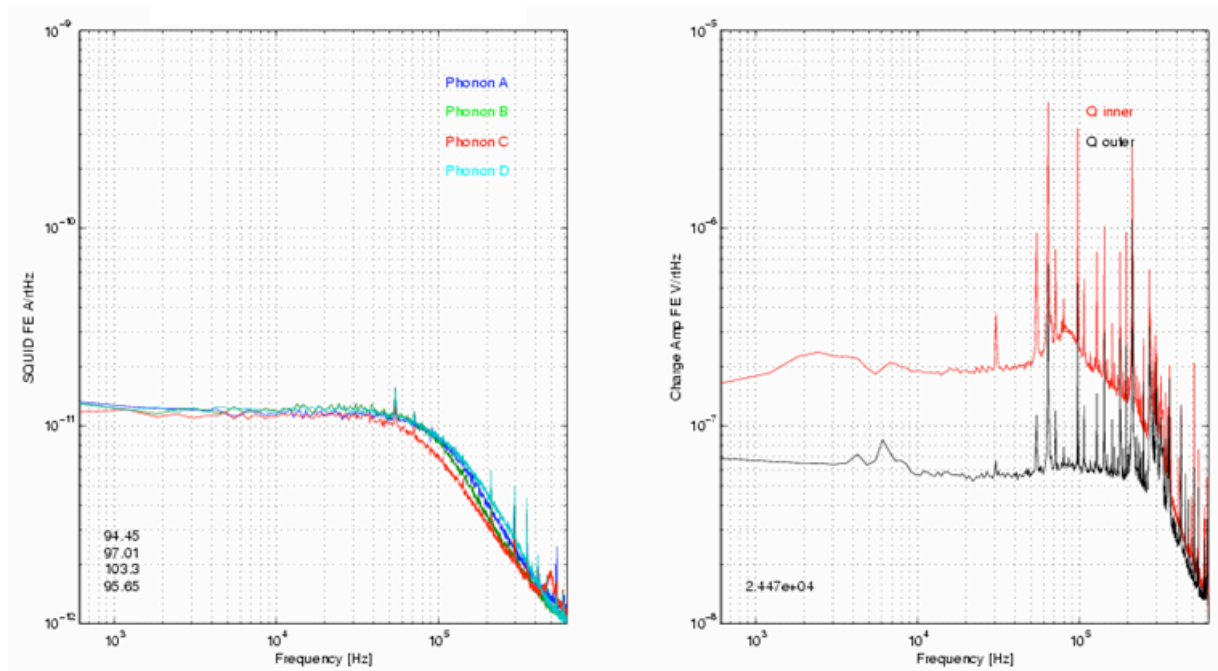


Figure 5.6: Phonon and charge noise spectra for a Ge ZIP detector located in tower 5. The most basic data quality check that is performed just after the data was recorded is to examine the noise level for 500 traces, and the average noise spectra for special features below 2 kHz for the phonon side and below 10 kHz for the charge noise spectra.

There are also a number of diagnostic monitoring plots that allow us to discard a given data run if there is an excessive trigger rate (e.g., possibly from excessive noise), if a veto panel is not recording any data for several minutes or if a phonon or charge channel is not behaving “normally” based on pulse template data. Furthermore, an event display called “pipedisplay” shown in Figure 5.7 allows us to evaluate a particular event just by glancing at the plots. The information included in pipedisplay is the phonon and charge traces for each detector, veto panel pulses, noise spectra, DC offsets, trigger thresholds, number of triggers, fridge base temperature and live time.

One of the principal tools to monitor any anomalous behavior in our ZIP detectors are the Kolmogorov-Smirnov (KS) tests. Anomalous behavior could be, for example,

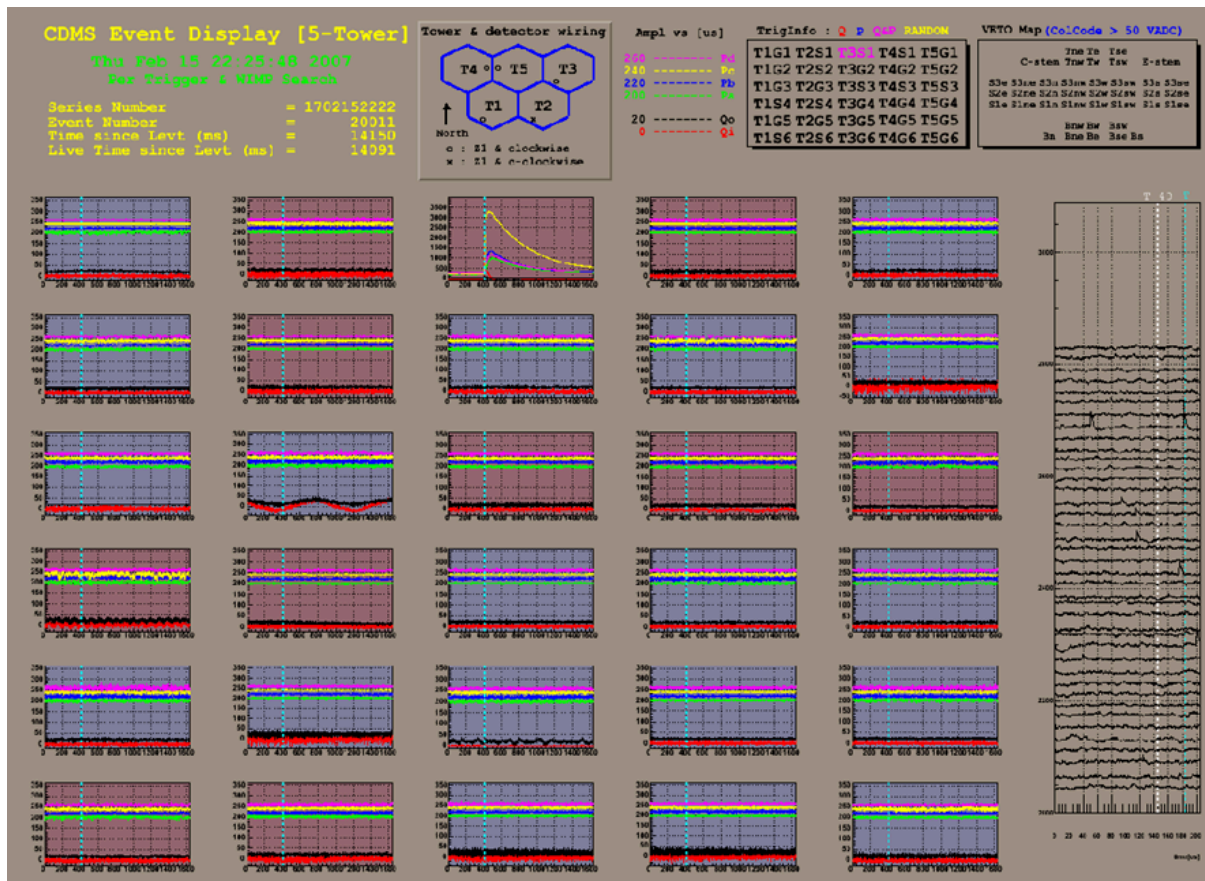


Figure 5.7: A snap shot of “Pipedisplay”, an event display that allows us to evaluate a given event on a run by looking at the traces for all 30 detectors including the veto panel traces on the right. It also includes the fridge base temperature and live time accumulated since the beginning of the run.

a shift in neutralization state in which the energy calibration changes and therefore excess events with a reduced ionization can begin to appear in the nuclear recoil band. The KS-test determines if two data sets differ significantly, while making no assumption of the distribution of the data. Using a good data set as a parent distribution, the KS tests can determine if the recently taken data set and the template data set can be drawn from the same parent distribution. The KS test cannot prove that two data sets are drawn from the same parent distribution, but can only say if they are not.

For Run 123 and 124 we compared the distributions of the reduced quantities for each data set with a reference data set (the template we know has good distributions). A series of KS tests was run for every low background (WIMP-search) data set and every barium (gamma calibration) data set. The quantities included in making the KS tests include timing, energy and noise related RQs. These KS tests led to the formation of cuts (including the data quality cuts) for R123 and R124.

5.4.3 Fiducial Volume Cut

The rejection of events with reduced ionization and phonon signals at large radius in the ZIP detector is made by the fiducial volume cut. These “edge” events may be undermined by distortions of the electric field, poor phonon sensor (QETs) coverage or reduced charge collection near the outer surface.

The main fiducial volume cut on the charge side is the Q-inner cut. Events with a charge signal mostly on the outer ring electrode (Q-outer) are cut by the Q-inner cut, and are discarded from the WIMP search event topology. The Run 123 and 124 Q-inner cut was defined in the following way:

1. Using a good Barium (gamma calibration) data set, a gaussian is fitted in Q-outer as a function of energy for a set of selected good Q-inner events, for several energy bins (from 0-300 keV)
2. A line is fitted to the mean and a parabola to the width of the gaussian fitted in Q-outer
3. Using the fits, the cut is set at $\pm 2\sigma$ from the mean

The efficiency of the Q-inner cut is measured using a neutron calibration event sample and values between ~ 65 and $\sim 75\%$ on average have been obtained. The efficiency decreases as the energy of the recoils increases. The physical reasons as

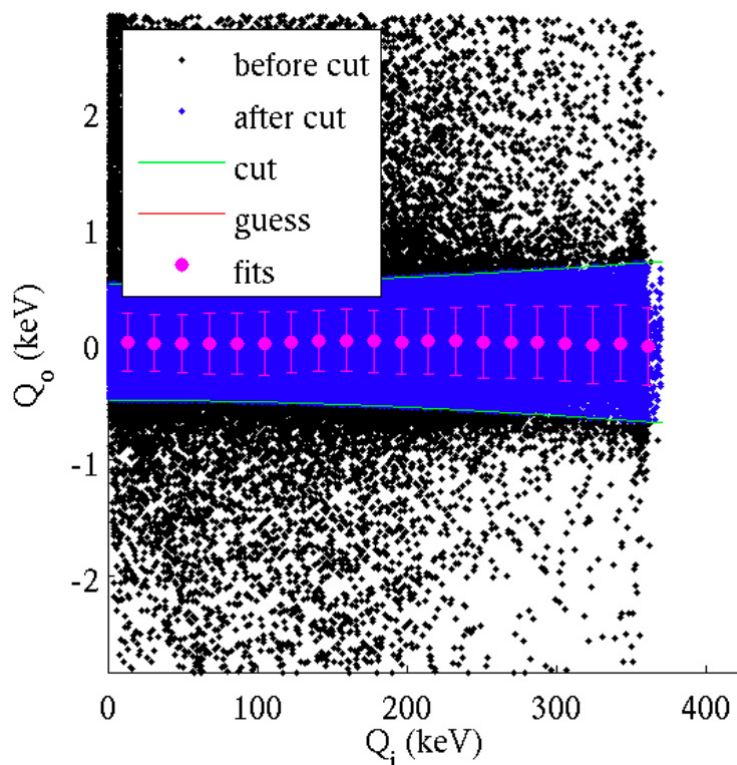


Figure 5.8: Events from a neutron calibration in the inner vs outer electrode space. The Q-inner cut is defined to maximize the inner electrode event population and excluding outer electrode events. The Q-inner cut is made calculating the mean (purple dots) of the Q-outer events as a function of Q-inner energy bins. The cut selects events in the $\pm 2\sigma$ band [193].

to why the efficiency of the Q-inner cut is lower at high energies could be that the electric field is somewhat distorted in the outer regions of the detector due to the grounded copper detection housing. Furthermore, it is easier to see a shared event between the inner and outer electrodes as the energy of the event increases, therefore the cut is more stringent at high energies i.e., has lower efficiency at high energies.

5.4.4 Thresholds

The charge threshold in the ZIP detectors is set 4σ above the mean of the Q-inner baseline as a function of total phonon energy for random trigger events. Figure 5.9 shows the Q-inner the number events as a function of total phonon energy for a Ge

detector in Tower 1. The threshold is set using a gaussian (blue curve) fit to the Q-inner noise traces.

Even though the phonon noise is considerably lower than the charge noise, the phonon threshold is set based on the efficiency to achieve good discrimination between nuclear and electron recoils (using the timing cut). The phonon thresholds therefore are set by using a sample of surface events and calculating the efficiency of rejection as a function of recoil energy. The threshold is set when the efficiency is approximately above a few percent. The analysis thresholds used in Run 123 and 124 are shown in Table 5.4.4.

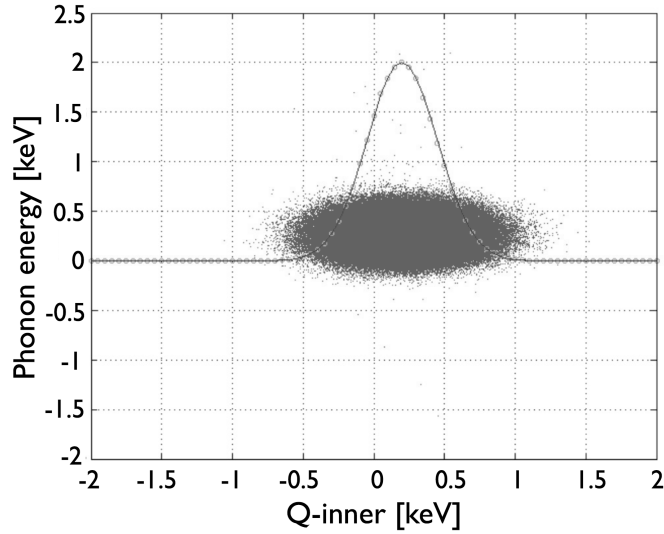


Figure 5.9: Q-inner events as a function of the total phonon energy (pt) for a Ge detector in Tower 1. The events were taken within the first 500 random triggers of the run, and therefore all were consistent with noise. The charge threshold cut is set at $\mu + 4\sigma$ where μ is the mean of the gaussian fit to the Q-inner events, and σ is the standard deviation [194].

5.4.5 Singles Cut

WIMP events are expected to be single interaction hits in the ZIP detector and the singles cut selects only events that have one interaction above threshold in one

	T1	T2	T3	T4	T5
Z1		7		10	10
Z2	10	7	10	10	
Z3		10	7	15	7
Z4	10	7	10	10	10
Z5	10	10	15	10	10
Z6			10	10	20

Table 5.1: Analysis thresholds in keV for the ZIP detectors used in Run 123 [195]. The rows correspond to each ZIP detector and the columns to each tower. Ge detectors are in bold and the rest are Si detectors.

	T1	T2	T3	T4	T5
Z1				10	
Z2	10				
Z3				15	
Z4		7		10	10
Z5	10			10	10
Z6				10	

Table 5.2: Analysis thresholds in keV for the ZIP detectors used in Run 124 [195]. The rows correspond to each ZIP detector and the columns to each tower. Ge detectors are in bold and the rest are Si detectors.

detector with all other of the detector signals below a lower threshold. Hence, a pair of thresholds is calculated for each ZIP detector: the upper threshold must be surpassed in order to consider that there was an interaction in that detector, and the lower threshold is used as a veto threshold. Single scatter events must exceed the high threshold in one detector and fall below the low threshold in all of the others. In Runs 123 and 124, the low and high phonon thresholds are set at 4σ and 6σ ,

respectively, above the mean phonon noise. These thresholds yield an efficiency in excess of 99%, as it is rare that any detector will happen to exceed its threshold due to noise in coincidence with a true pulse in another detector.

At times when the noise level is high, the thresholds are respectively set high for the singles cut and the efficiency of the cut is correspondingly reduced. For example, Figure 5.10 shows the variation in phonon noise as a function of the events date during Run 123 for Tower 1.

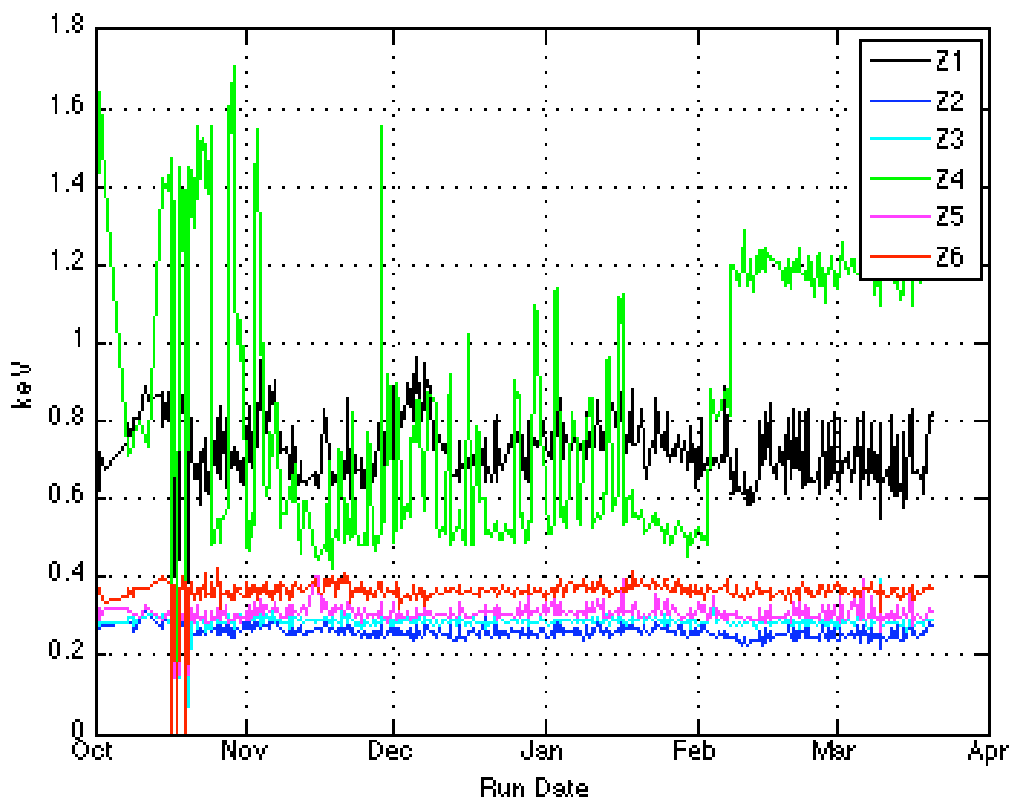


Figure 5.10: Time variation of the mean total phonon noise from the Tower 1 ZIP detectors [196]. The Run 123 and 124 Singles Cut takes into account the variation in the noise by doing a run-by-run estimation of fit parameters used to calculate the low (for tagging multiples) and high phonon thresholds.

The variations in noise can have a significant effect on the singles cut because a

detector that has poor resolution (or high noise) will tend to trigger more frequent false vetoes, as noise fluctuations drive the phonon signal intermittently over its low threshold. Noisy periods on any detector can thus reduce the efficiency of the singles cut and therefore, at the same time, reduced the livetime for WIMP recoils. Implementing run-by-run values for the various phonon means and resolutions reduces the overall efficiency loss due to periods of high noise. All detectors, even those sub-optimal detectors excluded from consideration for WIMP candidates, are included for consideration in vetoing candidate events. The achieved efficiency for the singles cut is 99.4% [197].

5.4.6 Yield Bands

The charge yield is one of the main discrimination parameters used in CDMS with the ZIP detectors, and is defined as

$$y = \frac{Q}{E_r} \tag{5.4}$$

where Q is the ionization collected by the inner electrode and E_r is the recoil energy (the energy from the phonon signal E_p corrected for the Luke phonon contribution). Electron recoils have a yield of ~ 1 and nuclear recoils of ~ 0.3 . We construct the electron and nuclear recoil bands by using gaussian fits in the plane of yield versus recoil energy (defined using the inner electrode and corrected quantities as described in Section 5.2 and 5.3) for gamma and neutron calibration data obtained with ^{133}Ba and ^{252}Cf respectively. The center of each band corresponds to the mean of the gaussian for each energy bin (5-10, 10-20, 20-30, 30-40, 40-50, 50-60, 60-70, 70-80 and 80-120 keV). The means are then fitted using the following functional form:

$$y = aE_r^{b-1}, \tag{5.5}$$

and the 1σ points are fitted by a line

$$\sigma E_r = c(aE_r^{b-1}) + d, \quad (5.6)$$

where a , b , c and d are fit parameters. The electron and nuclear recoil bands end up separated by $>2\sigma$ at 5 keV and the gamma rejection efficiency, just using the yield, is $>99.98\%$ in the 5-100 keV interval [143]. The electron recoil band is fit on the odd-event-numbered Ba calibration data (half of the total Ba calibrations is used to set initial cut with the reminder used for background estimates), with an initial guess provided by a fit to the Cf calibration data between $0.6 < y < 1.4$ and 10-120 keV. The nuclear recoil band is fitted on Cf calibration data between $0.05 < y < 0.6$ and 10-120 keV, and added together above 60 keV. Figures 5.11 and 5.12 show band definitions for the electron and nuclear recoil band respectively for detector T1Z5 (ZIP 5 in Tower 1).

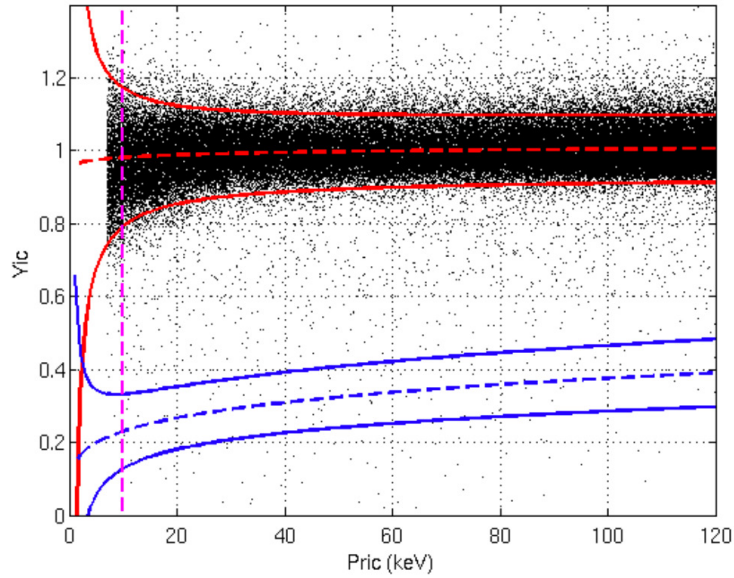


Figure 5.11: Yield as a function of recoil energy in detector T1Z5 (Ge) for events in a gamma calibration data set. The electron recoil band (or gamma band) is centered around ~ 1 (solid red) and the nuclear recoil band is shown as solid blue (see Figure 5.12) [198].

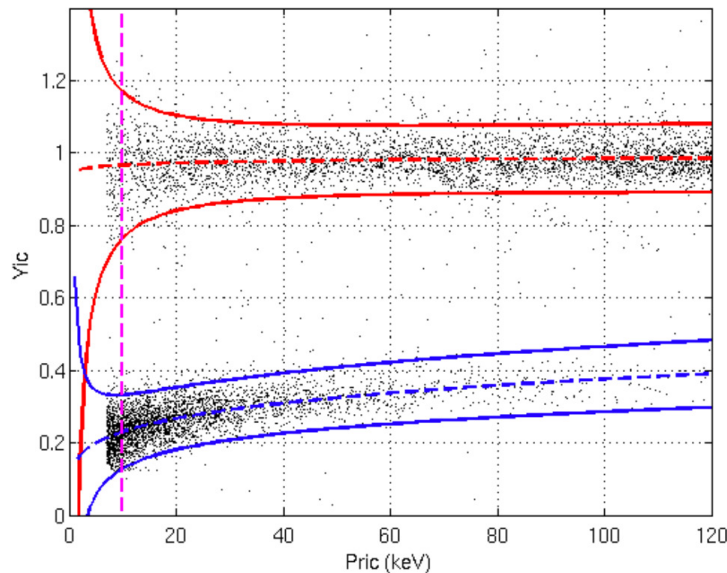


Figure 5.12: Yield as a function of recoil energy in detector T1Z5 (Ge). The nuclear recoil band is populated with nuclear recoils caused by neutrons from a ^{252}Cf source. There are also events in the electron recoil band that are caused by gammas emitted by the neutron source [198].

5.4.7 Veto Cut

The CDMS-II experiment at the Soudan Underground Laboratory is located beneath an overburden of 2090 meters of water equivalent (m.w.e.) that reduces the surface muon flux by a factor of 5×10^{-4} in order to reduce the number of cosmic-ray-induced nuclear recoils. Even though the experiment is situated half a mile underground, cosmic-ray muons interact directly with the shielding materials producing low-energy neutrons (few MeV in energy) that can produce a nuclear recoil in the ZIP detectors. Therefore, in order to reduce this type of events, the gamma and neutron passive shielding that surrounds the detectors is covered almost 100% by forty scintillator panels that comprise the muon veto system. Figure 5.13 shows a schematic drawing of the CDMS-II veto system.

Each panel consists of a 5-cm thick slab of Bicron BC-408 plastic connected to one or two 2-inch Hamamatsu R329-02 photomultiplier tubes. The veto panels are

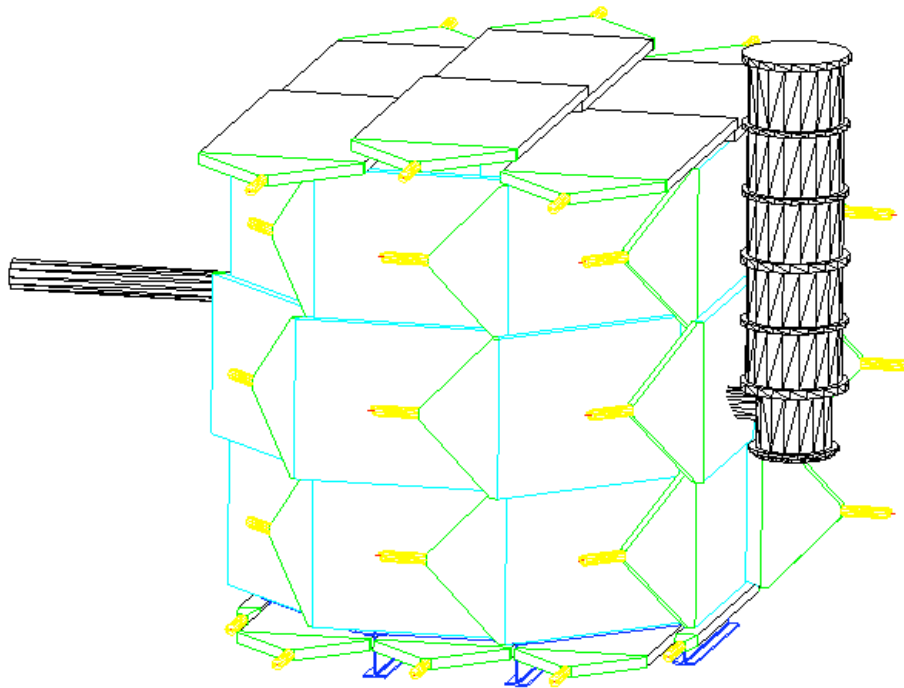


Figure 5.13: Schematic drawing of the CDMS-II veto system that consists of 40 plastic scintillator panels covering the passive shielding, icebox and towers holding the ZIP detectors. The cylindrical structure outside the veto system is the dilution refrigerator.

arranged so that adjacent panels overlap. The top panels extend well beyond the side panels, guaranteeing that the small gap between top and side panels does not allow a direct line of sight to the detectors inside the icebox. Given a 5-cm thickness for the plastic scintillator slabs that make the veto, it is easy to distinguish between muons and ambient photons since minimum ionizing muons typically deposit 10 MeV or more while the highest energy photon from radioactivity is about 2.6 MeV, as noted earlier. The muon detection efficiency for the entire veto system is estimated by counting the fraction of events with a muon tagged in the bottom panels that are also tagged by another veto side. In Run 119, the fraction of bottom-tagged events that had a muon in another side was $99.4 \pm 0.2\%$, directly giving the estimated efficiency for rejecting muons that stop in the shielding, while the product of the

two fractions yields the inefficiency for through-going muons. The efficiency for these through-going muons is estimated as $99.98 \pm 0.02\%$ [199]. On average, one muon per minute is incident on the veto, and the combined veto rate (dominated by the ambient photons) is ~ 600 Hz.

Events with detector signals are recorded regardless of whether or not there was cosmogenic energy deposition in the veto, but a subsequent analysis cut, the Run 123 and 124 veto cut, rejects events either with a veto trigger within 50 microseconds before the detector trigger, or with a reconstructed veto energy above a set threshold anywhere in the -180 to $+20$ microsecond window for which veto pulses are downloaded. The energy threshold used in the cut was set on a panel by panel basis, in order to maximize efficiency to detect muons without gaining deadtime with respect to the previous version of the cut, which had set the threshold for all panels at 50 pC. Figure 5.14 below shows for panel 4, one of the top panels, an energy deposition histogram, in units of pC, of 1 million events recorded in Run 123. The dashed green vertical line is the 50 pC mark where the threshold was previously set for an old version of this cut and the red dashed is where it is now set for Run 123 and 124 veto cut [200].

The efficiency of the veto cut for WIMP events is determined by considering the effective deadtime induced by each veto hit. There are random triggers taken throughout the run, i.e., events that are not triggered by the veto nor by the detectors but by a program that randomly selects $\sim 10\%$ of events compared to all events in a given run. By measuring the fraction of random triggers removed by the veto cut, we measure the accidental veto rate associated with this cut. The percent deadtime (efficiency) associated with the veto cut in data runs 123 and 124 are 2.4% (97.6% efficiency) and 3.4% (96.6% efficiency), respectively.

In Run 123 and 124, a total of 8 veto-coincident multiple-hit nuclear recoils have been found and no vetoed singles have been observed during these runs [181, 182]. In

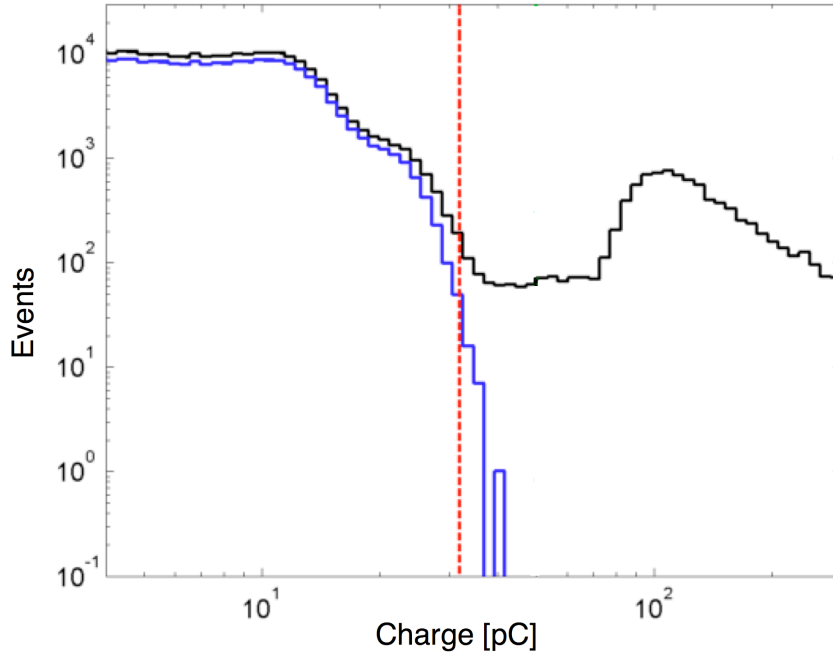


Figure 5.14: The charge deposited (black histogram) by cosmic rays and ambient photons in one of the scintillator panels that are part of the veto system. The events that peak at ~ 100 pC correspond mostly to muons passing through the 5 cm thick plastic scintillator. The vertical dashed line is where the veto cut was set for this panel [200].

Chapter 4 in Section 4.2.5 I discussed these events in detail and how they compare to the predictions made using Monte Carlo simulations.

5.4.8 Timing Cut

After all quality cuts, the yield cut and the veto cut, the events remaining in the 2σ nuclear recoil band are low energy betas and single scatter unvetoes neutrons. Before looking at the WIMP-search data (to remain blind) we set the cut that will filter out the beta events (or surface events) using the timing cut. Electron recoil events near the detector surface can have reduced ionization collection, leading to misidentification as neutrons or WIMP events if we only look at the ionization yield alone.

Phonon pulses from these surface recoils are faster than those from recoils in the detector bulk. Two timing quantities in the quadrant with the largest phonon signal or “local quadrant” are particularly good discrimination parameters: the time delay of the phonon signal relative to the fast ionization signal, and the phonon pulse risetime.

As discussed in Chapter 3 Section 3.4, two phonon timing parameters, the phonon delay time and the phonon risetime provide good rejection of surface-electron recoils while retaining reasonable acceptance of nuclear recoils. The delay and risetime phonon quantities are summed to form a timing parameter upon which selection cuts are applied.

To define the timing cut, we first combine the phonon delay and risetime to form this timing parameter. We require that candidates for WIMP-induced nuclear recoils exceed a minimum value for this timing parameter (see Figure 5.15). This minimum value is determined on a detector-by-detector basis by setting the allowed leakage (tuned to about half of an event). These cuts were set based on leakages from a subset of ^{133}Ba calibrations. The achieved discrimination is $>10^6$ with an average efficiency of $\sim 30\%$ when combined with the rest of the cuts previously discussed.

In Figure 5.16 the overall efficiency to nuclear recoils is shown when the Quality, Singles and Veto cuts are applied (about 90%), when the Fiducial volume cut is also applied (about 64%) and finally when the phonon timing cut is applied (about 30%).

The origin of the surface events is determined by the radioactive contamination of detector surfaces and also external gamma ray interactions that can release low-energy electrons from surfaces near the detectors. An analysis of the correlation between alpha-decay and surface-event rates shows that ^{210}Pb (a secondary product of the ^{222}Rn decay chain) is the major source of the surface event background [202]. The estimated surface event leakage was calculated using the observed number of single- and multiple-scatter events per detector and requiring them to be within the 2σ nuclear recoil band. The results are an overall expected background of 0.6 ± 0.5 events

due to surface events for the Run 123 and 124 WIMP-search runs (3.75 kg of Ge).

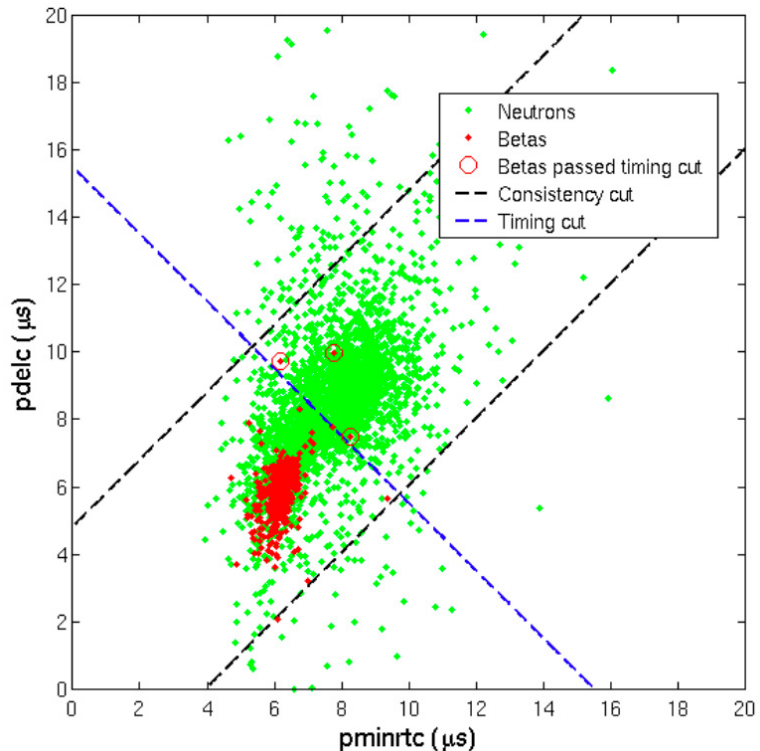


Figure 5.15: Delay vs. risetime parameter for a sample of neutron (green dots) and beta (red dots) events. The circled red dots are betas that pass the timing cut (dashed blue). Neutrons and WIMPs are selected by the blue dashed and the two perpendicular black dashed curves [201].

5.5 WIMP search results

Once all the analysis cuts are set, we unmasked the WIMP-search signal region. The actual unmasking or the “opening of the box” occurred on February 4, 2008. No events were observed in the box (signal region). A compilation of all the low-yield events in the detectors observed in the Run 123 and 124 is shown in Figure 5.17. Single scatter events passing all data selection cuts except the timing cut are shown on the upper plot of the figure. The lower plot of the figure shows four events that

passed the timing cut, but nevertheless remained outside the 2σ nuclear-recoil band.

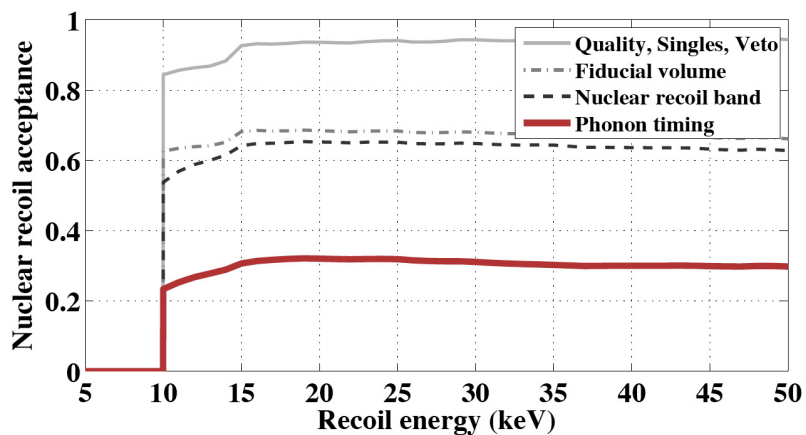


Figure 5.16: Efficiency (or acceptance) of several cuts as a function of recoil energy. Note that the main steps that reduce the efficiency (about $\sim 40\%$) are the fiducial volume cut and the phonon timing cut.

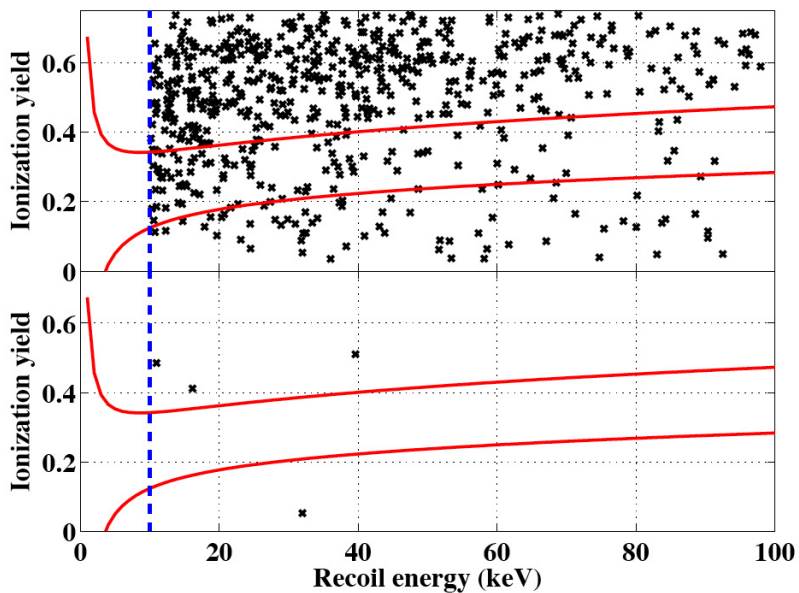


Figure 5.17: The ionization yield as a function of recoil energy for all the events in all detectors passing all cuts before (top) and after (bottom) applying the phonon timing cut. The four events that are shown on the bottom plot are able to pass the timing cut but lie outside the 2σ nuclear recoil band where neutrons and WIMPs are expected.

Based on the null observation of events, Figure 5.18 shows (upper solid curve) the 90% C.L. upper limit of the spin-independent WIMP-nucleon cross section for the first 5 tower run and based on standard assumptions about the galactic halo ¹, the limit is $6.6 \times 10^{-44} \text{cm}^2$. The standard assumptions of the galactic halo allow us to compare different direct detection experiments. Nevertheless, there is significant uncertainty on the density of WIMPs in our galaxy and it is currently an active subject of study.

Previously analyzed data taken at Soudan [203, 204] yield a modest improvement in sensitivity over previous CDMS results (upper curve in Figure 5.18). A combined limit using all the data taken at Soudan using Yellin's Optimal Interval method [205] results in an upper limit of $4.6 \times 10^{-44} \text{cm}^2$ at 90% C.L. for a $60 \text{ GeV}/c^2$ WIMP mass. This new limit corresponds to a factor of ~ 3 more sensitive than the previous CDMS-II limit and a factor of ~ 2 above $60 \text{ GeV}/c^2$ better than any other WIMP search to date. Furthermore, these data excludes some parameter space of SUSY models [208, 209].

¹The main standard assumptions about the galactic halo are the universal shape of the spherically averaged density following the NFW profile (presented in Chapter 1) and a density of $0.3 \text{ GeV}/c^2$ (which has a factor of ~ 2 uncertainty).

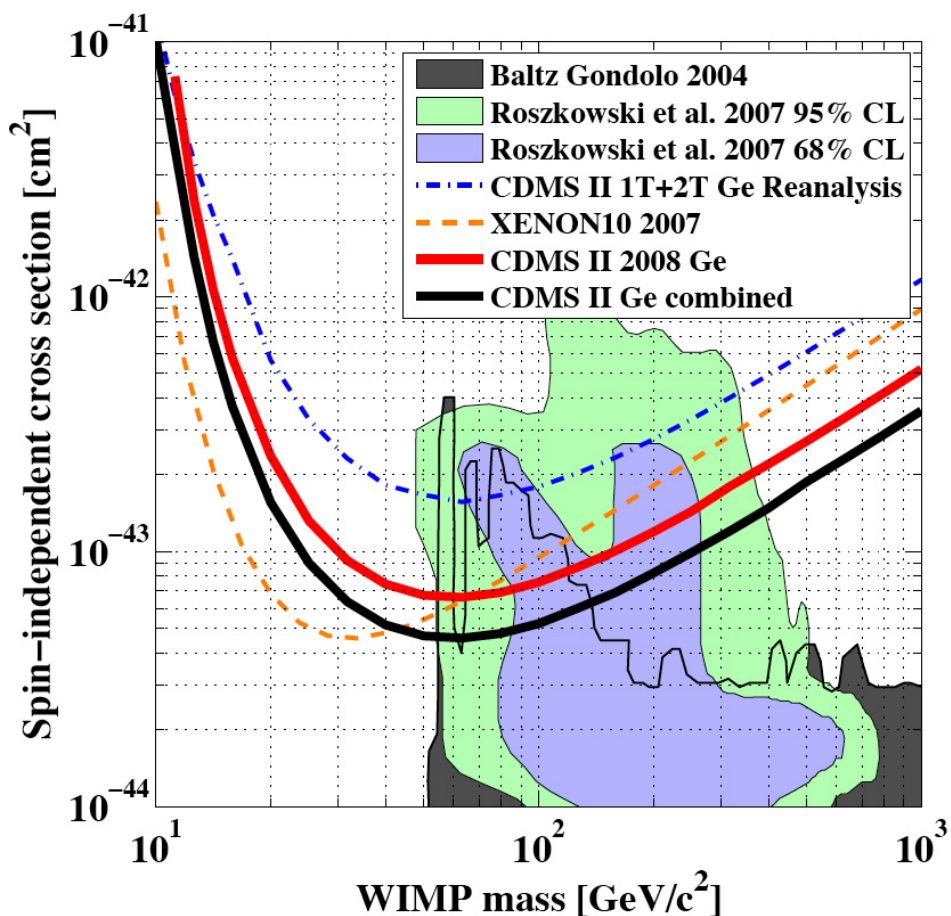


Figure 5.18: Spin-independent WIMP-nucleon cross-section upper limits at 90% C.L. as a function of WIMP mass. The blue dash-dot upper curve corresponds to the result of a re-analysis [142, 206] of our previously published data. The upper red solid line is the limit from the Run 123 and 124 data analysis. The combined CDMS limit (lower solid black line) has the same minimum cross-section as XENON10 [207] (orange dash) reports, but has more parameter space at higher masses. WIMP masses and cross section ranges expected from supersymmetric models described in [208] (grey) and [209] are shown (95% and 68% confidence levels in green and blue, respectively). Figure courtesy of [210].

Chapter 6

An Underground Cosmogenic Neutron Detector

6.1 Introduction

In Chapter 4, I discussed how the remaining component of cosmic rays deep underground (muons) and their secondaries can produce MeV neutrons that in turn lead to a nuclear recoil similar to those expected from WIMPs scattering of Ge and Si nuclei in the ZIP detectors. Furthermore, an estimation of these cosmogenic nuclear recoils was presented, based on a combined FLUKA and MCNPX simulation. In order to assign a systematic error to the estimate I discussed the relevant underground neutron data currently available upon which the Monte Carlo can be compared against, or benchmarked, in order to understand the accuracy of the estimation beyond the statistical power based on the number of events produced in the Monte Carlo. A factor of 3 systematic error has been assigned to the unvetoes rate, based on the shape of the spectrum of high-energy neutrons measured with the LVD experiment located at a depth of 3600 mwe. Motivated by the need to improve the existing benchmarks to the Monte Carlos and narrow the systematic error on the unvetoes

estimate, I will present a proposal for a new measurement that could yield as much as a factor of ~ 10 lower systematic error. The proposed measurement is based on an idea I conceived when studying active neutron veto schemes and ways to statistically predict the unvetted rate for CDMS-II at Soudan using a detector medium outside the gamma-ray (or high- Z) part of the CDMS-II shield. Professor Akerib proposed to study the possibility of a purpose build neutron detector based on the same detection principle. This work led to a successful DUSEL R&D project (also described in reference [211]) that we designed, and teamed up with Professor Harry N. Nelson from UCSB. In this Chapter I describe the purpose build cosmogenic neutron detector design studies and extend on the motivation. Furthermore, I describe how can the same detection principle be used as a complement in active neutron shield schemes that can also predict the number of unvetted events. Finally, I present recent ^{252}Cf neutron multiplicity data obtained using a small prototype detector and discuss the prospects for the final design to be deployed at the Soudan site.

6.2 Underground Neutron Data

WIMP searches must be performed underground to shield from cosmic rays, which produce secondary particles that could fake a WIMP signal. Nuclear recoils from fast neutrons in underground laboratories are one of the most challenging backgrounds to WIMP detection. Experiments that search for WIMP dark matter rely on passive and active shielding to reduce gamma and neutron backgrounds. To reduce the neutron background, passive hydrogen-rich shielding and active charged-particle detectors are commonly used to moderate neutrons and veto muon-induced events, respectively. To reduce the gamma background, high- Z materials such as lead are used to attenuate gammas from ambient radioactive sources. While the high- Z shielding is effective against gammas, the shield itself becomes a source of increased neutron background

due to secondary particles produced by unvetoes muon-induced neutrons that have energy above about 60 MeV. These neutrons have sufficient energy and low enough cross section on hydrogen that they penetrate the moderator and reach the gamma shield. They tend to interact there and cause spallation reactions, which produce multiple secondary neutrons with energy below 10 MeV. At these lower energies, the neutrons can reach the inner detector volume and cause WIMP-like nuclear recoils.

The high-energy neutrons and their parent reactions that originate with cosmic-ray muons are thus correlated with the unvetoes neutron events that mimic the WIMP signal. Neutron production by muons underground have been measured at a span of depths and muon energies, from about 20 meters of water equivalent (m.w.e.) depth and 10 GeV energy [212, 213, 214] to 5200 m.w.e. and 400 GeV [215]. An estimate of the neutron production as a function of muon energy for muons interacting in liquid scintillator has been obtained by Wang and co-workers [216] based on Monte Carlo simulations made with FLUKA [217] that is about a factor of two within the available data at that time for depths with a mean muon energy above 100 GeV. Since the interest is in neutrons with energy above ~ 60 MeV, this work is primarily sensitive to neutrons below this energy range as illustrated by Figure 5 in their paper [216]. Galbiati and Beacom [218] have calculated, using FLUKA [219], the production rates for ^{12}B in muon-induced showers and have probed the neutron production in the energy range of ~ 10 -100 MeV through the $^{12}\text{C}(n, p)^{12}\text{B}$ reaction and the calculation agrees well with measurements of ^{12}B at 2700 m.w.e. made by KamLAND [220].

At higher energies (>100 MeV) the shape of the neutron spectrum was compared to FLUKA [217] by Wang [216] and there is about a factor of two discrepancy with data taken with the liquid-scintillator LVD detector [221] at a depth of 3650 m.w.e and a mean muon energy of 270 GeV. Mei and Hime [222] claim that after making corrections for proton recoil quenching effects, the corrected LVD data agrees well with the shape of the spectrum predicted with FLUKA simulations. However, the

individual who performed the analysis of the data, V.A. Kudryavtsev has pointed out that this correction is inappropriate [223]. At present, there is no other data at this energy to inform the production of high energy neutrons, leaving the discrepancy unresolved. The LVD collaboration recently presented results on measuring neutron production above 20 MeV by muons in liquid scintillator [224], and a Monte Carlo simulation is under development by the collaboration to convert this measurement to an absolute flux.

Neutron production by 200 GeV muons occurs through hadronic showers generated by the muons interacting in the rock, and to some extent by direct muon spallation [216]. The CERN NA55 experiment measured neutron production via direct muon spallation by looking at the production of fast neutrons (>10 MeV) by 190 GeV muons on graphite, copper and lead [225] at three different angles from the muon beam. Araujo and co-workers [226] show that this experimental data lies above the Monte Carlo simulations from between a factor 3 to 10 depending on the measured angle. These measurements could overestimate the rate because of contamination by neutrons produced by secondaries of the muon-nucleus interaction. The possible systematic uncertainties leave the matter inconclusive, informing neither muon spallation production nor the total fast neutron yield above >10 MeV.

The measurements to date of neutrons at large depths involve either primary muon interactions in hydrocarbon liquid scintillator followed by cascade processes within the detector [221, 227], or muon interactions in higher- Z material such as Pb and Cu [228] in which neutron production is dominated by relatively low-energy electromagnetic properties. Of particular interest for dark matter experiments, as noted above, is when high-energy neutrons produced in the rock through muon interactions and hadronic cascades, followed by spallation in high- Z shielding, lead to a flux of neutrons of mostly 10 MeV and below. In the work described here our simulations and calculations indicate that a modest size detector, by exploiting the multiplicity distribution of the

spallation events, can provide a normalization of the neutron flux to a precision of about 12%. By measuring the high energy neutron flux at 2000 m.w.e. this will benchmark the neutron production by muon induced hadronic showers and provide a normalization of the unvetoes neutron background. I have chosen this depth because the muon-induced neutron production is dominated by hadronic processes according to Wang and co-workers [216] based on Monte Carlo simulations made with the particle production and transport code FLUKA [217] and because the rate is good enough for a modest detector size (see section 6.3) to be able to measure a rate of 70 ± 8 events/year for neutrons >60 MeV.

In addition to the interest for the shielding configurations for many dark matter experiments, improved knowledge and predictability of the muon-induced high energy neutron flux (>60 MeV) at depth will aid in the understanding of neutron induced backgrounds in double beta decay experiments. For example, as noted by Mei and Hime [222], knowledge of the neutron background is needed to estimate the background due to elastic and inelastic events that generate gamma rays near the 2 MeV endpoint, and to optimize shielding configurations that also typically involve massive lead and polyethylene shields to attenuate gammas and moderate neutrons. Thus for two major classes of low-background underground experiments, dark matter and double beta decay, a more precise measurement of the neutron background produced in the appropriate shield components will be of great utility, from the experiment planning stage through to data analysis.

6.3 Principle of the Instrument

The instrument I have designed is based on applying the Gd-loaded liquid-scintillator technique to measure the rate of events with multiple low energy neutrons produced in a Pb target. Our studies, which are presented in Section 6.4, indicate that at a

depth of 2000 m.w.e., the dominant source of these events is due to muon-induced high energy neutrons interacting in the Pb. Gadolinium has a high thermal-neutron capture cross section, and emits 8 MeV in gamma rays after the capture. Since neutrons thermalize and capture with a mean of about $10 \mu\text{s}$, measurements of the distinct capture times is a straightforward way to determine neutron multiplicity, and to tag and measure the underlying process of the fast-neutron production. This method, known as a Neutron Multiplicity Meter, has a long history of use, dating to searches for superheavy elements expected to decay to high-neutron-multiplicity final states [229], and more recently in accelerator-based applications [230].

The basic design of the Neutron Multiplicity Meter applied to measure high energy neutrons ($>60 \text{ MeV}$) underground employs the Gd-loaded liquid-scintillator detector ($\sim 0.5\%$ Gd content) atop a 200-cm-square by 60-cm-thick Pb target in which high energy neutrons produced by muon interactions in the rock walls of the cavern will mainly enter from above, penetrate the scintillator, and cause neutron spallation in the Pb, as illustrated in Fig. 6.1. The secondary low energy neutrons produced by the primary high energy neutron leave the Pb target and enter the Gd-loaded scintillator, where they are moderated and thermalized by the protons in the hydrocarbon which comprises the bulk of the scintillator. Within about $40 \mu\text{s}$, most will have captured on the gadolinium, and thus the essential problem of detecting neutral particles with high efficiency has been turned to an advantage: the neutrons which are released simultaneously are dispersed in time, and individually captured and counted. As the simulations below illustrate, this unique signature allows both for efficient tagging of neutron multiplicity events as well as rejection of random gamma backgrounds so effectively that typical low-background techniques are not required.

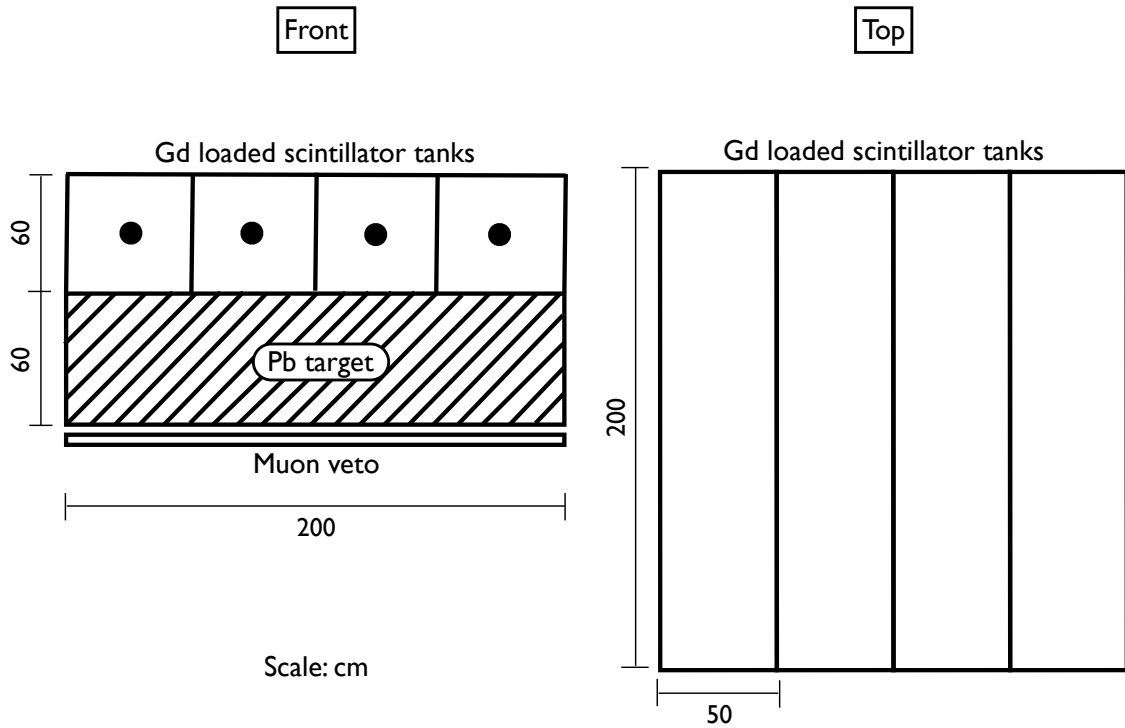


Figure 6.1: Conceptual drawing of the Neutron Multiplicity Meter for Deep Underground Muon-Induced High Energy Neutron Measurements.

6.4 Instrument Design Studies

In this section the design characteristics of the Neutron Multiplicity Meter adapted to measure high-energy neutron flux underground are developed. Extensive simulation studies of the muon-induced neutron background in the Soudan Mine at a depth of 2000 m.w.e. corresponding to 14 years of exposure have been performed using FLUKA simulation package [164, 165]. These studies, carried out for background estimates in the CDMS II experiment, are based on an angular distribution of muons matched to this depth, and normalized to the measured flux in the CDMS II plastic-scintillator veto system [203]. In the study, the muons are propagated into a rock-

wall cavern modeled as a 6-sided 10-m-thick rock shell surrounding a 4 m by 8 m by 4 m cavity. The CDMSII experimental setup is inside the cavity and near one of the walls. High energy neutron production due to muons occurs through direct muon spallation and subsequent hadronic showers that develop in the rock. The angular distribution of neutrons above 60 MeV, as depicted by the distribution in Figure 6.2, shows that the neutrons are mostly going downward at angles greater than about 0.88π radians, where π radians corresponds to the direction vertically downward. Given the predominantly downward direction, the rate of incident high-energy neutrons is proportional to the area of the Pb target, which defines the first criterion for the setup.

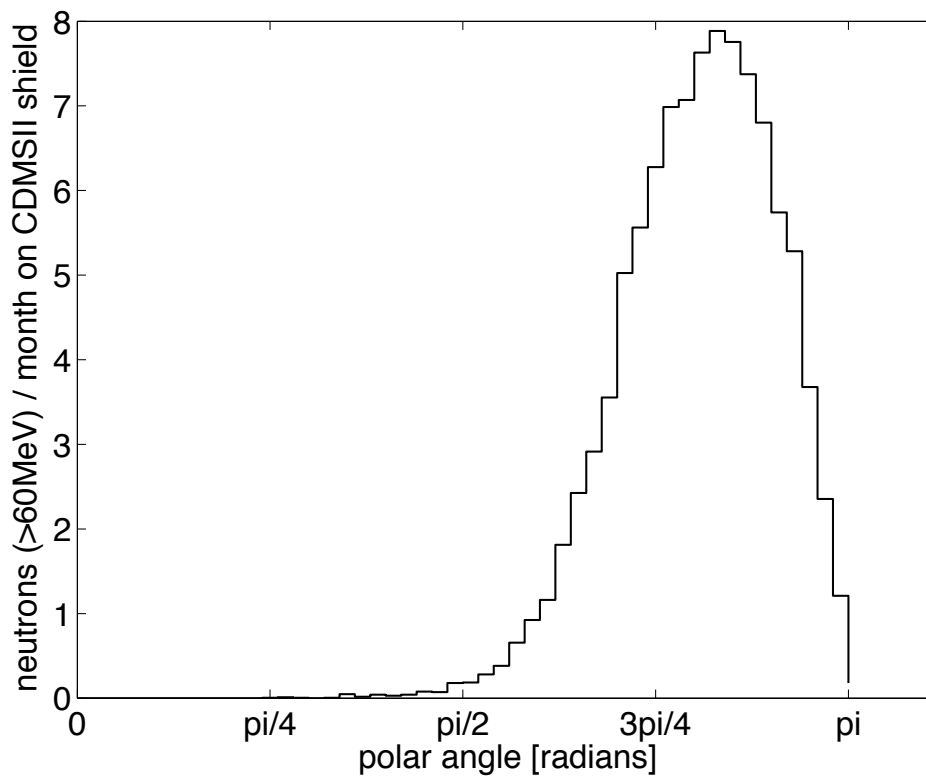


Figure 6.2: Polar angular distribution of the neutrons with energy greater than 60 MeV incident on the CDMSII shield. Neutrons tend to have downward direction at an angle of about 0.88π radians with respect to the normal vector from the floor. Therefore the area of the target is proportional to the rate of incident high energy neutrons.

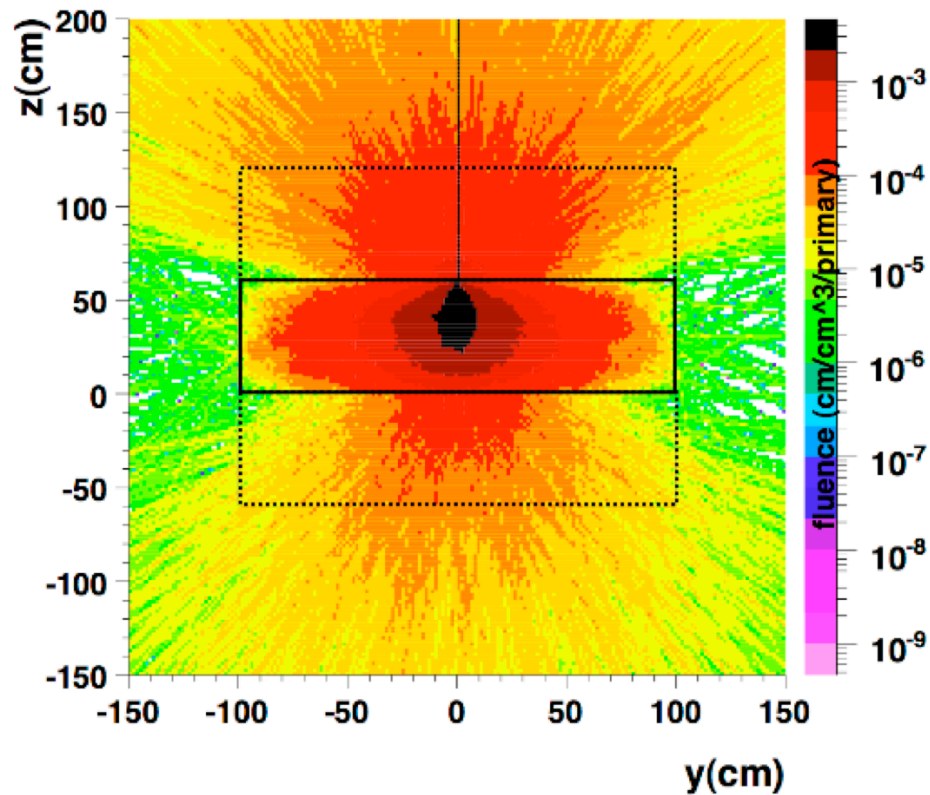


Figure 6.3: Neutron fluence plot of a FLUKA simulation that propagates a beam of 100 MeV neutrons on a 60-cm-thick Pb target. The upper and lower rectangles are reference surfaces delimiting the counting boundary for the upper and lower neutrons, respectively. The central rectangle from $z=0$ to 60 is the Pb target. The plot shows more evaporated neutrons going upwards than downwards (the forward direction relative to the beam) due to backscattering. This effect also causes very few neutrons to go forward as the thickness increases above about 20 cm.

The next criteria I consider for the Pb target are the optimal thickness and whether it is best placed above or below the scintillator tank. A simulation with FLUKA was performed by propagating a beam of 100-MeV neutrons at a 200 cm by 200 cm Pb target with thickness varying from 1 to 100 cm. I gauge the detectability of a subsequent multiplicity event by counting the number of secondary neutrons that emerge from the Pb with less than 10 MeV and are thus readily moderated and captured. I define the parameter P for both the top and bottom surfaces as the

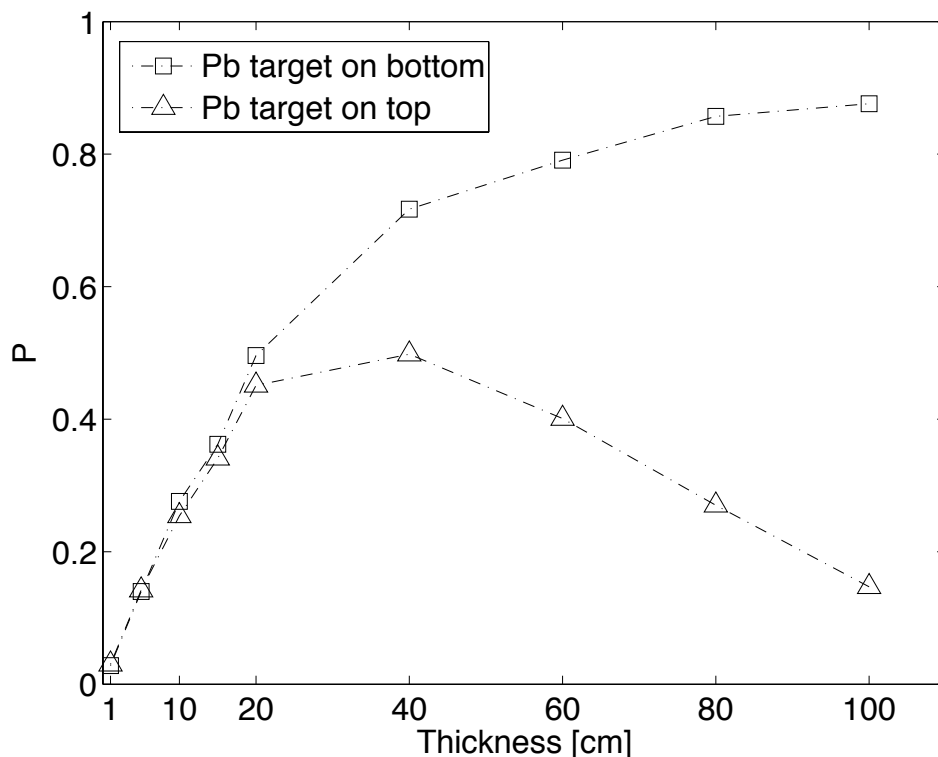


Figure 6.4: Simulation with FLUKA to explore optimal target thickness and position of the Gd-loaded scintillator tank with respect to the Pb target. The parameter P is defined as the fraction of events (relative to the number of 100-MeV incident neutrons) that has 3 or more neutrons of 10 MeV or less going towards the top or the bottom of the Pb target. (See text for details.) Since a given event may have 3 or more neutrons going to the top and 3 or more going to the bottom, it is possible to have $P_{\text{TOP}} + P_{\text{BOTTOM}} > 1$, for example as observed for 40-, 60- and 80-cm thickness.

fraction of events for which a downward-direction 100-MeV neutron results in at least 3 low-energy neutrons exiting either the side from which the neutron beam was incident (top) or the opposite side (bottom). The overall production point and neutron travel direction is illustrated in Figure 6.3, which shows the neutron fluence (neutron track length per unit volume) in units of cm per cm^3 per primary neutron, based on a FLUKA simulation for a 60-cm-thick target. Quantitative results for P are shown in Figure 6.4, where the “Pb target on bottom” means P is calculated for downward incident neutrons with upward-going secondaries to be detected in

a top-side scintillator detector, and “Pb target on top” means P is calculated for downward secondaries to be detected bottom-side.

I observe that the emission of neutrons is roughly isotropic as expected, and that the spallation reaction occurs within the first 15 cm of Pb. Furthermore, as the thickness of the target increases beyond 20 cm, more of the secondaries are going upwards than downwards. This effect is due to backscattering from the Pb, which acts roughly like a “neutron mirror” for low energy neutrons, since the elastic collisions off the Pb nuclei do little to reduce the energy of the comparatively light neutrons. Most important for the overall configuration, I observed that since the primary interaction rate is still increasing with thickness, the backscatter effect indicates that the multiplicity rate is higher on the top side, and higher for increasing thickness. To maximize the detected multiplicity rate, it is better to place the scintillator atop the Pb, which also has the advantage of tagging muons that strike the Pb directly.

So far, the detector configuration is to have the Gd-loaded scintillator on top of the Pb target. Since neutrons with an energy less than about 60 MeV will scatter off the protons in the scintillator, they will tend to either fail to reach the Pb or reach it with insufficient energy to produce a multiplicity of 3 or more. In other words, the scintillator will filter low energy neutrons and together with the requirement that the event has a multiplicity threshold of 3 or more secondary neutrons this will select only those primary neutrons with an incident energy of 60 MeV or more. To illustrate that high energy neutrons (>60 MeV) induce a multiplicity of 3 or more low energy neutrons on a Pb target, Figure 6.5 shows the induced detectable multiplicity, for a geometry of the Pb to have an area of 200 cm by 200 cm normal to the vertical, a thickness of 100 cm, and an incident downward-going neutron beam in FLUKA at energies of 60, 100, and 200 MeV. The detectable multiplicity was estimated by counting the number of neutrons below 10 MeV that enter a top-side detector with the same footprint as the Pb. The resulting multiplicity distributions for the three

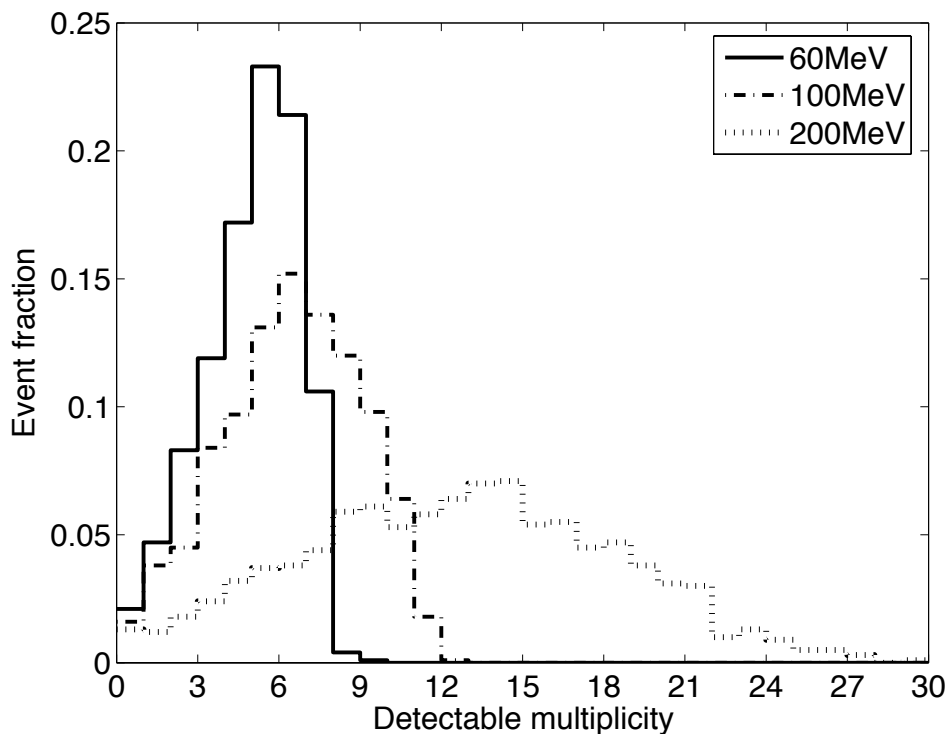


Figure 6.5: A FLUKA simulation was done with a fixed target thickness of 100-cm and varying the incident neutron beam energy in order to explore the correlations between the energy of the incident high-energy neutron on the target and the detectable multiplicity. If I reference the beam direction a “downward,” the detectable multiplicity is determined by counting the neutrons that reach a surface just above the Pb target.

energies are shown in Figure 6.5, where “Event Fraction” corresponds to the fraction of events with respect to the total number of incident neutrons. The plot shows that the majority of the events have a detectable multiplicity of 3 or more, and that there is an increase in multiplicity with primary neutron energy and although some information on the primary neutron energy is potentially available from the multiplicity distributions; at least an energy threshold on the primary neutron energy can be established using multiplicity, which has a fairly sharp turn on at 60 MeV for a multiplicity threshold of 3.

It is important to estimate the efficiency of the selection criteria for tagging high-energy neutron events as a function of multiplicity so that an optimization can be

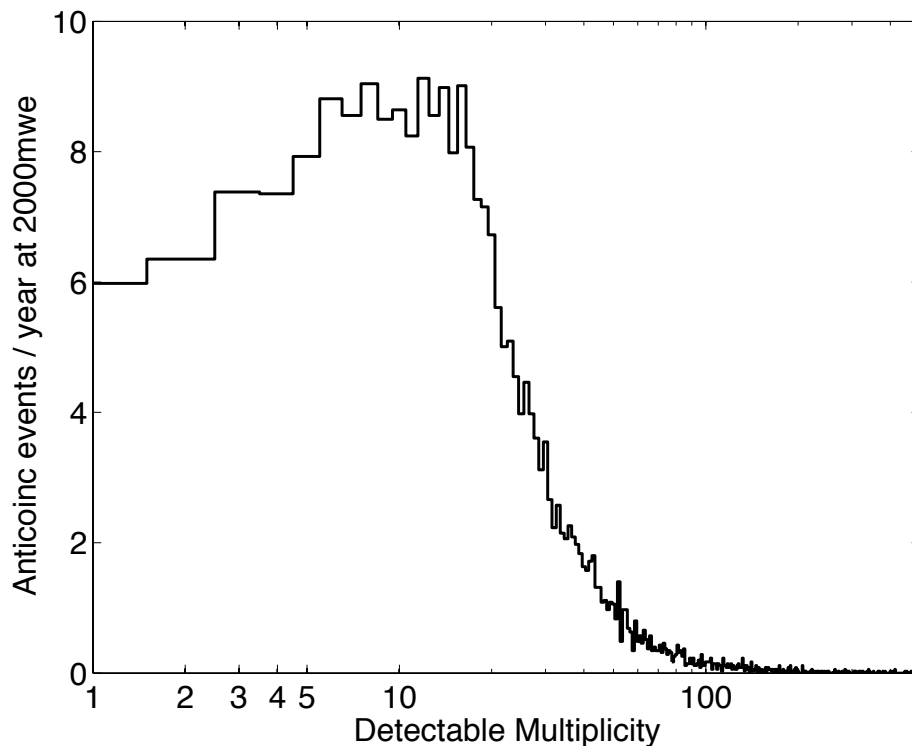


Figure 6.6: The detectable multiplicity from a Pb slab of 200 cm by 200 cm area and 60 cm thickness for the events estimated to be anticoincident with an energy deposition of 2 MeV or more from charged particles, including muons and hadrons. The detectable multiplicity was counted only by looking at neutrons with energy less than 10 MeV going towards a surface on top of the Pb target.

made to reject random coincidences and still achieve good efficiency for neutron-induced events. I identify a class of “clean” multiplicity events, that is, those that are clearly produced by high energy neutrons interacting in the target as opposed to other charged particles or gamma rays that may also have been produced by the parent muon. To estimate the rate of these events as a function of multiplicity I use the events with neutron energy above 60 MeV from our 14-year Soudan simulation in which associated gamma rays, muons, or hadrons deposit less than 2 MeV in the scintillator. The multiplicity is counted by considering only those secondaries with energy less than 10 MeV entering a top-side detector, and is plotted in Figure 6.6. To

see the effect of tightening the multiplicity cut to reduce the probability of random coincidences, the integral number of multiplicity-tagged events per year is plotted versus the minimum required multiplicity, and is displayed in Fig. 6.7. The total number of events changes only by about 10% between a minimum multiplicity of 3 and 10.

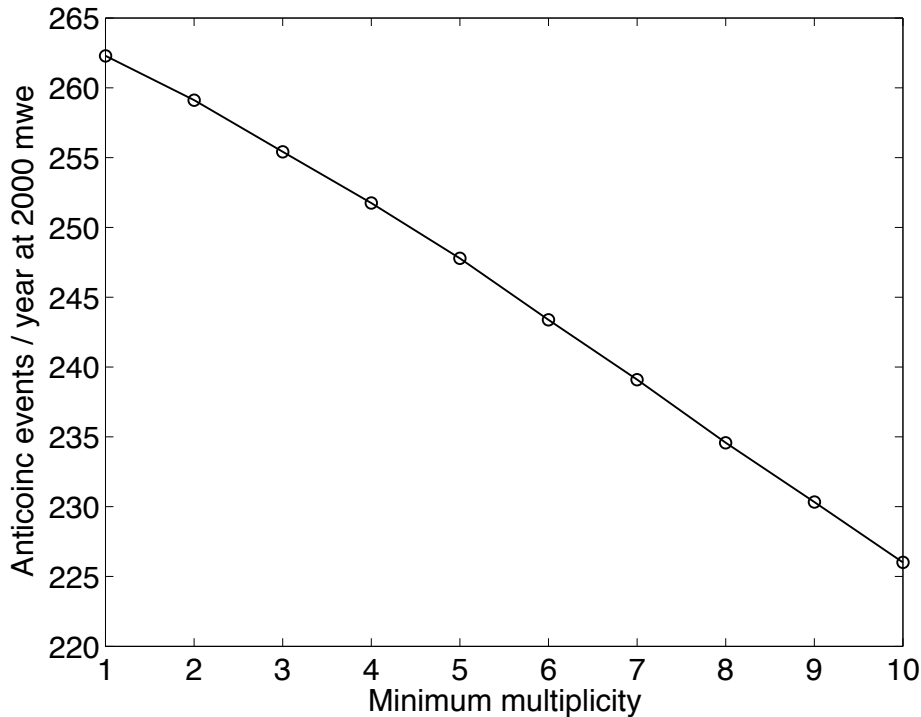


Figure 6.7: The total number of events as a function of minimum multiplicity. The total number of events changes only by about 10% between a minimum multiplicity of 3 and 10.

In determining the optimal thickness of the scintillator modules, we consider two requirements: the moderation of the secondary neutrons, and the absorption of the Gd capture gammas. The FLUKA simulation predicts that the spectrum of neutrons emerging from the Pb falls off almost completely by 5 MeV, as shown in Figure 6.8. A scintillator region of 10 cm thickness would be sufficient to moderate them. However, I found that containing the capture gammas requires a thicker detector. In order to find the optimal thickness, I used the low-energy simulation code, MCNP-PoliMi [183],

which includes the neutron-capture process. A beam of 0.5-MeV neutrons was propagated from the Pb up to a top-side scintillator tank, and the thickness of the tank was varied. In Fig. 6.9 the efficiency to detect the gamma cascade with a 3-MeV threshold is shown as a function of scintillator thickness. To allow for resolution effects, I have chosen 3 MeV as the nominal lower analysis threshold to gain immunity from gammas from natural radioactivity, the highest of which comes from ^{208}Tl with an energy of 2.6 MeV. I have found that the detection efficiency increases with thickness because of improved containment of the gamma cascade. The efficiency to detect 3 MeV energy depositions from gamma-rays in the Gd-loaded scintillator tanks is considered to be 100%, as this can be easily achieved with a 5" PMT for the configuration shown in Fig. 6.1.

To assess the rate of background coincidences that can mimic the signal, I have considered not just the energy criteria of nominally 3–8 MeV for individual captures, but also the time distribution of the captures. The time profile for the moderation, thermalization, diffusion and capture of multiple neutrons released simultaneously into the scintillator is broad, with a peak at about $10\ \mu\text{s}$ after emission and about 90% of captures occurring within the first $30\ \mu\text{s}$. It is the diffusion of the neutron what dominates the time between moderation and capture. A neutron burst results in a cleanly-separated readily-counted pulse train since the pulse widths of about 10 ns are narrow compared to the typical time between captures of order $1\ \mu\text{s}$.

Ambient gamma rays, which dominate the rate of random events in the detector, can mimic a high energy neutron event due to accidental coincidences within the time and energy window defined for multiplicity events. The rate of gamma-induced background as a function of the multiplicity criterion is shown in Fig. 6.10 for a time window of $40\ \mu\text{s}$ and three different gamma rates. The gamma rate at Soudan expected in the Gd liquid scintillator volume is about 600 Hz, based on gamma rates measured with the CDMSII plastic scintillator panels for a 1 MeV threshold [231].

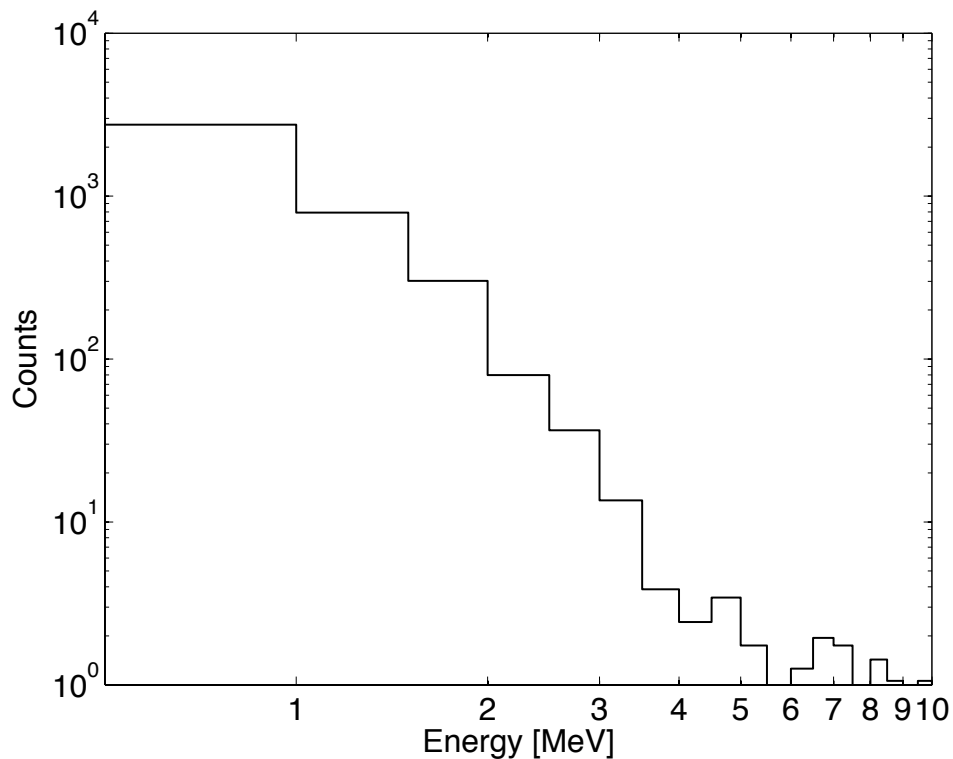


Figure 6.8: Energy spectrum of secondary neutrons produced by high-energy neutrons (flux shown in Fig. 6.2) incident on the Pb target. Neutrons mostly have energy below 5 MeV energy, and indicates that the thickness of the scintillator is not driven by the moderation requirements. Rather, I found that the thickness is driven by the need to efficiently contain the gammas emitted by the Gd.

A reduction of an order of magnitude in rate can be achieved with a threshold of 3 MeV, which will render the rate of accidental 3-fold multiplicity events to 10^{-2} per day, or about one order of magnitude below the multiplicity rate predicted from high-energy neutrons interacting in the Pb. Further reduction of the gamma ray rate can be achieved, if necessary, with a thin layer of Pb surrounding the scintillator. Alternatively, immunity from random coincidences can be gained by increasing the multiplicity criterion.

I have also considered the background due to neutrons from radioactivity, which are dominated by alpha-n reactions in the rock originating from alpha decays in the

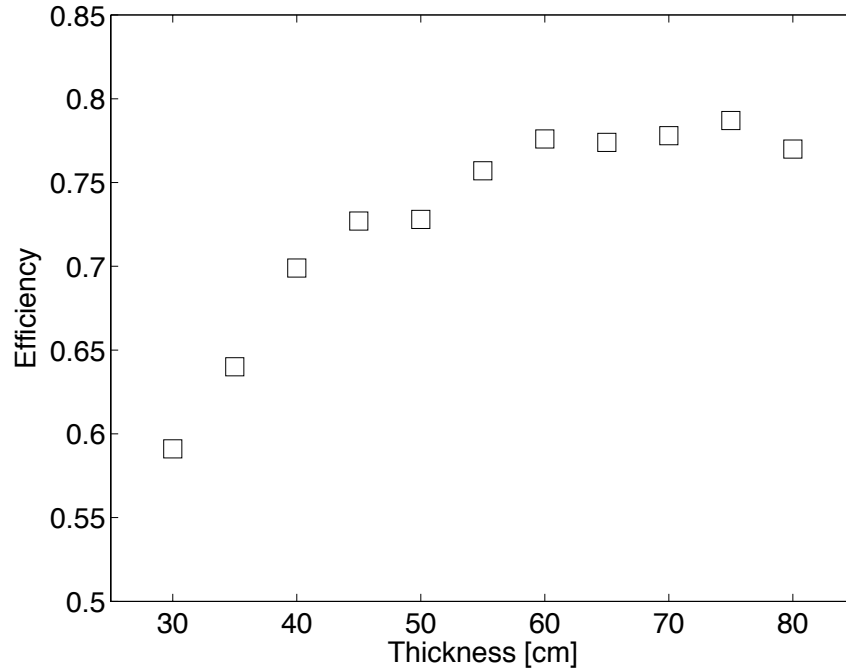


Figure 6.9: Simulation with MCNP-PoliMi [183] of the Pb target with Gd-loaded scintillator contained in tanks placed on top of the target. A beam of neutrons with energy 0.5 MeV was propagated from the Pb to the scintillator tank. The thickness of the scintillator tank was varied. Efficiency corresponds to the fraction of incident neutrons for which the energy deposited in the Gd-loaded scintillator by gamma rays is above 3 MeV.

uranium and thorium decay chains. The ambient rate of neutrons from radioactivity at Soudan is estimated from the measurements of the U/Th contamination in the Soudan rock [173] and cross referenced with measurements of both the U/Th level and neutron flux at the Kamioka mine [232]. The resulting flux estimate of about 2×10^{-5} neutrons/cm²/sec produces a rate of about 3 neutrons/sec in a detector with a scintillator volume of $200 \times 200 \times 60$ cm³, and is a negligible source of multiplicity events.

Spontaneous fission from the ²³⁸U in the rock could in principle produce events with multiplicity of 3 or more, although the most frequent multiplicity is 2. However, the relative rate of fissions to gammas from ²³⁸U in secular equilibrium is down by 6

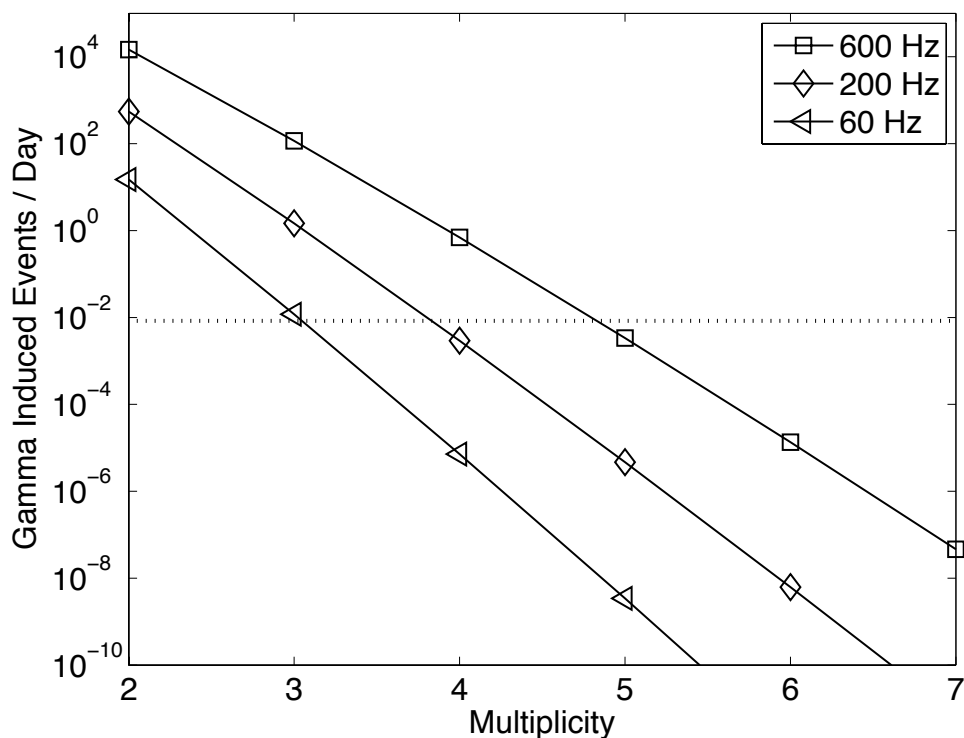


Figure 6.10: Ambient gammas can mimic a high energy neutron event due to accidental coincidences. The rate of gamma-induced background events is plotted as a function of the multiplicity of the events for a time window of 40 microseconds and three different gamma rates [229].

orders of magnitude. If the entire rate of ambient gammas is attributed to ^{238}U , the expected rate of multiplicity events from fission would still be negligible. However, if needed, a layer of 10–20 cm of polyethylene can easily shield them.

Events in which the muon itself passes through the scintillator are also considered. Most minimum ionizing muons will have sufficient pathlength of about 5 cm in the scintillator to be readily distinguished from Gd capture, allowing us to study muon-tagged events. For example, some of these muons will interact directly in the Pb, and produce a detectable population of neutron multiplicity events. While these events are of interest, they are dominated by low energy electromagnetic processes [227] and so are not as useful a cross check on the unvetted population, which is dominated by

higher-energy hadronic processes.

These tagged muon events will be identified by requiring more than 9 MeV in the scintillator, that is, above the maximum that can be caused by a neutron capture. However, this criterion will also include some events with no muon in the scintillator but which have instead a high-energy neutron that deposits more than 9 MeV by scattering in the scintillator. Based on a FLUKA simulation, the fraction of high-energy neutrons impinging on the apparatus that are in this category is about 35%, and will not be counted in the muon-free category of multiplicity events (which corresponds to the main population of interest, i.e., high energy neutrons produced by muons in the rock). The remaining 65% of incoming neutrons will deposit less than 9 MeV of prompt energy from the initial scatter followed by spallation of the Pb. When the prompt energy in these neutron-scatter-plus-multiplicity events is 3–8 MeV, it will be indistinguishable from events without a neutron scatter but one unit higher multiplicity. For example, a multiplicity-three event with 7 MeV of prompt energy will, to first approximation, appear the same as a multiplicity-four event with prompt energy below the 3-MeV threshold. Since both of these events are due to a high energy neutron, the inferred rate of high energy neutrons will not be biased.

Finally, muons that deposit less than 8–9 MeV in the scintillator (or none at all) but interact in the Pb and cause multiplicity events, represent a potential background to the multiplicity events due to high-energy neutrons. Of the estimated 350 muons/day that will pass through the Pb, there could be a few per day that cause such an event. However, these could be vetoed with a simple set of veto counters placed below the lead, and used in anticoincidence.

In summary, our design studies show that an apparatus consisting of a Pb target of 200 cm by 200 cm area by 60 cm thickness covered by a 60-cm-thick scintillation detector with Gd-capture detection efficiency of $\varepsilon_s(T)$, where T is the low energy threshold for each distinct capture, and assuming an efficiency to detect 3 MeV gamma-rays in

the Gd-scintillator tanks close to 100%, will yield a rate for M -fold multiplicity-tagged events of

$$R = N (1 - 0.35) (\varepsilon_s(T))^M \text{ events/year,}$$

where N is the number of high-energy neutrons that induce an event with M or more detectable neutrons emerging from the Pb and entering the scintillator, and the factor of $(1 - 0.35)$ is due to neutron interactions in the scintillator that exceed the high energy threshold. Our FLUKA and MCNP-PoliMi simulations indicate that $M=3$ gives $N=255$ and $T=3$ MeV gives $\varepsilon_s(T)=0.75$, and therefore $R = 70 \pm 8$ events/year. Depending on the actual gamma rate and spectrum, some optimization is possible for increasing R but protecting against random multiplicity events, for example, by increasing the multiplicity requirement and lowering the energy threshold. Generally speaking, our method is capable of measuring the rate of high-energy neutrons to about 12% statistical error in the span of a year at a depth of 2000 m.w.e. The expected number of background events, which is dominated by the rate of random gamma-induced coincidences, is expected to be at most 10 events/year, and could be further suppressed by optimizing the multiplicity and energy thresholds.

6.5 Statistical Predictors of the Neutron Leakage

In this section I present an application of a neutron multiplicity meter detector to a running dark matter experiment that serves as both an active shield and a monitor of the presence or rate of background events due to high energy neutrons. The idea exploits the same technique as a purpose-built instrument for background studies as described above. It's principal virtue in a WIMP search experiment is that it can closely monitor when a neutron background would appear in the data. A Gd-loaded liquid scintillator detector integrated into the shield would detect, using the multiplicity technique, the same population of events that cause a flux of low energy neutrons

inside the shielded WIMP detector volume, namely, neutron multiplicity events produced in a Pb gamma shield by an otherwise undetected high energy neutron. Since the underlying processes are the same, Monte Carlo simulations would give a very reliable measure of the ratio of the rate of multiplicity events in the external detector to the rate of WIMP-like events in the dark matter detectors due to the same neutron population.

Similar techniques to detect the presence of background sources have been successfully used, for example in the CDMS-I [233] and CDMS-II [204] experiments where multiple simultaneous nuclear-recoil events were used to determine the rate of single scatter nuclear recoils due to the same neutron background flux. The ratio of multiple nuclear recoil events to single nuclear recoils has the advantage of having a negligible source of systematic uncertainty since the neutron elastic cross sections on Ge and Si are very well known. Nevertheless, the rate of multiple nuclear recoil events is lower than the rate of single nuclear recoil events, and the uncertainty in the singles rate is dominated by the fluctuations of the multiples when only a small number has been observed.

In other words, tagged events that are correlated with the production of a single nuclear recoil due to a neutron can be used to statistically predict the absolute number of these nuclear recoils. If I call these tagged events “background predictors” then the number of unvetoed singles can be estimated by determining the ratio of single nuclear recoils to the background predictor events with a Monte Carlo simulation, and then counting the number of background-predictor events in the experiment. Narrowing the statistical and systematic uncertainty of this ratio improves the ability to monitor and subtract the neutron background. Dark matter experiments that have a Pb layer or any high- Z material as their gamma shield could use an external multiplicity meter to predict, in a statistical way, the number of unvetoed nuclear recoils due to neutrons. The background predictor events with high multiplicity are detected in the

multiplicity meter outside the high- Z material. A virtue of this configuration is that the gamma background due to contaminants in the scintillator and Gd are shielded by the high- Z material.

As a further illustration based on Fig. 6.4 for 100 MeV incident neutrons and a typical 15-20 cm thick gamma shield made of Pb, the fraction of high energy neutron events that produce multiple low energy neutrons going inside a Pb box will be roughly the same as outside. For example, the use of 60-80 cm of Gd-loaded liquid scintillator outside the gamma shield layer allows the moderation of low energy neutrons originating from the radioactivity in the rock and at the same time functions as a neutron multiplicity counter that would allow the prediction of the number of neutron-induced events in the signal region. Note that the multiplicity threshold in this case should be set high enough so that gamma induced multiplicity events are kept at a negligible level, since the Pb layer would be about 20 cm thick.

The effect plotted in Fig. 6.4 shows that the low energy neutrons produced from the neutron spallation reaction can be detected by clean low energy neutron detectors inside the gamma-ray shield (for example with plastic scintillator) but I have also found that outside of the gamma-ray shield, a 60-80 cm of Gd-loaded liquid scintillator with a threshold of a few MeV, would work as an active veto complementing the veto inside the gamma shield (or as a standalone veto depending on rejection requirements) and as a monitor of the muon-induced neutron background. Note that the thickness of the scintillator outside the gamma-shield is driven by trying to contain the gamma rays produced in the capture of a neutron by the Gd in order to have a high threshold to defeat ambient gammas from radioactivity, and also to keep moderating with high efficiency the neutrons produced from the radioactivity in the rock.

6.6 A new background predictor for CDMS at Soudan

In this section it will be described how does the use of a neutron multiplicity meter can be used in CDMS as both a neutron veto and as detector of the background predictor events that can be used to estimate the rate of unvetoes cosmogenically induced nuclear recoils. The multiplicity meter would be outside the Pb and it will consist of a detector of low energy neutrons with high efficiency such as Gd-loaded liquid scintillator or water.

In order to investigate the rates to be expected of background predictor events before a nuclear recoil is expected in the CDMS-II shield a simple simulation was made in which a beam of 100 MeV neutrons was shot into the Pb and inner polyethylene parts of the CDMS-II shield. Assuming the veto-anticoincident Ge-singles are originated by high energy neutrons, hence if some fraction of this events are tagged unambiguously, they could be used as the background predictor. The following results show that indeed the multiplicity events have a higher rate compared to the Ge-singles. Furthermore the systematic uncertainties such as the production rate of high-energy neutrons together with the multiplicity of the low energy neutrons generated at the spallation reaction, will cancel in the ratio of Multiplicity events to Ge-singles.

A FLUKA simulation was performed in which 1000 neutrons with an energy of 100 MeV were thrown vertically and downwards into the lead, inner polyethylene and copper layers of the CDMS-II shield (see figure 6.11). For each event, I looked if there was a neutron in the 100 keV to 10 MeV range going inside the innermost copper can. Furthermore, events where there were neutrons with less than 10 MeV going from the lead upwards “backsplash”.

The inelastic collision of the 100 MeV neutrons in the Pb shield produces neutrons with an energy less than 10 MeV that are:

1. back-splashed and do not reach the inside of the Cu cylinder and therefore

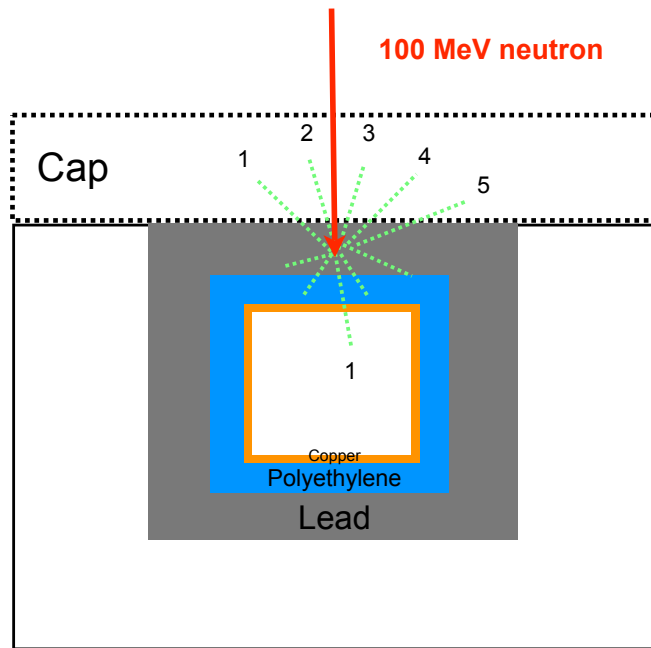


Figure 6.11: The CDMS gamma-ray shield, inner polyethylene and a copper cylinder inside of it with a thickness similar to that of the fridge copper cans. In red, a high-energy neutron with an energy of 100 MeV is depicted. The green dotted lines depict low energy neutrons (<10 MeV). The *Cap* corresponds to a cylindrical surface on top of the Pb shield with a radius equal to that of the outer polyethylene layer (~ 1 m) and a height of 40 cm.

would not be reaching the detectors,

2. go into the inside of the Cu cylinder and therefore could reach the detectors and produce a Ge-single and
3. events in which 1 and 2 are in coincidence.

What this study shows is that the rate of type-1 events is greater than the rate of type-2 events from the previous list. An event is defined as an incident neutron with 100 MeV energy on the Pb shield. If I call “cap” the cylindrical surface on top of the Pb shield with a diameters equal to the diameter of the outer polyethylene and with a height of 40 cm then, the results can be described as follows. For every 5 events

going inside the cap, each with 3 or more low energy neutrons (<10 MeV), there is 1 event with one or more low energy neutrons with with an energy between 0.1-20 MeV going into the copper cylinder (with sufficient energy to create a Ge nuclear recoil above 5 keV). Furthermore, for every 3 events going inside the cap, each with 5 or more low energy neutrons (<10 MeV), there is 1 event with one or more low energy neutrons with with an energy between 0.1-20 MeV.

Note that the neutrons going into the inside of the copper cylinder have not created a Ge nuclear recoil. For example, let assume that for every 20 neutrons going into the copper cylinder there is one nuclear recoil. Then, if a detection can be made of the multiple neutrons that go into the Cap with high efficiency using a multiplicity meter replacing the outer polyethylene, this would produce a new background predictor based on the high multiplicity events detected with the multiplicity meter. If I set a multiplicity threshold of 3, then I would have $5 \times 20 \times \epsilon_M^3$ events, at least, before a single Ge nuclear recoil is produced, where ϵ_M is the efficiency to detect a single low energy neutron with the multiplicity meter. If $\epsilon_M = 0.9$ than I would have about 70 to 1 ratio of background predictor events of this type to Ge-singles. If there is a multiplicity threshold of 5, then I would have about 35 to 1 ratio of background predictor events to Ge-singles.

6.7 Gd-loaded water as detector medium

In this section I will describe work that is being done at UC Santa Barbara in collaboration with the group at Case Western Reserve University. The main objective of the work is to investigate if Gd-loaded water can have sufficiently high efficiency in order to be an efficient neutron multiplicity meter for the purpose of counting high-energy neutrons at the Soudan Underground Laboratory along the lines described in the first part of this chapter, given that in terms of handling and cost, the Gd liquid scintilla-

tor makes is less attractive as compared to a Gd water based detector medium. One of the first prototypes is shown in Figure 6.12. The prototype consists in an acrylic cylinder with 61 cm in height and 22 cm in diameter, it is filled with water doped with small amounts of GdCl_3 and it was calibrated using muons crossing the top and bottom caps of the acrylic cylinder. There are two photomultiplier tubes (PMT), one on each end of the cylinder. The top PMT has a 2 in photocathode while the bottom one is 5 in. Furthermore the PMTs are coupled to the detector medium (GdCl_3 doped water) with Winston cones for improvement of the light collection efficiency ($\sim 60\%$ increase was observed). The thresholds were ~ 0.25 and 2 p.e. (photo electrons) for the 2 and 5 inch PMTs respectively.

A ^{252}Cf neutron source was introduced at the center of the cylindrical tank with the objective of measuring multiple low energy neutrons in a time window of several tens of microseconds. The ^{252}Cf neutron source emits neutrons through spontaneous fission reactions, and the number of emitted neutrons has a probability distribution with a mean multiplicity between 3 and 4, as shown in Figure 6.13.

The results for this early prototype are shown on Figure 6.14, showing the rate of multiplicity events as a function of neutron multiplicity for the case where there was no ^{252}Cf neutron source in the cylinder (blue) and for the case where the ^{252}Cf was present (red). Clearly the multiplicity distribution of the emitted neutrons from the source was measured. A good separation is observed between the data with and without the neutron source, confirming how powerful the event topology of the multiplicity events is in order to defeat the ambient gamma background from radioactivity. The same idea is intended for the purpose of underground neutron detection, in this case the source of multiple low energy neutrons would be the cosmogenic high energy neutrons. The gamma background causing the accidentals is not only produced by the ambient gammas but also by the ^{252}Cf neutron source due to some emission of gammas too. The single neutron efficiency achieved was approximately 40%. A new

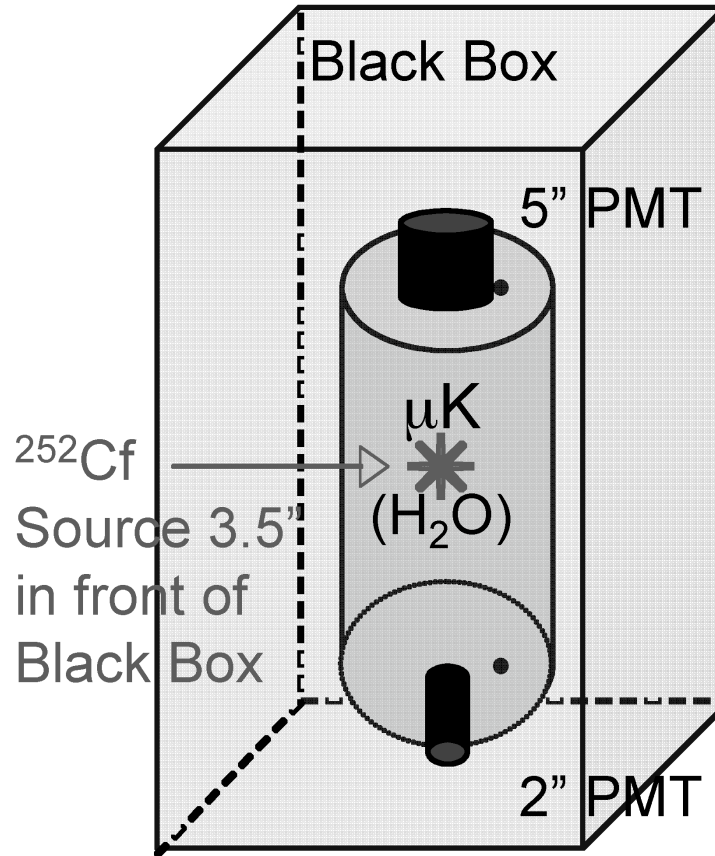


Figure 6.12: Neutron detector prototype build by the UCSB group. The detector medium is GdCl_3 and there is a 2 in and a 5 in photomultiplier tubes on each end of the cylinder. The cylinder has dimensions of 22 cm in diameter and 61 cm in height [234].

prototype is being build as this thesis is written that will further investigate how high the efficiency of GdCl_3 doped water can be obtained by using a larger prototype with improvements to light collection by reflective surface coating and larger PMTs. If the detector medium for the purpose build multiplicity meter described in the previous sections is made of inexpensive and stable Gd-loaded water, then one could think of using the detector medium on top and bottom of the Pb. Figure 6.4 shows that for 40cm thick Pb, there could be a substantial gain in number of neutrons per event and in efficiency (25% at the most since, from the P values for 40 cm thick Pb, $0.70+0.50=1.25$). If there is a 25% increase in efficiency this would increase the total

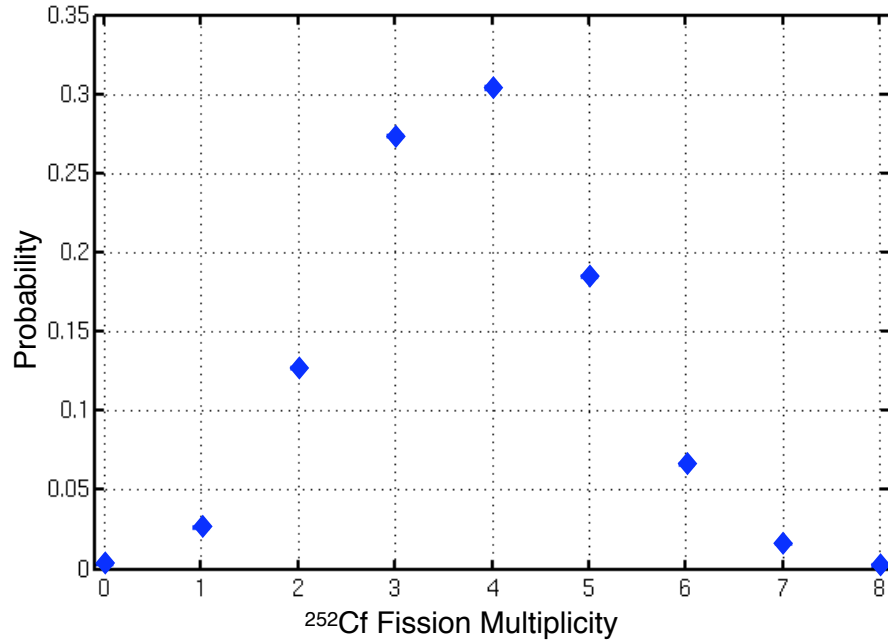


Figure 6.13: The ^{252}Cf multiplicity probability distribution.

rate in a year from 70 to 90 high energy neutrons. Furthermore, there is an overall increase in “detectable” multiplicity that aids in the high-energy neutron detection efficiency.

The measurements produced with this prototype have given confidence on the event topology that we will search deep underground where we expect the neutron multiplicity distribution (in anti-coincidence with large energy depositions in the detector medium) will be dominated by spallation reactions of high-energy neutrons in the Pb target, rather from a spontaneous fission neutron source. We expect that a larger prototype with better light collection as a product of larger PMTs and better reflective surfaces could eventually replace the use of Gd-loaded scintillator by Gd-loaded water.

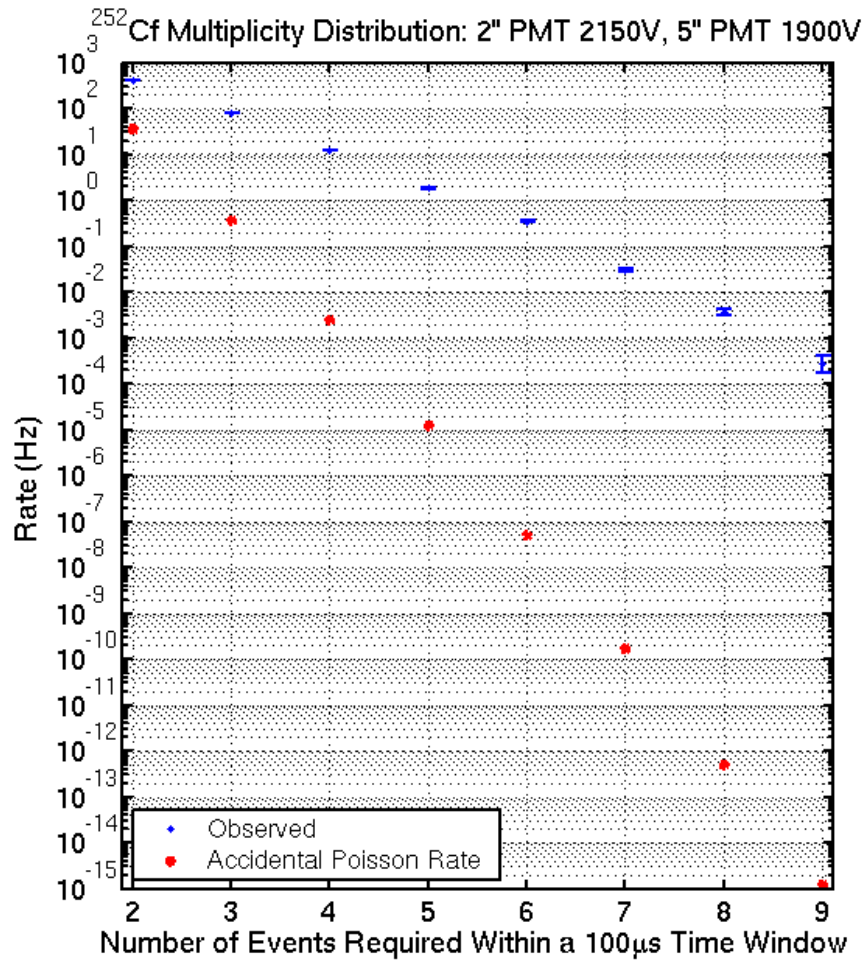


Figure 6.14: Multiplicity distribution measured from a ^{252}Cf with GdCl_3 doped water. The blue data points correspond to the gamma background induced multiplicity distribution while the red data points correspond to the ^{252}Cf neutron source induced multiplicity distribution [234].

6.8 Prospects for the Cosmogenic Neutron Detector Benchmarks

Measuring the absolute high-energy neutron flux and benchmarking the Monte Carlo simulations down to $\sim 12\%$ in a year at Soudan, will allow experiments like CDMS-II, to understand the statistical significance of a WIMP-signal if a few events are observed in the forthcoming data. Maintaining zero background or at least to understand the level of it with a narrow systematic uncertainty will be critical during the next 3 years since the LHC will begin physics runs shortly. Furthermore, the indirect detection experiment, GLAST, has been recently deployed to space and will yield very interesting results. Hence, as discussed in Chapter 1, only the complement between accelerator, direct and indirect detection experiments can provide the necessary cross checks to claim a WIMP discovery and a significant constraint in his properties.

On the side of the value of the underground cosmogenic neutron detector presented in this Chapter, I summarize the benefits and extend in other potential applications such as:

Veto Coincident Data

Even though I have mentioned that the benchmark for the unvetoes CDMS-II neutron rate estimate from Monte Carlo simulations comes from the measurement of the high-energy neutron flux that are in anti-coincidence with muons (mostly) in the detector medium, the cosmogenic neutron detector will provide a measurement of the muon-coincident population too. Furthermore, the angle of the muon could be estimated using the amount of energy deposited in the detector medium (either scintillator or water in this case) and a distribution of high-energy neutron flux as a function of angle could be produced.

Veto Anti-coincident Data

In addition to counting high-energy neutrons greater than ~ 60 MeV in energy, the multiplicity distribution of the low energy neutrons produced will be measured. By characterizing the low energy neutrons produced in the Pb target with a beam of high-energy neutrons could allow us to understand the spectrum of the incident high-energy neutron flux, i.e. there could be the possibility to extract some calorimetry information.

Forward and backward splash

Even though the design studies of the proposed cosmogenic neutron detector show an improved rate when the detector medium is on top of the Pb target, in the case where the detector medium is relatively cheap, one could think of implementing a configuration in which the detector medium is on top and on the bottom of the target. This would allow to benchmark the production of spallation neutrons by muons and high-energy neutrons underground that are “forward” and “backward” splashed, i.e., there would be some information on the angular distribution dependance of the low energy neutrons produced.

Measurements as a function of depth

Even though the cosmogenic neutron detector design was thought for the Soudan Underground Laboratory, at ~ 2000 mwe, one could do the same measurements made at the Soudan site, but as a function of underground depth. A wide variety of shallower sites exist and the rates will be significantly increased, providing better statistics. Nevertheless, since the mean muon energy decreases with depth, the processes that give rise to the unvetoes population, at 2000 mwe for example, could be significantly different from those at 500 mwe.

Different targets

There is the possibility to use different targets too. Even though the high-Z of the target allows for a robust multiplicity signal when an energetic neutron hits the target, one could think on the possibility of using Copper, Polyethylene, a Carbon-rich material or water at a shallower depth in order to understand the spallation reactions in these materials in an underground environment.

* * *

In the remaining of the thesis I will summarize and conclude the work presented, as well as discuss the prospects for CDMS-II at Soudan while maintaining zero-background to maximize discovery potential.

Chapter 7

Conclusions and Prospects for CDMS at Soudan

This thesis presents three main areas of research that I led or was heavily involved: the first 5 tower WIMP-search results, an estimate of cosmogenic backgrounds expected at the Soudan site, and a proposal for a new measurement of high-energy neutrons underground to benchmark the Monte Carlo simulations.

Based on the non-observation of WIMPs and using standard assumptions about the galactic halo [68], the 90% C.L. upper limit of the spin-independent WIMP-nucleon cross section for the first 5 tower run is $6.6 \times 10^{-44} \text{cm}^2$ for a $60 \text{ GeV}/c^2$ WIMP mass. A combined limit using all the data taken at Soudan using Yellin's Optimal Interval method [205] results in an upper limit of $4.6 \times 10^{-44} \text{cm}^2$ at 90% C.L. for a $60 \text{ GeV}/c^2$ WIMP mass. This new limit corresponds to a factor of ~ 3 improvement over any previous CDMS-II limit and a factor of ~ 2 above $60 \text{ GeV}/c^2$ better than any other WIMP search to date. Given that WIMP dark-matter could constitute $\sim 80\%$ of the matter content of the Universe, the significance of the measurement is—avoiding any biased exaggerations—of biblical proportions.

An estimation using FLUKA and MCNPX of the nuclear recoils produced by

cosmic-ray muons and their secondaries underground has been presented for a 5 tower Ge and Si configuration as well as for a 7 supertower array (1 supertower consists of 6 Ge detectors with 1 in thickness and 3 in diameter). The results of the Monte Carlo are that CDMS-II should expect $0.06 \pm 0.02^{+0.18}_{-0.02}$ /kg-year unvetoes single nuclear recoils in Ge for the 5 tower configuration, and $0.05 \pm 0.01^{+0.15}_{-0.02}$ /kg-year for the 7 supertower configuration. The systematic error is based on the available underground neutron data (that we are aware of) that is relevant to the unvetoes neutron population. Therefore, for the runs 123 and 124 we expect < 0.2 events from cosmogenic neutrons.

As the exposure of the CDMS-II increases at the Soudan site, narrowing the statistical and systematic error on the unvetoes rate will become crucial in order to maintain discovery potential and to reliably predict a zero-background environment. I have described a new instrument that, based on my design studies, could measure the absolute flux of high-energy neutrons to about 12% in the span of a year at the Soudan underground laboratory, yielding a factor of ~ 10 reduction of the systematic error. This measurement could play a major role in determining the statistical significance of a discovery if a few WIMP candidates are observed in the CDMS-II data over the next couple of years. An interesting context for WIMP direct detection is that we are at the beginning of the physics runs at the LHC and the recently deployed GLAST mission will make underground WIMP-searches even more interesting due to their complementary nature in terms of determining the existence of WIMP dark matter and its properties.

Furthermore, I have presented how could the implementation of the neutron multiplicity meter as a component of active shielding in low background experiments with cosmogenic neutron background challenges could improve their veto efficiency as well as how it would allow to predict, in a statistical way, the unvetoes neutron rate and, at the same time, benchmark the experiment's cosmogenic Monte Carlo simulations.

Bibliography

- [1] F. Zwicky, *Helv. Phys. Acta*, **6**, 110 (1933).
- [2] V. Rubin, W.K. Ford, *Astrophysical Journal*, **159**, 379 (1970).
- [3] M. Persic, P. Salucci and F. Stel, *Mon. Not. Roy. Astron. Soc.*, **281**, 27 (1996).
- [4] J. F. Navarro, C. S. Frenk and S. D. M. White, *Astrophysical Journal*, **490**, 493 (1997).
- [5] A. Toomre, *Evolution of Galaxies and Stellar Populations*, ed. B. M. Tinsley & R. B. Larson, New Haven: Yale Univ. Press, p. 401 (1977).
- [6] G. A. Mamon, *ApJL*, **401**, L3.
- [7] C. M. Baugh, S. Cole and C. S. Frenk, *MNRAS*, **283**, 1361 (1996).
- [8] V. Springel, S. D. M. White, G. Tormen and G. Kauffmann, *MNRAS*, **328**, 726 (2001).
- [9] A. Romanowsky, N. Douglas, M. Arnaboldi et al., *Science*, **301**, 1696 (2003).
- [10] A. Dekel et al., *Nature*, **437**, 707-710 (2005); 21st IAP meeting, *Mass Profiles and Shapes of Cosmological Structures*, ed. G. A. Mamon, F. Combes, C. Deffayet & B. Fort (Paris: EDP).
- [11] F. Zwicky, *Astrophysical Journal*, **86**, 217 (1937).

- [12] J. Oort, *Bull. Astron. Inst. Netherlands*, **6**, 249 (1932).
- [13] J. D. Bekenstein, *Phys. Rev. D*, **70**, 083509 (2004).
- [14] J. R. Brownstein and J.W. Moffat, *MNRAS*, **367**, 527 (2006).
- [15] F. W. Dyson, A. S. Eddington and C. R. Davidson, *Mem. R. Astron. Soc.*, **62**, 291 (1920).
- [16] D. E. Lebach et al., *Phys. Rev. D*, **75**, 1439 (1995).
- [17] Burles, Nollet and Turner *Big-Bang Nucleosynthesis: Linking Inner Space and Outer Space*, astro-ph/9903300.
- [18] W. Freedman et al., *Astrophysical Journal*, **553**, 47 (2001).
- [19] L. M. Krauss and B. Chaboyer, astro-ph/0111597
- [20] J. C. Mather et al., *Astrophysical Journal*, **420**, 445 (1994).
- [21] G. Hinshaw et al., *Astrophysical Journal*, **170**, 288 (2007).
- [22] W. C. Jones et al., *Astrophysical Journal*, **647**, 623 (2006).
- [23] C. L. Kuo et al., *Astrophysical Journal*, **600**, 32 (2004).
- [24] A. C. S. Readhead et al., *Astrophysical Journal*, **609**, 498 (2004).
- [25] C. Dickinson *MNRAS*, **353**, 732 (2004).
- [26] W. Baade, *Astrophysical Journal*, **88**, 285 (1938); C. Kowal, *Astron. J.*, **73**, 1021 (1968).
- [27] A. Reiss et al., *Astronomical Journal*, **116**, 1009 (1998).
- [28] S. Perlmutter et al., *Astrophysical Journal*, **517**, 565 (1999).

- [29] D. N. Spergel et al., *Astrophysical Journal*, **170**, 377 (2007).
- [30] S. Perlmutter, *Physics Today*, **56**, 53 (2003).
- [31] M. M. Colless et al., *MNRAS*, **328**, 1039 (2001).
- [32] M. Tegmark et al., *Astrophysical Journal*, **606**, 702 (2004).
- [33] S. Cole et al., *MNRAS*, **362**, 505 (2005).
- [34] B. Paczyński, *Astrophysical Journal*, **304**, 1 (1986).
- [35] K. Griest, *Astrophysical Journal*, **366**, 412 (1991).
- [36] R. J. Nemiroff, *Astron. Astrophys.*, **247**, 73 (1991); A. De Rujula et al., *Astron. Astrophys.*, **254**, 99 (1992).
- [37] S. D. M. White, C. S. Frenk and M. Davis, *Astrophysical Journal*, **274**, L1-5 (1983).
- [38] D. Clowe et al., *Astrophysical Journal*, **609**, 596 (2004).
- [39] D. Clowe et al., *Astrophysical Journal*, **648**, 109 (2006).
- [40] Ya. B. Zel'dovich, *Zh. Eksp. Teor. Fiz.*, **48**, 986 (1965).
- [41] Ya. B. Zel'dovich, L. B. Okun and S. B. Pikelner, *Usp. Fiz. Nauk.*, **84**, 113 (1965).
- [42] H.-Y. Chiu, *Phys. Rev. Lett.*, **17**, 712 (1996).
- [43] G. Jungman, M. Kamionkowski and K. Griest in *Physics Reports*, bf 267, 195 (1996).
- [44] B. Lee and S. Weinberg, *Phys. Rev. Lett.*, **39**, 165 (1977).

- [45] H. Dahle, *The NOT in the 2000s*, ed. N. Bergvall, L. O. Takalo and V. Pirola (Piikkio: Univ. Turku), **45** (2000).
- [46] H. Dahle et al., *Astrophysical Journal*, **579**, 227 (2002).
- [47] N. A. Bahcall, L. M. Lubin and V. Dorman, *Astrophysical Journal*, **447**, L81 (1995).
- [48] N. Bahcall et al., *Astrophysical Journal*, **541**, 1 (2000).
- [49] Gordon L. Kane, *TASI lectures: weak scale supersymmetry -a top-motivated-bottom-up approach*, arXiv:hep-ph/0202185v2.
- [50] J. Ellis, J.S. Hagelin, D.V. Nanopoulos, K.A. Olive and M. Srednicki, *Nucl. Phys. B*, **238**, 453 (1984).
- [51] Dan Hooper and Edward Baltz, *Annu. Rev. Nucl. Part. Sci.*, **58** (2008).
- [52] R. D. Peccei, H. R. Quinn, *Phys. Rev. Lett.* **38**, 1440 (1997); *Phys. Rev. D* **16**, 1791 (1977).
- [53] P. G. Harris et al., *Phys. Rev. Lett.*, **82**, 904 (1999).
- [54] J. E. Kim, *Phys. Rev. Lett.*, **43**, 103 (1979).
- [55] M. A. Shifman, A. I. Vainshtein and V. I. Zakharov, *Nucl. Phys. B*, **166**, 493 (1979).
- [56] A. R. Zhitnitskii, *Soviet Journal of Nuclear Physics*, **31**, 269 (1980).
- [57] M. Dine, W. Fischler and M. Srednicki, *Phys. Lett. B*, **104**, 199 (1981).
- [58] G. G. Raffelt, *Phys. Rep.*, **198**, 1

- [59] E. W. Kolb and M. S. Turner, *The Early Universe, Frontiers in Physics*, Vol. 69 (1990).
- [60] M. S. Turner, *Phys. Rep.*, **197**, 67 (1990).
- [61] R. Bradley et al., *Reviews of Modern Physics*, **75**, 777 (2003).
- [62] P. Sikivie, *Phys. Lett. B*, **567**, 1 (2003).
- [63] P. Sikivie, *Phys. Rev. Lett.* **51**, 1415 (1983); *Phys. Rev. D* **32**, 2988 (1985).
- [64] Karl van Bibber and Leslie J. Rosenberg, *Physics Today*, August 2006.
- [65] S. J. Asztalos et al., *Phys. Rev. D* **69**, 011101 (2004).
- [66] Gianpalo Carosi and Karl van Bibber, *Cavity Microwave Searches for Cosmological Axions*, arXiv:hep-ex/0701025v1.
- [67] W. de Boer et al., *Eur. Phys. J.*, **33**, S981 (2001); W. de Boer et al., *Physical Letters B*, **636**, 13 (2006); *Physical Review Letters*, **95**, 209001, (2005).
- [68] J. D. Lewin and P.F. Smith *Astroparticle Physics*, **6**, 87 (1996).
- [69] R. J. Gaitskell, *Annu. Rev. Nucl. Part. Sci.*, **54**, 315 (2004).
- [70] A. K. Drukier, K. Freese and D. N. Spergel, *Phys. Rev. D*, **33**, 3495 (1986).
- [71] K. Freese, J. Frieman and A. Gould, *Phys. Rev. D*, **37**, 3388 (1988).
- [72] D. N. Spergel, *Phys. Rev. D*, **37**, 1353 (1988).
- [73] B. Morgan, A.M. Green and N.J.C. Spooner, *Phys. Rev. D*, **71**, 123501 (2005).
- [74] C.J. Copi, L.M. Krauss, D. Simmons-Duffin, S.R. Stroiney, *Phys. Rev. D*, **75**, 023514 (2007) arXiv:astro-ph/0508649.

- [75] N. Gehrels and P. Michelson, *Astropart. Phys.*, **11**, 277 (1999).
- [76] Hank Sobel, *DMSAG Draft Report*, AAAC Meeting (2007).
- [77] S.P. Langley, *Proceedings of the American Academy of Arts and Sciences XVI* (1981).
- [78] C. Enss and D. McCammon, *Journal of Low Temperature Physics*, **151**, 5 (2008).
- [79] webpage: <http://www.cresst.de>
- [80] G. Angloher, et al., *Astroparticle Physics*, **23**, 325 (2005).
- [81] webpage: <http://edelweiss2.in2p3.fr>
- [82] V. Sanglard et al., *Phys. Rev. D*, **71**, 122002 (2005).
- [83] E. Aprile et al., *New Astron. Rev.*, **49**, 289 (2005).
- [84] D.B. Cline et al., *Nucl. Phys. B Proc. Suppl.*, **124**, 229 (2003).
- [85] A. Rubbia, *Nucl. Phys. B Proc. Suppl.*, **149**, 197 (2005).
- [86] R. Brunetti et al., *New Astron. Rev.*, **49**, 265 (2005).
- [87] A. Hitachi et al., *Phys. Rev. B*, **27**, 5279 (1983).
- [88] J.A. Nikkel et al., *Astropart. Phys.* (2007) submitted.
- [89] D.N. McKinsey and K.J. Coakley, *Astropart. Phys.*, **22**, 355 (2005).
- [90] M.G. Boulay and A. Hime, *Astropart. Phys.*, **25**, 179 (2006).
- [91] G.J. Alner et al., *Nucl. Instrum. and Meth. in Phys. Res. A*, **535**, 644 (2004).
- [92] D. Dujmic et al., *Nucl. Instrum. and Meth in Phys. Res. A*, **584**, 327 (2008).

- [93] G.J. Alner et al., *Nucl. Instrum. and Meth. in Phys. Res. A*, **555**, 173 (2005).
- [94] D.A. Glaser, *Nucl. Phys. B (Proc. Suppl.)* **36**, 3 (1994).
- [95] W.J. Bolte et al., *Nucl. Instr. and Meth. in Phys. Res. A*, **577**, 569 (2007).
- [96] E. Behnke et al., *Science*, **319**, 933 (2008).
- [97] C.E. Aalseth et al., *Experimental constraints on a dark matter origin for the DAMA annual modulation effect*, arXiv:0807.0879 [astro-ph].
- [98] P.S. Barbeau, J.I. Collar and O. Tench, *JCAP*, **09**, 009 (2007).
- [99] P. Benetti et al., *Nucl. Instrum. and Methods in Phys. Res., Sect A*, **574**, 83 (2007).
- [100] R. Bernabei et al., *La Rivista del Nuovo Cimento*, **26**, 1 (2003).
- [101] R. Bernabei et al., *Phys. Lett. B*, **389**, 757 (1996); R. Bernabei et al. *Phys. Lett. B*, **424**, 195 (1998); R. Bernabei et al., *Phys. Lett. B*, **450**, 448 (1999); P. Belli et al., *Phys. Rev. D*, **61**, 023512 (2000).
- [102] R. Bernabei et al., *First results from DAMA/LIBRA and the combined results with DAMA/NaI*, arXiv:0804.2741v1.
- [103] C. Savage, P. Gondolo and K. Freese, *Phys. Rev. D*, **70**, 123513 (2004).
- [104] P. Gondolo and G. Gelmini, *Phys. Rev. D*, **71**, 123520 (2005).
- [105] N.W. Evans, F. Ferrer and S. Sarka, *Phys. Rev. D*, **69**, 123501(2004).
- [106] L. Pieri, E. Branchini and S. Hofmann, *Phys. Rev. Lett.*, **05**, 211301 (2005).
- [107] F. Aharonian et al., [The HESS Collaboration], arXiv:astro-ph/0408145.
- [108] J. Albert et al., [The MAGIC Collaboration], *Astrophys. J.*, **638**, 101 (2006).

- [109] K. Kosack et al., [The VERITAS Collaboration], *Astrophys. J.*, **608**, 97 (2004).
- [110] K. Tsuchiya et al., [The CANGAROO-II Collaboration], *Astrophys. J.*, **606**, 17 (2005).
- [111] D. P. Finkbeiner, *Astrophys. J.*, **614**, 186 (2004).
- [112] D. P. Finkbeiner, [arXiv:astro-ph/0409027](https://arxiv.org/abs/astro-ph/0409027).
- [113] V. Barger, Wai-Yee Keung and G. Shaughnessy, [arXiv:0709.3301](https://arxiv.org/abs/0709.3301).
- [114] F. Halzen and D. Hooper, *Phys. Rev. D*, **73**, 123507 (2006).
- [115] T. DeYoung [IceCube Collaboration], *Int. J. Mod. Phys. A*, **20**, 3160 (2005).
- [116] P. Sapienza, *Nucl. Phys. Proc. Supple.*, **145**, 331 (2005).
- [117] S. Desai et al., [Super-Kamiokande Collaboration], *Phys. Rev. D* **70**, 083523 (2004) [Erratum-ibid. D **70**, 109901 (2004)].
- [118] E. A. Baltz and J. Edsjo, *Phys. Rev. D*, **59**, 023511 (1999).
- [119] A. Morselli and P. Picozza, *Prepared for the 4th International Workshop on the Identification of Dark Matter (IDM 2002)*, York, England, 2-6 Sep 2002.
- [120] S. W. Barwick et al.[HEAT Collaboration], *Astrophys. J.*, **482**, 191 (1997); S. Coutuet al.[HEAT Collaboration], in Proceedings of the 27th ICRC (2001).
- [121] Olzem Jan [AMS Collaboration], *Talk given at the 7th UCLA Symposium on Sources and Detection of Dark Matter and Dark Energy in the Universe*, Marina del Rey, CA, Feb 22-24 (2006).
- [122] M. Sapinski [AMS Collaboration], *Acta Phys. Polon. B*, **37**, 1991 (2006); C. Goy [AMS Collaboration], *J. Phys. Conf. Ser.*, **39**, 185 (2006).

- [123] I. V. Moskalenko and A. W. Strong, *Astrophys. J.*, **493**, 694 (1998).
- [124] F. Donato, N. Fornengo and P. Salati, *Phys. Rev. D*, **62**, 043003 (2000).
- [125] K. Mori, C. J. Hailey, E.A. Baltz, W.W. Craig, M. Kamionkowski, W.T. Serber and P. Ullio, *Astrophys. J.*, **566**, 604 (2002).
- [126] C.J. Hailey et al., *Nucl. Instr. and Meth. in Phys. Res. B*, **214**, 122 (2004).
- [127] C.J. Hailey et al., *Journal of Cosmology and Astroparticle Physics*, **1**, 7 (2006).
- [128] L. Arruda, F. Barao and R. Pereira, ArXiv e-prints **710** (2007), 0710.0993.
- [129] D.S. Akerib, E. Aprile et al.(S1 Dark Matter Working Group) , *Deep Underground Science and Engineering Lab*, astro-ph/0605719v2.
- [130] J. Edsjo, in preparation.
- [131] S. Dawson, E. Eichten and C. Quigg, *Phys. Rev. D*, **31**, 1581 (1985).
- [132] E.A. Baltz, M Battaglia, M.E. Peskin and T. Wizansky, *Phys. Rev. D*, **74**, 103521 (2006).
- [133] T. Shutt et al., in *Low Temperature Detectors*, edited by F.S. Porter, D. McCammon, M. Galeazzi and C.K. Stahle, AIP Conference Proceedings No. 605 (AIP, Melville, New York, 2002), p. 513.
- [134] B. Neganov and V. Trofimov, *Otkrytia, Izobreteniya*, **146**, 215 (1985).
- [135] P.L. Luke, *J. Appl. Phys.*, **64**, 6858 (1988).
- [136] T. Shutt, Ph. D. Thesis, University of California, Berkeley, 1993 (<http://cdms.berkeley.edu/Dissertations/>).

- [137] P.D. Barnes, Jr. , *Ph. D. Thesis*, University of California, Berkeley, 1996
(<http://cdms.berkeley.edu/Dissertations/>).
- [138] J.D. Taylor et al., *Adv. Cryog. Eng.*, **41**, 1971 (1996).
- [139] D.S. Akerib et al., *Nucl. Instr. and Meth. in Phys. Res. A*, **400**, 181 (1997).
- [140] V. Mandic, *Ph. D. Thesis*, University of California, Berkeley, 2004
(<http://cdms.berkeley.edu/Dissertations/>).
- [141] K.D. Irwin et al., *Rev. Sci. Instrum.*, **66**, 5322 (1995).
- [142] R.W. Ogburn, Ph.D. thesis. Stanford University, 2008
(<http://cdms.berkeley.edu/Dissertations/>).
- [143] T. Saab, *Ph. D. Thesis*, Stanford University, 2002
(<http://cdms.berkeley.edu/Dissertations/>).
- [144] R. Clarke, Ph. D. Thesis, Stanford University, 1999
(<http://cdms.berkeley.edu/Dissertations/>).
- [145] T. Shutt et al., *Nucl. Instrum. and Meth. in Phys. Res. A*, **444**, 340 (2000).
- [146] J. Allison et al., *IEEE Trans. Nucl. Sc.*, **53**, 270 (2006).
- [147] T. Bruch, *Comparison of Ba calibration data with MC simulations*, Internal R123 Ebook Notes # 93.
- [148] GEANT Version 3.21.04, *GEANT User's Guide*, CERN, Geneva (1995).
- [149] S. Kamat, *Ph. D. Thesis*, Case Western Reserve University, 2005
(<http://cdms.berkeley.edu/Dissertations/>).
- [150] W. R. Leo, *Techniques for Nuclear and Particle Physics Experiments*, Springer-Verlag (1988).

- [151] T. Bruch, *Comparison of Run 123 gamma spectra with MC simulations*, CDMS ebook note, January 2008.
- [152] L. Baudis, *Gamma background, before/after purge*, CDMS Run 118 ebook note #224, May 2004.
- [153] CDMS Collaboration, in preparation.
- [154] J. Hall, *Neutron Activation of Copper*, CDMS ebook note #104, October 2007.
- [155] S. Agostinelli et al., GEANT4 Collaboration, *Nucl. Instrum. and Meth. in Phys. Res.*, **A506** (2003).
- [156] W.B. Wilson, et al. *Los Alamos National Laboratory Report*, LA-13639-MS, 1999.
- [157] T. Florkowski, L. Morawska and Rozanski, *Nucl. Geophys.*, **2**, 1 (1998).
- [158] M. Tarka, CDMS ebook note.
- [159] G. Heusser, M. Laubenstein, H. Neder, *Radioactivity in the Environment*, **8**, 495 (2006).
- [160] D.S. Leonard et al. (EXO Collaboration) arXiv:0709.4524v1 [physics.ins-det].
- [161] P. Grinberg, S Willie and R.E. Sturgeon, *Anal. Chem.*, **77**, 2432 (2005).
- [162] J. A. Formaggio and C. J. Martoff, *Annu. Rev. Nucl. Part. Sci.*, **54**, 361 (2004).
- [163] Thomas K. Gaisser, *Cosmic Rays and Particle Physics*, Cambridge University Press (1990).
- [164] A. Fasso', A. Ferrari, J. Ranft, and P.R. Sala, *FLUKA: a multi-particle transport code*, **CERN-2005-10** (2005), **INFN/TC_05/11**, **SLAC-R-773**.

- [165] A. Fasso', A. Ferrari, S. Roesler, P.R. Sala, G. Battistoni, F. Cerutti, E. Gadioli, M.V. Garzelli, F. Ballarini, A. Ottolenghi, A. Empl and J. Ranft, *The physics models of FLUKA: status and recent developments*, Computing in High Energy and Nuclear Physics 2003 Conference (CHEP2003), La Jolla, CA, USA, March 24-28, 2003, (paper MOMT005), eConf C0303241 (2003), arXiv:hep-ph/0306267.
- [166] J.S. Hendricks et al. LA-UR-07-6632 available from <http://mcnpx.lanl.gov>
- [167] C. Berger et al. *Phys. Rev. D*, **40**, 2163 (1989).
- [168] M. Ambrosio et al. *Phys. Rev. D*, **52**, 3793 (1995).
- [169] M. Anglietta et al. *Astropart. Phys.*, **3**, 311 (1995).
- [170] M. Crouch, *Proc. Int. Cosmic Ray Conf., 20th, Moscow*, **6**, 165 (1987).
- [171] Y. Andreev et al. *Proc. Int. Cosmic Ray Conf., 26th, Moscow*, **6**, 200 (1987).
- [172] K. Hagiwara et al., *Phys. Rev. D*, **66**, 010001 (2002).
- [173] K. Ruddick *NuMI-L-210*, NuMI-Minos Internal Note, September 1996.
- [174] R. Nelson, CDMS Internal Note 0307001.
- [175] S. Yellin, *Throwing Muons on the Surface of a Box in the Soudan Mine*, CDMS Internal Note, September 2004.
- [176] O. C. Allkofer and P. K. F. Greider, *Cosmic Rays on Earth*, Volume 25-1, Fachinformationzentrum, Germany, 1984.
- [177] S. Miyake, *Rapporteur Paper on Muons and Neutrons*, PICRC, **5** (1973).
- [178] P. Cushman, *Comparison of the Input Muon Distributions used for CDMS Neutron Simulations*, CDMS Internal Note, December 2006.

- [179] S. Kasahara, *Ph. D. Thesis*, University of Minnesota, March 1997
(<http://www.hep.umn.edu/theses/kasahara.ps.gz>).
- [180] P. Antonioli et al., *Astropart. Phys.*, **7**, 357 (1997).
- [181] R. Hennings-Yeomans, *R123 Veto-coincident low yield events*, CDMS ebook note #151, July 2007.
- [182] R. Hennings-Yeomans, *R124 Veto-coincident low yield events and R123/R124 combined rates*, CDMS ebook note #190, July 2007.
- [183] S.A. Pozzi, E. Padovani, and M. Marseguerra, *Nucl. Instrum. and Meth. in Phys. Res.* **A513**, 550-558 (2003).
- [184] S. Kamat, *Propagation of 1 MeV neutrons in a block of Germanium using Geant 3*, CDMS backgrounds ebook note, February 2003.
- [185] H. R. T. Wulandari, PhD Thesis, Technischen Universitt Munchen, 2003.
- [186] Sunil R. Golwala, *Ph. D. Thesis*, University of California at Berkeley, 2000
(<http://cdms.berkeley.edu/Dissertations/>).
- [187] Donald D. Driscoll, *Ph. D. Thesis*, Case Western Reserve Univesity, 2008
(<http://cdms.berkeley.edu/Dissertations/>).
- [188] Clarence L. Change, *Ph. D. Thesis*, Stanford University, 2004
(<http://cdms.berkeley.edu/Dissertations/>).
- [189] J. Filippini and R. Hennings-Yeomans, *New datum calibrations for Run 123*, CDMS ebook note #16 and #17, December 2006.
- [190] M. Pyle, *Possible Explanations of Energy Dependance seen in Timing Parameters*, CDMS ebook note #26, March 2006.

- [191] J. Filippini, *Effect of noise features on OF charge resolution*, CDMS ebook note #46, March 2007.
- [192] J. Filippini, *Effect of noise features on OF charge resolution*, CDMS ebook note #46, March 2007.
- [193] M. Pyle and B. Serfass, *Run 123: Preliminary Qinner cut*, CDMS ebook note #60, May 2007.
- [194] X. Qiu and L. Duong, *R123 Charge Threshold Cut*, CDMS ebook note #95, August 2007.
- [195] J. Filippini, *Preliminary R123 Efficiencies*, CDMS ebook note #160, December 2007.
- [196] J. Filippini, *Run-by-Run Fits to R123 Noise Blobs*, CDMS ebook note #153, December 2007.
- [197] J. Filippini, *R123 Singles Efficiencies*, CDMS ebook note #145, December 2007.
- [198] J. Filippini, *Third pass at R123 bands*, CDMS ebook note #111, October 2007.
- [199] J. Sander, *Measuring the Veto Muon Rejection Efficiency*, CDMS (Run 119) ebook note #323, February 2006.
- [200] R. Hennings-Yeomans, *Veto cut for R123: cVTStrict123*, CDMS ebook note #94, August 2007.
- [201] X. Qiu, *Run 123 pminrtc+pdelc timing parameter surface event cut*, CDMS ebook note #118, November 2007.
- [202] CDMS Collaboration, inpreparation.
- [203] D.S. Akerib et al. (CDMS Collaboration), *Phys. Rev. D* , **72**, 052009 (2005).

- [204] D.S. Akerib et al. (CDMS Collaboration), *Phys. Rev. Lett.* **96**, 011102 (2006);
D.S. Akerib et al., (CDMS Collaboration), *Phys. Rev. D*, **73**, 011102 (2006).
- [205] S. Yellin, *Phys. Rev. D*, **66**, 032005 (2002).
- [206] CDMS Collaboration, in preparation.
- [207] J. Angle et al., (XENON Collaboration), *Phys. Rev. Lett.*, **100**, 021303 (2008).
- [208] E.A. Baltz and P. Gondolo, *JHEP* 10(2004) 052.
- [209] L. Roszkowski et al., *JHEP*, 07(2007) 075.
- [210] R.J. Gaitskell, V. Mandic and J. Filippini, <http://dmttools.brown.edu>
- [211] R. Hennings-Yeomans and D.S. Akerib, *Nucl. Instr. and Meth. in Phys. Res.*,
A574, 89 (2007).
- [212] F. Boehm et al., *Phys. Rev. D* **62**, 092005 (2000).
- [213] R. Hertenberger, M. Chen, and B.L. Dougherty, *Phys. Rev. C* **52**, 3449 (1995).
- [214] L.B. Bezrukov et al., *Yad. Fiz.* **17**, 98 (1973) [*Sov. J. Nucl. Phys.* **17**, 51 (1973)].
- [215] M. Aglietta et al., *Nuovo Cimento Soc. Ital. Fis., C* **12**, 467 (1989).
- [216] Wang et al., *Phys. Rev. D* **64**, 013012 (2001).
- [217] A. Fassio' et al., *Proceedings of the 3rd Workshop on Simulating Accelerator
Radiation Environments (SARE 3)*, edited by H. Hirayama, KEK Proceedings
No. 97-5 (KEK, Tsukuba, Japan, 1997), p. 32.
- [218] C. Galbiati and J.F. Beacom *Phys. Rev. C* **72**, 025807 (2005)

- [219] A. Fass'o et al., *Electron-photon transport in FLUKA: Status*, Proceedings of the MonteCarlo 2000 Conference, Lisbon, October 23-26 2000, A. Kling, F. Barao, M. Nakagawa, L. Tavora and P. Vaz eds., Springer-Verlag Berlin, p. 159 (2001); Fass'o A et al., *FLUKA: Status and Prospective for Hadronic Applications*, Proceedings of the MonteCarlo 2000 Conference, Lisbon, October 23- 26 2000, A. Kling, F. Barao, M. Nakagawa, L. Tavora and P. Vaz eds., Springer-Verlag Berlin, p. 955 (2001).
- [220] KamLAND Collaboration, T. Araki et al., *Phys. Rev. Lett.* **94**, 081801 (2005).
- [221] M. Aglietta et al. (LVD Collaboration), in Proc. of 26th Intern. Cosmic Ray Conf., Salt Lake City (USA), August 17-25, 1999 (hep-x/9905047).
- [222] D.-M. Mei and A. Hime, *Phys. Rev. D* **73**, 053004 (2006).
- [223] V.A. Kudryavtsev (private communication).
- [224] N. Agafonova et al., *Study of muon-induced neutron production, propagation and energy spectrum with the LVD detector at LNGS*, Proceeding of the 29th International Cosmic Ray Conference, Pune, 239 (2005).
- [225] V. Chazal et al., *Nucl. Instrum. and Meth. in Phys. Res.*, **A490**, 334 (2002).
- [226] H.M. Araujo, V.A. Kudryavtsev, N.J.C. Spooner, and T.J. Sumner, *Nucl. Instrum. and Meth. in Phys. Res.*, **A545**, 398-411 (2005).
- [227] F.F. Kalchukov et al., *Il Nuovo Cimento*, **18**, 517 (1995).
- [228] G.V. Gorshkov and V.A. Zyabkin, *Sov. J. Nucl. Phys.* **7**, 470 (1968); *ibid.* **12**, 187 (1971); G.V. Gorshkov, V.A. Zyabkin, and R.M. Yakovlev, *ibid.* **13**, 450 (1974); *ibid.* **18**, 57 (1974).
- [229] E. Cheifetz et al., *Phys. Rev. C* **6**, Vol. 4, 1348 (1972).

- [230] U. Jahnke et al., *Nucl. Instrum. and Meth. in Phys. Res.*, **A508**, 295-314 (2003).
- [231] J. Sander, CDMS Internal Notes (private communication).
- [232] M. Nakahata *LRT2004* Conference, <http://lrt2004.sno1ab.ca>, December 2004.
- [233] D.S. Akerib et al. (CDMS Collaboration), *Phys. Rev. D* **68**, 082002 (2003).
- [234] Harry N. Nelson et al., *Private Communication*, March 2008.